AD-A199 170

DTIC FILE COPY

(2)

AGARD-CP-403

AGARD-CP-403

AGARD

ADVISORY GROUP FOR AEROSPACE RESEARCH & DEVELOPMENT

7 RUE ANCELLE · 92201 NEUILLY SUR SEINE FRANCE

AGARD CONFERENCE PROCEEDINGS No.403

Static Aeroelastic Effects on High Performance Aircraft

DTIC
ELECTE
DEC 2 1 1987
S D

NORTH ATLANTIC TREATY ORGANIZATION

DISTRIBUTION AND AVAILABILITY ON BACK COVER

DISTRIBUTION STATEMENT A
Approved for public release
Distribution Unlimited

87 12 10 020

AGARD-CP-403

NORTH ATLANTIC TREATY ORGANIZATION

ADVISORY GROUP FOR AEROSPACE RESEARCH AND DEVELOPMENT

(ORGANISATION DU TRAITE DE L'ATLANTIQUE NORD)

AGARD Conference Proceedings No.403

STATIC AEROELASTIC EFFECTS ON HIGH PERFORMANCE AIRCRAFT

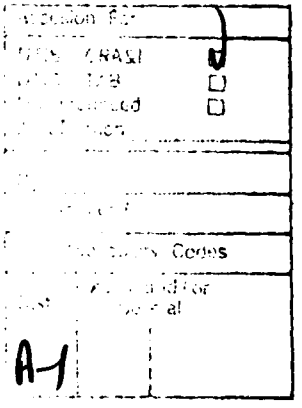

DTIC
COPY
INSPECTED
4

Papers presented at the 63rd Meeting of the Structures and Materials Panel of AGARD, in Athens, Greece, 28 September—3 October 1986.

THE MISSION OF AGARD

The mission of AGARD is to bring together the leading personalities of the NATO nations in the fields of science and technology relating to aerospace for the following purposes:

- Exchanging of scientific and technical information;
- Continuously stimulating advances in the aerospace sciences relevant to strengthening the common defence posture;
- Improving the co-operation among member nations in aerospace research and development;
- Providing scientific and technical advice and assistance to the Military Committee in the field of aerospace research and development (with particular regard to its military application);
- Rendering scientific and technical assistance, as requested, to other NATO bodies and to member nations in connection with research and development problems in the aerospace field;
- Providing assistance to member nations for the purpose of increasing their scientific and technical potential;
- Recommending effective ways for the member nations to use their research and development capabilities for the common benefit of the NATO community.

The highest authority within AGARD is the National Delegates Board consisting of officially appointed senior representatives from each member nation. The mission of AGARD is carried out through the Panels which are composed of experts appointed by the National Delegates, the Consultant and Exchange Programme and the Aerospace Applications Studies Programme. The results of AGARD work are reported to the member nations and the NATO Authorities through the AGARD series of publications of which this is one.

Participation in AGARD activities is by invitation only and is normally limited to citizens of the NATO nations.

The content of this publication has been reproduced
directly from material supplied by AGARD or the authors.

Published July 1987

Copyright © AGARD 1987
All Rights Reserved

ISBN 92-835-0424-0

Printed by Specialised Printing Services Limited
40 Chigwell Lane, Loughton, Essex IG10 3TZ

PREFACE

There are several static aeroelastic effects and related problems which are of considerble importance in the design of modern high-performance aircraft. Static aeroelastic effects are manifested in the form of changes in the aerodynamic load or lift distribution on the aircraft. These changes affect the structural integrity of the vehicle, its static aeroelastic and flight stability, the effectiveness of control surfaces, and the overall flight performance. The characteristics and magnitude of these aeroelastic effects are dependent on the aerodynamic shape of the vehicle, its structural stiffness, and the particular flight conditions primarily in terms of Mach number and dynamic pressure. For optimal structural and flight control system design, all these static aeroelastic effects must be taken into account in a realistic manner, and this demands coordinated effort in several areas.

In this Specialists' meeting on "Static Aeroelastic Effects on High-Performance Aircraft" instances of these problems are reviewed and it is demonstrated how modern tools for structural and aeroelastic analyses can be successfully applied in view of structural optimization. The individual papers of the Meeting cover many aspects of static aeroelasticity not only for military aircraft but also for modern transport aircraft. The various papers also address problems and recent progress in windtunnel model testing, in particular measurement of static deformations on windtunnel models.

H.Försching
Chairman, Subcommittee on
Aeroelasticity

ABSTRACT

Modern high performance aircraft designs tend to employ very thin airfoils having a degree and a distribution of stiffness far from the ideal; in consequence, there is a loss of control effectiveness and manoeuverability. Moreover, the introduction of the highly forward-swept-wing planform poses a static aeroelastic effect of fundamental importance; these effects are felt at model as well as at full scale. This meeting was organized not only to review instances of these problems but to see how successfully modern tools for structural and aeroelastic analysis can be applied.

The individual papers of the meeting cover many aspects of static aeroelasticity not only for military aircraft but also for modern transport aircraft. The various papers also address problems and recent progress in wind tunnel model testing, in particular measurement of static deformations on wind tunnel models.

RESUME

Les avions modernes à hautes performances ont tendance à utiliser des voilures très minces ayant un degré de rigidité et une répartition de cette rigidité qui sont loin de l'idéal; en conséquence, on observe une perte d'efficacité des commandes et de maniabilité. En outre, l'introduction de la forme d'ailes à forte flèche négative pose un problème d'effet aéroélastique statique d'une importance capitale; de tels effets se ressentent sur les maquettes aussi bien qu'en vrai grandeur. Cette réunion a été organisée non seulement pour passer en revue des exemples de ces problèmes mais aussi pour voir dans quelle mesure les outils modernes destinés à l'analyse structurale et aéroélastique peuvent être utilisés efficacement.

Les exposés particuliers présentés au cours de la réunion traitent de nombreux aspects de l'aéroélasticité statique non seulement des avions militaires mais aussi des avions de transport modernes. Les différents exposés traitent également des problèmes recontrés et des progrès récents enregistrés au cours des essais sur maquette en soufflerie, en particulier en ce qui concerne la mesure des déformations statiques observées sur des maquettes en soufflerie.

CONTENTS

Examples of Static Aeroelastic Effects on Present Combat Aircraft Projects

by

W. E. Sharpe
Principal Aerodynamicist

and

J. B. Newton
Senior Aerodynamicist

Aerodynamics Department,
British Aerospace Plc,
Military Aircraft Division,
Warton, Preston,
Lancashire, PR4 1AX

Abstract

The paper first describes results of static aeroelastic calculations for a recent canard/cranked delta fighter project, in which a complete aircraft aerodynamic and structural model is used to demonstrate fully-interacted "free" aircraft deflection modes and resulting stability effects. The significance of these results is illustrated by comparison with corresponding "fixed root" calculations, thereby indicating a requirement for complete aircraft aeroelastic modelling at the earliest possible stage in project design.

Aeroelastic modelling of external stores in the context of store/aircraft integration is also discussed.

Finally, the correction of high-speed wind-tunnel model results for aeroelastic distortion is addressed, indicating those parameters which are likely to be significantly affected.

Notation

B	Moment of inertia in pitch
Q	Free-stream dynamic pressure = $\frac{1}{2}\rho V^2$
ρ	Ambient density
V	Free-stream velocity
S	Wing reference area
b	Wing span
$\bar{c}$	Wing mean aerodynamic chord
C_L	Lift coefficient = lift/QS
C_M	Pitching moment coefficient = pitching moment/$QS\bar{c}$
C_ℓ	Rolling moment coefficient = rolling moment/QSb
α	Aircraft incidence
g	Acceleration due to gravity
n	Normal acceleration factor
$\dot{q}$	Pitch acceleration
$C_{L_{\alpha,n,\dot{q}}}$	Lift derivatives due to α, n and $\dot{q}$ respectively
$C_{M_{\alpha,n,\dot{q}}}$	Pitching moment derivative due to α, n and $\dot{q}$ respectively
p	Steady state roll rate
ξ	Differential flaperon angle
C_{ℓ_p}	Roll damping derivative = $\partial C_\ell / \partial(pb/2V)$
C_{ℓ_ξ}	Flaperon roll derivative = $\partial C_\ell / \partial \xi$

Notation ctd.

N	Store normal force
Y	Store side-force
η_p	Roll damping aeroelastic efficiency
η_ξ	Flaperon aeroelastic efficiency

1. Introduction

Much attention is paid to static aeroelastic optimisation of combat aircraft structures during the preliminary design stage with the aim of achieving minimum structural mass while meeting a range of aeroelastic design requirements.

This paper concentrates on the aerodynamic aspects of the optimisation and illustrates the changes to stability and control, and loading as the design progresses from the component aeroelastic assessment to the full aircraft representation. The effect of aeroelastics on wind tunnel model design is also discussed.

Five topics are chosen to illustrate the importance of static aeroelasticity on aerodynamic design. The first three

* Aircraft Roll Requirement
* Aircraft Pitch Effectiveness
* Effect of Aeroelastics on Aircraft Longitudinal Stability

are related to a wing-foreplane configuration. The fourth subject

* Effect of Aeroelastics on Store Design Loads

discusses stores mounted under a variable sweep wing. The final topic

* Aeroelastics Considerations in Wind Tunnel Model Design

concentrates on the complexity of modular model design which allows versatility during configuration development.

2.0 Aircraft Roll Requirement

Conventional combat aircraft have historically used ailerons or spoilers to generate roll power. More recently, with the advent of all moving tail surfaces, differential tailplane has been used to augment roll performance particularly at high speed where ailerons are prone to control reversal while the all moving surfaces maintain reasonable effectiveness.

For close coupled canard configurations differential deflection of the foreplane produces negligible rolling moment due to opposing aerodynamic interference on the wing; therefore it is necessary to resort to wing trailing edge flaperons to produce aircraft roll power. Because the flaperons are therefore the only means of producing roll control*, the roll requirement generally dictates the structural optimisation.

Wing twist requirements to meet aircraft performance at cruise and combat 'g' are often compromised by the primary need to produce rolling moment at high speed (Ref 1). Divergence speed limits and flutter frequency separation are also included in the optimisation requirements. Other secondary requirements include optimum flap twist to maintain aircraft performance, and limits on wing to flaperon deflection, i.e., flap bowing, to ensure the control surface remains aerodynamically effective.

The roll requirement is generally defined in terms of aircraft time to bank. For convenience this is then interpreted as an equivalent maximum steady roll rate for the structural optimisation. The following equation defines the aeroelastic roll effectiveness given the maximum allowable differential flaperon angle and required steady roll rate.

$$\eta_p C_{\ell_p} \frac{pb}{2V} = \eta_\xi C_{\ell_\xi} \xi$$

Therefore roll effectiveness $\frac{\eta_\xi}{\eta_p} = \frac{C_{\ell_p}}{C_{\ell_\xi}} \frac{pb}{2V} \frac{1}{\xi}$

* Outboard leading edge controls have in the past been used to augment roll control, and increasing aeroelastic effectiveness with speed makes this an attractive option. However, because leading edge devices are primarily a means of controlling flow over the wing, differential movement can produce undesirable aerodynamic effects and should only be used as a palliative action.

It is evident that rigid aerodynamic distributions representing both roll damping C_{ℓ_p} and flaperon roll power C_{ℓ_ξ} must be included in the structural optimisation together with aerodynamic influence coefficients to allow the change in aerodynamics due to structural distortion to be calculated. Successive iterations within the optimisation program produce an idealised minimum weight structure to meet the strength and aeroelastic requirements. The idealised structure is subsequently 'engineered' to respect the practical aspects of structural design. A trade study including the flaperon actuators and associated hydraulic systems, controlled by actuation load, ideally produces the optimum total mass.

The flight conditions to which the structure is optimised are dependent on the aircraft role and defined as part of the aircraft specification. For an interceptor aircraft this includes both subsonic and supersonic high speed conditions, for example, M = 0.9 sea level (S.L.) and M = 1.6 at the design diving speed (V_L). However, the corner point of the flight envelope, i.e., V_L at low altitude requires consideration because experience shows minimum flaperon effectiveness occurs at this flight condition. Results at three flight conditions are therefore presented in this paper, namely M = 0.9/S.L., M = $1.2/V_L$ and M = $1.6/V_L$.

2.1 Flaperon Roll Effectiveness

Figure 2 shows the variation of flaperon roll effectiveness with dynamic pressure at the three chosen flight conditions for the configuration given in Figure 1. Three points to be observed are:

(i) Minimum flaperon roll effectiveness occurs at M = 1.2 and therefore justifies inclusion in the optimisation criteria.

(ii) Minimal outboard flaperon effectiveness is available at M = $1.2/V_L$. Any small variation in structural properties could render the control totally ineffective and therefore any apparent roll power should not be relied upon.

(iii) There is a significant reduction in effectiveness between fixed root wing representation and fully flexible aircraft. It is important to take this effect into account during the early phases of optimisation when it may be necessary to consider the wing in isolation with fixed root structure because the configuration is otherwise not frozen.

2.2 Aircraft Roll Rate

The aeroelastic effectiveness already described is interpreted in terms of percentage maximum required steady roll rate in Figure 3 for the wing optimised to requirements at M = 0.9 S.L. and M = $1.2/V_L$. The consequent roll performance at M = $1.6/V_L$ is also shown.

A prohibitive mass penalty results if the maximum required steady roll rate is required at the M = $1.2/V_L$ flight condition. However, this condition is not usually included in the primary operating zone and therefore the requirement can be relaxed to a magnitude which allows the aircraft to retain control particularly at low level. This is described as the minimum allowable steady roll rate.

The main points illustrated in Figure 3 are:

(i) Having optimised the wing to requirements at M = 0.9 and M = 1.2, excess roll rate is available at M = 1.6.

(ii) There is a marked reduction in rigid roll rate between wing in isolation and the full configuration particularly at M = 1.2 where the increased roll damping is aggravated by adverse effects of flaperon on fin.

(iii) An allowance for the difference between the fixed root wing and fully flexible aircraft should be included in early optimisation work.

(iv) The small contribution of outboard flaperon to roll rate is discounted at M = $1.2/V_L$ because of its potential zero effectiveness.

The trough in roll performance at M = $1.2/V_L$ is well illustrated in Figure 4. There is a marked recovery with increasing altitude, with an almost constant rate being available at 20,000ft. over the full Mach number range.

3.0 Aircraft Pitch Effectiveness

The comparison of flaperon roll and pitch effectiveness is illustrated in Figure 5. This clearly shows the flaperons to have much greater aeroelastic effectiveness in pitch than roll at all comparable flight conditions and hence why generally it is not necessary to include a pitch effectiveness requirement in the structural optimisation.

The aeroelastic mechanism is different for the two cases. An aeroelastic lift loss is generated in both roll and pitch, but the loss occurs predominantly on the outer wing forward of the rigid lift centre due to flaperon deflection. Hence, with roll, there is an inboard shift of centre of pressure, thus aggravating the loss of rolling moment. In pitch there is an aft shift of centre of pressure which enhances the pitching moment.

4.0 Effect of Aeroelastics on Aircraft Longitudinal Stability

In early design phases it is convenient to consider separately the aeroelastic effect on load distributions representing different aircraft parameters, for example, incidence, sideslip, inertia. The variation of rigid non-dimensional lift distribution with aircraft incidence, integrated, represents C_{L_α} and C_{M_α} and hence $C_{M_\alpha}/C_{L_\alpha}$ which as a first approximation represents the rigid aircraft longitudinal stability. However, the aeroelastics resulting from this case cannot be taken in isolation to represent the aeroelastic longitudinal stability. The aircraft mass distribution with an applied unit vertical acceleration, taken as a separate aeroelastic case, generates aerodynamic lift due to structural distortion and which, in combination with applied inertia, gives an effective shift of centre of gravity varying with speed. The true change of longitudinal stability can be obtained by combining the aeroelastics resulting from the individual incidence and mass cases. The latter cases are termed fully flexible 'fixed' aircraft aeroelastics because the structural model must be fixed in space, being unbalanced by other forces.

The fully flexible 'free' aircraft aeroelastics are obtained by balancing lift and pitching moment due to incidence by inertia loads resulting from vertical and pitch acceleration. For an aircraft weight W and unit incidence,

$$\frac{nW}{QS} = C_{L_\alpha} + C_{L_g}.n + C_{L_{\dot{q}}}.\dot{q}$$

$$\frac{qB}{QS\bar{c}} = C_{M_\alpha} + C_{M_g}.n + C_{M_{\dot{q}}}.\dot{q}$$

Solutions for n and $\dot{q}$ give the combining factors to produce the total aerodynamic contribution representing the fully flexible 'free' aeroelastic C_{L_α} and C_{M_α} and thus longitudinal stability.

$$C_{L_\alpha}\text{free} = C_{L_\alpha}\text{fixed} + C_{L_g}.n + C_{L_{\dot{q}}}.\dot{q}$$

$$C_{M_\alpha}\text{free} = C_{M_\alpha}\text{fixed} + C_{M_g}.n + C_{M_{\dot{q}}}.\dot{q}$$

The importance of this effect is illustrated in Figure 6. The diagram shows rigid 'fixed' and 'free' aeroelastic contributions to C_{L_α}, C_{M_α}, and $C_{M_\alpha}/C_{L_\alpha}$ at M = 0.9 S.L. and M = $1.2/V_L$. At M = 0.9 the 'fixed' results give an apparent significant reduction in stability whereas the more representative 'free' interpretation shows little change from rigid. A significant difference between 'fixed' and 'free' is also evident at M = 1.2.

5. Effects of Aeroelastics on Store Design Loads

Most modern combat aircraft are designed to carry stores externally, e.g., weapons, fuel tanks and systems pods. Prediction of installed store loads consequently forms a major part of the aircraft design and flight-clearance process. For wing-mounted stores the aeroelastic behaviour of the wing/pylon/store configuration can have a significant effect on store carriage loads (and hence release/jettison behaviour) and must be adequately allowed for in the design and flight clearance stages of project development.

An example of these effects has been chosen from aeroelastic calculations for a typical missile and systems pod carried on the inboard and outboard under-wing pylons of a current variable-geometry combat aircraft (fig. 7).

In this study, a finite-element model of the total aircraft structural flexibilities (including pylons, internal control rods and ERU attachments, but with rigid stores) is used in conjunction with a subsonic aerodynamic panel model (Vortex Lattice) of the aircraft store configuration (fig. 7) to calculate store loads for the rigid and flexible aircraft.

Typical results are shown in figs. 8, 9 for the variations of store normal force and side force (body axes) with free-stream dynamic pressure during a symmetric, high 'g' manoeuvre at Mach 0.9.

The loads are expressed as percentages of the total "rigid" load and, in the case of normal force, separated into aerodynamic and inertia components.

These results clearly show the significant effects of aeroelastic distortions (primarily wing and pylon bending) at high dynamic pressures on total store loads, even for these "high density" stores for which inertia loads tend to dominate the total normal force (e.g. 27% increase in pod normal force; 41% increase in missile side force).

Hence some approximate allowance for these effects must be made in the estimation of initial design loads for a new combat aircraft, based on similar experience from previous projects. When the stage is reached where detailed structural and aerodynamic descriptions of the aircraft become available, the effect of total aircraft flexibility on installed store loads should be evaluated as a basis for store carriage and release/jettison flight clearances.

6. Aeroelastic Considerations in Wind Tunnel Model Design

To facilitate the aerodynamic optimisation of a combat aircraft configuration it is often necessary to test a multitude of wing geometries. The variables can include L.E. and T.E. sweep, thickness, camber, twist and different combinations of control surface deflection. It is logical therefore to manufacture wind tunnel models in component form with detachable wings and separate leading and trailing edges.

Construction of such a modular wing is illustrated in fig. 10. Here the surface is attached to the fuselage by means of a tongue joint. If stiffness checks show appreciable deflections on the wing due to this form of attachment, it may be necessary to add shear spigots fore and aft to reduce the effect of wing torque. Control surface deflection is simulated by interchangeable segments which are attached to the main wing using lap joints. The size of lap must be sufficient to ensure a continuous deflected shape under load but not too large to degrade the stiffness of the centre main panel. This modular construction is structurally more flexible than the usual solid wind tunnel model and it is therefore necessary to check the aeroelastic characteristics of such a model.

The wind tunnel model must first be represented structurally and may be analysed using finite solid elements. However, it is often sufficient to abbreviate this description using Engineer's Bending Theory including bending, torsion, and shear as separate terms. To represent a low aspect ratio surface it is necessary to use a curved flexural axis which follows a constant percentage chord on the outer wing, then continuing as a radius inboard to finish perpendicular to the body side. The method over-predicts torsional stiffness but, by suitably scaling the individual flexibilities from bending, torque and shear, a good match can be obtained with data from comprehensive model load/deflection tests.

Aeroelastic distortion results from this structural modelling indicate appreciable losses may occur at the dynamic pressures associated with high speed wind tunnel testing. At low supersonic Mach numbers, for example, roll power from trailing edge flaperon deflection can be in the order of 30% less than that obtained from an equivalent rigid wind tunnel model. It is necessary therefore to produce comprehensive aeroelastic data for the model to enable 'rigid data' to be calculated using the flexible model load measurements.

Conclusions

The examples given in this paper serve to highlight the importance of overall configuration static aeroelastic effects in the design of a new high performance combat aircraft. The relative magnitudes of these effects will obviously depend on the chosen aircraft layout and stores carriage arrangement, and may well have some influence on this choice, but nevertheless, the following main points should be given due consideration in the initial project design phase:-

(i) For close-coupled canard configurations, the roll-rate requirements used for wing/flaperon structural optimisation must take account of likely reductions from the isolated, fixed-root wing values, due to aerodynamic and structural interactions of the full configuration, particularly at $M = 1.2/V_L$.

(ii) Such a wing, optimised for roll-rate at M = 0.9 and M = 1.2, sea-level, will give good high-altitude supersonic roll characteristics.

(iii) In the assessment of aircraft longitudinal stability there is a significant difference between "fixed" and "free" aeroelastic analyses, the more realistic "free" results (requiring a knowledge of mass distribution to calculate balancing "inertia" loads) indicating little change from the rigid values.

(iv) For wing-mounted stores, aeroelastic distortion of the wing and pylon can result in significant effects on installed store loads, particularly sideforce (and hence yawing moment), for which due allowance, based on experience, must be made in producing initial design loads. At a stage in the project when a complete aircraft aeroelastic model is available, calculations of fully flexible installed loads should be made as an input to store carriage and release/jettison flight clearances.

(v) High-speed wind tunnel models of combat aircraft configurations can exhibit significant aeroelastic effects. An example is the effect on wing mounted control surface forces and moments, particularly when the model is of "modular wing" construction. Corrections of flexible model data to a "rigid" standard is necessary before accounting for true aeroelastic effects in the full-scale aircraft aerodynamic description. These corrections can readily be made using simple Engineer's Bending Theory, matched to model deflection measurement, together with standard aerodynamics prediction techniques.

References

1. Booker, D. Aeroelastic Tailoring for Control and Performance - Are Requirements Compatible? Paper 19 of AGARD-CP-319, 1981.

Acknowledgements

This work has been carried out with the support of the Procurement Executive, Ministry of Defence.

The authors also wish to acknowledge those members of the Aerodynamics Department at Warton, past and present, whose work has been freely drawn upon in the compilation of this paper.

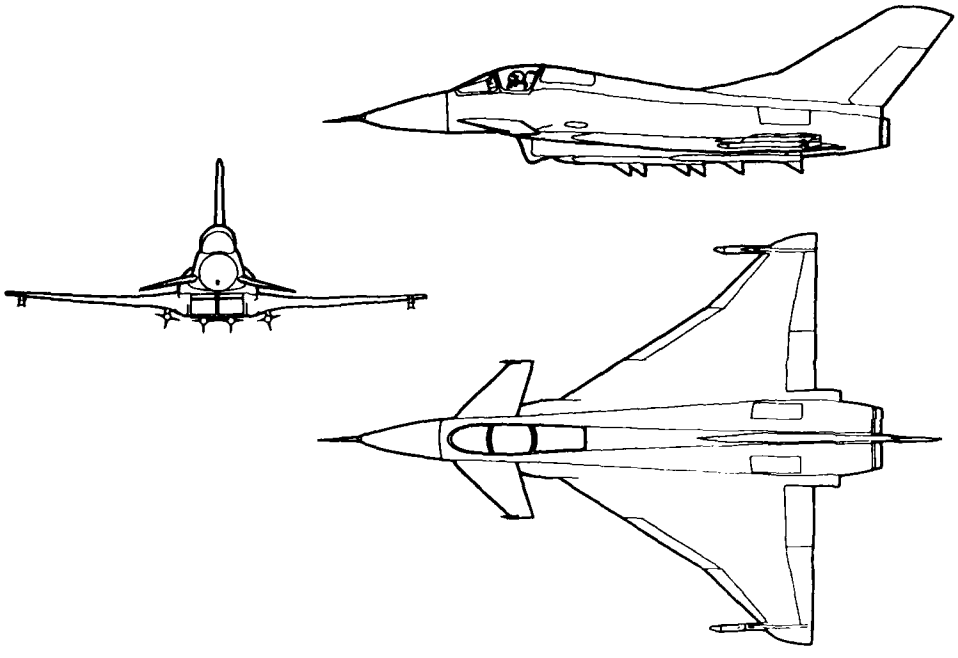

FIGURE 1 TYPICAL CLOSE-COUPLED CANARD DELTA

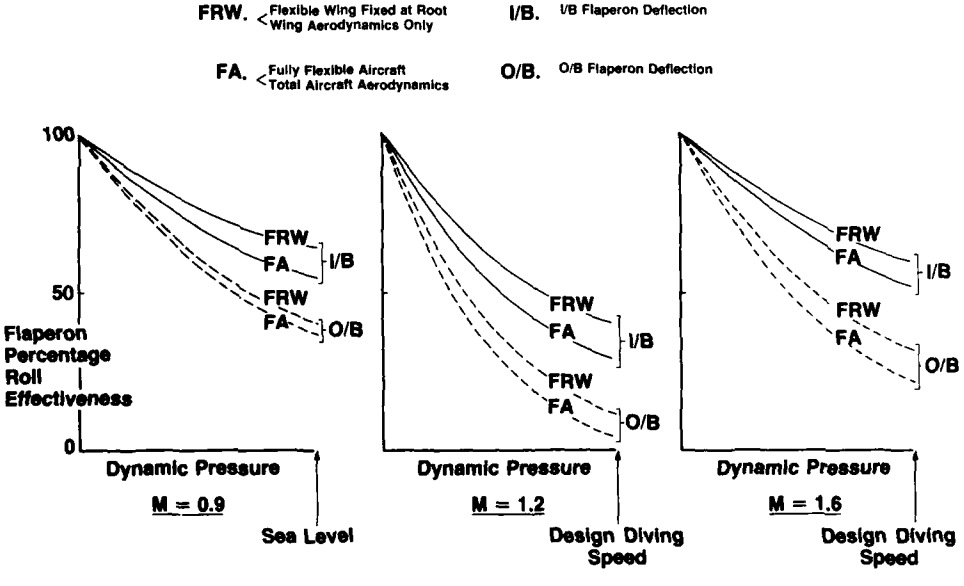

FIGURE 2 FLAPERON AEROELASTIC ROLL EFFECTIVENESS

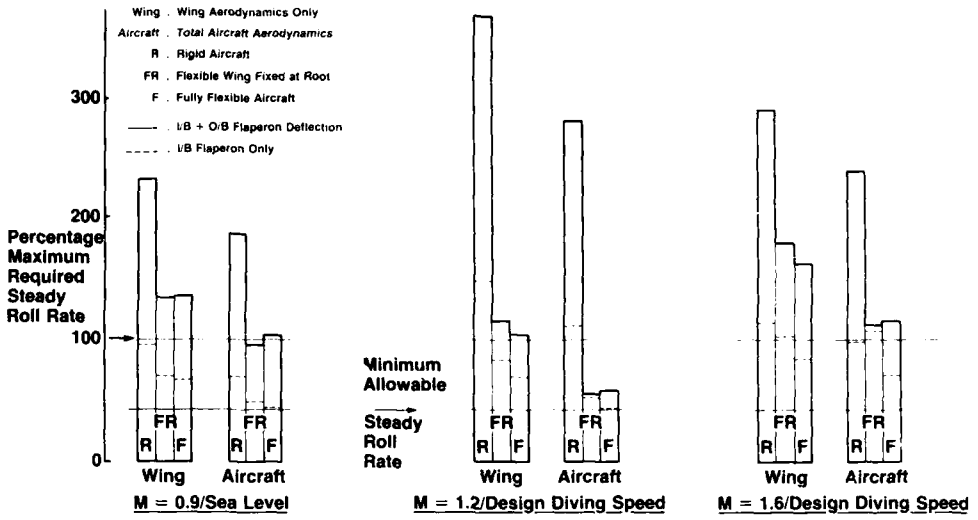

FIGURE 3 AEROELASTIC EFFECTS ON STEADY ROLL RATE

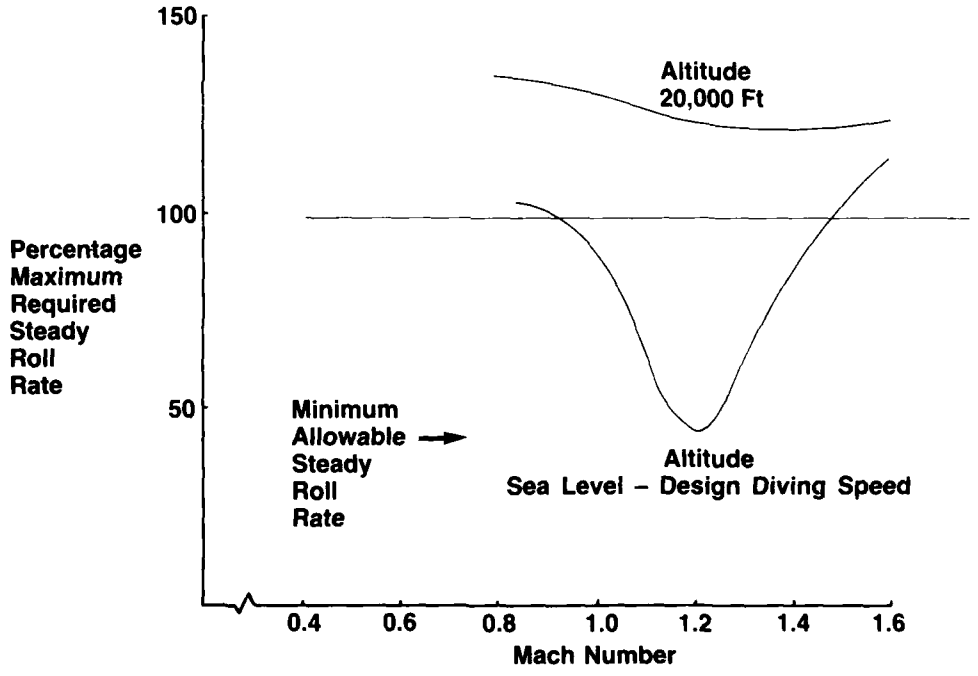

FIGURE 4 AIRCRAFT STEADY ROLL RATE

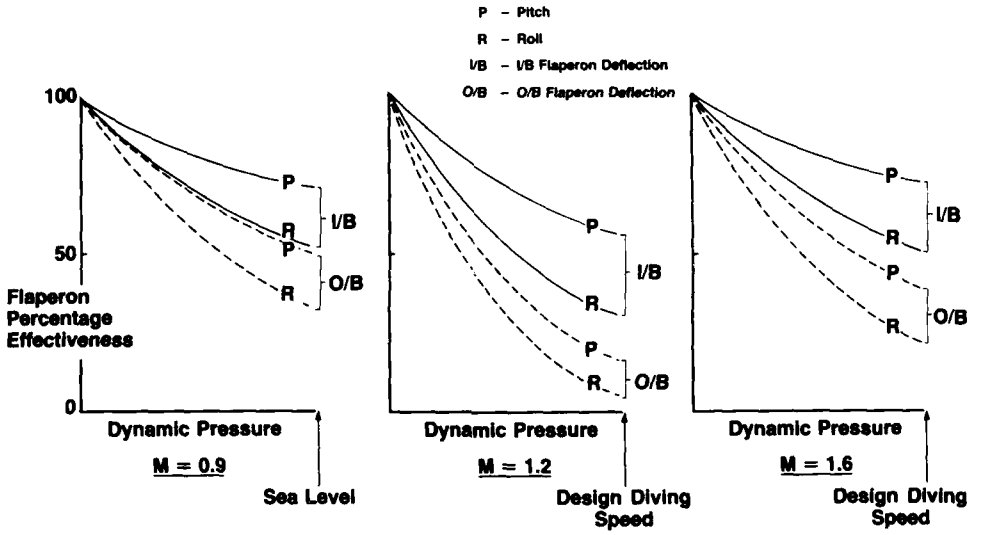

FIGURE 5 COMPARISON OF FLAPERON AEROELASTIC ROLL AND PITCH EFFECTIVENESS

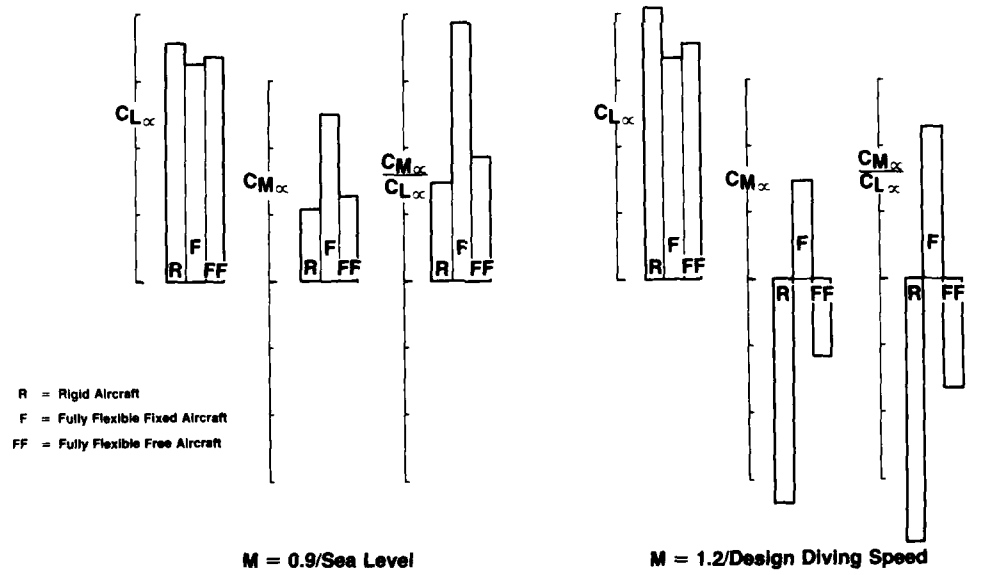

FIGURE 6 AEROELASTIC EFFECT ON LONGITUDINAL STABILITY

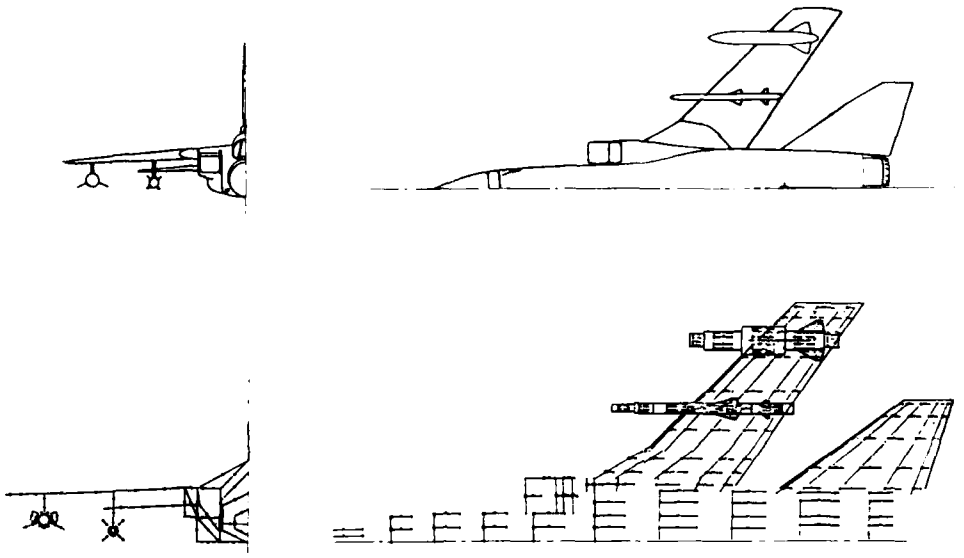

FIGURE 7 VORTEX-LATTICE MODELLING OF THE AIRCRAFT/STORES CONFIGURATION

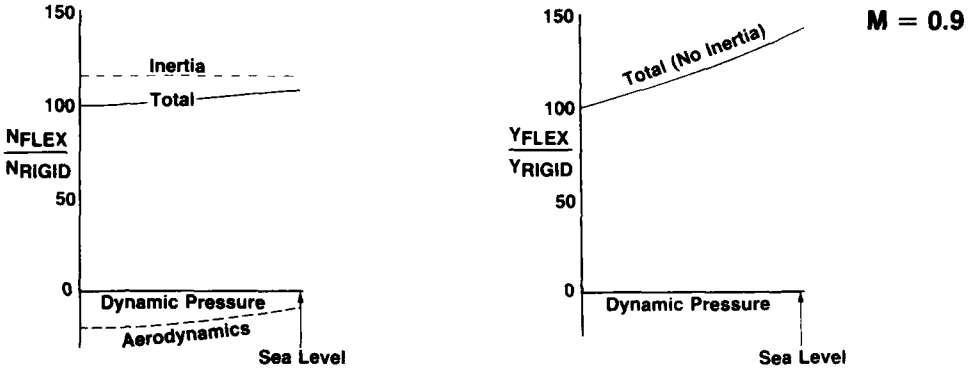

FIGURE 8 MISSILE LOADS (I/B STATION)

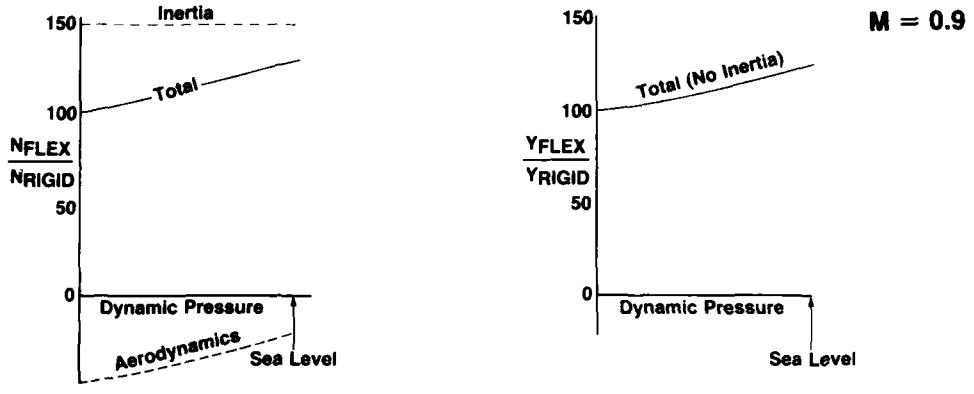

FIGURE 9 SYSTEMS POD LOADS (O/B STATION)

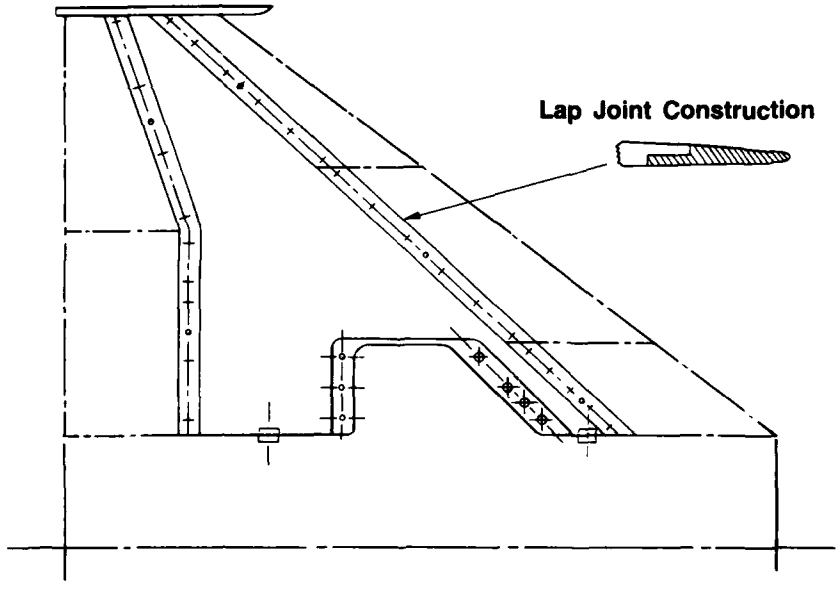

FIGURE 10 EXAMPLE OF A WIND TUNNEL MODEL MODULAR WING

TENDANCES ACTUELLES DE L'ANALYSE AEROELASTIQUE DES AVIONS MILITAIRES

TRENDS IN AEROELASTIC ANALYSIS OF COMBAT AIRCRAFT

BY
C.PETIAU AND S.BRUN

AVIONS MARCEL DASSAULT - BREGUET AVIATION
78, QUAI MARCEL DASSAULT
92214 - SAINT-CLOUD

SUMMARY

After recalling the general principles of aeroelastic coupling with structural finite element analysis, we explain the simplifying assumptions of static aeroelasticity.

Then we describe the technique of load basis reduction used in in the branche CHARGE of ELFINI, the general aircraft structure analysis program of AMD-BA.

This technique allows to separate the big expensive computation of F.E. resolutions and theoritical aerodynamic analysis, from aeroelastic coupling and flight maneuver computation.

We give details about some specific points :

- Mechanical and aerodynamic non linear effects in statics and dynamics
- Optimization, differentiation of flexible aerodynamic derivatives
- Model adjustment on flight measurements.

It appears that we hold some satisfying solutions to the most of the problems, except those due to aerodynamic transonic non linearities.

I - INTRODUCTION

Le calcul des structures a été révolutionné dans les années 1970 par les techniques d'analyses par Eléments Finis, qui aujourd'hui, en s'en donnant les moyens, permettent de résoudre les problèmes d'élasticité avec pratiquement la précision que l'on veut.

Le calcul des charges et aéroélasticité "classique" basé peu ou prou, sur des modèles élastiques de poutre longue, s'est très vite révélé dépassé notamment pour les avions à voilure Delta.

Nous avons dû faire un investissement considérable pour mettre le calcul des charges et d'aéroélasticité statique à la hauteur du calcul élastique par Eléments Finis ; plus récemment les modélisations de commande de vol électrique ont nécessité le même effort pour l'aéroélasticité dynamique ; il a fallu en particulier assurer que la limite statique des modèles dynamiques corresponde au modèle statique.

Ces travaux se sont traduits par l'élaboration de la branche CHARGE de notre logiciel ELFINI (qui regroupe autour d'un noyau central d'analyse par Eléments Finis toutes les disciplines du calcul des structures d'avions).

Nous en décrivons ici les grandes lignes, après un rappel des équations générales de l'aéroélasticité dynamique et des hypothèses simplificatrices conduisant à l'aéroélasticité statique.

La principale caractéristique de notre approche est son système de gestion, basé sur les principes de base de charges et de base de formes aérodynamiques, qui permettent d'effectuer les gros calculs de résolutions Eléments Finis, et d'aérodynamique théorique, indépendamment du couplage et des calculs de manoeuvres qui sont peu coûteux.

Nous détaillons quelques points spécifiques, et de développement, intéressants :

- Traitement des divers types de non linéarité en statique et en dynamique
- Optimisation, technique de dérivation des coefficients aérodynamiques souples par rapport aux paramètres de conception
- Identification du modèle sur les mesures en vol.

Il ressort de l'ensemble que nous tenons des réponses satisfaisantes à la plupart des problèmes, excepté, malheureusement, au calcul des charges en transsonique.

2 - PRINCIPES DES CALCULS D'AEROELASTICITE

2.1 - Aéroélasticité linéaire sur Modèle E.F., Equations générales

Les points de départ de ces calculs sont :

- un modèle Elastique par Eléments Finis de l'avion complet n'omettant en particulier aucune surface portante (condition du couplage automatique avec les calculs aérodynamiques) ; nous avons pratiqué, pour ces modèles, de l'ordre de 10 000 à 40 000 degrés de liberté (D.D.L.) en fonction de l'avancement du projet (Fig.1 et 2).
- des calculs d'Aérodynamique linéaire par méthode de singularité (Doublets, Sources) sur des modèles comportant de 500 à 3000 facettes (fig. 4).

Pour alléger les calculs on procède à des réductions de base conduisant aux relations suivantes :

- En élasticité :

Soit X le vecteur déplacement des DDL Eléments Finis, on choisit un système de DDL réduit x relié à X par la relation

(1) $$X = [V]x$$

On décompose x en 3 types de composantes soit $x : \begin{pmatrix} x_r \\ x_g \\ x_s \end{pmatrix}$

. x_r = composantes du mouvement de corps solide associé aux formes rigides

. x_s = composantes des déformées souples associées à des formes de base (Vs), inertiellement orthogonales aux précédentes ; les (Vs) sont : soit les modes propres souples de la structure, soit combinaisons des composantes de la "base de charge" sur lesquelles nous revenons § 2.3.

. x_g = mouvement des gouvernes associé aux formes (V_g)

Soit l'équation d'équilibre dynamique dans la base

(2) $$m\ddot{x} + \nu\dot{x} + kx = f_{aéro} + F_{autre}$$

. La matrice de masse :

$$[m] = {}^t[V]\,[M]\,[V] = \begin{pmatrix} m_{rr} & 0 & m_{rg} \\ 0 & m_{ss} & m_{sg} \\ m_{gr} & m_{sg} & m_{gg} \end{pmatrix}$$

. La matrice de rigidité :

$$[k] = {}^t[V]\,[K]\,[V] = \begin{pmatrix} 0 & 0 & 0 \\ 0 & k & 0 \\ 0 & 0 & 0 \end{pmatrix}$$

. La matrice d'amortissement (ν) est du même type que (k)

. Le chargement faéro est lié aux coefficients de pression Kp du calcul aérodynamique par la relation

$$f_{aéro} = {}^t[V]\,F_{aéro} = \frac{1}{2}\rho v^2 \;\; {}^t[V]\,\left[\frac{\delta F}{\delta Kp}\right] Kp$$

Nous revenons au § 2.3 sur l'établissement de l'opérateur de transfert des Kp aérodynamiques sur les noeuds E.F.

. f autre = ^{t} (V) F autre représente l'action des forces non aérodynamiques (poids, poussée réacteur, effort train etc..) nous le considérons comme constant pour simplifier l'exposé.

. En aérodynamique théorique linéaire.

On pose que la forme aérodynamique "portante", somme de la forme initiale, du mouvement rigide, des déformations et des braquages de gouverne est une combinaison de formes aérodynamiques élémentaires dont les effet de portance se combinent linéairement.

On peut utiliser pour ces formes aérodynamiques élémentaires :

- soit directement les formes associées aux DDL mécaniques,

- soit des formes spécifiques indépendantes des DDL élastiques (Déformations polynomiales des surfaces portantes, mouvements rigides par zone, voir §.2.5).

La deuxième procédure à l'avantage de rendre l'ensemble des calculs aérodynamiques indépendant des calculs d'élasticité.

Un opérateur de lissage (L) relie alors les déplacements q de la base aérodynamique au déplacement E.F. soit : $q = [L]x$

Dans les méthodes de singularité linéaire (Portance par doublets, voir réf.2) on établit un opérateur linéaire reliant les Kp des facettes du maillage aérodynamique aux incidences locales de ces mêmes facettes soit :

(3) $$Kp = [A]\alpha$$

En aérodynamique instationnaire où on résout l'équation du potentiel linéarisé dans le domaine fréquence, cet opérateur devient $[A(\frac{\omega}{v})]$ complexe ; nous le décomposons en partie stationnaire et partie transitoire soit :

(4) $$[A(\tfrac{\omega}{v})]_{instationnaire} = [A]_{stationnaire} + [A(\tfrac{\omega}{v})]_{transit.}$$

L'intérêt majeur de cette décomposition est qu'on peut obtenir [A] (terme prépondérant en basse fréquence) par des théories aérodynamiques plus sophistiquées et qu'on peut le recaler sur les résultats de soufflerie et de vol (voir § 3.1).

Les incidences locales des facettes α sont liées aux déplacements et vitesses des noeuds E.F. par des opérateurs géométriques soit

(5) $$[\alpha] = \alpha o + [\frac{\delta\alpha}{\delta X}]X + [\frac{\delta\alpha}{\delta \dot{X}}]\,(\frac{\dot{X}}{V})$$

- Equations générales couplées

En rassemblant les relations 1 à 5 on aboutit à l'équation du mouvement couplé.

(6) $$[m]\ddot{x} + [\mathcal{V}]\dot{x} + [k]x = f_{autre} + \frac{1}{2}\rho v^2 \{[C_o] + [C_1]x + \frac{1}{v}[C_2]\dot{x} + \{C_{tr.}(\tfrac{\omega}{v})x\}\}$$

En décomposant x en termes de commande des braquages de gouvernes xg et en termes de réponses des modes rigides xr et modes souples xs ; la partition du système 6 conduit à :

(7) $$\begin{pmatrix} m_{rr} & 0 \\ 0 & m_{ss} \end{pmatrix}\begin{pmatrix} \ddot{x}_r \\ \ddot{x}_s \end{pmatrix} + \left\{\begin{pmatrix} 0 & 0 \\ 0 & \nu \end{pmatrix} + \frac{1}{2}\rho v\,[C_2]_{r-s,r-s}\right\}\begin{pmatrix} \dot{x}_r \\ \dot{x}_s \end{pmatrix} +$$

$$\left\{\begin{pmatrix} 0 & 0 \\ 0 & k \end{pmatrix} + \frac{1}{2}\rho v^2\left\{[C_1]_{r-s,r-s} + \left(\varphi(\tfrac{\omega}{v})\right)_{r-s,r-s}\right\}\right\}\begin{pmatrix} x_r \\ x_s \end{pmatrix} =$$

$$-\begin{pmatrix} m_{rg} \\ m_{sg} \end{pmatrix}\ddot{x}_g + \frac{1}{2}\rho v^2\left\{\frac{1}{v}[C_2]_{r-s,g}\dot{x}_g + \left([C_1]_{r-s,g} + \left(\varphi_{ins}(\tfrac{\omega}{v})\right)\right)x_g + A_o\right\}$$

Soit une représentation dans le domaine fréquence :

(8) $$[D(\tfrac{1}{2}\rho v^2, \tfrac{\omega}{v})]\begin{pmatrix} \cdot \\ x_r \\ x_s \end{pmatrix} = [g(\tfrac{1}{2}\rho v^2, \tfrac{\omega}{v})]\, x_g$$

- Commandes de vol électriques

Le mouvement des gouvernes est fonction des ordres du pilote Cpil et des mesures des capteurs du mouvement Ccap. Pour les modèles linéaires on établit les fonctions de transfert du type :

(9) $$x_g(\omega) = [H_{pil}(\omega)]\, C_{pil} + [H_{cap}(\omega)]\, C_{cap}$$

Les mesures des capteurs CDVE étant elles-mêmes fonction des DDL x soit :

(10) $$Ccapt = [Vcapt]x$$

Reportant les relations 8 et 9 dans 7 on obtient, pour le transfert commande pilote -> mouvement, des équations analogues à 7 et 8 avec des termes supplémentaires de couplage par les CDVE indépendant des pressions dynamiques, de la forme :

(8') $$D'(\tfrac{1}{2}\rho v^2, \omega)\begin{pmatrix} x_r \\ x_s \end{pmatrix} = g'(\tfrac{1}{2}\rho v^2, \omega)\, C_{pil}$$

- Efforts généraux, efforts internes, contraintes et déformations.

Ce sont les sorties ordinaires des calculs de charges, elles sont des fonctions linéaires des déplacements Eléments Finis soit :

(10) $$\sigma = \left(\frac{\delta\sigma}{\delta X}\right) X = \left(\frac{\delta\sigma}{\delta X}\right)[V]x = [\frac{\delta\sigma}{\delta x}]x$$

Conduisant aux fonctions de transfert des réponses structurales en fonction du mouvement des gouvernes, de la forme :

(11) $$\sigma = [\frac{\delta\sigma}{\delta x_o}]\, [D(\tfrac{1}{2}\rho v^2, \tfrac{\omega}{v})]^{-1}\, [g(\tfrac{1}{2}\rho v^2, \tfrac{\omega}{v})]\, x_g$$

2.2 - Hypothèses simplificatrices en aéroélasticité statique

Les mouvements étant suffisamment lents, deviennent négligeables dans l'équation (7) du mouvement couplé :

. Les forces d'inertie des déformées souples et des mouvements de gouvernes.

. Les termes d'amortissements aérodynamiques et structuraux des mêmes modes.

. Les forces aérodynamiques transitoires.

Ce qui conduit pour le système d'équation d'équilibre général 7 à la forme :

(12) $$[m_r]\ddot{x}_r - \tfrac{1}{2}\rho v\,[C_{2r,r}]\dot{x}_r - \tfrac{1}{2}\rho v^2\,\{[C_{1r,r}]x_r + [C_{1r,s}]x_s$$

$$= \tfrac{1}{2}\rho v^2\,\{[C_{1r,g}]x_g + C_{or}\} + f_{r\ autres}$$

$$[k]x_s = \tfrac{1}{2}\rho v\,\{[C_{2r,s}]\dot{x}_r\} + \tfrac{1}{2}\rho v^2\,\{[C_{1rr}]x_r + [C_{1ss}]x_s$$

$$+ [C_{1s,g}]x_g\} + f_{s\ autres}$$

Comme il n'apparaît plus de dérivée des DDL souple dans la deuxième ligne il est possible d'éliminer ces DDL souples dans l'équation du mouvement par la relation :

(13)
$$x_s = [I - \frac{1}{2}\rho v^2 [S_s]]^{-1} \{\frac{1}{2}\rho v [S_{\dot{r}}] x_{\dot{r}} + \frac{1}{2}\rho v^2 ([S_r]_{xr} + [S_g]_{xg} + [S_o]) + x_{S_o}$$

Les matrices (S) représentent les déformations unitaires des modes souples sous les effets aérodynamiques des divers modes, soit :

(14)
$$[S_r] = [k]^{-1} [C_{1s,r}] \qquad [S_{\dot{r}}] = [k]^{-1} [C_{2s,r}]$$

$$[S_s] = [k]^{-1} [C_{1s,s}] \qquad [S_g] = [k]^{-1} [C_{1s,g}]$$

La singularité de la matrice $D = [I - \frac{1}{2}\rho v^2 [S_s]]$ ("Flexibilité" des modes souples aéroélasticité couplée) correspond à la divergence statique.

On élimine les DDL souples en reportant (13) dans la première ligne de 12 pour aboutir à l'équation de la mécanique du vol du mouvement rigide aéroélasticité éliminée, soit :

(15)
$$[m_{rr}] \ddot{x}_r - \frac{1}{2}\rho v [C'_2] x_r - \frac{1}{2}\rho v^2 [C'_1] x_r =$$

$$\frac{1}{2}\rho v^2 \{[C'_g] x_g + [C'_o]\} + f'_o$$

Avec les opérateurs de coefficients aérodynamique "aéroélasticité éliminée"

(16)
$$[C'_2] = [C_{2r,r}] + \frac{1}{2}\rho v [C_{1r,s}] [D]^{-1} [S_{\dot{r}}]$$

$$[C'_r] = [C_{1r,r}] + \frac{1}{2}\rho v^2 [C_{1r,s}] [D]^{-1} [S_r]$$

$$[C'_g] = [C_{1r,g}] + \frac{1}{2}\rho v^2 [C_{1r,s}] [D]^{-1} [S_g]$$

On présente sous forme "homographique" analogue les opérateurs d'effort généraux, déformations et contraintes

soit

(17)
$$\sigma = \frac{1}{2}\rho v^2 \{\frac{1}{v}[\frac{\delta\sigma'aéro}{\delta x_{\dot{r}}}] \dot{x}_r + [\frac{\delta\sigma'aéro}{\delta x_r}] x_r + [\frac{\delta\sigma'aéro}{\delta x_g}] x_g + \sigma'aéro_o\} + \sigma_o$$

dont les coefficients (Effet unitaire d'aérodynamique "aéroélasticité éliminée" s'écrivent sous des formes du type :

(18)
$$[\frac{\delta\sigma'aéro}{\delta x_r}] = [\frac{\delta\sigma aéro}{\delta x_r}] + \frac{1}{2}\rho v^2 [\frac{\delta\sigma aéro}{\delta x_s}] [D]^{-1} [S_r]$$

avec

$$[\frac{\delta\sigma aéro}{\delta x_r}] = [\frac{\delta\sigma}{\delta x_s}] [S_r] \;,\; [\frac{\delta\sigma aéro}{\delta x_s}] = [\frac{\delta\sigma}{\delta x_s}] [S_s]$$

(Effet unitaire d'aérodynamique aéroélasticité non éliminée).

Le calcul des charges statiques s'effectue complètement à partir :

- des calculs de manoeuvre par intégration de l'équation 15 de la mécanique du vol aéroélasticité éliminée
- la remontée aux efforts généraux et internes, aux déformations et contraintes par les relations 15.

2.3 - Organisation des calculs d'aéroélasticité et de charges statiques

2.3.1 - Généralités

Il a fallu répondre aux impératifs suivants apparemment contradictoire :

- Nécessité d'une précision des calculs des charges d'une qualité équivalente à celle du calcul des contraintes par Eléments Finis,
- Sophistication devant rester homogène avec les hypothèses simples des calculs d'aérodynamique linéarisée recalés sur des essais de soufflerie et les vols,
- Maniement simple des calculs pour pouvoir traiter avec des délais et coûts raisonnables des analyses dans un domaine à paramètres multiples (Type de manoeuvres, configuration massique et d'emports extérieurs, mach, altitude),
- Evolution avec les raffinements des modèles structuraux et Aérodynamiques, les résultats de soufflerie.

Pour cela on sépare les calculs en deux phases :

- Les calculs volumineux qui sont menés indépendamment du couplage aéroélastique, des configurations massiques et des hypothèses de recalage empirique, ce sont :
  - . la résolution des Eléments Finis sous des chargements de base
  - . les calculs d'aérodynamique théorique.

  On en extrait des opérateurs "concentrés" du type :
  - . décomposition des charges de pression aérodynamique unitaires dans les chargements de base,
  - . lissage des déplacements de base du modèle élastique dans les déformées de base de la surface aérodynamique
  - . efforts généraux, déformations et contraintes en quelques centaines de points sensibles, pour chaque déplacement de base.
- A partir de ces opérateurs on obtient par des calculs de faible volume :
  - . les coefficients aérodynamiques "avion souple",
  - . le mouvement de l'avion en manoeuvre par intégration des équations de la mécanique du vol,
  - . l'évolution correspondante des efforts généraux et des contraintes aux points contrôlés,
  - . la recherche automatique des cas enveloppes dimensionnants,
  - . la reconstitution dans ces cas, pour des analyses complètes, de l'ensemble des déplacements du modèle EF ; on peut reconstituer les forces aux noeuds pour les transferts vers des modèles raffinés.

La définition exacte des configurations massiques et les recalages empiriques interviennent au début de cette deuxième phase.

Nous résumons planche 3 l'organigramme de cette technique qui est fondée sur la notion de base de charges.

2.3.2 - Principes de la réduction dans une base de charges

L'idée directrice est de considérer que toutes les charges appliquées sur la structure sont combinaisons linéaires de cas de charges de base, (couramment de l'ordre de 300 à 500), soit :

$$F = (P)\,\mu$$

- Charges de base

Les cas de charges de base rassemblés dans l'opérateur (P) sont partagés en 3 catégories :

$$P = (P_{inertie}\ P_{aéro},\ P_{autre})$$

. $(P_{inertie})$ correspond à des cas élémentaires de charges d'inertie dus aux accélérations des mouvements rigides (et des forces centrifuges pour les analyses non linéaire de mouvement solide), sur une décomposition des masses de l'avion (Masses de base, composées de celles de l'avion vide et des masses variables unitaires), de façon à pouvoir reconstituer par combinaison les forces d'inertie du mouvement rigide dans toutes les situations.

. ($P_{aéro}$) correspond à des charges de pression élémentaires :

. pour les surfaces portantes les composantes correspondent à des pressions unitaires aux noeuds d'une "grille de pression" Eléments Finis (voir planche 5), cette grille est indépendante des "facettes" où sont calculés les Kp dans les programmes d'aérodynamique théorique,

. pour les corps fuselés les composantes de ($P_{aéro}$) correspondent aux composantes du torseur des charges appliquées par "tranche".

. (P_{autre}) correspond aux diverses composantes discrètes type poussée réacteur, effort train etc...

- Déformées de Base (B)

Elles sont calculées par résolution du modèle Eléments Finis sous l'ensemble des cas de charges de base, soit

$$[B] = [K]^{-1} P$$

- Opérateur réduit

A partir de (P) et (B) on extrait les opérateurs suivants, suffisants pour mener les calculs d'aéroélasticité et de charges.

- Opérateur $[\delta\sigma / \delta u]$ des efforts généraux, efforts unitaires, contraintes et déformations aux points sensibles ; on retient pour l'évaluation des charges seulement quelques centaines de composantes.

- Pour permettre l'orthogonalisation ultérieure des déformées de base aux modes rigides sans accès aux tableaux (P) et (B) :

. les torseurs des résultantes des cas de charges des bases :

$$[\frac{\delta fr}{\delta u}] = {}^t[V_r] [P]$$

. les quantités de mouvements rigides des masses de base dans les déformées de base

$$[\frac{\delta xr}{\delta u}] = {}^t[V_r] [M_i] [B]$$

2.3.3 - Calculs aérodynamiques

Ils fournissent les opérateurs donnant les coefficients de pression en fonction des incidences facettes

$$K_p = K_{po} + [A]\alpha$$

L'organisation des calculs est compliquée par le fait qu'on exploite simultanément les résultats de différentes méthodes :

- Méthode de singularité linéaire pour les effets de portance en subsonique et supersonique, le maillage pouvant dépendre du Mach et de la fréquence réduite en instationnaire.

- Méthodes plus coûteuses, d'Eléments Finis ou de différences finies (Transsonique), qui, en pratique, ne s'appliquent que pour le calcul des effets rigides et de gouverne.

- Recalage sur les résultats de soufflerie et de vol, qui eux aussi ne concernent que les effets rigides et de gouvernes (voir § 2.3.6).

On doit gérer l'ensemble de ces résultats reposant sur des discrétisations indépendantes des champs de Kp et des incidences locales.

2.3.4 - Formes aérodynamiques de base

Les calculs d'aérodynamique linéaire ne nécessitent pas une description de la déformation aéroélastique par autant de DDL que le calcul élastique, c'est pourquoi on choisit généralement d'exprimer la forme de la surface portante comme combinaison de quelques dizaines de formes élémentaires soit :

$$\vec{S}(M) = \vec{S}_o(M) + \Sigma q_i \vec{S}_i(M)$$

On décompose les déformations de surface de base en deux familles :

- Pour les surfaces portantes continues, des déformations polynomiales de la surface moyenne du type :

$$z(x,y) = z_o(x,y) + \Sigma q_i x^{\alpha i} y^{\beta i}$$

(Les monomes de base $x^{\alpha i} y^{\beta i}$ doivent former des suites complètes).

- Pour les "corps" des mouvements rigides locaux

A partir de la définition de formes de base on établit les opérateurs géométriques

$$\delta\alpha / \delta q, \ \delta\alpha / \delta \dot{q}$$

donnant les incidences des facettes aérodynamiques en fonction du mouvement de la forme aérodynamique soit :

$$\alpha = [\frac{\delta\alpha}{\delta q}] q + [\frac{\delta\alpha}{\delta \dot{q}}] \dot{q}$$

2.3.5 - Opérateurs permettant le couplage

- Opérateurs de transfert des Kp sur les composantes aérodynamiques de la base de charges $[\delta u / \delta Kp]$

Ils permettent de s'affranchir de la versatilité des maillages aérodynamiques. Ils sont établis pour chaque type d'aérodynamique :

. par lissage aux moindres carrés des pressions pour le passage de Kp des surfaces portantes aux "noeuds" de la "grille des pressions" de base.

. par calcul des torseurs résultant des champs de Kp locaux pour les charges de base "par tranche" des corps fuselés.

. par transfert aux Noeuds E.F. puis "projection" sur les composantes ($V_{aéro}$) soit :

$$(\frac{\delta u}{\delta Kp}) = {}^t[V_{aéro}] (\frac{\delta F}{\delta Kp}) \ Kp$$

L'opérateur creux $[\delta F / \delta Kp]$ est élaboré automatiquement à partir des fonctions d'interpolation des déplacements normaux des Eléments Finis de la surface aérodynamique N(r), en satisfaisant au mieux à la conservation des travaux virtuels soit :

$${}^t FX = \int_{\text{surface aéro}} Kp(M) \ N(M) \ {}^t X ds$$

- Opérateur de lissage des formes élastiques de base dans les formes aérodynamiques de base. Ils correspondent à la relation

$$q = [l_b] u + [l_r] x_r + [l_g] x_g$$

$[l_b]$ est obtenu par lissage au moindre carré par minimisation des distances entre formes soit

$$\int_{\text{surface}} | {}^t N(M) Bu - [S(M)] q |^2 dS$$

$[l_r]$ et $[l_b]$ désignent les correspondances de composantes, les modes rigides et de gouvernes devant être inclus dans la base aérodynamique.

2.3.6 - Banque de données aérodynamique, recalage

Dans cette phase délicate on rassemble dans la banque de charges sous forme de composantes les résultats des divers calculs aérodynamiques et d'essais de soufflerie, soit l'élaboration des tableaux :

$$[\frac{\delta u}{\delta q}(M)] = [\frac{\delta u}{\delta Kp}] [\frac{\delta Kp}{\delta \alpha}(M)] \frac{\delta \alpha}{\delta q}$$

$$[\frac{\delta u}{\delta \dot{q}}(M)] = [\frac{\delta u}{\delta Kp}] [\frac{\delta Kp}{\delta \alpha}(M)] \frac{\delta \alpha}{\delta \dot{q}}$$

L'opération prend une certaine complexité du fait que les calculs aérodynamiques sophistiqués et les résultats de soufflerie ne portent généralement que sur quelques effets rigides (incidence, dérapage, braquage de gouverne).

La procédure la plus rapide est l'élaboration directe des tableaux $[\delta u / \delta xr,g]$ et $[\delta u / \delta xs]$ indépendamment des $[\delta u / \delta q]$ et $[\delta u / \delta \dot{q}]$ qui ne sont utilisés que pour les charges des effets souples.

Cette technique simple peut être contestée pour les puristes, en considérant que certaines formes simples peuvent coïncider avec les formes rigides. (Un débraquage des gouvernes dû à la souplesse de la timonerie n'a pas de raison d'être traité autrement que l'effet de braquage de la gouverne) ; l'idée est alors de recaler la partie "rigide" de chaque effet souple et de croire à la théorie pour la différence.

A partir de l'opérateur $[Lr\text{-}g,q]$ de lissage des formes "souples" q dans les x_r, x_g (obtenus par moindres carrés avec la meme intégration que l'opérateur de lissage (L) des Eléments Finis dans les q), il vient :

$$[\frac{\delta u}{\delta q}(M)]_{recalé} = [\frac{\delta u}{\delta q}(M)]_{théo.} (I - \frac{\delta q}{\delta x_{r.g}} [Lr\text{-}g,q]) +$$

$$[\frac{\delta u}{\delta q}(M)]_{recalé} \frac{\delta q}{\delta x_{r.g}} [Lr.g,q]$$

Les manipulations conduisant au $\delta u / \delta xr$ recalé sur la soufflerie et le vol sont effectuées par des théories de complexité diverse :

- Manipulation "à la main", pour reconstituer des courbes d'efforts généraux sur les corps,
- Recalage automatique, à partir d'une fonction d'affinité paramétrée, sur les résultats de pesée partielle en soufflerie ou sur des contraintes mesurées en vol (voir § 3.4).
- Récupération directe de résultats mesure de pression.

2.3.7 - Couplage

Ce n'est qu'à cette étape qu'on définit la configuration exacte de calcul soit :

- La répartition de masse (combinaison des masses de base)
- Le Mach et les hypothèses aérodynamiques
- La pression dynamique.

On se place virtuellement dans une base (Vr, Vs, Vg) où les formes souples (Vs) sont orthogonales aux modes rigides, elles sont déduites de (B) à partir des considérations suivantes :

- Les charges de base sont équilibrées par les forces d'inertie induites correspondant aux accélérations rigides
- Les déformées de base sont orthogonales aux modes rigides.

Il en résulte la relation entre (Vs) et (B)

$$[Vs] = \{ I - [V_r] (m_{rr})^{-1} {}^t[V_r] [M] \} [B] \{ I - (\frac{\delta u}{\delta xr}) (m_{rr})^{-1} (\frac{\delta fr}{\delta u}) \}$$

A partir de cette définition nous constituons directement (sans reconstitution de (Vs)) les opérations nécessaires au couplage aéroélastique soit :

- Les termes nécessaires à l'orthogonalisation aux modes rigides

  . La matrice de masse rigide $[m_{rr}]$ par combinaison des masses élémentaires

$$[m_{rr}] = \Sigma\ Mi[m_{rri}]$$

  . Les quantités de mouvements rigides des composantes de base

$$[\frac{\delta xr}{\delta u}] = {}^t[V_r]\ [M]\ [B] = \Sigma\ M_i[\frac{\delta xr}{\delta u}]_i$$

  . Les effets d'accélération rigides $[\delta u/\ \delta xr]$ par combinaisons des composantes d'inertie de la base de charges

- L'opérateur de lissage des x_s dans les formes aérodynamiques de base devient :

$$l_s = (l_b - l_r\ (m_{rr})^{-1}\ \frac{\delta xr}{\delta u})\ (I - \frac{\delta u}{\delta \ddot{x}}\ (m_{rr})^{-1}\ \frac{\delta fr}{\delta u})$$

- L'opérateur des déformations souples aéroélastiques par les effets aérodynamiques de base

$$[\frac{\delta xs}{\delta q}] = [I - \frac{\delta u}{\delta \ddot{x}}\ [m_{rr}]^{-1}\ \frac{\delta fr}{\delta u}]\ [\frac{\delta u}{\delta q}]$$

A partir de là on se ramène aux opérateurs de la théorie générale du § 2.2. :

- Les matrices (Sx) de déformation aéroélastique sous les effets du mode (Voir relation 13 § 2.2)

$$[S_r] = [\frac{\delta xs}{\delta q}]\ [l_r],\ [S_{\dot{r}}] = [\frac{\delta xs}{\delta \dot{q}}]\ [l_r],\ [S_s] = [\frac{\delta xs}{\delta q}]\ [l_s]$$

- Les coefficients aérodynamiques bruts de la relation 12

$$[C_{lr,s}] = [\frac{\delta fr}{\delta u}]\ [\frac{\delta u}{\delta q}]\ l_r$$

$$[C_{2r,r}] = [\frac{\delta fr}{\delta u}]\ [\frac{\delta u}{\delta \dot{q}}]\ l_r$$

$$[C_{lr,g}] = [\frac{\delta fr}{\delta u}]\ [\frac{\delta u}{\delta q}]\ l_g$$

$$[C_{lr,s}] = [\frac{\delta fr}{\delta u}]\ [\frac{\delta u}{\delta q}]\ l_s$$

- L'opérateur des réponses d'efforts et contraintes

$$[\frac{\delta \sigma}{\delta xs}] = [\frac{\delta \sigma}{\delta u}]\ (I - (\frac{\delta u}{\delta \ddot{x}r})\ (m_{rr})^{-1}\ [\frac{\delta fr}{\delta u}])$$

$$[\frac{\delta \sigma}{\delta xr}] = [\frac{\delta \sigma}{\delta u}]\ [\frac{\delta u}{\delta q}]\ [l_r]$$

qui donne accès aux coefficients aérodynamiques et aux réponses d'efforts "aéroélasticité éliminée" (Relation 16 et 18 du § 2.2).

- Opérateur de reconstitution des charges de base aéroélasticité éliminée.

Les charges de base se reconstituent en fonction des paramètres de mécanique du vol pseudo-rigide par la relation :

$$u = \frac{1}{2}\rho v^2\ \{\frac{l}{v}\ [\frac{\delta u'}{\delta \dot{x}r}]\dot{x}r + [\frac{\delta u'}{\delta xr}]\ xr$$

$$+ [\frac{\delta u'}{\delta xg}]xg + U_{aéro_o}\ \} + u_o$$

dont les opérateurs se déduisent des matrices $[S_r]$ et $[D]$ par des relations du type :

$$[\frac{\delta u'}{\delta xr}] = \frac{1}{2} \rho v^2 \{I - (\frac{\delta u}{\delta xr}) (m_{rr})^{-1} (\frac{\delta fr}{\delta u})\} [D]^{-1} [S_r]$$

ce qui permet dans les configurations désirées de reconstituer les déplacements avec les charges Eléments Finis pour les relations :

$$D = [B]u + [V_r]xr \qquad \text{et} \qquad F = [P]u$$

2.3.8 - Calcul des manoeuvres et de charges dimensionnantes

Les charges résultent de manoeuvres calculées en résolvant l'équation (15) de la mécanique du vol aéroélasticité éliminé. On remonte aux contraintes d'efforts internes aux points sensibles par la relation (17), on reconstitue les charges de base par la relation 20.

Le coût des calculs dans la phase de couplage étant faible (ils peuvent être effectués en mode interactif si on le désire), on balaye facilement le domaine d'analyse (Type de manoeuvre, configuration massique, Mach, altitude, hypothèse aérodynamique).

La recherche des cas de charges enveloppes est effectuée à partir des vecteurs u de chaque manoeuvre par la procédure automatique suivante :

- Un cas de charge est déclaré enveloppe s'il conduit à une valeur extrémale de la contrainte, à une tolérance près, sur au moins 1 point sensible (composante de σ)
- Un algorithme trouve le nombre de cas de charges minimal tel qu'en chaque point sensible, les valeurs extrémales des contraintes, soient atteintes sous au moins 1 cas de charge (à la tolérance près)
- L'élargissement de la tolérance permet de réduire le nombre de cas enveloppe
- Le processus est associatif

Pour les cas dimensionnants on reconstitue les déplacements Eléments Finis par combinaison des déplacements et charges de base ; la reconstitution des charges permet de calculer en détail sur des modèles Eléments Finis raffinés après une opération de transfert des charges.

Un point, soulevé très souvent, est la définition des manoeuvres à prendre en compte pour le calcul des charges de dimensionnement, notamment pour le cas des avions à commandes de vol électriques.

On peut employer la stratégie simple suivante :

- Etablissement des charges et dimensionnement de la structure pour des manoeuvres simples forfaitaires dont le choix résulte des clauses techniques de l'appareil et de l'expérience qu'on a des avions précédents.
- Etablissement systématique pour tout le domaine Mach, masse, pression dynamique, des coefficients aérodynamiques, aéroélasticité éliminée (C') et des contraintes unitaires $(\delta\sigma'/\delta xr]$ fourniture des valeurs extrémales $\sigma_{extr.}$
- Calcul systématique des σ dans toutes les simulations de mécanique du vol avec CDVE.

En cas de dépassement des $\sigma_{limites}$

- Soit on modifie le réglage des CDVE
- Soit on rediscute le dimensionnement en définissant de nouvelles manoeuvres pour les charges forfaitaires.

2.4 - Remarques - Méthodes allégées

La méthode de réduction dans une base de chargement et une base de forme aérodynamique demande des manipulations et des données initiales relativement complexes, elle est avantageuse pour l'étude de l'aéroélasticité et des charges dans un domaine de vol complet.

Pour les cas moins ambitieux nous avons prévu deux types d'allégements :

- Utilisation d'une base élastique de modes propres, qui demande beaucoup moins de données que la base de charges, le coût ordinateur pour une configuration massique est du même ordre, il se multiplie par le nombre de configuration massique.
- Coïncidence des formes de base aérodynamiques et élastiques, qui évite les opérations de lissage, mais rend une partie des manipulations aérodynamiques dépendante des résultats de l'élasticité.

Ces deux allégements peuvent être introduits indépendamment ou simultanément.

Les réductions de base modale ont l'inconvénient de présenter une susceptibilité à la troncature difficilement appréciable a priori, les erreurs de troncature rejaillissent plus directement sur le calcul des contraintes que sur celui des coefficients aérodynamiques souples.

La méthode de base de chargement peut être considérée comme "exacte" à partir du moment où on admet la décomposition des charges dans les cas de base, deux considérations rendent négligeables les effets de troncature :

- L'effet de "Saint Venant" qui fait que les forces agissent principalement par leur torseur résultant, qui est préservé le plus localement possible dans notre approche.
- Le fait qu'on veille à décomposer chaque "espèce topologique" de charges (Inertie, Pression, Forces concentrées) dans les sous espèces de (P) appropriés.

Les effets de troncature des charges dus aux formes aérodynamiques sont insignifiants (eu égard à la précision des calculs), le lissage dans la base de forme réduite peut même améliorer les résultats des calculs pour des structures présentant des défauts locaux de rigidité.

3 - POINTS SPECIFIQUES ET DE DEVELOPPEMENT

3.1 - Calculs dynamiques

Il importe de rendre compatible avec le modèle d'aéroélasticité statique les modèles de calculs de stabilité, dynamique (Flutter, accrochage CDVE) et des réponses dynamiques transitoires.

Pour l'aérodynamique instationnaire il ne faut pas que la rusticité relative des méthodes employées (Doublets, sources) affecte la partie stationnaire et a fortiori les champs des effets rigides.

C'est pourquoi nous ne prenons dans les calculs instationnaires que la partie transitoire soit :

$$A\left(\frac{\omega}{v}\right)tr = A\left(\frac{\omega}{v}\right)_{inst} - [A]_{stationnaire}$$

Rendu dans la base de charges les effets aérodynamiques instationnaires deviennent :

$$\frac{\delta u}{\delta q}\left(\frac{\omega}{V}\right) = \frac{\delta u}{\delta q}\ \text{stat.}_{\text{rec.}} + i\,\frac{\omega}{v}\ \frac{\delta u}{\delta \dot{q}}\ \text{stat.}_{\text{rec.}} + \frac{\delta u}{\delta Kp}\,[A[\tfrac{\omega}{v}]]\,\left(\frac{\delta \alpha}{\delta q} + i\frac{\omega}{v}\,\frac{\delta \alpha}{\delta \dot{q}}\right)$$

Pour le modèle dynamique élastique nous pratiquons deux techniques principales :

- Utilisation d'une réduction de base modale calculée indépendamment de la base de charges ; les forces généralisées sont transmises par la relation :

$$f = [V]_t\ \ [P]^u$$

- Calcul dynamique directement dans le sous espace des formes (B) de la base de charges, orthogonalisées aux modes rigides, qui rend en quasi stationnaire le modèle dynamique strictement identique au modèle statique ; cette technique nécessite l'élimination des composantes redondantes de la base de charge.

Il existe aussi des techniques hybrides :

- Base modale enrichie de déformées de base (Indispensable pour les forces extérieures ponctuelles, type trains d'atterrissage)
- Base des modes du sous espace (B) éventuellement tronqués

3.2 - Calcul non linéaire

3.2.1 - Non linéarités aérodynamiques

En pratique il est impossible de les négliger, les cas dimensionnants, correspondant le plus souvent au domaine transsonique où l'aérodynamique est complètement non linéaire.

Pour la pratique courante nous procédons par recalage des effets rigides sur la soufflerie (ou le vol voir § 3.4).

On établit des effets rigides "secant" par zone du domaine incidence braquage de gouverne, à partir de l'interpolation des mesures ; les calculs d'aéroélasticité et de manoeuvre prennent dans la base de donnée aérodynamique la table correspondante à l'incidence et au braquage calculé (Processus itératif pour les manoeuvres stabilisées).

Les effets souples $\delta u / \delta q$ (dont la partie rigide et gouverne, est recalée) restent calculés par les théories subsonique ou supersonique.

En développement nous testons deux approches :

- Méthode des petites perturbations transsoniques dont le coût raisonnable permet de se ramener au processus linéaire par calcul des effets de déformation élémentaire.

- Méthode plus sophistiquée de différences finies et Eléments Finis (réf. 3, 4) pour lesquels on ne peut envisager que des analyses pour des "formes" données soit Kp(q) ; on adopte alors pour les calculs d'équilibre en manoeuvre une méthode itérative type "Newton modifiée" avec comme "solveur" l'opérateur approché $[\delta Kp / \delta q]lin.$ des théories linéarisées soit le schéma suivant :

- Analyse linéaire aéroélastique

  . coef. souples

  . manoeuvre

  → $[\delta Kp / \delta q]lin.$ → $q_{équil.}$

- Calcul Aéro N.L. sur forme $q_{équil.}$

  → $Kp(q_{équil})$

- modification Kpo

  → $Kp_o = Kp(q_{équil}) - [\delta Kp / \delta q]lin\ q_{équil.}$

- Analyse linéaire aéroélastique et manoeuvre avec Ko

  → $q_{équil.}$

3.2.2 - Non linéarité mécanique

- Vitesse de rotation (forces centrifuge)

On ajoute au champs de forces d'inertie linéaire le terme de force centrifuge

$$\vec{F} = \Sigma\ mi\ \vec{\Omega} \wedge (\vec{\Omega} \wedge \vec{GM})$$

qui s'exprime dans la base de charge en fonction des produits des rotations rigides sous la forme :

$$U_{centrifuge} = [Cent]\ \dot{x}_{ri}\ \dot{x}_{rj} \quad 4 \leqslant i \leqslant 6$$

L'opérateur [Cent] est une combinaison linéaire des composantes "Force centrifuge" de la base de charge :

$$Pcent = \sum_{ij}^{noeuds} M^{noeuds}\ C_i\ C_j$$

A partir de là l'aéroélasticité des termes de forces centrifuges s'élimine, pour aboutir à une équation d'équilibre aéroélasticité éliminée analogue à (15), mais comportant des termes en produit de rotation rigide dépendant du badin.

- Non linéarité géométrique

Pour le calcul des charges l'effet le plus significatif vient des variations de rigidité induit par les grands braquages de gouverne.

Si on veut traiter exactement le problème il faut itérer avec des analyses E.F. gouvernes braquées, qui sont dispendieuses si on ne procède pas par sous structuration.

- Non linéarité de contact

C'est un cas très fréquent résultant de l'effet des jeux où des montages à "patte calante" des charges extérieures.

On dispose de deux méthodes de résolution par condensation sur les DDL de contact, très peu dispendieuses :

. contact hyperstatique (applicable à l'isostatique en dynamique), condensation en flexibilité

- le modèle EF est calculé sans tenir compte du contact
- on enrichit la base de charge des réactions unitaires des points de contact
- on traite les jeux comme des composantes de σ

. on résout l'équation d'équilibre aéroélasticité éliminée 15 avec des réactions de contact unitaires (Apparaissant dans le terme f'o), on obtient les jeux correspondant, soit la relation :

$$j = [\phi]\, r + j_o$$

Les conditions de contact ajoutent les inéquations :

$$r \geq 0 \quad si \quad j = 0$$

$$j \geq 0 \quad si \quad r = 0$$

L'ensemble est résolu par une technique d'optimisation (Itération de gradient conjugué "sphérique"), qui fournit les réactions d'équilibre r, qui sont reportées comme second nombre de l'équation d'équilibre 15.

. Contact isostatique (Essentiellement le cas des jeux dans les timoneries de gouverne en dynamique).

Il vaut mieux utiliser la procédure "duale" de condensation en rigidité suivante ;

- résolution E.F. en supposant le contact
- ce sont les réactions de contact qu'on introduit dans les σ
- on résout les équations d'équilibre aéroélastique avec des jeux unitaires qui apparaissent comme des braquages de gouvernes, on obtient les réactions correspondantes, soit la relation :

$$r = [K]j + r_o$$

A laquelle on rajoute les conditions de contact résolues comme précédemment

si $\quad r \geq 0 \qquad j = 0$

si $\quad j \geq 0 \qquad r = 0$

- Non linéarité de servo commande (saturation, non linéarité du modèle hydraulique dynamique).

On procède à la condensation en "rigidité" du problème de façon analogue pour aboutir aux relations

$$f_{servo} = [K]d_{servo} + f_{o\ servo}$$

à laquelle on rajoute les équations d'équilibre statique (ou dynamique) de chaque servo-commande

$$d_{servo} = \underset{\text{non lin.}}{\text{fonction}}(f_{servo}, \text{consignes}, \underset{\text{hydraul.}}{\text{paramètres}}, \underset{\text{précéd.}}{\text{états}})$$

Système d'équations condensé non linéaire "dur" à résoudre par une technique BFGS avec "Line Search".

- Trains d'atterrissage

Le couplage au train d'atterrissage s'apparente à celui des servos, nous l'avons décrit en détail dans la référence 5.

- Non linéarités en dynamique

Elles exigent une intégration dans le domaine temps que nous traitons de manière implicite (méthode de Newmark ou de Houbolt), conduisant, à chaque pas de temps, à résoudre un équilibre quasi statique avec des coefficients de "rigidité" *modifiés (addition de* $\frac{\alpha}{\Delta t^2}[M] + \frac{\beta}{\Delta t}(\nu - \frac{1}{2}\rho v C_r)$ et un second membre modifié par des termes fonctions des états précédents, à cela près toutes les techniques de résolution des équilibres non linéaires statiques précédemment cités sont valables.

Le problème théorique délicat est la prise en compte des forces aérodynamiques transitoires qui ne sont définies que dans le domaine fréquence, *nous développons deux techniques :*

. rationalisation basé sur le lissage de l'aérodynamique par des polynômes en ω qui conduit à :

$$Ut_r = a_1 \dot{q} + a_2 \ddot{q} + \ldots + a_n q^n$$

dont les termes en dérivés se prennent aisément en compte dans l'intégration implicite.

. intégration par convolution à partir des réponses en Kp ; a des échelons d'incidence locale dont les coefficients sont identifiés par transformée de Fourier aux fréquences de calcul de l'opérateur $[A(\frac{\omega}{V})]$

Ce type d'intégration, qui fait apparaître des termes correctifs venant du passé, se prend en compte aisément dans l'intégration implicite.

3.3 - Optimisation

L'usage intensif de la technique d'optimisation structurale par AMD-BA depuis une décennie, a exigé dès le départ, la prise en compte de contraintes d'ordre aéroélastique portant essentiellement sur les efficacités de gouvernes et de vitesses de Flutter.

Nous avons exposé en détail dans les références 6, 7 et 8 ces méthodes qui ont passablement modifié le processus de dimensionnement de nos avions.

Ces techniques exigent la fourniture au moniteur d'optimisation, de l'analyse des "contraintes" d'aéroélasticité et leurs dérivations par rapport à des paramètres de conception λ (Echantillonnage) dont les matrices de rigidité (K) et de masse (M) dépendent linéairement soit :

$$[K] = [K_o] + \Sigma\, \lambda i\, [K_i]$$

$$[M] = [M_o] + \Sigma\, \lambda i\, [M_i]$$

Nous résumons ici la technique spécifique pour effectuer, à meilleur compte, les itérations d'analyse et de dérivation, qui s'organise sensiblement différemment du calcul général exposé § 2.3.

- Analyse

qs représentant le lissage des effets souples Xo dans les formes aérodynamique de base, il vient :

21
$$q_s = \frac{1}{2}\rho v^2 [L] \{B_s\, q_s + B_r\, x_r + B_{\dot{r}}\, x_{\dot{r}} + B_g\, X_g + X_o\}$$

Les opérateurs B. correspondent aux résolutions type :

$$B_s = [K]^{-1} \quad P \frac{\delta u}{\delta Kp} A \frac{\delta \alpha}{\delta qs} = [K]^{-1} Ps$$

(L'opération B. = $(K)^{-1}$ P. se sous-entend comme comprenant, en plus de la résolution, les orthogonalisations de P. et X. aux modes rigides).

On tabule avant les itérations les opérateurs de charges élémentaires en posant :

22 $$D' = I - \frac{1}{2} \rho v^2 \, L \, B_s$$

il vient la relation d'élimination des

23 $$q_s = \frac{1}{2} \rho v^2 \, [D']^{-1} \, L \, \{B_r \, x_r + B_{\dot{r}} \, x_{\dot{r}} + B_g \, x_g + X_o\}$$

Les coefficients aérodynamiques et aéroélasticité éliminés prennent des formes du type :

24 $$C'_{rr} = C_{rr} + \frac{1}{2} \rho v^2 \, C_{r,q_s} \, \mu$$

$$\text{avec } [\mu] = D'^{-1} \, L \, B_r$$

- Dérivation

Sachant que $d\,(K^{-1} F) = - K^{-1} \, dK \, X$ la différenciation de 22 conduit à :

25 $$dq_s = - \frac{1}{2} \rho v^{2'} \, L \, K^{-1} \, dK \, \{B_s \, q_s + B_r \, x_r + B_{\dot{r}} \, x_{\dot{r}} + B_g \, X_g + X_o\}$$

en éliminant qs par 23 il vient

$$dq_s = - \frac{1}{2} \rho v^2 \, D^{-1} \, L \, K^{-1} \, dK \, \{B_r \, x_r + B_{\dot{r}} \, x_{\dot{r}} + B_g \, x_g + X_o\}$$

en différenciant 24 il vient :

$$dC'_{rr} = \frac{1}{2} \rho v^2 \, C_{r,q_s} \, d\mu$$

$$dC'_{rr} = - \frac{1}{2} \rho v^2 \, C_{r,q_s} \, D^{-1} \, L \, K^{-1} \, dK \, \{B_r + B_o \, \mu\}$$

Préférable sous les formes :

$$dC'_{r,r} = - \frac{1}{2} \rho v^2 \, \{K^{-1} \, (C_{r,q_s} \, D^{-1} \, L)_t \}_t \, dK (B_r + B_o \, \mu)$$

dont le gros des calculs représente la résolution des équations d'équilibre EF avec autant de seconds membres que de coefficients aérodynamiques surveillés dans l'optimisation, à chaque Mach et chaque pression dynamique envisagée.

$$dC'_{r,r} = - \frac{1}{2} \rho v^2 \, C_{r,q_s} \, D^{-1} \, (K^{-1} \, L_t)_t \, dK (B_r + B_o \, \mu)$$

dont le gros des calculs représente des résolutions de l'équilibre EF en nombre égal à celui des formes aérodynamiques de base (Indépendamment des coefficients, Mach, pression, pris en compte).

3.4 - Identification

L'idée directrice est de corriger le modèle théorique en fonction des mesures en vol, pour permettre des extrapolations au-delà des points du domaine effectivement testé.

Nous avons exposé en détail la technique que nous utilisons dans la référence 9.

L'avion est instrumenté, en plus des capteurs classiques des paramètres de mécanique du vol, de plusieurs centaines de jauges de contraintes dont la disposition résulte d'un compromis entre la surveillance des points sensibles de la structure et la couverture des divers "chemins" d'efforts internes.

- Par des étalonnages au sol on corrèle les contraintes calculées aux contraintes mesurées sous de nombreux chargements (plusieurs dizaines) les principaux "chemins" d'efforts devant être excités, il en résulte, après correction un opérateur $\delta\sigma / \delta F$ fiable.

- Les mesures en vol sont effectuées sur des manoeuvres permettant de séparer au mieux chaque effet aérodynamique élémentaire (incidence braquage et gouverne, etc...), ces manoeuvres dites "stimulus" sont des oscillations de tangage ou de roulis à fréquence variable (programmées dans les CDVE).

- On sépare par une opération de lissage les réponses aérodynamiques élémentaires $\sigma_{r\ mes}$, dites "mesurées", ces résultats intermédiaires sont validés par recoupements sur d'autres manoeuvres.

- On pose que les différences avec la théorie ne proviennent que de la distorsion des champs de pression aérodynamique rigide élémentaire par une fonction dépendant de paramètres λ inconnus (pour les effets "souples" on croit à la théorie).

Les techniques de recalage, décrites § 2.3.5, et l'ensemble de l'analyse, permettent le calcul des réponses des jauges en fonction de λ soit $\sigma_r(\lambda)$, le processus de dérivation fournissant $\delta\sigma_r / \delta\lambda$ est assez complexe, il est décrit en détail dans la référence

- Le problème d'identification est posé sous la forme

$$\lambda^2 \quad \text{minimum}$$

en satisfaisant aux inégalités

$$\sigma_{r\ mes} - \varepsilon \leqslant \sigma_r(\lambda) \leqslant \sigma_{r\ mes} + \varepsilon$$

Soit chercher la solution la plus proche possible de la théorie reconstituant les mesures à une tolérance de précision près.

L'intérêt de cet approche, par rapport aux méthodes classiques de moindres carrés, est de ne pouvoir être mis en défaut par les combinaisons de paramètres "non observables" (pris alors à leurs valeurs théoriques), et que les données de précisions des mesures ε peuvent être évaluées.

Pour être appliquée telle qu'elle, cette technique exige la séparation d'effets aérodynamiques linéarisés, ce qui pose des problèmes en transsonique.

Remarque

La même technique d'identification par réponse de jauges s'applique (plus simplement) sur les essais en soufflerie, pour la reconstitution de champs de pression "utile" à partir de mesures sur maquette instrumentée de jauges de contraintes.

4 - CONCLUSIONS

Nous disposons aujourd'hui d'un état de l'art en calcul des charges satisfaisant, pour couvrir en statique et en dynamique :

- L'ensemble des phénomènes, linéaires ou raisonnablement linéarisables

- La plupart des problèmes non linéaires mécaniques

Le problème délicat de la gestion de ces calculs dans un domaine multiparamètres (Manoeuvres, configurations massiques, Mach, pression dynamique) est résolu à faible coût par les techniques de base de charges et base de formes aérodynamiques.

Le point vraiment épineux est celui des non linéarités aérodynamiques en transsonique, qui affectent malheureusement le calcul de la plupart des cas de charge dimensionnants ; les méthodes de calcul simple sont trop inexactes et les méthodes sophistiquées trop coûteuses pour qu'on puisse balayer raisonnablement le domaine des configurations ; même l'identification de modèle sur le vol est très délicate en transsonique.

Ces aspects négatifs se compensent partiellement :

- pour la voilure, par le fait qu'une bonne partie des manoeuvres dimensionnantes est défini par les torseurs résultants des charges plutôt que par les paramètres aérodynamiques ; ainsi pour une manoeuvre de facteur de charge stabilisée, le fait, qu'en tout état de cause, l'avion porte son poids et qu'une proportion relativement constante de la portance se situe sur la voilure, atténue notablement, pour le moment de flexion à l'emplanture, les erraticités des répartitions de pression.

- que les commandes de vol "digitales" modernes peuvent être dotées de système correcteur maintenant l'avion dans un domaine donné d'accélération (voir de contrainte).

REFERENCES

1 - C.PETIAU & D.BOUTIN
Aëroélasticité et optimisation en avant-projet
Agard conference proceeding n°334
Aeroelastic considerations in the preliminary design of Aircraft
London 1983

2 - R.DAT
Vibration aéroélastique, cours de l'Ecole Centrale des Arts et Manufacture.

3 - V.BILLEY, J.PERIAUX, P.PERRIER, B.STOUFFLET
2D and 3D Euler computation with finite element in aérodynamic.
Congrés international sur les systèmes hyperboliques.
St-Etienne - Juin 86.

4 - M.O.BRISAUX, G.GLOVINSKI, J.PERIAUX, G.POIRIER
On numerical solution of non linear problem in fluid dynamics by least square methods and finite element method.
3 st International conference on finite element in non linear mechanics
FENOMECH 84 Stuttgard.

5 - C.PETIAU
Méthode simulation numérique du système avion atterrisseur
Agard conference proceeding n°326
Aircraft dynamic response to damaged and repared runway
Brussel 1982.

6 - C.PETIAU & G.LECINA
Eléments finis et optimisation des structures aéronautiques
Agard conference proceeding n°280
"The use of computer as a design tool" - Munich 1978.

7 - G.LECINA & C.PETIAU
Optimisation of aircraft structure
Fundations of structure optimization approach
Edited by A.J.Morris - 1982 John Waley & Sons Ltd.

8 - C.PETIAU & M.DE LAVIGNE
Analyse aëroélastique et identification des charges en vol
Agard conferences proceeding n°375
"operational loads data - Sienne 1984.

MODELISATION MIRAGE 2000

Planche 1

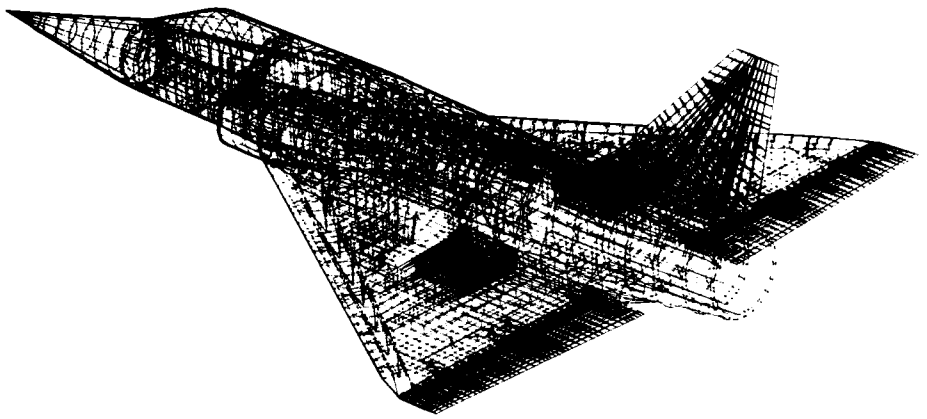

Planche 2

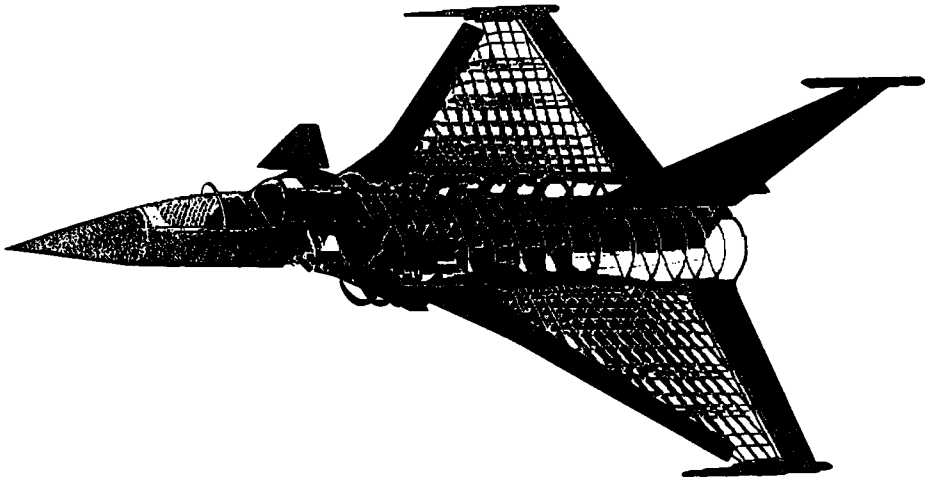

MODELISATION RAFALE

Planche 3

ORGANIZATION OF STATIC AEROELASTICITY BY BASIC LOADS METHOD

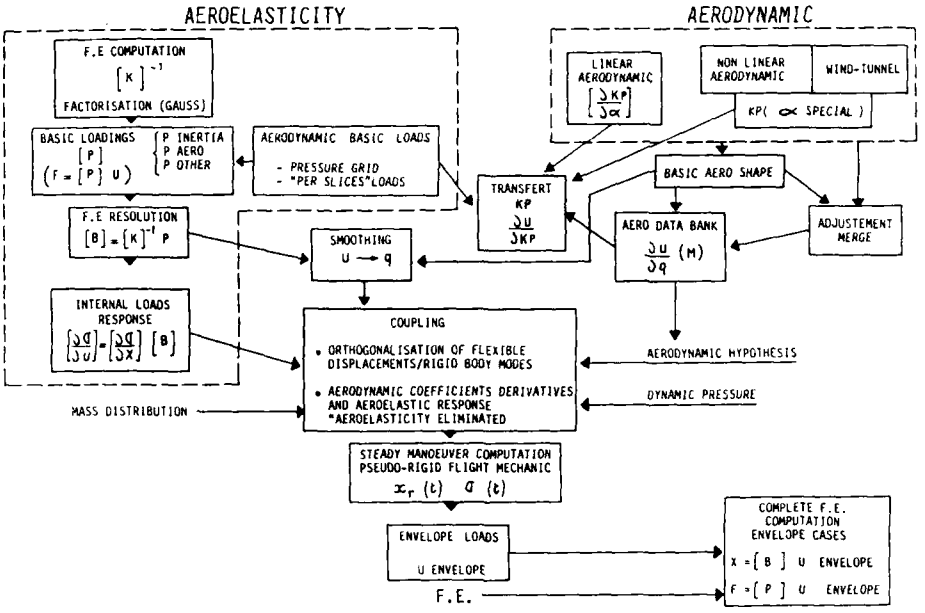

Planche 4

MODELE AERODYNAMIQUE
Champ de pression
Effet d'incidence . Mach 0,8

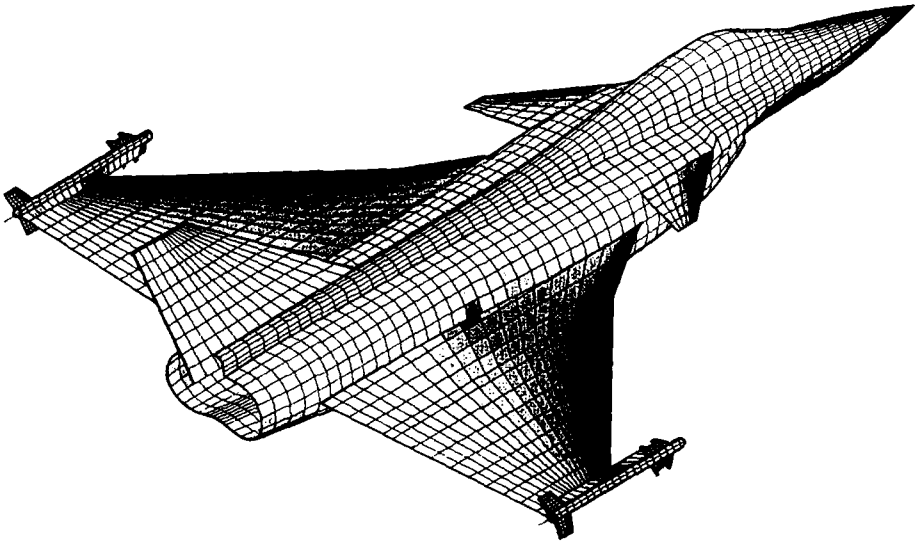

TRANSFERT DES CHARGEMENTS AERODYNAMIQUES Planche 5

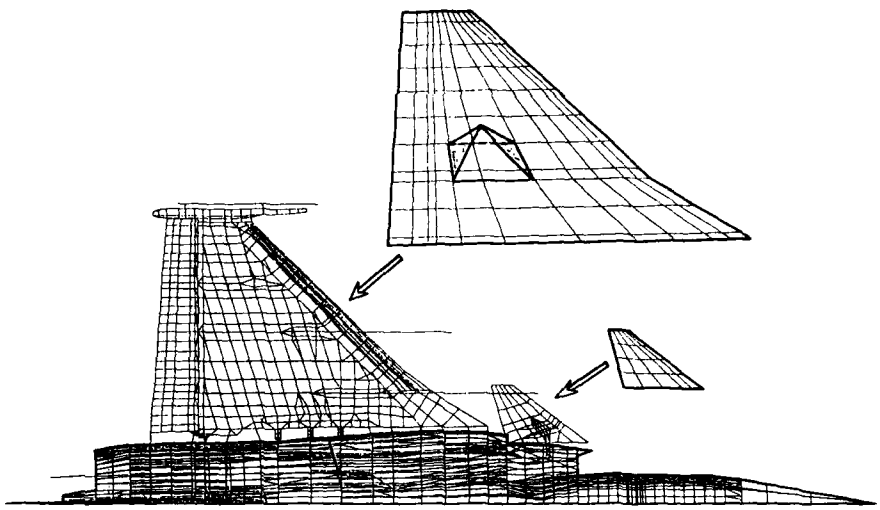

MODELE DE DISCRETISATION DES PRESSIONS Planche 6

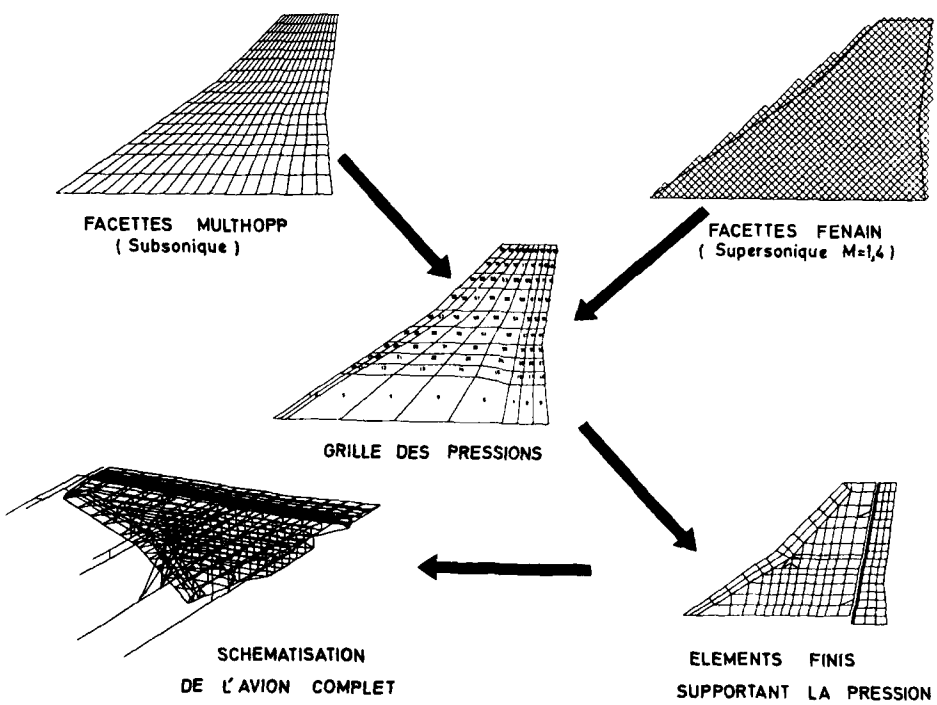

EXEMPLE DE CHAMP DE PRESSION

Planche 7

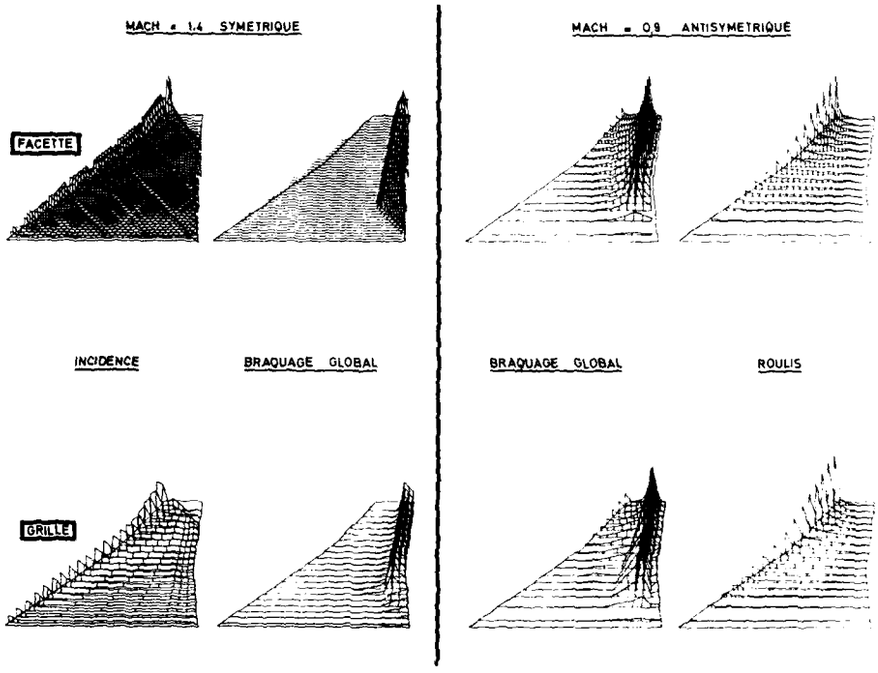

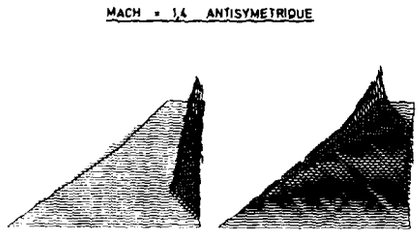

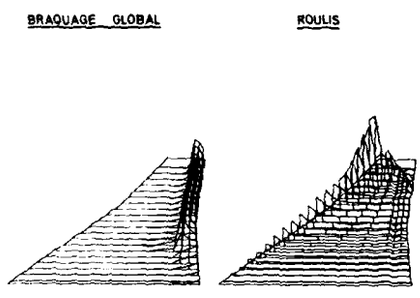

Planche 8

COEFFICIENTS AERODYNAMIQUES APPARENTS
Effet de braquage . Mach 1

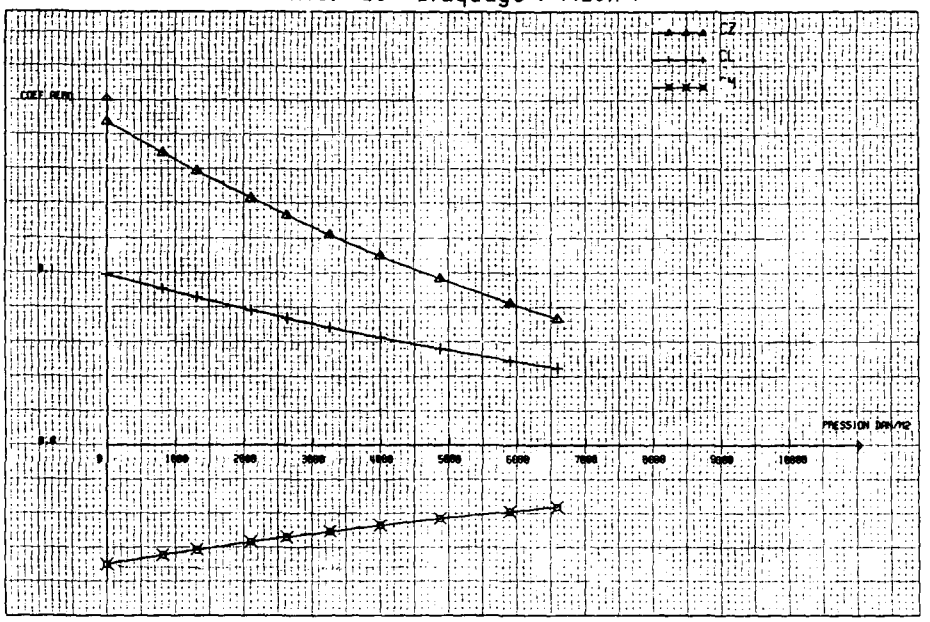

Planche 9

ATTACHE PRINCIPALE DE VOILURE : FY = f (Mach, P dyn)
pour effet unitaire de gauchissement

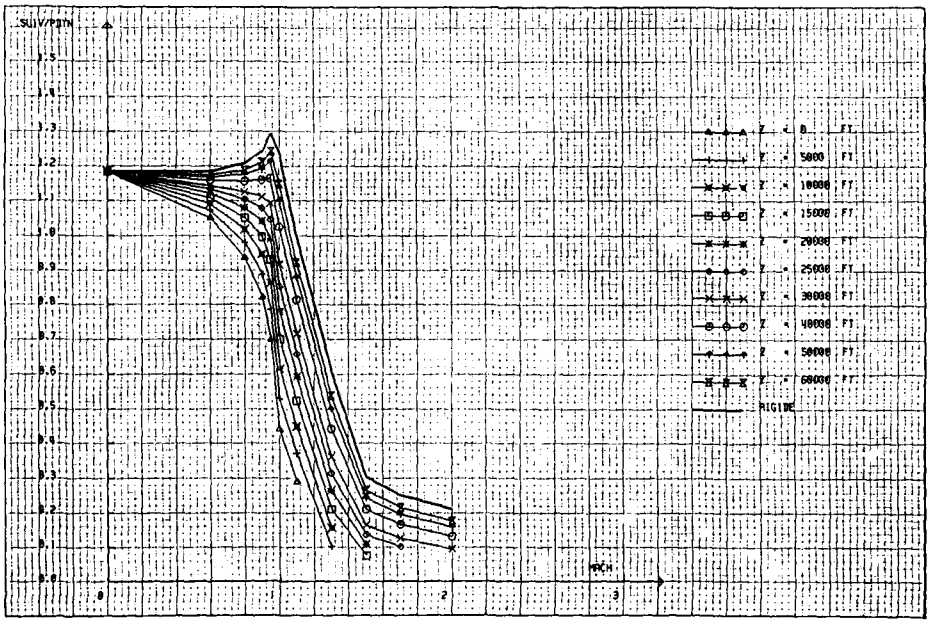

Planche 10

DEFORMEES AEROELASTIQUES

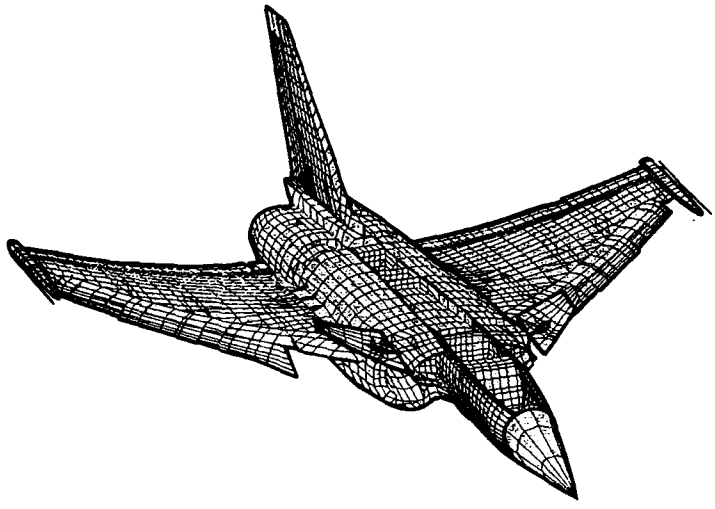

Mach 0.9 facteur de charge 9g (déformations * 5)

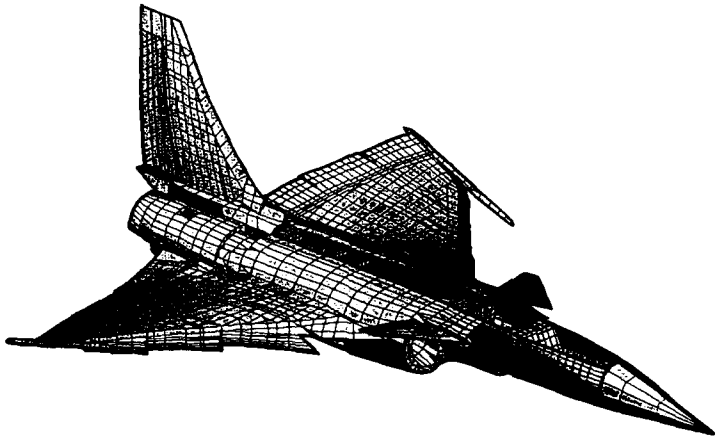

Mach 0.9 roulis stabilisé 260°/s (déformations * 8)

Planche 11

MODES DE VIBRATIONS

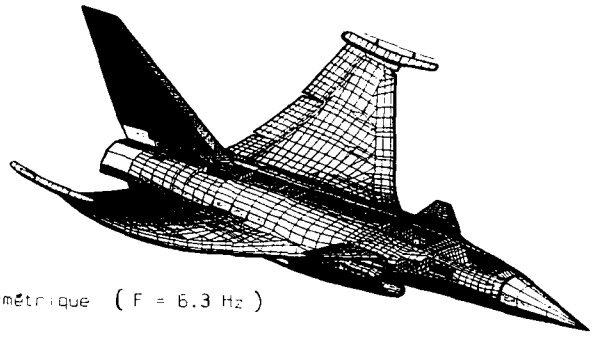

1er mode symétrique (F = 6.3 Hz)

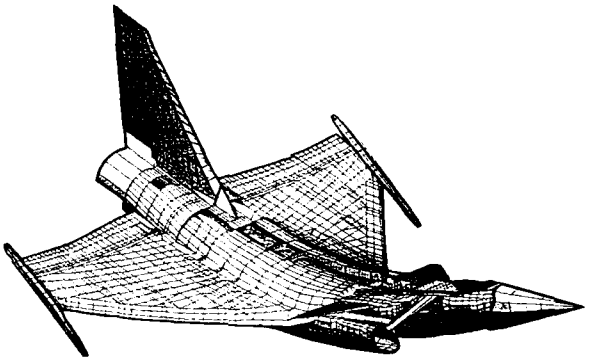

2ème mode symétrique (F = 10.2 Hz)

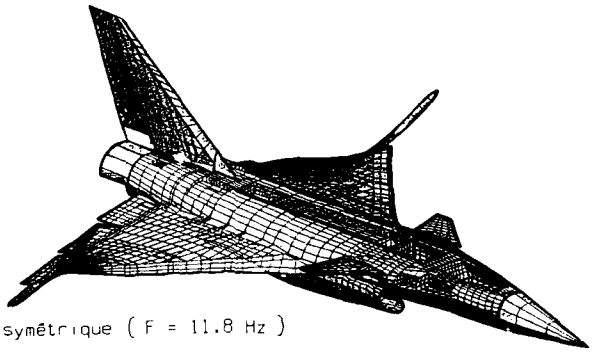

3ème mode symétrique (F = 11.8 Hz)

STATIC AEROELASTIC CONSIDERATIONS IN THE DEFINITION OF DESIGN LOADS FOR FIGHTER AIRPLANES

by

G. SCHMIDINGER
O. SENSBURG

MESSERSCHMITT-BOELKOW-BLOHM GmbH.
Helicopter and Airplane Division
8000 Munich 80, P.O. Box 801160, W.-Germany

ABSTRACT

The paper initially is starting with some typical effects of static aeroelastic correction factors in context with the definition of structural design loads for major aircraft components. The influences on response parameters and resulting design loads are shown as well as the aeroelastic optimization of trailing edge flaps with respect to geometry, efficiency and hingemoments.

INTRODUCTION

Over the last 20 years the implication of static aeroelastics has increasingly been recognized and respective publications reflect their influence on aerodynamics, control efficiency, performance and structural optimization.

In the beginning these influences of static aeroelastics have been evaluated quite independantly by the different technical disciplines, but in the last decade, use of structural optimization programs especially in designing carbon fibre structural components led to the development of tools for aeroelastic tailoring. These tools now represent a productive link between the technical departments in order to achieve an integrated design and it may be pointed out, that the quality of results to a large extent reflect the skill of project structural managers in coordinating the increasingly complex and coherent technical aspects.

DETERMINATION OF AEROELASTIC LOADS

A survey of important considerations on general aeroelastics is given e.g. in the References of the 60th AGARD Meeting last year (see List of References). Some special areas of interest in context with the definition of design loads for a flexible aircraft are emphasized here.

Table 1 shows a simplified example, how static aeroelastic application rules may be dealt with. The aircraft aerodynamic model is first treated as a set of major aircraft components and the influences of the different state variables on longitudinals - as angle of attack, control terms and damping terms - are summarized in a set of rigid aerodynamic coefficients/derivatives. Static aeroelastics are then either added ($\Delta c..$) or factored ($f_L..$) and considered as a shift of aerodynamic centre of pressure ($x..$).

The structure of laterals is in general analogue - even in reality being more complicated from e.g. determination of dihedral effects etc. - and only fin and rudder as well as store components are added in order to generate the major aerodynamics/aeroelastics of those. The areas of interest intended to be pointed out are displayed in the table:

- aeroelastic wing correction $f_{L_1}(\alpha)$

- aeroelastic inertia increment $\Delta c_{L_{n_z}}$ and
- aeroelastic fin correction $f_{y_1}(\beta)$
- aeroelastic inertia increment $\Delta c_{l_{\dot{p}}}$

The typical shapes of those aeroelastic corrections are shown in Fig. 1 as a function of dynamic pressure and partly additionally dependant on Mach.

Wing Design

Fig. 2 shows in graph 2a a comparison of the static aeroelastic factor f_{L_1} derived from theoretical linear theory with those derived from a "strip method" using the nonlinear rigid wing spanwise local lift from windtunnel measurements versus angle of attack (AOA) as shown in graph 2b. It is obvious, that spanwise AOA effects have an important influence on the flexible total wing lift curve as shown in graph 3c. Whilst the resultant flexible wing lift curve is quite acceptable in the linear region it deviates strongly in the nonlinear region. A comparison of windtunnel measured lift from a rigid bent wing model (designed for a high "g"/α condition) shows, that the "strip method" matches quite well the windtunnel test results in the design condition.

From this experience it can be derived, that also for the definition of incremental effects as e.g. inertias ($\Delta c_{L,m_{n_z}}$) a proper relation of the AOA range in the nonlinear region is mandatory and can only be treated in an iterative process using combined conditions (e.g. AOA + n_z).

In forgetting aeroelastic tailoring to achieve trailing edge flap effectiveness - to be treated at the end - it may be pointed out, that the effects of these static aeroelastics on structural wing design can be regarded as a secondary effect (from shifting the aeroelastic wing load distribution inboard or even outboard) because changes in wing lift from aeroelastics must be compensated by increasing or also decreasing the aircrafts AOA in order to design for a constant load factor.

Fin and Forebody Design

For these components the sitution is quite different because e.g. a horizontal gust case may become critical and the resultant sideslip angle really produces a fin efficiency and resultant design load coincident with f_{y_1} and forebody loads coincident with the aeroelastic increment $\Delta c_{y_B}(\beta)$ as shown on Fig. 1. Thereof these factors are realized as primary effects on design loads and the c.p. shift only as a secondary influence.

Horizontal Tail Loads

Fig. 3 shows the application of steady aeroelastics on the derivation of horizontal tail loads. First it can be seen, that the response calculation using flexible aerodynamics reflects an increased AOA in comparison to the rigid value in order to achieve the same magnitude of design load factor. Secondly a smaller tailplane load is necessary for initiation of the manoeuvre (according to MIL-Spec.) but an increased tailplane load for checking the manoeuvre. In a swept wing stable configuration the latter effect can be explained by reduced stability and it becomes even more pronounced for an unstable aircraft, where very small control loads (tailplane, foreplane or trailing edge flap) for initiation of the pitch manoeuvre are produced but relatively high loads arise in order to check the manoeuvre (instability effect).

Effects of Inertia Terms on Responses and Related Loads

Based on the same "strip method" as quoted above for derivation of wing aeroelastics Fig. 4 shows the inertia bending effect from a roll acceleration $\dot{p}$ for different store adaptions on a medium swept wing-using windtunnel measured spanwise distributions. The aeroelastic deflection results in local AOA changes leading to an inertia rolling moment $\Delta c_{l_{\dot{p}}}(\alpha)$ for the wing alone and an increment for outboard stores respectively as shown on the right hand side of Fig. 4.

In performing a MIL-Spec. rapid rolling manoeuvre considering this $\Delta c_{l_{\dot{p}}}$ term it is revealed, that the resulting acceleration $\dot{p}$ is increasing by up to 40 % as shown in Fig. 5. This $\dot{p}$ produces a change in local load factors of:

Δn_z o/b store = $\dot{p} \cdot \Delta y/g$ or
Δn_y u/f store = $\dot{p} \cdot \Delta z/g$

thus leading to increased net (aero + inertia) normal and side forces by up to 50 % for the 0 "g" case.

In this context an interesting relationship between the moment of inertia and the aeroelastic increment $\Delta c_{l\dot{p}}$ may be worth mentioning. Fig. 6 shows, that a proper combination of the inertia and aerodynamic configuration (aeroelastic effects of outboard stores exist only in line with remarkably increased inertias) is mandatory in order to avoid undue roll accelerations.

Optimization of Trailing Edge Flaps

An empirical formula for the relationship between the aeroelastic roll efficiency factor k_ξ and the aeroelastic hingemoment reduction k_{HM} for ailerons on a delta-canard-fin configuration can approximately be expressed as shown in Fig. 7. It is seen, that half of the aeroelastic efficiency reduction can be assumed for the hingemoment. In demonstrating this very simple relationship on steady roll performance it becomes quite obvious, that flap design hingemoments are strongly influenced by a careful optimization, which shall be treated here below.

This strong influence of the aircraft elastic structure on aerodynamic loading is first shown by the aeroelastic correction factor of an outboard trailing edge flap (Fig. 8) and the respective chordwise distribution shown in Fig. 9.

It will be shown how high sustained roll rates can be achieved at high dynamic pressures with aeroelastic tailoring of a carbon fibre wing, whilst minimizing hinge moment demand and therefore hydraulic power and flow requirements.

A certain roll rate was chosen as design aim at Ma 1.6, 20000 ft, which makes the aircraft agile and competitive. All calculations were performed with the TSO-Computer program /6/ with a MBB-modified optimization algorithm. The program can minimize the structural weight by proper laying of CFC laminates in direction and thicknesses fulfilling in this case static strength and efficiency (stiffness) requirements simultaneously. Because a plate model is used for structural representation quick changes of geometry, like flap size, are posssible which would be very time consuming on a finite element model. On the other hand there is a certain loss of accuracy so that results should be taken as tendencies rather than fixed values of structural weight.

Aim of the Study

The aim of the exercise was to optimize the CFC wing laminates (with respect to weight) in thickness and direction - always fulfilling the rollrate required - in such a way that the lowest trailing edge hinge moments could be found. Flap size - chord and length - were varied parametrically. An estimate of the exchange rate of trailing edge hinge moments with weight is given in Fig. 10. This figure shows that halving necessary hinge moments by making flaps more efficient could save about 60 kg weight.

In order to have all possible flap travel available for rolling it is necessary to do required trimming with the foreplane. The final outcome of the investigations are flaps of optimum size, which cannot be found by applying pure aerodynamic considerations.

Search for Optimum Trailing Edge Size

Due to strong influences of elastic deformations on stationary aerodynamic forces at high dynamic pressures the classical aerodynamic approach with rigid derivatives must be replaced by a method, which optimizes the structural weight fulfilling the roll requirement. It should be emphasized that all parametric investigations must be done by optimizing the structure in thickness and layer direction for every point investigated - which could mean different laminate thickness and directions for each point. A study taking an optimized structure for one point and analyzing another point could be misleading.

The study was conducted in two steps:

1. Find the maximum possible chord flap

2. Define a split line for two flaps

Investigated Flap Geometry

The scope of the study is shown on Fig. 11. Different inboard flap chords were not investigated because the requirement was also to get the largest chord flaps aeroelastically possible necessary to assure controllability at high subsonic Mach numbers where longitudinal static instability is the highest and flap deflection may be restrictive.

Results

Fig. 12 shows the hinge moment and required flap angle to fulfill the roll requirement for flap version I. It shows a steep gradient for hinge moment reduction near the strength design which flattens considerably at 40 kNm. Flap deflection shows similar behaviour. It should be noted that the flap deflection for the rigid wing cannot physically be reached with the given t/c ratio and material properties. Rigid flap in this investigation means a flap which is continously driven. Two optimization runs were made with flexible flaps driven at two spanwise positions (0.2 and 0.5 wing span) which showed that flap angle goes up whereas hinge moment goes down. These results should not be applied as a general rule as is shown in Fig. 13. This figure presents results for flap version II (40 % outboard chord). The behaviour of hinge moment and flap angle is similar but 40 kNm can be reached with less structural weight. When the flexible flap was introduced the flap angle went up considerably whereas the hinge moment did not reduce. A boundary for increasing the flap chord outboard is the flutter speed with tip missile and the request for a reasonable torsional box to get a high enough missile attachment stiffness. As a matter of interest flutter speeds of the clean wing were calculated and are presented in Fig. 14. From this figure it can be deduced that for the clean wing there is no difference between wing with flap I or flap II. Flutter speed increases with structural weight because torsion frequency goes up. In Fig.15 v-g plots and vibration modes for one case are presented. In Fig. 16 the added mass (above the mass for strength design) as a function of the hinge moment is plotted. The optimum hinge moment is about 45 kNm for a full span flap. The bigger chord outboard flap II was chosen for further investigations, because it clearly shows a total mass reduction against flap I.

Flap Split Definition

In order to define the flap split spanwise two exercises were performed. The full span flap was cut outboard down to 80% and 60 % span - always fulfilling the roll requirement with an optimized structure. As shown in Fig. 17 this is the wrong way to go. Hinge moment and flap deflection increase above reasonable values of

40 kNm and 15 deg. (to stay in the linear regime of aerodynamics)

and cannot be reduced by added mass because gradients are too flat.

In Fig. 18 the fullspan flap is cut inboard to 80 % and 54 % span. The hinge moment goes down now but deflection becomes marginal (close to 15 deg.) when a 54 % outboard span flap is used alone to fulfill the roll requirement. It is also impossible to install 30 kNm at such a far outboard position as 54 %. Fig. 19 shows clearly that the optimum lies around 35 kNm installed hinge moment, which is lower than for full span flap (Fig. 16). A possible way to go is shown in Fig. 20, where a flap split is taken at 40 % outboard flap span (referred to total flap span) and different flap angles are used inboard and outboard. Table 2 shows that it is best to use maximum deflection from outboard flap respecting the limits of

20 kNm and 15 deg. angle

because ratio $\frac{\text{flexible hinge moment}}{\text{flexible wing roll moment}}$

is :
- 1.5 x better than full flap
- 2 x better than inboard flap

Proposed Flap Split

The following conditions must be fulfilled:

- biggest possible outboard span flap with maximum angle
- not exceed 20 kNm with outboard flap
- not exceed 15 deg. flap angle

Two cases could be calculated (without changing the aerodynamic grid) shown in Fig. 21. A split of 50 % i/b and 50 % o/b flap was selected. With a linear interpolation of the results shown in Fig. 21 this would give an outboard hinge moment of 22 kNm.

Additionally two benefits of this configuration should be mentioned:

- same actuator could be used for i/b and o/b flap
- about 5 kNm hinge moment is still available at the maximum roll condition when 40 kNm are installed as a total.

CFC Wing Laminate Thickness and Directions

For the selected case the laminates are shown as isothickness in Fig. 22. An unbalanced laminate was chosen because it gives lowest structural weight. It is interesting to note that the +45 deg. layer, which is primarily responsible for increasing flap efficiency, is increasing its thickness outboard to produce higher stiffness.

REFERENCES

/1/ WILSON, E. G. Jr.
Static Aeroelasticity in the Design of Modern Fighters
AGARD-Report No. 725, 1986

/2/ SCHNEIDER, G; ZIMMERMANN, H.
Static Aeroelastic Effects on High Performance Aircraft
ARD-Report No. 725, 1986

/3/ RODDEN, W. P.
Secondary Considerations on Static Aeroelastic Effects on High-Performance Aircraft
AGARD-Report No.725, 1986

/4/ FOERSCHING, H, W.
Grundlagen der Aeroelastik
Springer-Verlag; Berlin-Heidelberg-New York, 1974

/5/ SENSBURG, O.; ZIMMERMANN, H.
Impact of Active Control on Structures Design
AGARD-CP-241, October 1977

/6/ SCHWEIGER, J.; SENSBURG, O.; BERNS, H. J.
Aeroelastic Problems of a Tailless CFC-Sailplane
Second International Symposium on Aeroelasticity and Structural Dynamics
Aachen, April 1985

/7/ GOEDEL, H; HOERNLEIN, H.; KEPPELER, D.; SENSBURG, O.
Modern Trends in Aircraft Structural Design
60th Meeting of the Structures and Materials Panel of AGARD
San Antonio/Texas, 21-26 April 1985

/8/ SENSBURG, O.; SCHMIDINGER, G.; FUELLHAS, K.
Integrated Design of Structures
68th Meeting of the Flight Mechanics Panel of AGARD, 1986

LONGITUDINALS	BODY	WING	TAILERON	REMARK
FLEX. LIFT	$= C_{L_B}(\alpha) \cdot + \Delta C_{L_{B\alpha}} \cdot \alpha$	$+ \boxed{C_{L_W}(\alpha) \cdot f_{L_1}}$	$+ C_{L_T}(\alpha) \cdot f_{L_2}$	α-TERMS
			$+ C_{L_T}(\eta) \cdot f_{L_3}$	CONTROL TERMS *
	$+ C_{L_B}(\dot{\alpha}+q) \cdot f_{L_4}$	$+ C_{L_W}(\dot{\alpha}+q) \cdot f_{L_5}$	$+ C_{L_T}(\dot{\alpha}+q) \cdot f_{L_6}$	DAMPING TERMS
	$+ \Delta C_{L_{B\dot{q}}} \cdot \dot{q}$	$+ \Delta C_{L_{W\dot{q}}} \cdot \dot{q}$	$+ \Delta C_{L_{T\dot{q}}} \cdot \dot{q}$	INERTIA TERMS
	$+ \Delta C_{L_{B n_z}} \cdot n_z$	$+ \boxed{\Delta C_{L_{W n_z}} \cdot n_z}$	$+ \Delta C_{L_{T n_z}} \cdot n_z$	
FLEX. PITCH	$= C_{m_B}(\alpha) + \Delta C_{m_{B\alpha}} \cdot \alpha$	$+ \left[C_{m_W}(\alpha) + \frac{C_{L_W}(\alpha) \cdot X_1}{\bar{C}}\right] \cdot f_{L_1}$	$+ \left[C_{m_T}(\alpha) + \frac{C_{L_T}(\alpha) \cdot X_2}{\bar{C}}\right] \cdot f_{L_2}$	α-TERMS *
			$+ \left[C_{m_T}(\eta) + \frac{C_{L_T}(\eta) \cdot X_3}{\bar{C}}\right] \cdot f_{L_3}$	CONTROL TERMS *
	$+ C_{m_B}(\dot{\alpha}+q) \cdot f_{L_4}$	$+ C_{m_W}(\dot{\alpha}+q) \cdot f_{L_5}$	$+ C_{m_T}(\dot{\alpha}+q) \cdot f_{L_6}$	DAMPING TERMS *
	$+ \Delta C_{m_{B\dot{q}}} \cdot \dot{q}$	$+ \Delta C_{m_{W\dot{q}}} \cdot \dot{q}$	$+ \Delta C_{m_{T\dot{q}}} \cdot \dot{q}$	INERTIA TERMS
	$+ \Delta C_{m_{B n_z}} \cdot n_z$	$+ \boxed{\Delta C_{m_{W n_z}} \cdot n_z}$	$+ \Delta C_{m_{T n_z}} \cdot n_z$	
* FLAP, SLAT, AIRBRAKE, SPOILERS AND INFLUENCE ON ZERO DISTR. AND C.P. SHIFT FOR DAMPING TERMS NOT SHOWN !				
LATERALS	WING BODY	TAILERON	FIN	
FLEX. SIDEFORCE			$+ \boxed{C_{y_F}(\beta) \cdot f_{y_1}} + C_{y_F}(\delta_R) \cdot f_{y_2}$	
FLEX. YAWING	STRUCTURE OF FORMULARE AS IN LONGITUDINALS			
FLEX. ROLLING	$+ \boxed{C_{l_{\dot{p}_W}} \cdot \dot{p} + \Delta C_{l_{\dot{p}_{STORES}}} \cdot \dot{p}}$			
$\Delta C_{..}$ = flex. incr./$f_{L..}$, $f_{y..}$ = flex. corr. factor/$x_{..}$ = flex. c.p. shift				

TABLE 1 STRUCTURE OF AEROELASTIC APPLICATION RULES (SIMPLIFIED)

Flap	Rolling Moment rigid (kNm)/1° defl.	Rolling Moment flex. (kNm)/1° defl.	Rolling moment effect.	Hingemoment rigid (kNm)/1° defl.	Hingemoment flex. (kNm)/1° defl.	Hingemoment effect.	flex. H/M / flex. R/M	H/M flexible (kNm)	essential defl.for Roll/Req.
full span rigid	42.33	22.51	0.352	5.352	4.653	0.869	0.206	42.06	9.04
I/B only rigid	22.34	13.7	0.613	3.887	3.455	0.900	0.252	31.23	9.04
O/B only rigid	19.99	8.8	0.440	1.335	1.199	0.899	0.136	10.84	9.04
full span flex.	42.33	18.45	0.436	5.352	3.836	0.717	0.207	42.27	11.02
I/B only flex.	22.34	11.56	0.518	3.837	2.842	0.741	0.245	31.32	11.02
O/B only flex.	19.99	7.12	0.356	1.335	0.931	0.697	0.130	10.26	11.02

TABLE 2 I/B AND O/B FLAP II (RIGID AND FLEXIBLE)

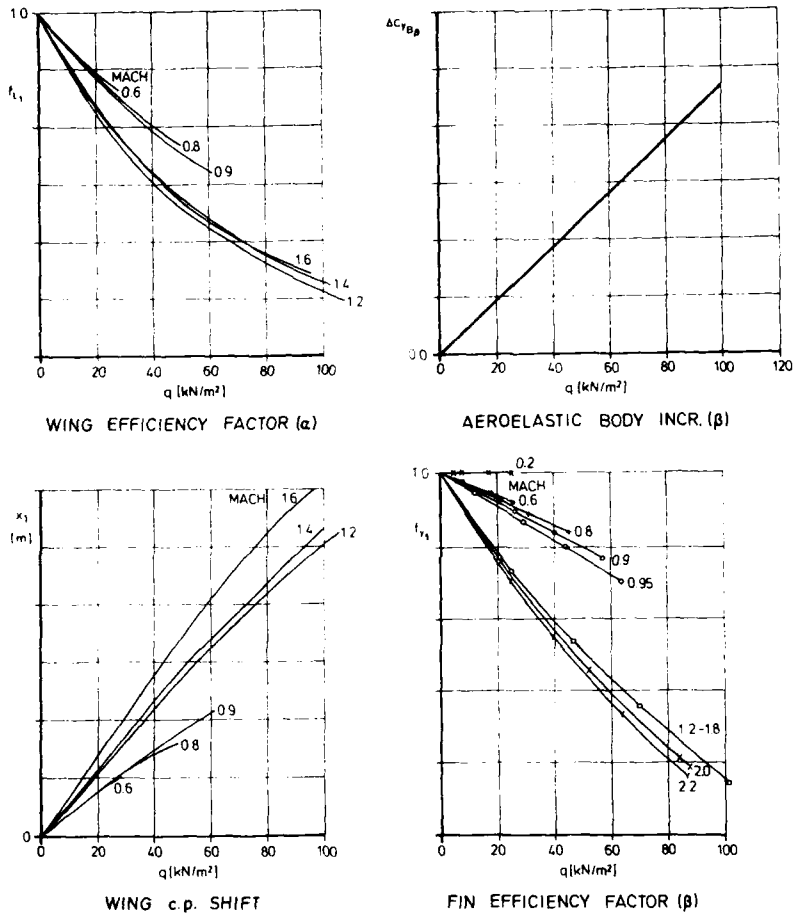

FIG. 1 TYPICAL AEROELASTIC CORRECTIONS

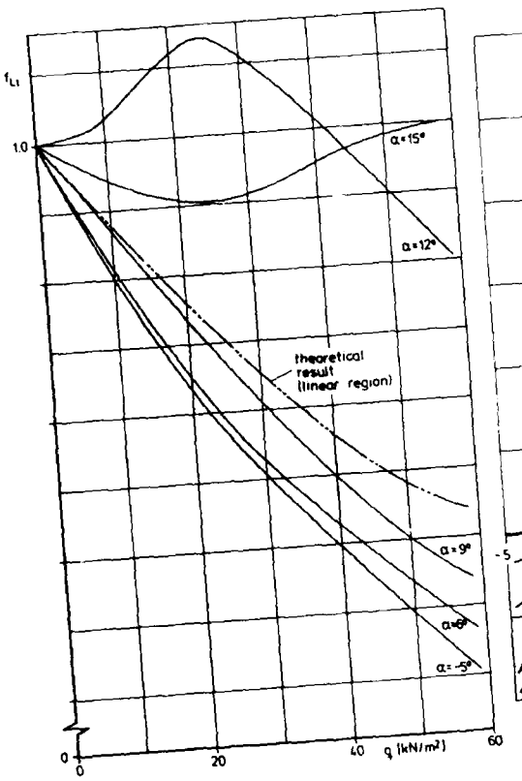

FIG. 2a EXP. WING LIFT AEROELASTIC CORRECTION

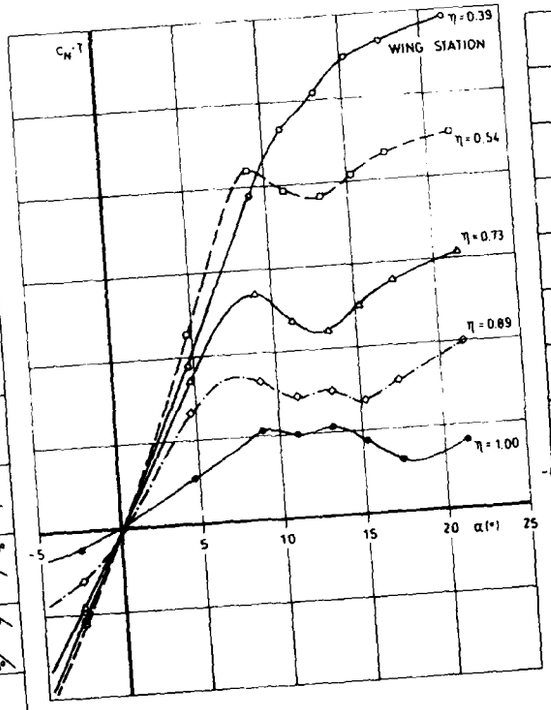

FIG. 2b WINDTUNNEL MEASURED LOCAL LIFT
(RIGID WING)

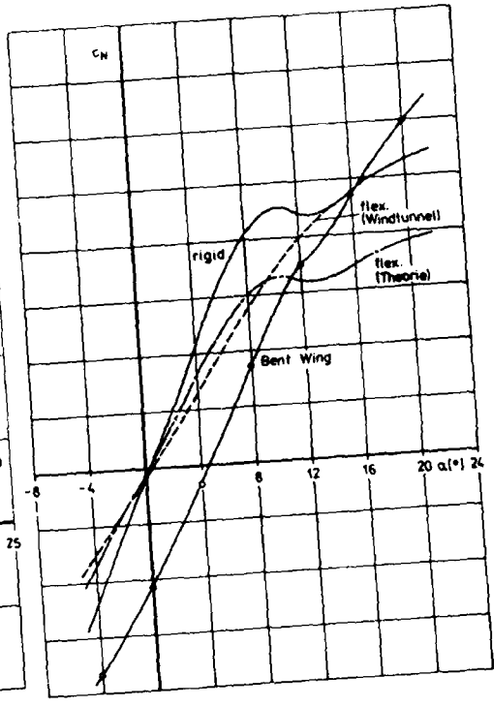

FIG. 2c NORMAL FORCE COEFFICIENT

FIG.2

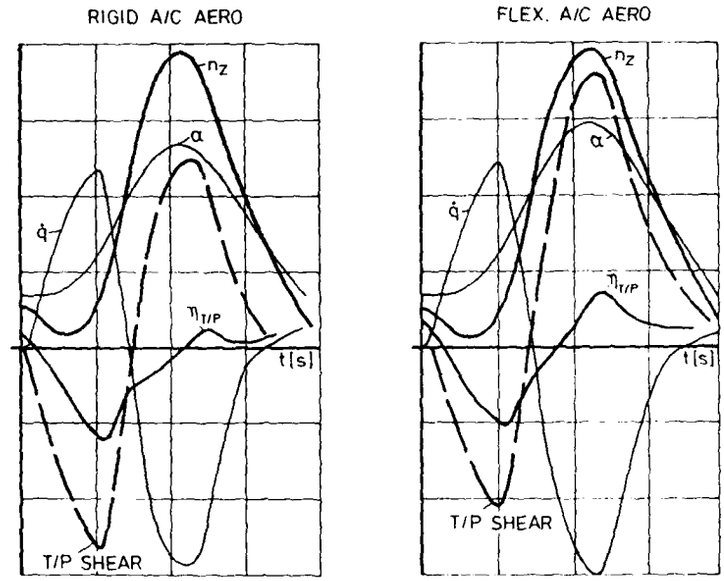

FIG. 3 MIL-SPEC PITCH MANOEUVRE

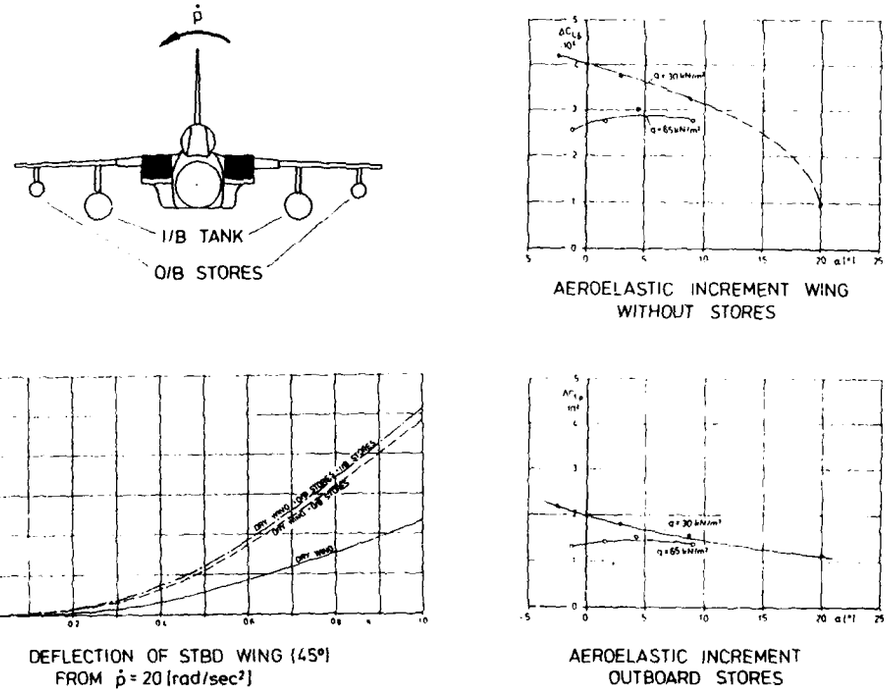

FIG. 4 AEROELASTIC INCREMENTS DUE TO INERTIA EFFECTS ($\dot{p}$)

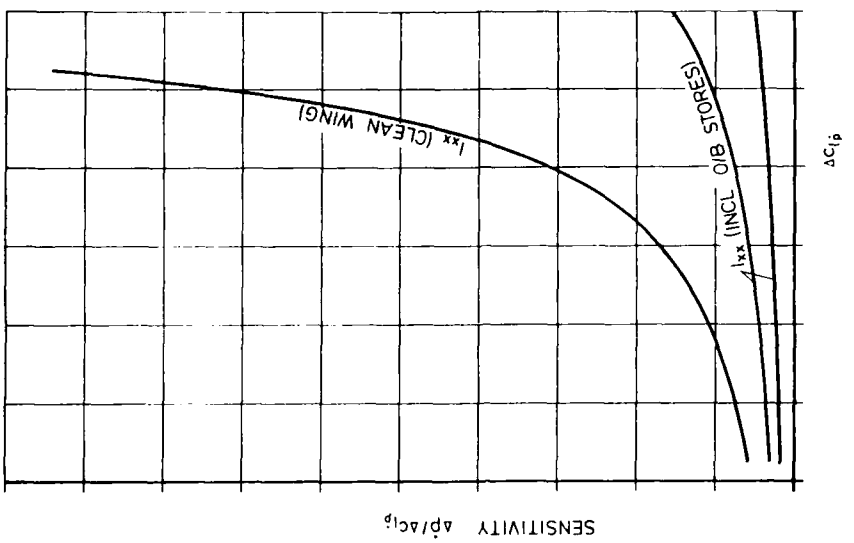

FIG. 6 FUNCTIONAL RELATIONSHIP BETWEEN I_{xx} AND $\Delta C_{l_{\dot{p}}}$

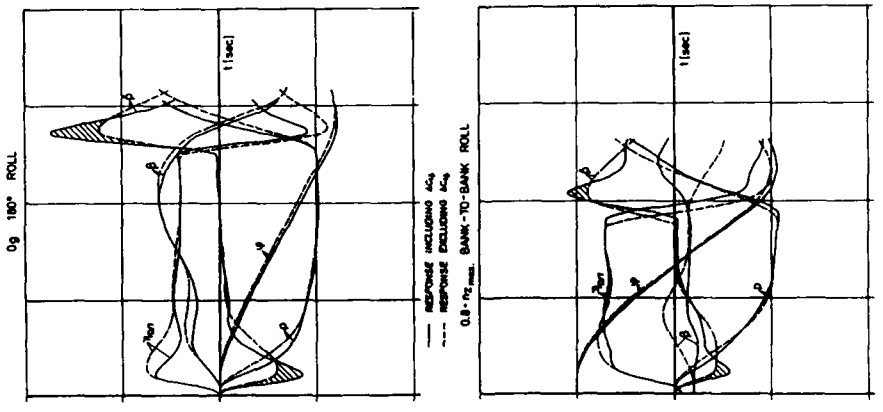

FIG. 5 MIL-SPEC ROLLS SHOWING FLEX. EFFECT $\Delta C_{l_{\dot{p}}}$

$$\boxed{k_{HM} \sim \frac{1+k_\xi}{2}}$$

$$\xi = \frac{c_{l_p} \cdot s/v \cdot p \cdot k_p}{c_{l_\xi} \cdot k_\xi}$$

$$HM_{flex.} = q \cdot F \cdot b \cdot c_{h_\xi} \cdot \xi \cdot k_{HM}$$

OR

$$HM_{flex.} \sim HM_{rigid} \cdot k_p \cdot \frac{1+k_\xi}{2 \cdot k_\xi}$$

LEADING TO:

k_ξ	k_p	DESIGN - $HM_{flex.} / HM_{rigid}$
1.0	0.9	0.9
0.8	|	1.0
0.6	|	1.2
0.4	|	1.6
0.2	0.9	2.7

FIG. 7 INFLUENCE OF AEROELASTIC ROLL EFFICIENCY ON DESIGN HINGE MOMENT

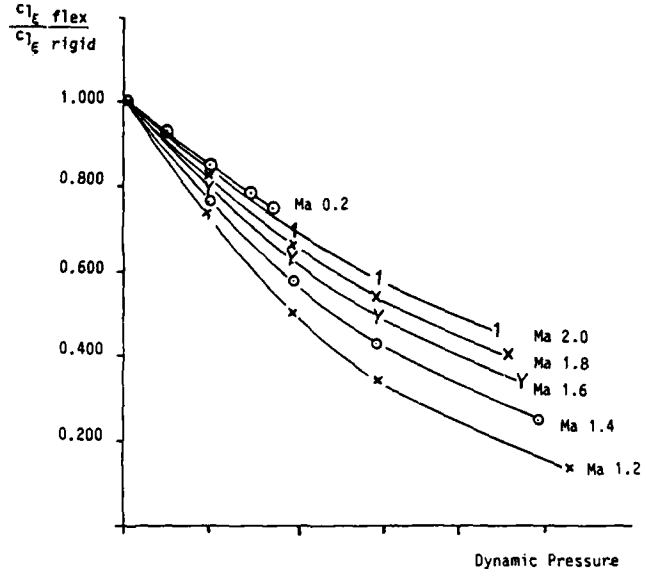

FIG. 8 AEROELASTIC CORRECTION FACTOR TRAILING EDGE FLAP O/B

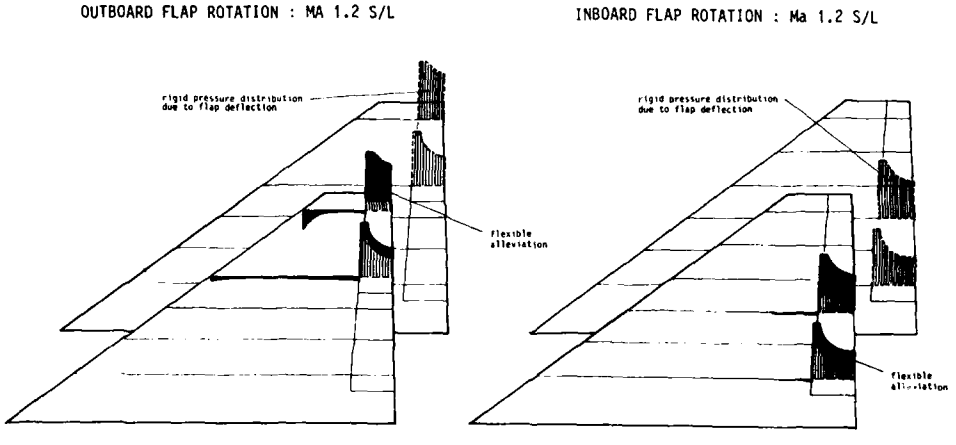

FIG. 9 ELASTIC PRESSURE DISTRIBUTION

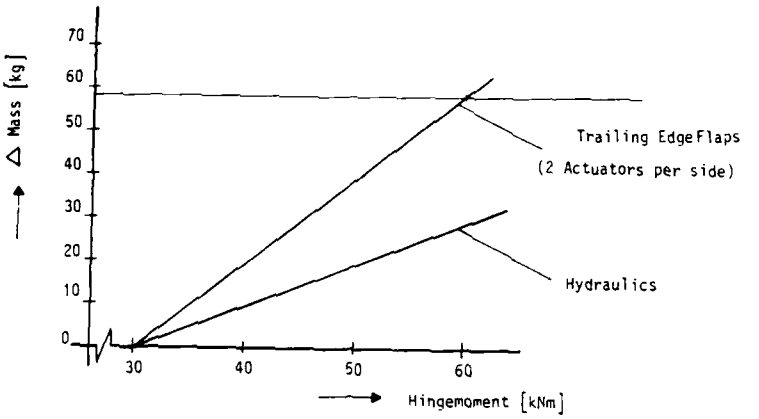

FIG. 10 ADDED MASS AS A FUNCTION OF TRAILING EDGE HINGE MOMENT

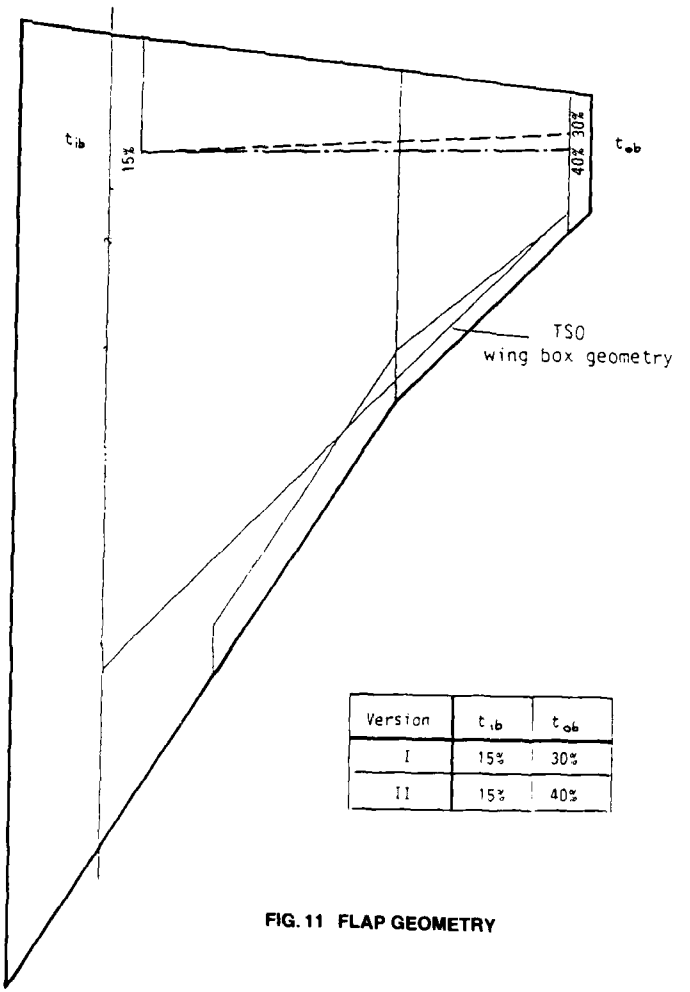

Version	t_{ib}	t_{ob}
I	15%	30%
II	15%	40%

FIG. 11 FLAP GEOMETRY

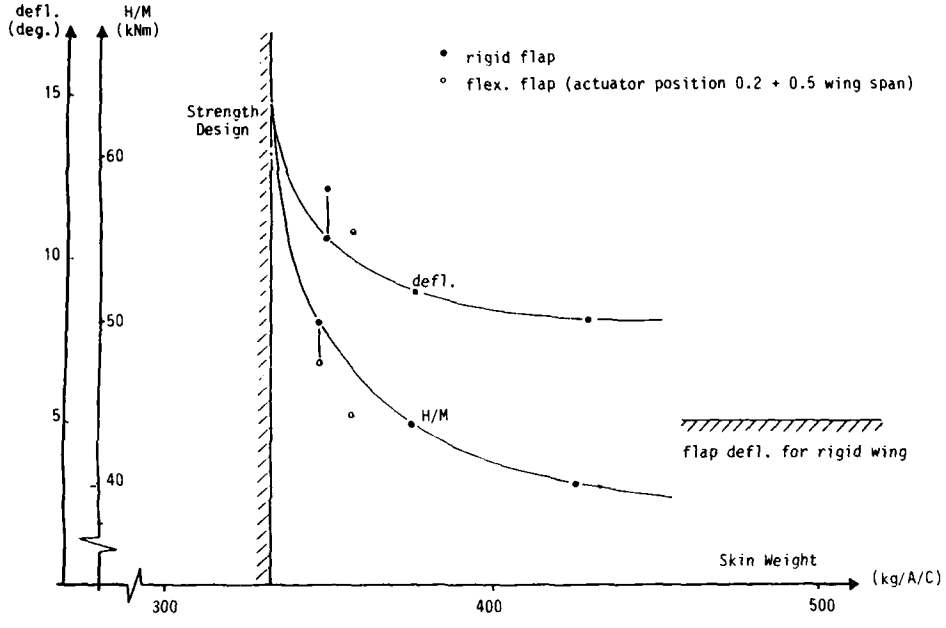

FIG. 12 DEFLECTION AND HINGE MOMENT FOR FLAP I (MACH 1.6, 20 000 ft)

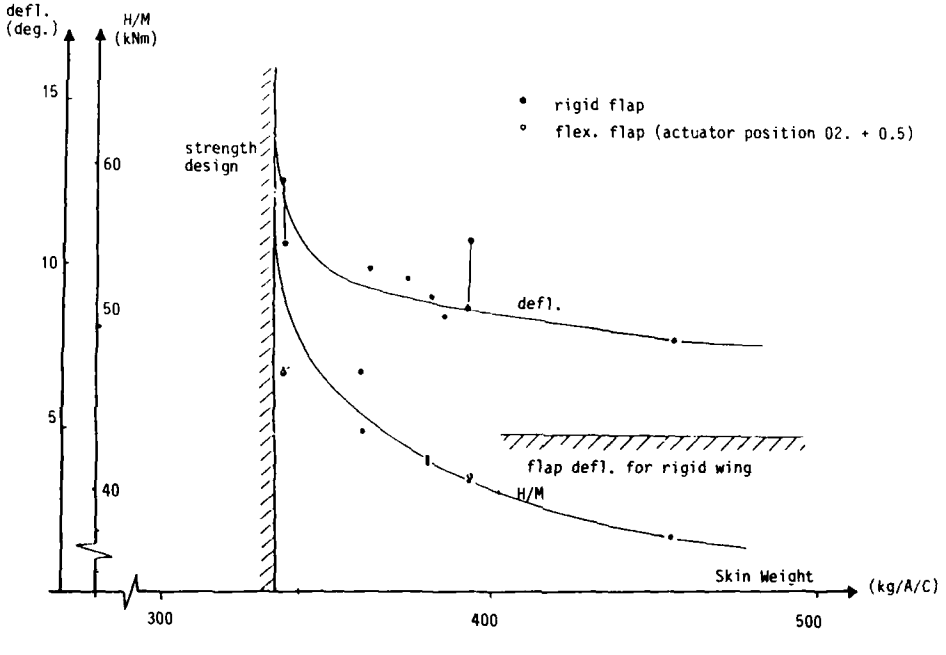

FIG. 13 DEFLECTION AND HINGE MOMENT FOR FLAP II (MACH 1.6, 20 000 ft)

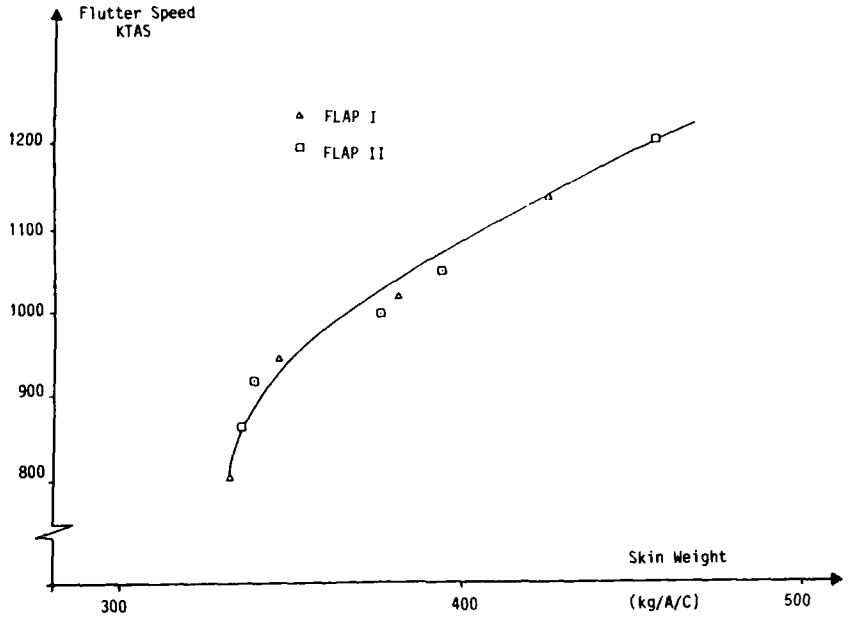

FIG. 14 FLUTTER SPEED VS SKIN WEIGHT

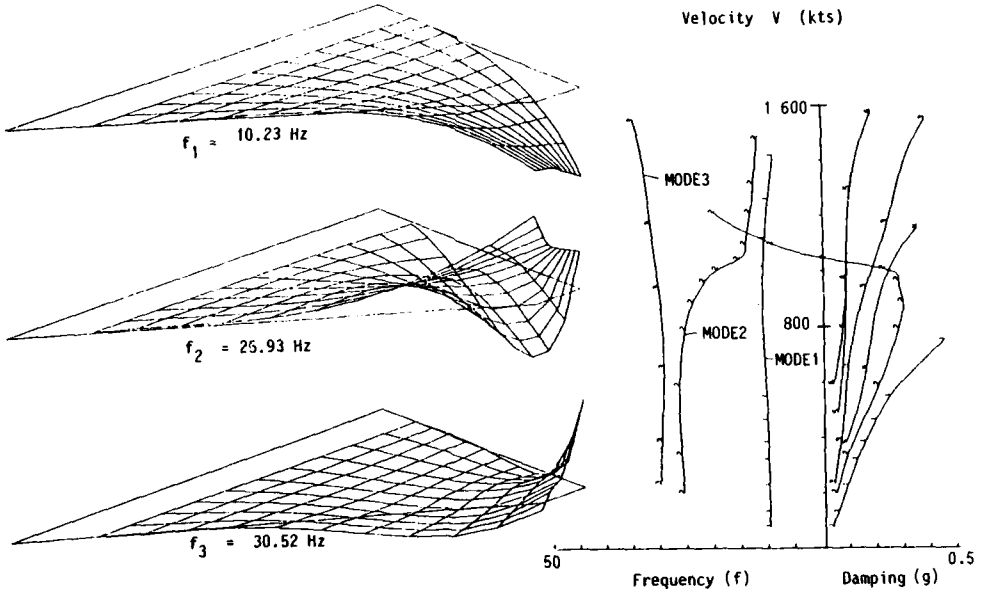

FIG. 15 V-g PLOT AND VIBRATION MODES FOR FLAP II

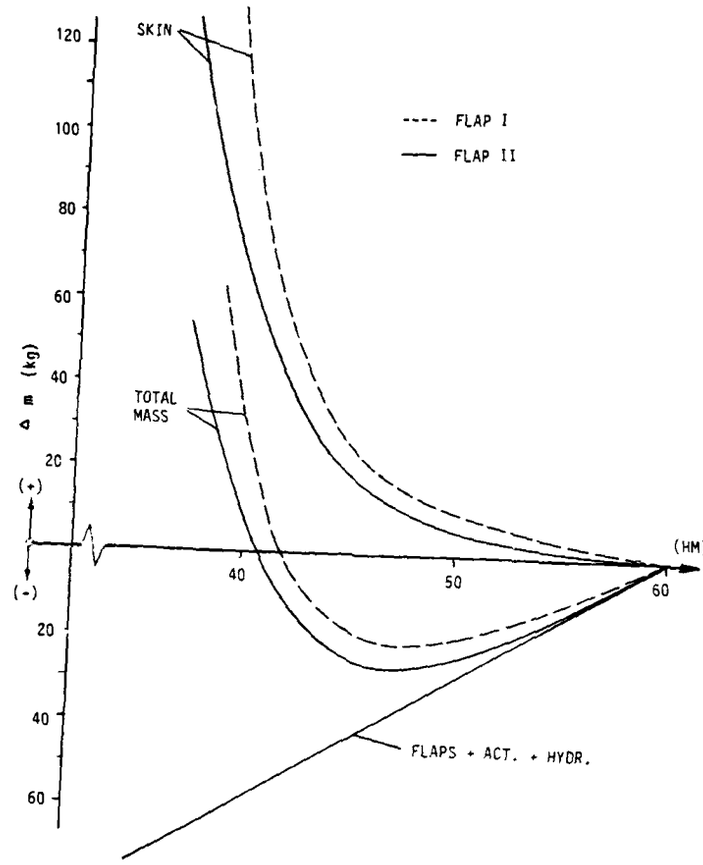

FIG. 16 ADDED MASS AS A FUNCTION OF HINGE MOMENT

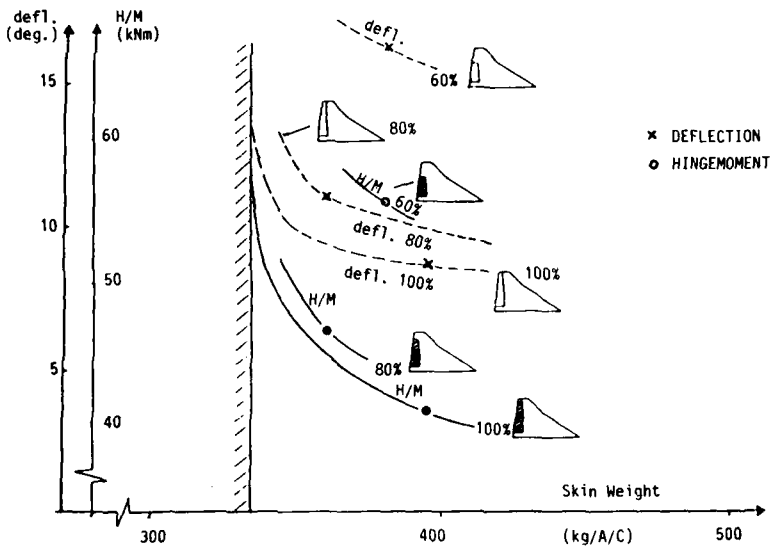

FIG. 17 VARIATION OF I/B FLAP SPAN (FLAP II)

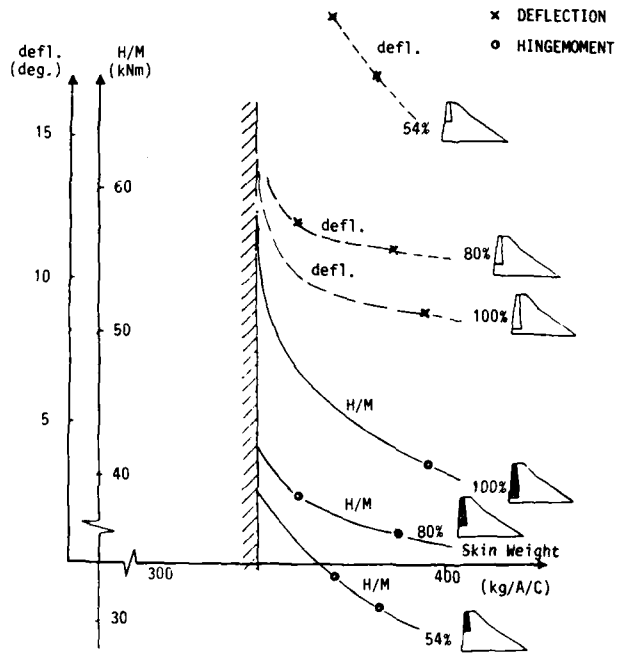

FIG. 18 VARIATION OF O/B FLAP SPAN (FLAP II)

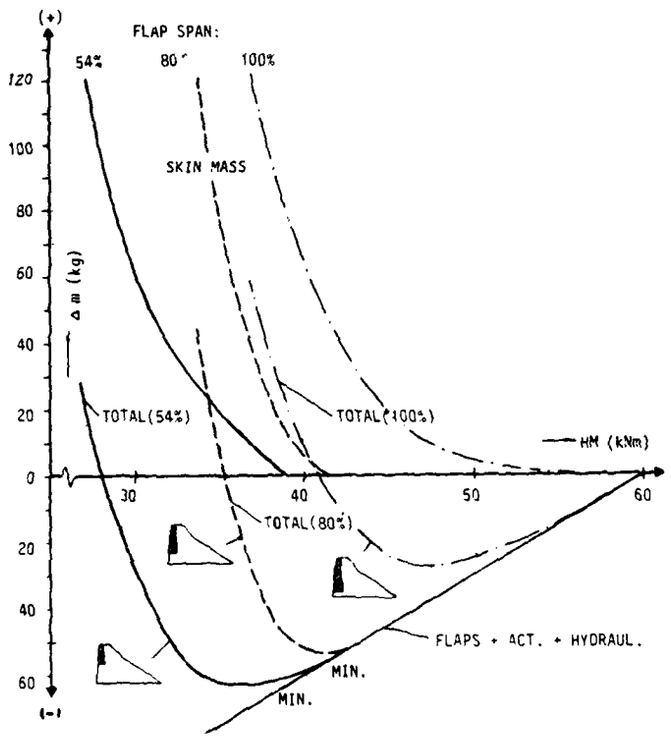

FIG. 19 ADDED MASS AS A FUNCTION OF HINGE MOMENT FOR VARIOUS OUTBOARD FLAP SPANS

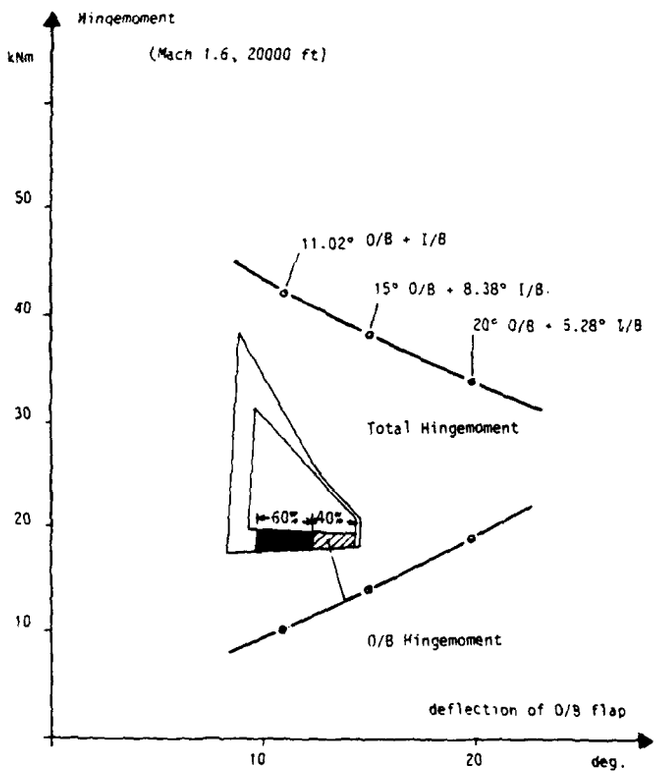

FIG. 20 COMBINATIONS OF I/B AND O/B FLAP

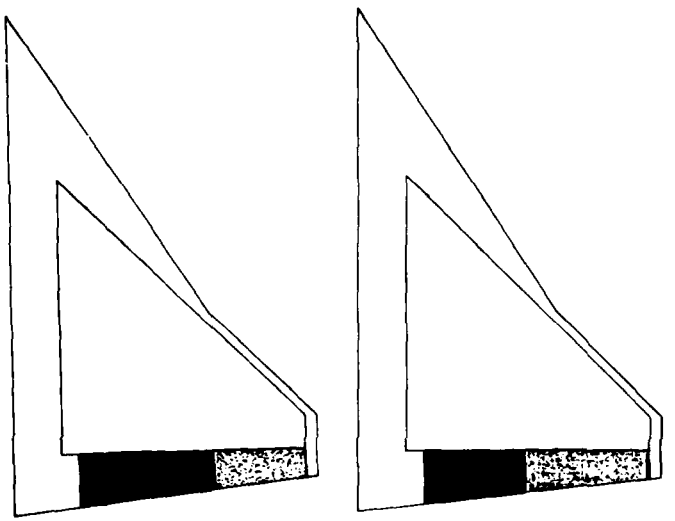

Percentage Flaperon	60%	40%	46%	54%
Flap angle (IB/OB)	6.23°	15°	3.5°	15°
Hinge-Moment (IB/OB) (kNm)	23.8	14.0	8.38	24.98
Total Hinge Moment (kNm)	37.8		33.4	

FIG. 21 RESULTS FOR DIFFERENT FLAP SPLITS

THICKNESS DISTRIBUTION LAYER 1
(+ 45°)

WEIGHT = 110.214

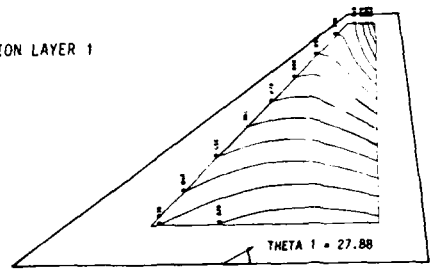

THICKNESS DISTRIBUTION LAYER 2
(-45°)

WEIGHT = 82.944

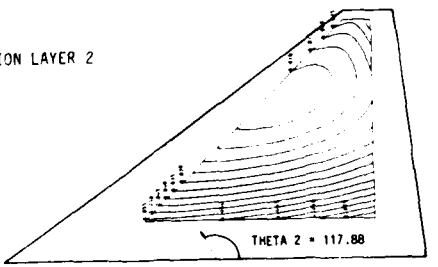

THICKNESS DISTRIBUTION LAYER 3
(MAIN FIBRE DIRECTION)

WEIGHT = 249.527

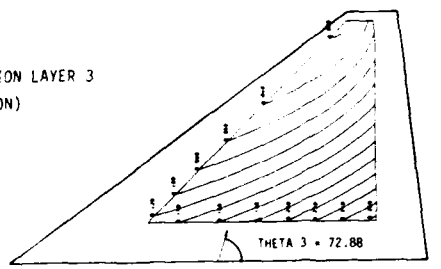

FIG. 22 THICKNESS DISTRIBUTION

ANALYSE AEROELASTIQUE DES AVIONS

MODERNES DE TRANSPORT

J ROUSTAN

M. CURBILLON

AEROSPATIALE - Division Avions

Direction des Etudes Toulouse

316 Route de Bayonne BP 3153

31053 TOULOUSE

RESUME :

Sur les avions de transports modernes, les phénomènes aéroélastiques statiques jouent un rôle très important tant au niveau des qualités de vol que des efforts appliqués à la structure.

Après avoir présenté la méthode utilisée par l'Aérospatiale pour la prise en compte et le calcul de ces effets, cette communication aborde quelques aspects particuliers liés à cette approche. Les différents points abordés sont illustrés par quelques résultats d'études.

ABSTRACT :

Static aeroelastic phenomena play a very important role on modern transport aircraft, as regards both handling qualities and loads applied to the structure.

After presenting the method used by Aerospatiale for taking these effects into consideration and calculating them, this lecture deals with some particular aspects associated with this approach. The various points discussed are illustrated by some results of our investigations.

REFERENCES

1. Détermination des coefficients aérodynamiques en avion souple en vol symétrique.

A. MARSAN AGARD CP 46

2. Approche aérospatiale de l'étude du flottement au niveau de l'avant projet.

M. CURBILLON AGARD CP 354

3. New developments and applications of the subsonic doublet-lattice method for non planar configurations.

W.P. RODDER, J.P GIESING AND T.P KALMAN. AGARD CP 80/71

4. Optimisation statique et aéroélastique des avions

J.M THOMAS International Symposium on aeroelasticity
Nuremberg Octobre 1981

5. Optimisation des structures

J. LOCATELLI

(Note Aérospatiale)

NOTATIONS

C_L^R : Coefficient de portance en avion rigide

$\frac{\partial C_L^R}{\partial \alpha}$: Gradient de portance lié à l'incidence en avion rigide

α^R : Incidence en avion rigide

α_0^R : Incidence de portance nulle en avion rigide

$\frac{\partial C_L^R}{\partial \delta}$: Gradient de portance lié au braquage d'une gouverne en avion rigide

δ^R : Braquage gouverne en avion rigide

$\{F_\alpha\}^R$: Répartition des forces locales liée à un effort d'incidence en avion rigide

$\{F_{C_L=0}\}^R$: Répartition de forces locales liée à l'effet portance nulle en avion rigide

$\{F_\delta\}^R$: Répartition de forces locales liée à un effet de braquage gouverne en avion rigide

$\{F_\Delta\}$: Répartition de forces locales liée à une déformée (Δ) de l'avion souple

$\{\Delta\}$: Déformation de l'avion souple

$[A]$: Matrice de coefficients d'influence aérodynamique

$[C]$: Matrice de flexibilité

$\{F\}$: Répartition de forces locales

n : Facteur de charge verticale

M : Masse avion

$\bar{q}$: Pression dynamique $= \frac{1}{2} \rho V^2$

S : Surface de référence

Δ_α^S : Variation d'incidence due à l'effet de souplesse

$\Delta^S\delta$: Variation de braquage gouverne due à l'effet de souplesse

$\{\Delta\}_{/Ref}$: Déformée avion par rapport à une référence

$\{1\}^T$: Matrice colonne unitaire transposée (matrice ligne)

$\{F\}^R$: Répartition de forces locales avion rigide

$\{\Delta F\}^S$: Répartition de forces locales liée à l'effet de souplesse

α^S : Incidence en avion souple

α_0^S : Incidence de portance nulle en avion souple

δ^S : Braquage gouverne en avion souple

$\frac{\partial C_L}{\partial \alpha}^{s}$: Gradient de portance lié à l'incidence en avion souple

$\frac{\partial C_L}{\partial \delta}^{s}$: Gradient de portance lié au braquage gouverne en avion souple

$\frac{\partial C_L}{\partial n}^{s}$: Gradient de portance lié au facteur de charges en avion souple

$\Delta^{s}\frac{\partial C_L}{\partial \alpha}$: Variation de gradient de portance lié à l'incidence due à l'effet de souplesse

$\Delta^{s}\frac{\partial C_L}{\partial \delta}$: Variation de gradient de portance lié à l'effet de braquage due à l'effet de souplesse

$\Delta^{s}\alpha_o$: Variation d'incidence de portance nulle due à l'effet d'incidence

$\Delta^{s}\frac{\partial C_L}{\partial n}$: Variation de gradient de portance liée au facteur de charge due à l'effet de souplesse

η : Rendement aéroélastique

$\{K_L.l\}$: Répartition de coefficients de portance locaux

$\left\{\frac{x_{AC}}{l}\right\}$: Positions du foyer local en envergure

l : Corde géométrique locale

$\eta = \frac{y}{b}$: envergure réduite

$\eta_{cl.\delta p}$: Rendement en moment de roulis lié au braquage δ_p des ailerons $= \dfrac{\frac{\partial C_l}{\partial \delta p}^{s}}{\frac{\partial C_l}{\partial \delta_p}}$

p : Vitesse de roulis stabilisée

1 - INTRODUCTION :

L'évolution des avions modernes de transport se traduit par une recherche continue de l'augmentation des PERFORMANCES dans tous les domaines :

- vitesse,
- Aérodynamique,
- Structure,
- Qualité de vol,
- Propulsion,
- Masses,

Concorde a présenté un "bond", mais la génération des avions actuels ou futurs, s'ils "restent" dans le domaine subsonnique, n'en confirment pas moins cet objectif.

Pour nous aéroélasticiens ceci se traduit par :

- des surfaces portantes aux profils très évolués et de grands allongements, pour lesquelles les aérodynamiciens investissent heures d'ordinateur et de soufflerie.
- des structures où la chasse aux kilogrammes superflus est lancée à travers des Modèles Eléments Finis toujours plus fins et de procédures d'optimisations attrayantes,

d'où des avions de plus en plus souples.

Pour s'en convaincre il suffit de regarder la forme prise par un A310 en cours d'essais statique. (Voir planche 1).

Il en résulte donc que les phénomènes aéroélastiques sont devenus une composante majeure dans cette recherche de la performance. Nous nous intéressons ici plus particulièrement aux phénomènes statiques où les déformations misent en jeu sont suffisament lentes.

2 - GENERALITES :

Les effets de l'aéroélasticité statique se manifestent dans tous les équilibres associés aux différentes manoeuvres effectuées par l'avion en vol. Il en résulte des modifications des répartitions d'efforts locaux et des conditions d'équilibre.

Dans la mesure ou l'on veut être performant, il est nécessaire d'éliminer au maximum les incertitudes.

Il faut donc être capable d'explorer tout le domaine de vol avion en avion souple tant pour les problèmes de qualités de vol que pour les problèmes d'efforts généraux.

Par ailleurs les simulateurs de vol sont de plus en plus utilisés soit comme outil de développement soit pour l'entrainement des équipages. Là aussi nous trouvons des moyens de simulation de plus en plus performants et réalistes. Il est donc nécessaire qu'ils puissent prendre en compte les effets de souplesse.

La recherche de la performance au niveau conception et dimensionnement de la structure nous conduit à introduire des contraintes ou des objectifs aéroélastiques dans le processus d'optimisation structurale.

Nous pouvons donc résumer nos objectifs : (planche 2)

. Explorer tout le domaine de vol en avion souple

. Données simulateurs en avion souple

. Optimisation aéroélastique.

3 - AEROELASTICITE STATIQUE ET MECANIQUE DU VOL :

Les deux premiers objectifs ci-dessus concernent l'impact de l'aéroélasticité statique sur la mécanique du vol et de ses conséquences : conditions d'équilibre, qualités de vol, efforts généraux.

Compte tenu du problème posé et des objectifs précédents l'approche Aérospatiale consiste à introduire les effets de souplesse sous la forme de coefficients correcteurs des données aérodynamiques avion rigide afin de conserver le modèle mathématique utilisé en mécanique du vol traditionnelle.

3.1 - Les "outils" aérodynamiques et structuraux :

L'étude de l'aéroélasticité statique consiste à étudier les relations entre déformations et forces induites dans le cycle :

forces -> déformations -> forces induites -> déformations -> .....

. Forces aérodynamiques (Pl. 3)

Le cycle précédent fait apparaitre deux types de forces :

- forces initiales déclenchant le cycle
- forces induites

Les forces initiales sont celles associées à l'avion rigide. Pour les forces aérodynamiques elles résultent des pressions mesurées en soufflerie ou calculées théoriquement.

Elles sont rattachées par exemple aux effets :

- incidence $\alpha^R \longrightarrow \{F_\alpha\}^R$
- portance nulle $C_L^R = 0 \longrightarrow \{F_{CL=0}\}^R$
- braquage gouverne $\delta^R \longrightarrow \{F_\delta\}^R$

Les forces induites (F_Δ) sont celles résultants des déformations de la structure (Δ).
La méthode employée pour les calculer utilise des matrices de coefficients d'influences aérodynamiques stationnaires [A] calculées par la méthode des réseaux de doublets (Réf 3) d'où :

$$\{F_\Delta\} = \bar{q}\,[A]\{\Delta\}$$

A défaut de données soufflerie ou theoriques plus évoluées ces matrices permettent d'obtenir des forces initiales de bonnes qualités acceptables pour des études préliminaires.

Ceci est dû en particulier aux possibilités de notre code de calcul autorisant un maillage fin (500 "pavés" aérodynamiques par demi-avion) et à un recalage global en portance pour les effets Mach.

. Déformations (Planche 4)

Le calcul des déformations est effectué en utilisant une matrice de flexibilité [C] reliant forces locales (F) et déformations locales (Δ)

$$\{\Delta\} = [C]\{F\}$$

Cette matrice de flexibilité [C] est calculée par le code Eléments Finis ASELF développé à l'Aérospatiale.
La schématisation structurale peut aller du modèle poutre simplifiée (voir Ref. 2) au modèle éléments finis avion complet traité par assemblage de sous-structures. La méthode des sous-structures étant parfaitement adaptée au travail en coopération ou en groupes opérationnels spécialisés.

3.2 - Coefficients aérodynamiques en avion souple

Le principe général de l'approche utilisée à l'Aérospatiale est dû à M.A MARSAN qui l'a appliquée à l'étude du comportement de Concorde en vol symétrique stationnaire (Référence 1).

3.2.1 - Principe et organisation générale du calcul (Pl. 5 à 7)

Pour ne pas alourdir l'exposé et éviter une suite d'expressions matricielles fastidieuses, le principe et l'organisation générale du calcul seront appliqués à :

- l'équation d'équilibre en forces pour des conditions de vol symétrique sous facteur de charge n à vitesse de tangage nulle,

- un avion avec empennage et gouverne de profondeur, l'empennage étant considéré comme fixe. L'avion rigide est alors représenté par les coefficients aérodynamiques :

  - gradient de portance avion avion complet ——————— $\frac{\partial C_L^R}{\partial \alpha}$

    (Fuselage + voilure + empennage)

  - incidence de portance nulle en avion en avion complet ——— α_o^R
  - gradient de portance lié au braquage de la gouverne de profondeur — $\frac{\partial C_L^R}{\partial \delta}$

En conséquence, l'équation d'équilibre avion rigide s'écrit d'une manière très schématique :

$$n.Mg = \bar{q}.S.\left(\frac{\partial C_L^R}{\partial \alpha}.(\alpha^R - \alpha_o^R) + \frac{\partial C_L^R}{\partial \delta}.\delta^R\right) \quad (1)$$

Pour des conditions de vol identiques, l'effet de souplesse ne modifie pas la résultante des efforts aérodynamiques mais entraine une variation des paramétres d'équilibre $\Delta^s\alpha$ et $\Delta^s\delta$ ainsi qu'une déformation de la structure $\{\Delta\}$.

La résultante aérodynamique n'étant pas modifiée le système d'efforts associé aux effets de la souplesse est donc en équilibre. Ceci s'écrit sous la forme

$$0 = \bar{q}.S.\left(\frac{\partial C_L}{\partial \alpha}^R . \Delta^s\alpha + \frac{\partial C_L}{\partial \delta}^R . \Delta^s\delta\right) + \bar{q}.\{1\}^T[A]\{\Delta\} \qquad (2)$$

et l'on obtient l'équation d'équilibre en avion souple en ajoutant le système nul (2) à l'avion rigide (1), d'où

$$n.M.g = \bar{q}.S.\left(\frac{\partial C_L}{\partial \alpha}^R\left((\alpha^R + \Delta^s\alpha) - \alpha_0^R\right) + \frac{\partial C_L}{\partial \delta}^R(\delta^R + \Delta^s\delta)\right) + \bar{q}.\{1\}^T[A]\{\Delta\} \qquad (3)$$

quant aux déformations de la structure elles sont dues à toutes les forces agissant sur l'avion provenant des effets rigides $\{F\}^R$ et souples $\{\Delta F\}^S$, soit

- $\{\Delta\} = [C]\left\{\{F\}^R + \{\Delta F\}^S\right\}$
- $\{F\}^R = \bar{q}\{F_\alpha\}^R.\alpha^R + \bar{q}\{F_{C_L=0}\}^R + \bar{q}\{F_\delta\}^R + n.\{m.g\}$
- $\{\Delta F\}^S = \bar{q}\{F_\alpha\}^R.\Delta^s\alpha + \bar{q}\{F_\delta\}^R.\Delta^s\delta + \bar{q}[A]\{\Delta\}$

$$\{\Delta\} = [B]^{-1}[C]\left\{\bar{q}\{F_\alpha\}^R(\alpha^R + \Delta^s\alpha) + \bar{q}\{F_\delta\}^R(\delta^R + \Delta^s\delta) + \bar{q}\{F_{C_L=0}\} + \{m.g\}n\right\} \qquad (4)$$

$$[B] = \left[[I] - \bar{q}[C][A]\right]$$

En remplaçant $\{\Delta\}$ equation (4) dans l'equation d'equilibre (3) nous arrivons a la formulation mettant en evidence la forme definitive et simple de l'equation d'equilibre en avion souple

$$\begin{aligned} n.M.g = {} & \bar{q}.S.\frac{\partial C_L}{\partial \alpha}^R(\alpha^R + \Delta^s\alpha) + \bar{q}^2\{1\}^T[A][B]^{-1}[C]\{F_\alpha\}^R(\alpha^R + \Delta^s\alpha) \\ & - \bar{q}.S.\frac{\partial C_L}{\partial \alpha}^R.\alpha_0^R + \bar{q}^2\{1\}^T[A][B]^{-1}[C]\{F_{C_L=0}\}^R \\ & + \bar{q}.S.\frac{\partial C_L}{\partial \delta}^R.(\delta^R + \Delta^s\delta) + \bar{q}^2\{1\}^T[A][B]^{-1}[C]\{F_\delta\}^R(\delta^R + \Delta^s\delta) \\ & + \bar{q}\{1\}^T[A][B]^{-1}[C]\{m.g\}n \end{aligned}$$

$$n^s.M.g = \bar{q}.S.\left(\frac{\partial C_L}{\partial \alpha}^s(\alpha^s - \alpha_0^s) + \frac{\partial C_L}{\partial \delta}^s.\delta^s + \frac{\partial C_L}{\partial n}^s.n^s\right) \qquad (5)$$

où apparaissent :

- les conditions d'équilibres en avion souple α^s et δ^s
- l'expression des coefficients aérodynamiques en avion souple $\frac{\partial^s C}{\partial}$

$$\frac{\partial^s C_L}{\partial \alpha} = \frac{\partial^R C_L}{\partial \alpha} + \Delta^s \frac{\partial C_L}{\partial \alpha} \longrightarrow \Delta^s \frac{\partial C_L}{\partial \alpha} = \frac{\bar{q}}{S} \{1\}^T [A][B]^{-1}[C]\{F_\alpha\}$$

$$\frac{\partial^s C_L}{\partial \delta} = \text{- - - - - - - -} \longrightarrow \Delta^s \frac{\partial C_L}{\partial \delta} = \text{- - - - - - - - - - -}$$

$$\alpha_o^s = \alpha_o^R + \Delta^s \alpha_o \longrightarrow \Delta^s \alpha_o = -1 \Big/ \frac{\partial^s C_L}{\partial \alpha} \cdot \left[\Delta^s \frac{\partial C_L}{\partial \alpha} \cdot \alpha_o^R + \frac{\bar{q}}{S} \{1\}^T [A][B]^{-1}[C] \{F_{C_L=0}\} \right]$$

$$\frac{\partial^s C_L}{\partial n} = \Delta^s \frac{\partial C_L}{\partial n} \longrightarrow \Delta^s \frac{\partial C_L}{\partial n} = \frac{1}{S} \{1\}^T [A][B]^{-1}[C]\{mg\}$$

Ceux ci comprennent le terme traditionnel avion rigide $\frac{\partial^R C}{\partial}$ plus une partie due à la souplesse $\Delta^s \frac{\partial C}{\partial}$, sauf pour le dernier qui n'a pas d'équivalent en avion rigide
Dans certains cas, en particulier pour les effets gouvernes le terme correctif lie à la souplesse peut se présenter sous la forme d'un facteur multiplicatif ou rendement η

$$\frac{\partial^s C}{\partial} = \eta \times \frac{\partial^R C}{\partial}$$

3.2.2 - Forme des coefficients souples :

Le principe général de cette approche est en fait appliqué aux équations de forces et de moments tant pour des manoeuvres longitudinales que latérales. Il en ressort un grand nombre de termes correctifs associés à la formulation utilisée pour l'avion rigide. Par exemple pour rester dans le domaine longitudinal, la formulation complète du coefficient de portance C_L^S s'écrit :

$$C_L^S = C_L^{WFP} + \frac{S_H}{S}\left(C_L^T + C_{L\delta q}\right) + C_{Lq}\cdot\frac{q\,l_a}{l} + \Delta C_L\delta_{Sp}$$

$$+ \Delta C_L\cdot\delta_{AB} + \Delta C_L\cdot\delta_{LD} + \Delta C_L\cdot\delta_{Ail} + \Delta C_{L\cdot n}$$

$C_L^{WFP} = \frac{\partial C_L^{WFP}}{\partial \alpha}\left(\alpha^S - \alpha_o^S\right)$: portance de l'avion sans empennage (WFP = Wring + fuselage + pods)

$C_L^T = \frac{\partial C_L^T}{\partial \alpha}\left(\alpha^S - \varepsilon^S + i_H\right)$: portance de l'empennage horizontal (T = tail) liée à l'incidence

ε = déflection

i_H = braquage de l'empennage horizontal

$C_{L\delta q} = \frac{\partial C_L^S}{\partial \delta q}\cdot\delta q^S$: portance de l'empennage lié au braquage de la gouverne de profondeur

$C_{Lq} = \frac{\partial C_L^S}{\partial q\frac{l_a}{V}}\cdot\frac{q\,l_a}{V}$: portance de l'avion complet lié à la vitesse de tangage

$$= f\left(\frac{\partial C_L^{WFP}}{\partial q\frac{l_a}{V}}, \frac{\partial C_L^T}{\partial q\frac{l_a}{V}}, x_{cq}, \frac{\partial C_L^{WFP}}{\partial \alpha}, \frac{\partial C_L^T}{\partial \alpha}, \alpha^S\right)$$

$\Delta C_L\cdot\delta_{Sp}, \Delta C_L\cdot\delta_{AB}, \Delta C_{L\cdot LD}, \Delta C_L\cdot\delta_{Ail}, \Delta C_{L\cdot n}$ = portances asssociées aux braquages spoilers, aérofreins, lift dumper ailerons et au facteur de charges n,

Tous les coefficients précédents font intervenir des termes correctifs pour tenir compte des effets de souplesse.

Quelques exemples de termes correctifs sont donnés planches 8 à 10.

Planche 8 : Exemple de termes fonctions du Mach et de la pression dynamique

$-\Delta \frac{\partial C_L^{S\,WFP}}{\partial \alpha}$ = variation du gradient de portance lié à l'incidence due à l'effet de souplesse

On retrouve une évolution en Mach du même type que celle du coefficient en avion rigide alors que l'évolution en pression dynamique est plus ou moins de type parabolique. (Non linéarité associée à l'inversion de la matrice [B].

$-\eta C_{L\,\delta q}^{T}$ = rendement aéroélastique en gradient de portance lié au braquage de la gouverne de profondeur

L'évolution en Mach, s'il y en a une, se manifesterait au niveau du $\Delta^S C_{L\delta q}$ par l'intermédiaire de l'évolution du coefficient rigide $C_{L\,\delta q}^{R}$

$$\Delta C_{L\,\delta q}^{S} = C_{L\,\delta q}^{R} \left(\eta_{C_L \delta q} - 1 \right)$$

Planche 9 : Variation du gradient de portance associé au facteur de charge. $\Delta^* \frac{\partial C_L}{\partial n}$

On retrouve l'évolution plus ou moins parabolique en pression dynamique, l'effet de la répartition de masse se traduisant par une sorte de translation.

Planche 10 : Effet de souplesse sur l'incidence de portance nulle. $\Delta \alpha_o^S$

Nous faisons ressortir ici une des possibilités originale de la formulation retenue, à savoir la possibilité de fournir l'effet de souplesse sur l'incidence de portance nulle référencée soit à la forme bâti ou forme de construction (dite forme à n = 0 g) soit à la forme optimisée de croisière ou forme maquette (dite à n = 1g) suivant la référence retenue pour l'incidence de portance nulle en avion rigide.

Pour une pression dynamique $\bar{q}$ = 0 nous remarquons : que la variation d'incidence à portance nulle référencée à la forme bâti (ou n = 0g) est nulle car l'avion n'est pas déformé et que la variation d'incidence de portance nulle référencée à la forme maquette (n = 1g) est différente de zéro. Elle représente la différence d'incidence de portance nulle entre les formes maquettes (n = 1g et bâti (n =0 g)).

3.3 - Charges en avion souple : (Pl. 4)

Nous avons vu précédemment que l'effet de souplesse se traduisait par une modification des conditions d'équilibre $\alpha^R \rightarrow \alpha^S = \alpha^R + \Delta\alpha$ et $\delta^R \rightarrow \delta^S = \delta^R + \Delta^S\delta$ ainsi que par des déformations $\{\Delta\}$.

L'examen de l'équation d'équilibre de l'avion souple (Equation (3) Planche 5) montre que les répartitions de charges liées aux variations d'incidence et de braquage sont prises directement en compte en utilisant les répartitions unitaires établies en avion rigide.

$$n.Mg = \bar{q}.S\left(\frac{\partial C_L}{\partial \alpha}\Big)^{R}\underbrace{(\alpha^R+\Delta^S\alpha)}_{\alpha^S}-\alpha_o^R\right)+\frac{\partial C_L}{\partial \delta}\Big)^{R}\underbrace{(\delta^R+\Delta^S\delta)}_{\delta^S}\Big)+\bar{q}\{1\}^T[A]\{\Delta\} \quad (3)$$

$$\left\{F^R_{\alpha=1}\right\}\cdot\alpha^S \qquad \left\{F^R_{\delta=1}\right\}\cdot\delta^S \qquad \{\Delta F\}$$

Par contre il est nécessaire de calculer les charges liées aux déformations
$\{\Delta F\} = [A]\{\Delta\}$

Les déformations, comme le montre l'équation (4) planche 6 dépendent des efforts d'incidences, de braquage, de portance nulle et d'inerties. Les charges liées à la souplesse, c'est à dire les déformations sont calculées pour un effet unitaire de chacun de ces paramètres. Par exemple pour l'effet d'incidence nous aurons :

$$\{\Delta F\}_{\Delta^S C_{L\alpha}=1} = \bar{q}\,[A][B]^{-1}\left\{F^R_{\alpha=1}\right\}\cdot\frac{1}{\Delta^S\frac{\partial C_L}{\partial \alpha}}$$

Les charges souples peuvent être présentées directement sous forme d'efforts locaux unitaires $\{\Delta F\}_{\Delta C=1}$ où sous la forme de portances et de foyers locaux
(voir planche 11)

La combinaison efforts avion rigide- efforts liés aux déformations est faite au niveau de l'établissement des efforts généraux

3.4 - Divergence des surfaces portantes

L'étude de la divergence des surfaces portantes est l'étude du comportement du cycle

Efforts → déformations → efforts induits → déformations → ...

Dans le cas ou ce comportement est divergent, les déformations $\{\Delta\}$ tendent vers l'infini

D'apres l'équation de déformations :

$$\{\Delta\} = [B]^{-1}[C]\{F\}$$

ceci se produit si $[B] = [[I] - \bar{q}[C][A]]$ est singulière. Pour un nombre de Mach donné, la recherche de la vitesse de divergence à l'altitude Z revient à déterminer la valeur de $\bar{q} = \frac{1}{2}\rho V^2$ qui rend la matrice $[B]$ singulière

3.5 - Commentaires et remarques

Dans l'approche proposée pour la prise en compte des phénomènes aéroélastiques statiques sous forme de coefficients aérodynamiques avion souple, les relations entre déformations et efforts aérodynamiques induits font appel à des matrices de coefficients aérodynamiques stationnaires $[A]$ et une matrice de flexibilité $[C]$

Hors une matrice de flexibilité est toujours associée à des conditions limitées (appuis, encastrement).
Ceci peut laisser penser que les termes correctifs de souplesse mis en évidence dans notre approche sont fonctions de ces conditions limites. Il n'en est rien heureusement car :

a) Comme nous l'avons vu précédemment les effets de souplesses forment un système de forces en équilibre, donc les réactions aux appuis sont nulles.

b) Les déformations à considérer sont celles par rapport à l'avion rigide ramené à son centre de gravité.

De la remarque a) il ressort que la forme avion est indépendante des appuis et la remarque b) demande que cette forme soit définie par rapport au centre de gravité avion.

Ceci est visualisé planche 13.

Sous l'effet du système de forces f, f et F = 2 f la forme avion est identique soit encastrée au CG (appuis A1) ou appuyée en extrémités de voilure (appuis A2) (remarque a).

La remarque b, c'est-à-dire déformées par rapport au centre de gravité nécessite de ne pas utiliser brutalement les matrices de flexibilité. En effet, une matrice de flexibilité donne des déformations par rapport aux appuis (C1 pour la condition d'appui A1, C2 pour la condition A2). Ceci conduirait donc à des termes correctifs $\Delta^s C_1$ et $\Delta^s C_2$ différents. Par contre, si l'on respecte la remarque b) dans le cas A2, c'est à dire si l'on évalue la déformée par rapport au CG soit C'2 qui est alors égale à C1, nous obtenons les mêmes termes correctifs. $\Delta^s C'_2 = \Delta^s C_1$

En conséquence, si nous voulions être rigoureux, nous aurions une matrice de flexibilité par configuration massique.

En fait, afin de ne pas trop pénaliser le volume des calculs et compte tenu des rigidités mises en jeux au niveau de la jonction voilure-fuselage, nous considérons qu'une seule matrice de flexibilité **[C]** calculée directement avec des appuis aux intersections de la nervure d'emplanture et des longerons avant et arrière est tout à fait acceptable et justifiable.

4 - EFFICACITE DES GOUVERNES EN AVION SOUPLE :

4.1 - Importance de l'effet de souplesse (Pl 15)

L'effet de souplesse se traduit par une modification de l'efficacité rigide des gouvernes. Dans le cas d'une aile en flèche arrière équipée d'ailerons en extrémités, il apparait une perte d'efficacité qui peut aller jusqu'à l'inversion.

Traditionnellement les effets de la souplesse associés au braquage des gouvernes sont donnés sous forme de rendements aéroélastiques η qui sont le rapport entre l'efficacité gouverne en avion souple et l'efficacité gouverne en avion rigide.

Par exemple pour le gradient au moment de roulis lié au braquage des ailerons nous avons

$$\eta_{Cl.\delta_p} = \frac{\frac{\partial^s C_l}{\partial \delta_p}}{\frac{\partial C_l^R}{\partial \delta_p}} = 1 - \frac{\bar{q}\{Y\}^T[A][B]^{-1}[C]\{F\delta_r\}}{\frac{\partial^R C_l}{\partial \delta_p}}$$

La connaissance de tels paramètres est donc très importante pour :

- la définition des gouvernes : . emplacement
  . géométrie
- le choix des fonctions des gouvernes pour :
  . qualités de vol
  . contrôle des charges
  ...
- le dimensionnement avion (rigidités)

4.2 - Efficacité des ailerons externes A300 B

Afin d'illustrer l'impact réel de l'aéroélasticité statique nous présentons ci-après les résultats d'études et d'essais en vol effectués sur l'A300 B concernant la vitesse d'inversion des ailerons externes

4.2.1 - Calculs avant vol : (planche 16)

L'A300 B est équipé d'ailerons externes et d'ailerons internes. Les ailerons internes sont utilisés dans tout le domaine de vol et sont donc appelés ailerons toutes vitesses. Les ailerons externes ne sont utilisés qu'à basses vitesses et sont appelés ailerons basses vitesses. (Ils sont vérouillés en position neutre lorsque M ≤ 0,6).

Dans notre étude nous nous interessons à une commande en roulis particulière assurée par les seuls ailerons externes et ce même à grande vitesse (Ailerons internes et spoilers inhibés).

En considérant une manoeuvre de roulis simplifiée (ou manoeuvre à 1 degré de liberté) dont l'équation en avion souple s'écrit :

$$I_x \cdot \frac{dp}{dt} = \bar{q}\, S\, \ell \cdot \frac{\partial^s C_l}{\partial \delta_p} \cdot \delta_p^s + \bar{q}\, S \ell^2 \frac{\partial C_l}{\partial p \frac{\ell}{V}} \cdot p \frac{\ell}{V}$$

la vitesse de roulis stabilisée est proportionnelle au gradient en moment de roulis lié au braquage ailerons

$$\frac{\partial^s C_l}{\partial \delta_p} = \eta_{Cl.\delta_p} \times \frac{\partial^R C_l}{\partial \delta_p}$$

Sur la base de cette approche simplifiée la vitesse d'inversion en roulis, c'est à dire vitesse avion à laquelle la vitesse de roulis stabilisée est nulle ($p_s = 0$), est égale à la vitesse de rendement en moment de roulis des ailerons nul ($\eta_{Cl.\delta_p} = 0$.)

Pour les ailerons externes A300 B à M = 0,85 la vitesse de rendement nul calculée est de V = 426 kts CAS.

4.2.2 - Essais en vol (planche 17)

Une campagne d'essais en vol a été effectuée sur l'A300B N°3 avec une commande de roulis assurée par les seuls ailerons externes. Les manoeuvres de roulis stabilisées ont été réalisées à M = 0,85 à différentes vitesses pour un braquage des ailerons externes identique en amplitude.

Les résultats sont donnés planche 17

à V = 385 kts la vitesse de roulis stabilisée est d'environ 2°s/s

à V = 403 kts elle est pratiquement nulle (assiette latérale ø voisine de 0)

à V = 420 kts elle est inversée et d'environ - 2°/s

4.2.3 - Comparaison calculs/essais : (planche 18)

Les essais en vol donnent une vitesse d'inversion en roulis $V^{e}_{p=0}$ = 400 kts CAS alors qu'un calcul sur la base d'une équation simplifiée donne $V^{c}_{\eta=0}$ = 426 kts CAS

Dans ce cas simplifié la vitesse d'inversion en vitesse de roulis est identifiée à une vitesse d'inversion en moment de roulis des ailerons. Si nous considérons une approche un peu plus fouillée, il ressort que la vitesse de roulis Po obtenue dans les 10 premières secondes après un échelon de gauchissement δp est donnée, en moyenne, par la relation

$$-\begin{bmatrix} C^{s}_{\ell_p} & C^{s}_{\ell_\beta} \\ C^{s}_{n_p} & C^{s}_{n_\beta} \end{bmatrix} p_o = \begin{bmatrix} C^{s}_{\ell\delta_p} & C^{s}_{\ell_\beta} \\ C^{s}_{n\delta_p} & C^{s}_{n_\beta} \end{bmatrix} \frac{V}{\ell} \cdot \delta_p$$

Les simulations effectuées avec une commande des ailerons externes identique à celle des vols conduisent aux vitesses de roulis données planche 18. On notera que dans ces conditions la vitesse d'inversion en vitesse de roulis trouvée par le calcul est alors de
= 408 kts.

La différence avec la valeur calculée à l'aide de la manoeuvre simplifiée est principalement due au rôle important du lacet inverse induit par l'aileron ($C^{s}_{n\delta_p}$).

La comparaison calculs/essais est alors très bonne. Remarquons qu'il est aussi possible de calculer la vitesse d'inversion en roulis en recherchant la vitesse qui annule le déterminant de la matrice

$$\begin{bmatrix} C^{s}_{\ell\delta_p} & C^{s}_{\ell_\beta} \\ C^{s}_{n\delta_p} & C^{s}_{n_\beta} \end{bmatrix}$$

5 - OPTIMISATION AEROELASTIQUE :

Comme nous venons de le voir les conséquences des effets aéroélastiques statiques peuvent conduire à des situations inacceptables vis à vis du réglement à satisfaire (pas d'inversion de commande pour des vitesses inférieures à VD + 20% dans les cas sans panne)

Aussi il est primordial d'évaluer ces effets très tôt afin de pouvoir mettre en oeuvre des modifications pour améliorer la situation si nécessaire

Dans ce dernier cas, les modifications à proposer doivent conduire à une pénalité massique minimum en jouant à la fois sur une meilleure répartition de la masse travaillante d'origine et sur une minimisation de la masse structurale associée aux renforcements.

Pour atteindre ces objectifs, l'Aérospatiale a introduit des critères d'aéroélasticité statique (principalement le rendement gouverne) dans le processus d'optimisation statique développé dans le cadre de son propre code de calcul structure par éléments finis ASELF.

L'intégration des critères d'aéroélasticité s'est faite sur le principe de l'architecture générale existante du code d'optimisation statique. En effet, comme pour les contraintes statiques, les critères aéroélastiques statiques n'ont pas de formulation explicite en fonction des paramètres d'optimisation.

Il a donc fallu déterminer un mode d'évaluation approché relatif à ces critères, moyennant des recalages ou réanalyses à périodicité appropriée

L'ensemble des contraintes statiques et aéroélastiques est pris en compte au sein du module de recherche de l'optimum.
Ceci s'effectue en deux étapes :

- formulation et acquisition des grandeurs aéroélastiques
- formulation de ce nouveau type de contraintes au sein du processus d'optimisaiton

Pour cette deuxième étape, c'est à dire exprimer quantitativement les critères et contraintes aéroélastiques en fonction des paramétres de conception, une approche linéaire par développement de Taylor du premier ordre est utilisée, comme pour les contraintes statiques.

Des considérations de formulation, de tailles des problèmes matriciels à résoudre, des interfaces entre grilles, nous ont conduit à abandonner l'utilisation de matrices de flexibilité pour le calcul des déformations.

Celles ci sont exprimées sous forme d'une combinaison linéaire de déformées de base analytiques. Ceci a également l'avantage de conduire à une formulation purement géométrique permettant de ne calculer qu'une seule fois les coefficients aérodynamiques relatifs à ces déformées de base.

Compte tenu de cette intégration dans le processus d'optimisation statique, les critères d'aéroélasticité et leur sensibilité en fonction des paramétres sont traités automatiquement par le processus général ainsi que leur réactualisation en fonction du redimensionnement itératif de la structure.

Avec cette approche la convergence vers la solution optimale est obtenue en quatre à six réanalyses éléments finis avec un coût informatique du module d'optimisation tout à fait négligeable.

6 - CONCLUSION

A travers cette revue des phénomènes aéroélastiques statiques affectant les avions modernes de transport nous avons mis en évidence leur importance tant au niveau de la conception qu'au niveau de la justification.

Il en ressort qu'il est absolument nécessaire de disposer "d'outils" de calcul appropriés et fiables.

Par ailleurs, si l'on veut pouvoir être efficace, il faut qu'ils soientt utilisables dès la phase de pré-dimensionnement.

Ceci veut dire, que si l'on veut être PERFORMANT, pour rester dans le challenge évoqué au début de ce document, il est indispensable d'associer étroitement, l'AEROELASTICITE STATIQUE aux premières phases de CONCEPTION d'un avion.

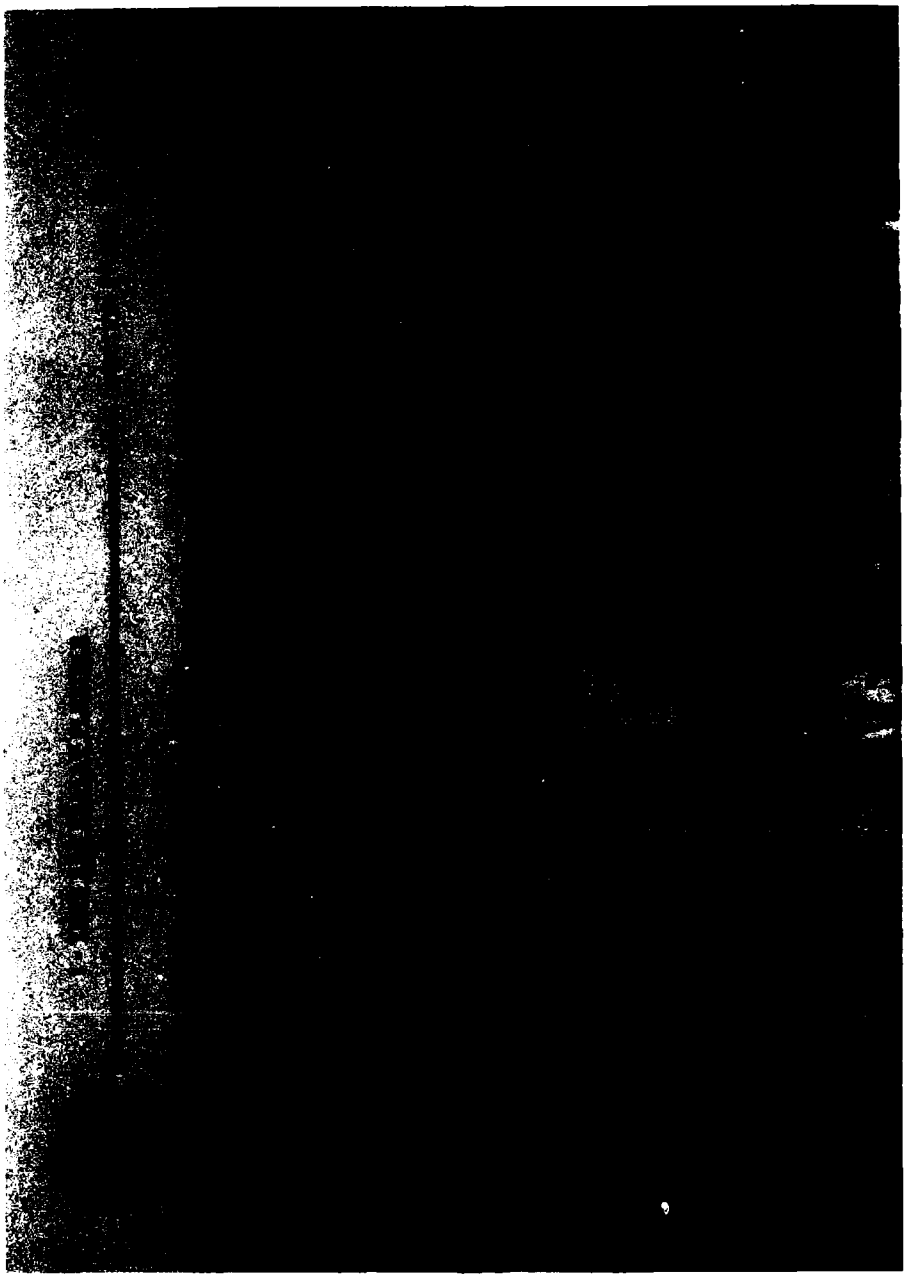

2 - STATIC AEROELASTICITY

DIRECTION ETUDES TOULOUSE

➡ AEROSPATIALE OBJECTIVES :

- To prospect the complete flight envelope with the flexible aircraft
  - Handling qualities
  - Loads
- To introduce the flexible aircraft in the flight simulators
- To perform aeroelastics optimisation

➡ MEANS :

Aircraft static aeroelastic effects involve relations between deformations and induced forces

→ Induced forces - aerodynamic effects

→ Deformations- structure - effects

Pl. 1

3 - AERODYNAMIC EFFECTS

DIRECTION ETUDES TOULOUSE

- Initial effects

$$C_L^R = \frac{\partial C_L^R}{\partial \alpha} \cdot (\alpha^R - \alpha_o^R) + \frac{\partial C_L}{\partial \delta} \cdot \delta^R$$

α^R → $\{F_\alpha\}^R$; $C_L^R = 0$ → $\{F_{C_L=0}\}^R$; δ^R → $\{F_\delta\}^R$

➡ Load distributions -rigide A/C

- Induced effects (Theoritical aerodynamic)

$$\{F_\Delta\} = \bar{q} [A] \{\Delta\}$$

Doublet lattice method

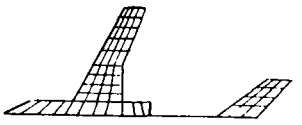

Pl 2

4 - STRUCTURAL EFFECTS

DIRECTION ETUDES TOULOUSE

● Flexibility matrix

$$\{\Delta\} = [C]\{F\}$$

Stick model

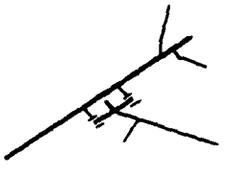

Finite Element Model

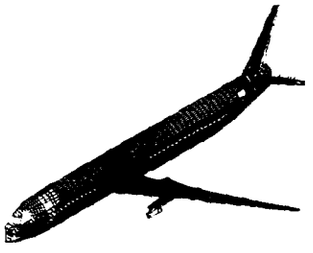

Pl. 3

5 - STATIC AEROELATIC EFFECTS

DIRECTION ETUDES TOULOUSE

Aerospatial approach (principle)

● Rigid A/C $\quad n.Mg = \bar{q}.S.\left(\frac{\partial C_L}{\partial \alpha}.(\alpha^R - \alpha_o^R) + \frac{\partial C_L}{\partial \delta}.\delta^R\right)$ (1)

● Flexibility effects

→ Aerodynamic resultant not modified

→ Modification of - $\alpha^R \rightarrow \Delta^S\alpha$
- $\delta^R \rightarrow \Delta^S\delta$
- $\{\Delta\}$

→ Induced aerodynamic effects in equilibrium

$$0 = \bar{q}.S.\left(\frac{\partial C_L}{\partial \alpha}.\Delta^S_\alpha + \frac{\partial C_L}{\partial \delta}.\Delta^S_\delta\right) + \bar{q}.\{\lambda\}^T[A]\{\Delta\} \quad (2)$$

● Flexible A/C = (1) + (2)

$$n.Mg = \bar{q}.S.\left(\frac{\partial C_L}{\partial \alpha}\left((\alpha^R + \Delta^S_\alpha) - \alpha_o^R\right) + \frac{\partial C_L}{\partial \delta}(\delta^R + \Delta^S_\delta)\right) + \bar{q}.\{\lambda\}^T[A]\{\Delta\} \quad (3)$$

Pl. 4

5 - STATIC AEROELASTIC EFFECTS

● *Flexible A/C deformations*

- $\left\{\Delta\right\} = \left[C\right]\left\{\left\{F\right\}^R + \left\{\Delta F\right\}^S\right\}$
- $\left\{F\right\}^R = \bar{q}\left\{F_\alpha\right\}^R \cdot \alpha^R + \bar{q}\left\{F_{C_L=0}\right\}^R + \bar{q}\left\{F_\delta\right\}^R + n.\left\{m.g\right\}$
- $\left\{\Delta F\right\}^S = \bar{q}\left\{F_\alpha\right\}^R \cdot \Delta^S\alpha + \bar{q}\left\{F_\delta\right\}^R \cdot \Delta^S\delta + \bar{q}\left[A\right]\left\{\Delta\right\}$

$$\Rightarrow \quad \left\{\Delta\right\} = \left[B\right]^{-1}\left[C\right]\left\{\bar{q}\left\{F_\alpha\right\}^R(\alpha^R + \Delta^S\alpha) + \bar{q}\left\{F_\delta\right\}^R(\delta^R + \Delta^S\delta) + \bar{q}\left\{F_{C_L=0}\right\} + \left\{m.g\right\}.n\right\} \quad (4)$$

$$\left[B\right] = \left[\left[I\right] - \bar{q}\left[C\right]\left[A\right]\right]$$

Pl.5

5 - STATIC AEROELASTICS

$$n.M.g = \bar{q}.S.\frac{\partial C_L^R}{\partial\alpha}(\alpha^R + \Delta^S\alpha) + \bar{q}^2\left\{1\right\}^T\left[A\right]\left[B\right]^{-1}\left[C\right]\left\{F_\alpha\right\}^R(\alpha^R + \Delta^S\alpha)$$
$$- \bar{q}.S.\frac{\partial C_L^R}{\partial\alpha}.\alpha_o^R + \bar{q}^2\left\{1\right\}^T\left[A\right]\left[B\right]^{-1}\left[C\right]\left\{F_{C_L=0}\right\}^R \qquad (3) + (4)$$
$$+ \bar{q}.S.\frac{\partial C_L^R}{\partial\delta}.(\delta^R + \Delta^S\delta) + \bar{q}^2\left\{1\right\}^T\left[A\right]\left[B\right]^{-1}\left[C\right]\left\{F_\delta\right\}^R(\delta^R + \Delta^S\delta)$$
$$+ \bar{q}\left\{1\right\}^T\left[A\right]\left[B\right]^{-1}\left[C\right]\left\{m.g\right\}.n$$

$$\Rightarrow \quad n^S.M.g = \bar{q}.S\left(\frac{\partial C_L^S}{\partial\alpha}(\alpha^S - \alpha_o^S) + \frac{\partial C_L^S}{\partial\delta}.\delta^S + \frac{\partial C_L^S}{\partial n}.n^S\right) \qquad (5)$$

$$\frac{\partial C_L^S}{\partial\alpha} = \frac{\partial C_L^R}{\partial\alpha} + \Delta^S\frac{\partial C_L}{\partial\alpha} \quad \longrightarrow \quad \Delta^S\frac{\partial C_L}{\partial\alpha} = \frac{\bar{q}}{S}\left\{1\right\}^T\left[A\right]\left[B\right]^{-1}\left[C\right]\left\{F_\alpha\right\}$$

$$\frac{\partial C_L^S}{\partial\delta} = \text{- - - - -} \quad \longrightarrow \quad \Delta^S\frac{\partial C_L}{\partial\delta} = \text{- - - - - - - - - - - -}$$

$$\alpha_o^S = \alpha_o^R + \Delta^S\alpha_o \quad \longrightarrow \quad \Delta^S\alpha_o = -1\Big/\frac{\partial C_L^S}{\partial\alpha}\left[\Delta^S\frac{\partial C_L}{\partial\alpha}.\alpha_o^R + \frac{\bar{q}}{S}\left\{1\right\}^T\left[A\right]\left[B\right]^{-1}\left[C\right]\left\{F_{C_L=0}\right\}\right]$$

$$\frac{\partial C_L^S}{\partial n} = \Delta^S\frac{\partial C_L}{\partial n} \quad \longrightarrow \quad \Delta^S\frac{\partial C_L}{\partial n} = \frac{1}{S}\left\{1\right\}^T\left[A\right]\left[B\right]^{-1}\left[C\right]\left\{mg\right\}$$

Pl.6

6 - FLEXIBLE A/C AERODYNAMIC DERIVATIVES

$$\frac{\partial C}{\partial}^{S} = \frac{\partial C}{\partial}^{R} + \Delta^{S}\frac{\partial C}{\partial} \qquad \text{or} \qquad \frac{\partial C}{\partial}^{S} = \eta * \frac{\partial C}{\partial}^{R} = f(M, \bar{q})$$

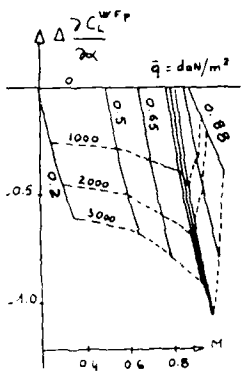

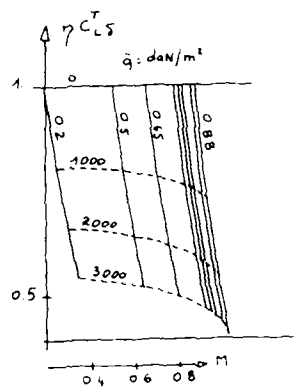

p. 7

6 FLEXIBLE A/C DERIVATIVES

$$\frac{\partial C_L}{\partial n}^{S} = \Delta^{S}\frac{\partial C_L}{\partial n} = f(M, \bar{q}, m)$$

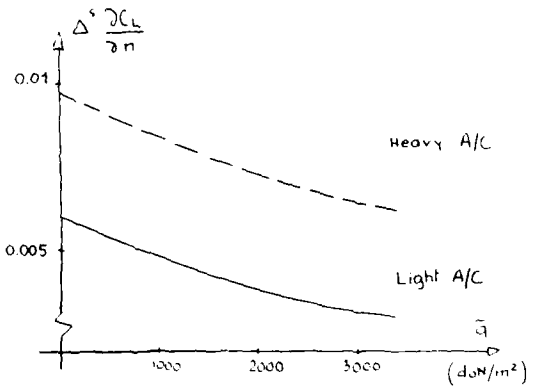

p. 8

6 - FLEXIBLE A/C DERIVATIVES

DIRECTION ETUDES TOULOUSE

$$\alpha_o^S = \alpha_o^R + \Delta^S\alpha_o = f\left(M, \bar{q}, \text{shape}\ {}^{n=0}_{n=1}\right)$$

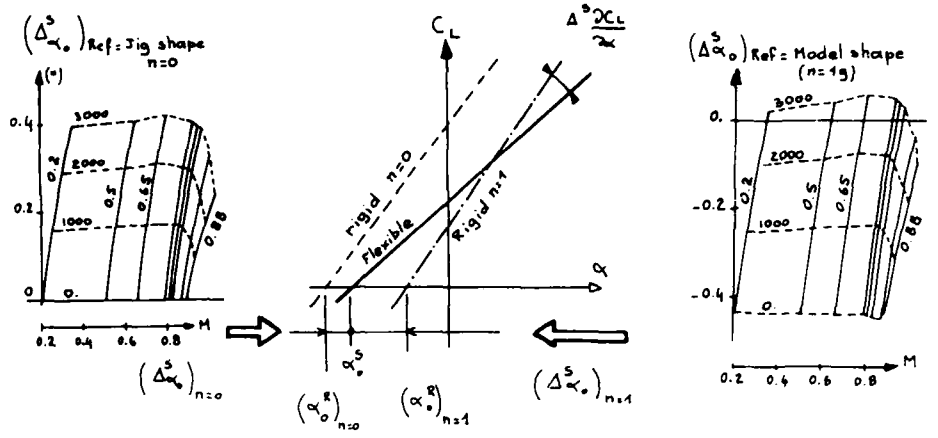

Pl 9

7 - FLEXIBLE A/C LOADS

DIRECTION ETUDES TOULOUSE

● Load distributions associated to a unit effect · $\Delta^S C = 1$

→ load distributions $\left\{\Delta^S F\right\}_{\Delta^S C = 1}$

→ general loads $\left\{K_L^S . \ell\right\}_{\Delta^S C = 1}$ $\left\{\frac{x_{ac}^S}{\ell}\right\}$

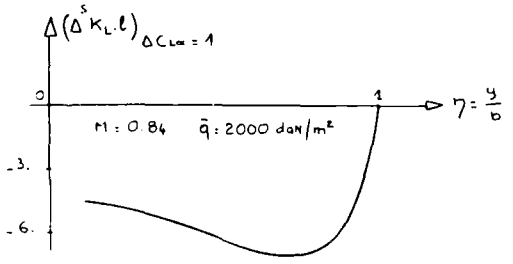

Pl 10

8 - COMMENTS

DIRECTION ETUDES TOULOUSE

- Flexibility matrix [c] = f (supports)

- AS approach independant of the supports
  - flexible induced aerodynamic loads in equilibrium
  - [c] = deformations / rigid A/C C.G

Pl 11

8 - COMMENTS

DIRECTION ETUDES TOULOUSE

- [c] / rigid A/C CG

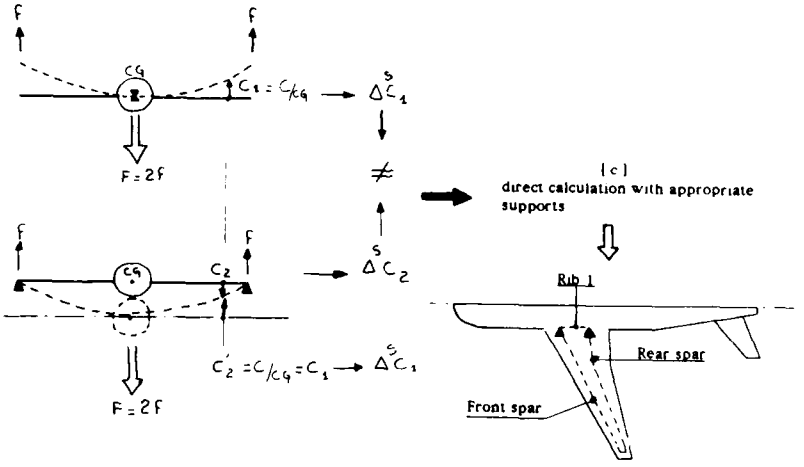

Pl 12

10 - DIVERGENCE

DIRECTION ETUDES TOULOUSE

● Behaviour of the cycle loads → deformations → loads →

● Divergence - $\{\Delta\} = \infty$

$$\{\Delta\} = \left[[Y] - \bar{q}[C][A]\right]^{-1}[C]\{F\} = [B]^{-1}[C]\{F\}$$

➡ divergence - $[B]$ singular

➡ $\bar{q} = \frac{1}{2}\rho V^2$ → $[B]$ singular - divergence conditions

Pl 13

10 - CONTROLS EFFICIENCY

DIRECTION ETUDES TOULOUSE

● Flexibility ➡ controls efficiency modifications

(back sweep - possibility of reversal)

$$\eta_{C_{\ell\delta_P}} = \frac{C^{S}_{\ell\delta_P}}{C^{R}_{\ell\delta_P}} = 1 - \frac{\bar{q}\{Y\}^T[A][B]^{-1}[C]\{F_{\delta_P}\}}{C^{R}_{\ell\delta_P}}$$

$\eta_{C_{\ell\delta_P}}$ ➡ — Definition of controls - geometry.

— Choice of controls fonctions

- Handling qualities
- Load control
- - - - - -

— A/C sizing

Pl. 14

10 - CONTROLS EFFICIENCY

DIRECTION ETUDES TOULOUSE

A300 B outer aileron

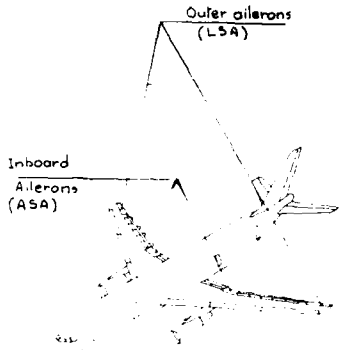

Outer ailerons = low speed ailerons

$\delta_p = 0 \quad M > 0.6$

● Pre flight calculations

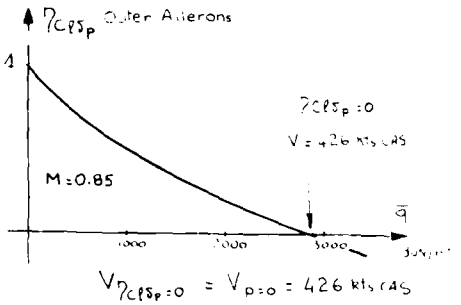

$V_{\eta_{C\ell\delta_p}=0} = V_{p=0} = 426$ kts CAS

(Simplified roll manoeuver 1 d.o.f.)

P' 15

11 CONTROLS EFFICIENCY

DIRECTION ETUDES TOULOUSE

A300B Outer ailerons

● Flight test results

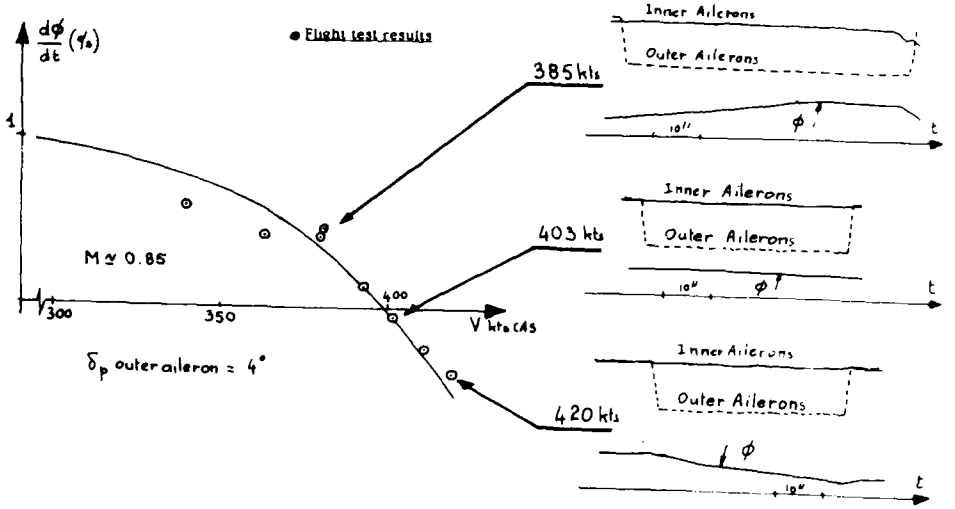

P' 16

11 - CONTROLS EFFICIENCY

DIRECTION ETUDES TOULOUSE

A 300 B outer ailerons

● Comparison flight tests / calculations

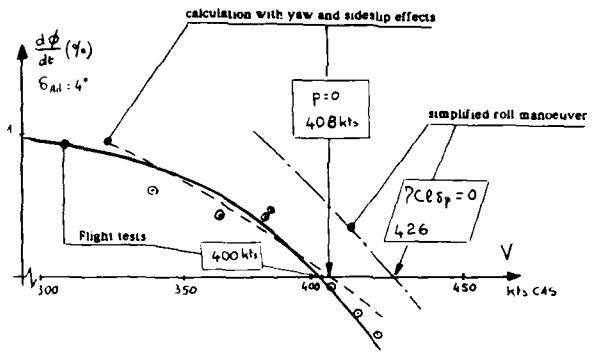

Pl (17)

11 - AEROELASTIC OPTIMISATION

DIRECTION ETUDES TOULOUSE

● Introduction of aeroelastic constrains in ASELF optimisation process
(mainly controls efficiency)

● 2 steps → acquisition of aeroelastics factors

Size of the problem → deformations by basic reference shapes combination

→ appropriate formulation of the problem inside the optimisation process

Pl (18)

STATIC AEROELASTIC EFFECTS ON THE FLUTTER OF A SUPERCRITICAL WING

E. Carson Yates, Jr.
Chief Scientist
Loads and Aeroelasticity Division
NASA Langley Research Center
Hampton, Virginia 23665-5225

Li-Chuan Chu
Research Engineer
PRC Kentron Corporation
Hampton, Virginia 23666
U. S. A.

SUMMARY

It is well known that wings with supercritical airfoils generally have lower transonic flutter speeds than similar wings with conventional airfoils and that small increases in angle of attack from zero and the accompanying static aeroelastic deformations have further detrimental effects on transonic flutter. This paper presents the results of an effort to calculate the effects of angle of attack and the associated aeroelastic deformation on the flutter of a highly swept supercritical wing (TF-8A) by use of the modified strip analysis employed in previous studies of this wing. The spanwise distributions of steady-state section lift-curve slope and aerodynamic center required as input for these calculations were obtained from static aeroelastic calculations for the wing by use of the FL022 transonic code and an assumed dynamic pressure. The process is iterative so that flutter can be obtained at the same dynamic pressure as that used to calculate the statically deformed shape and loading about which the flutter oscillation occurs (matched conditions). The results of this investigation show that the unconventional backward turn of the transonic dip in the experimental flutter boundary for angles of attack greater than zero is caused by variations in mass ratio and not by static aeroelastic deformation, although inclusion of the latter appears to be required for quantitative accuracy in the calculations. For the very high subsonic Mach numbers of this investigation, however, quantitative accuracy will also require inclusion of viscous effects on shock strength and location.

SYMBOLS

$a_{c,n}$	nondimensional distance from midchord to section aerodynamic center measured perpendicular to elastic axis, positive rearward, fraction of semichord
b	semichord of wing measured perpendicular to elastic axis at station η
b_r	semichord of wing at spanwise reference station (η = 0.75)
C_{L_0}	wing lift coefficient at α=0
C_{L_α}	wing lift-curve slope
C_ℓ	section lift coefficient for a section perpendicular to elastic axis
$C_{\ell_{\alpha,n}}$	section lift-curve slope for a section perpendicular to elastic axis
C_m	section-pitching moment coefficient referred to midchord for a section perpendicular to elastic axis
k	reduced frequency, $b_r\omega/V\cos\Lambda_{ea}$
M	freestream Mach number
m_r	mass of wing per unit span at spanwise reference station (η = 0.75)
q	freestream dynamic pressure
V	freestream speed
V_I	flutter-speed index, $\frac{V}{b_r\omega_r\sqrt{\mu_r}}$
α	angle of attack at wing root
η	nondimensional coordinate measured from wing root along elastic axis, fraction of elastic axis length
Λ_{ea}	sweep angle of elastic axis

μ_r mass ratio based on spanwise reference station (η = 0.75), $m_r/\pi\rho b^2$

ρ freestream density

ω circular frequency of vibration

ω_r reference frequency, frequency of first uncoupled torsional mode of wing

INTRODUCTION

It is well known that the use of supercritical airfoils, rather than conventional airfoils, can have adverse effects on the transonic flutter characteristics of lifting surfaces. The effects include reduction of transonic flutter speeds (refs. 1 to 3) and increased rate of degradation of flutter speed with small increases in angle of attack (refs. 4 and 5). In order to gain insight into these deleterious effects and the physical phenomena involved, a computational flutter study was conducted half a dozen years ago for a flutter model of the supercritical wing of the TF-8A airplane (fig. 1). Since adequate aerodynamic theories for three-dimensional unsteady transonic flow were not available, the modified strip analysis (refs. 6 to 12) was used. Spanwise distributions of steady-state section lift-curve slope and aerodynamic center, required as input to the flutter calculations, were obtained from wind-tunnel pressure measurements on another model of the same airplane.

The calculated flutter results compared well with experiments for 0^0 and 1^0 angles of attack but did not reproduce the drastic decline in transonic flutter speeds shown by the experiments at 2^0 and 3^0 angles of attack (ref. 5). The trends seemed to indicate, however, that the latter discrepancy was caused at least to some extent by the fact that the pressure model, from which the aerodynamic inputs were obtained, was two orders of magnitude stiffer than the flutter model and hence deformed statically much less than the flutter model.

The present investigation was initiated to address that problem. The same methodology is used except that the spanwise distributions of section lift-curve slope and aerodynamic center are obtained from static aeroelastic calculations for the flutter model employing the FLO22 full-potential code (ref. 13). Dynamic pressure is iterated between the aeroelastic calculation and the flutter calculation in order to obtain flutter at the same dynamic pressure as that used to calculate the static deformation and loading. The objective of this investigation is not to develop new methodology but to study the physical phenomena involved.

FLUTTER ANALYSIS METHOD

The modified strip analysis (ref. 6) is formulated for wing strips oriented normal to the elastic axis and is based on stripwise application of Theodorsen-type aerodynamics (ref. 14) in which the lift-curve slope of 2π and aerodynamic center at quarter chord are replaced, respectively, by the lift-curve slope and aerodynamic center for the same strip of the three-dimensional wing at the appropriate Mach number and angle of attack. The downwash collocation point, where the downwash induced by the aerodynamic load is set equal to the kinematic downwash, is modified accordingly. The aerodynamic admittance function (circulation function) is modified for compressibility by use of two-dimensional unsteady compressible-flow theory (ref. 15).

The simple example of section lift L on an unswept wing can be used to illustrate the changes to Theodorsen aerodynamics that are involved in the modified strip analysis.

For a three-dimensional wing in compressible steady flow, the section lift is given in terms of the section lift-curve slope $C_{\ell_{\alpha,n}}$ and the static angle of attack α or alternatively the downwash $Q=\alpha V$.

$$L = C_{\ell_{\alpha,n}} \alpha \frac{\rho}{2} V^2 (2b) = C_{\ell_{\alpha,n}} \rho V b Q$$

For two-dimensional incompressible oscillatory flow, the section lift as given by Theodorsen can be expressed in similar form.

$$L = 2\pi\rho V b Q C + \text{noncirculatory terms}$$

Now, however, the lift-curve slope for two-dimensional incompressible flow is 2π, and the circulatory lift is multiplied by an aerodynamic admittance function (circulation function) $C(k)=F_I + iG_I$. The downwash Q is the unsteady downwash evaluated at the three-quarter-chord point which is the collocation point for induced and kinematic downwash in two-dimensional incompressible flow. Noncirculatory lift terms which have no counterpart for steady flow are also included.

For three-dimensional compressible oscillatory flow, the Theodorsen form of the expression is retained for the modified strip analysis

$$L = C_{\ell_{\alpha,n}} \rho V b Q C + \text{noncirculatory terms}$$

but with three modifications: (a) The lift-curve slope is no longer 2π but the value for the particular section of the three-dimensional wing at the particular Mach number, angle of attack, and other conditions being studied. (b) The downwash collocation point is no longer at three-quarter chord but is relocated to satisfy the trailing-edge condition for the particular section lift-curve slope and aerodynamic-center position involved. (c) The circulation function for incompressible flow is modified in magnitude only to account for compressibility.

$$C(k,M) = \frac{\sqrt{F_C^2 + G_C^2}}{\sqrt{F_I^2 + G_I^2}} (F_I + iG_I) = \frac{F_C}{F_I} (F_I + iG_I)$$

where subscripts C and I indicate values for two-dimensional compressible and incompressible flow, respectively. Similar modifications are also made, of course, in the corresponding expression for section pitching moment (refs. 6 and 7). Note that no arbitrary user-selected parameters are included in the expressions in order to improve the agreement with experimental flutter data or with other calculations.

The modified strip analysis has consistently given good flutter results for a broad range of swept and unswept wings at speeds up to hypersonic (ref. 7), including effects of wing thickness (refs. 9 and 10) and angle of attack (ref. 11). In particular, this method which was developed in the mid 1950's (ref. 6) was used successfully in 1959 to calculate transonic flutter characteristics for some swept wings with conventional airfoils (ref. 8). In 1979, it was used to calculate transonic flutter of the present supercritical wing at essentially zero angle of attack with exceptionally good results (ref. 3). That study was extended in 1980 to include nonzero angles of attack (ref.5).

PREVIOUS FLUTTER CALCULATIONS FOR TF-8A WING

For Experiments in Freon-12

In the calculations for the TF-8A wing shown in figure 2 (from ref. 3), the required aerodynamic parameters were obtained from steady-state surface pressure measurements in the Langley 8-foot Transonic Tunnel (ref. 16). In the subsonic range, agreement between calculated and measured flutter boundaries is excellent. In the transonic range, a transonic dip is calculated which closely resembles the experimental one with regard to both shape and depth. However, the calculated dip occurs at about 0.04 Mach number lower than the experimental one. The reason for this difference is not known with certainty. There is some evidence, however, that indicates that the difference may be associated with model size relative to tunnel dimensions. The pressure model from which the aerodynamic coefficients were obtained for use in the flutter calculations was smaller relative to tunnel size than was the flutter model.

Note also that the experimental flutter data in figure 2 as well as the aerodynamic parameters used in the corresponding flutter calculations were obtained at essentially zero angle of attack. Consequently, the associated static aerodynamic loads and aeroelastic deformations were small and were not expected to influence flutter characteristics to any significant extent.

The experimental flutter data shown in figure 2 were obtained with Freon-12* gas used as test medium. Therefore, the associated values of mass ratio (fig. 3) were relatively low.

For Experiments in Air

The good results shown in figure 2 (from ref. 3) encouraged an extension of the study to examine the effects of angle of attack on flutter (ref. 5). The required aerodynamic parameters $C_{l\alpha,n}(n)$ and $a_{c,n}(n)$ were obtained from the same wind-tunnel pressure data as before, and representative values are shown in figures 4 and 5.

Figure 4 shows representative spanwise distributions of section lift-curve slope and aerodynamic center obtained from measured surface pressures at two subsonic Mach numbers. Nonlinearity with respect to angle of attack is minor at Mach number 0.25 but increases as Mach number rises to 0.80, especially in the aerodynamic center location. Note that the TF-8A wing was designed for an unusually high drag-rise Mach number (M=0.99).

As Mach number increases further, nonlinearity (as typified in fig. 5) becomes substantial and portends growing sensitivity of flutter speed to changes in angle of attack. Note, however, that the aerodynamic model on which the pressures were measured was two orders of magnitude stiffer than the flutter model in both bending and torsion. Consequently, aeroelastic deformation of the aerodynamic model was small, and the effects of angle of attack shown here are essentially aerodynamic (rather than aeroelastic) in origin.

---

* Freon is a registered trademark of E. I. DuPont de Nemours Co., Inc.

The corresponding flutter results for angles of attack from 0 deg to 3 deg are shown in figures 6(a) to 6(d) (from ref. 5). Note that the mass-ratio values shown on the figures for these experiments in air are considerably higher than those for the experiments in Freon-12 which were shown in figures 2 and 3.

At each Mach number for which the aerodynamic experiments were conducted (ref. 16), pressures on the wing surface were measured at two levels of freestream dynamic pressure, and both were used in the flutter calculations of reference 5 as indicated by the solid and dash lines in figures 6(a) to 6(d). Moreover, the Mach numbers for the aerodynamic experiments did not coincide with the experimental flutter Mach numbers. Therefore, no attempt was made to match experimental flutter conditions point for point with respect to Mach number and mass ratio. Instead, the flutter calculations were made only for the maximum and minimum experimental values of mass ratio at each angle of attack.

For α = 0 (fig. 6(a)), static aeroelastic deformations of the flutter model were not significant, and the conventionally shaped experimental flutter boundary is reasonably well predicted by the calculated values which are about 6 percent conservative at M = 0.85 and a bit more so at the bottom of the transonic dip.

When α is increased to 1^0 (fig. 6(b)), the depth and location of the transonic dip are still adequately predicted, but the unconventional backward turn of the experimental boundary is not.

When α is further increased to 2^0 and 3^0 (figs. 6(c) and 6 (d), respectively), the backward turn of the experimental transonic flutter boundary becomes much more pronounced, and the bottom of the dip obviously drops drastically although the actual bottom is not defined by the available data points. The extent of this decline is not adequately predicted by the calculations. There is some evidence to indicate, however, that this discrepancy was caused at least to some extent by the fact that the pressure model, from which aerodynamic parameters were obtained for the flutter calculations, did not deform aeroelastically nearly as much as the flutter model did. Hence the aerodynamic parameters were not those relevant to the statically deformed wing shape about which the experimental flutter motion occurred. See reference 5 for more detailed discussion.

Experimental transonic flutter data for angles of attack up to 2.05 deg are presented in reference 17 for a high-aspect-ratio supercritical wing with, however, lower sweep angle and lower drag-rise Mach number than those for the TF-8A. The wing of reference 17 was provided some degree of flexibility in pitch, but the torsional stiffness of the wing itself appears to have been sufficiently high to prevent twisting deformations of significant magnitude. The measured transonic flutter boundary for that wing at 2.05 deg angle of attack is remarkably similar to the flutter boundary calculated for the TF-8A wing at 2 deg angle of attack using aerodynamic parameters obtained with the comparatively stiff pressure model of reference 16 (fig. 6(c)). The flutter boundaries for both wings show a relatively broad conventional-looking initial transonic dip followed by a steeper, narrower, deeper, and lower second dip. Second dips of this sort have been observed in wind-tunnel flutter-test results for other models under conditions for which static aeroelastic deformations would be expected to be mimimal (e.g., ref. 18).

Finally, it is illuminating to examine the variation of mass ratio with Mach number for the experimental flutter data shown in figures 6(a) to 6(c). On the curves of these parameters (fig. 7) the only firm values are those represented by the symbols which correspond to the "hard" flutter points in figures 6(a) to 6(c). The curves faired through the symbols in figure 7, however, are consistent with the curves faired through the "hard" flutter points in figures 6(a) to 6(c).

For α = 0, the variation of mass ratio is moderate and of conventional form (compare fig. 3). For α = 1 deg and especially for α = 2 deg, on the other hand, the deep backward-turning transonic dips shown in figures 6(b) and 6(c) correspond to substantial increases in mass ratio. These wide excursions in mass ratio indicate that the experimental flutter boundaries follow substantially different tracks across the flutter-speed surface (defined by $V_I = f(M,\mu_r)$) for α = 0, 1, and 2 degrees. The large values of mass ratio in themselves would produce low values of flutter-speed index. This point will be addressed subsequently in this paper. See also the more detailed discussion of the flutter-speed surface and the implications for flutter experiments and data interpretation in Appendix C of reference 10 and in reference 12.

PRESENT ANALYSIS

The inadequacy of the available experimental aerodynamic data for application to conditions involving significant static aeroelastic deformation of the flutter model led to the present study in which the required aerodynamic parameters were obtained from static aeroelastic calculations (fig. 8) incorporating FL022 aerodynamics (ref. 13). Pressure distributions were thus computed for the aeroelastically deformed wing at a given Mach number, several angles of attack, and an initially chosen dynamic pressure. Since experimental flutter data were available, the Mach numbers and dynamic pressures were taken to be those for the measured flutter points. The calculated pressures were integrated to generate spanwise distributions of section lift and pitching-moment coefficients. These coefficients were then spline fitted as functions

of angle of attack, and the spline curves were analytically differentiated to produce section lift-curve slopes and moment-curve slopes (and hence aerodynamic centers) for the angles of attack at which the flutter data were measured. The spanwise distributions of section lift-curve slope and aerodynamic center were input to the modified strip analysis to generate generalized aerodynamic forces for use in the FAST flutter-analysis program (ref. 19). The resulting flutter dynamic pressure could then be used to modify the dynamic pressure input to the static aeroelastic calculation and the process iterated to produce flutter and static deformation (and associated pressure distributions) for the same (matched) dynamic pressure.

The FL022 finite-difference code (ref. 13) implements a nonconservation form of the full potential equation. It was employed in this investigation because it had been previously incorporated into a static aeroelastic analysis (ref. 20) and previously used by the present first author in some unpublished calculations of the type presented here but for a different supercritical wing.

RESULTS AND DISCUSSION

For all of the flutter calculations made with aerodynamic parameters from FL022, the Mach number, angle of attack and mass ratio for the experimental flutter points were essentially duplicated. As in reference 3 and 5, six measured natural modes of vibration were used in all flutter calculations. In figs. 9 and 10, the results are compared with the previously shown experimental flutter points and with the flutter boundaries calculated with the experimental aerodynamic parameters described previously (e.g., figs. 4 and 5; see also ref. 5). Note that the present calculations have been limited to the subsonic side of the transonic dip. Investigation of the subsonic side was considered to be sufficient to indicate the occurrence, character, and causes of the backward-turning transonic dip.

Calculations for Design Shape of Wing

An initial set of aerodynamic (FL022) calculations was made for the wing deformed into its design shape and treated as rigid. The spanwise distributions of section lift-curve slope and aerodynamic center thus obtained were used in some initial flutter calculations. The resulting nondimensional flutter speeds V_I are represented by the diamond symbols in figs. 9 and 10. For zero angle of attack (fig. 9(a)), the calculated flutter speeds are in good agreement with experiment and differ very little from those obtained with the experimental aerodynamic parameters for (normally) the design shape. At α = 1 deg (fig. 9(b)), the agreement is again good at the lowest experimental Mach number and mass ratio, but the calculated points become progressively unconservative as mass ratio increases to 547. It is important to note, however, that the backward turn of the flutter boundary is clearly indicated by the three calculated points, thus indicating that varying aeroelastic deformation is not essential to produce this behavior. Instead, the backward turn shown here is caused by the indicated variation in mass ratio. If the three calculated points are compared on the basis of a constant mass ratio, say μ_r = 450. (results not shown), no backward turn appears. Results that are qualitatively similar to those in fig. 9(b) for α = 1 deg are shown in fig. 9(c) for α = 2 deg.

These progressively more unconservative predictions of flutter-speed index as mass ratio increases were anticipated from these calculations in which static aeroelastic deformation was neglected. Consider the experimental flutter boundary shown in figs. 9(c) and 10 for the flexible flutter model. As mass ratio increases, the flutter-speed index (and hence flutter dynamic pressure) decreases. As dynamic pressure decreases, static aeroelastic deformation (notably wing washout) diminishes, and section lift-curve slopes increase, especially over the outboard sections of the wing. As section lift-curve slopes increase, flutter dynamic pressure and flutter-speed index decrease. In other words, as mass ratio increases, diminishing static aeroelastic deformation of the flutter model contributes to lower flutter-speed index, and that effect is not included in the calculations for the rigid design shape (figs. 9(b) and (c) and fig. 10). Moreover, static loads and deformations and their effects should increase with increasing angle of attack, and the effects just described are indeed observed in figs. 9(a), (b), and (c) to become more pronounced as angle of attack increases. In fact, the effects of static deflection appear to be negligible at zero angle of attack (fig. 9(a)).

In fig. 10 the experimental and calculated transonic dips in fig. 9(c) have been enlarged and the calculations extended to show the bottom portion of the dip which has been calculated by use of the mass-ratio variation for α = 2 deg shown in fig. 7. The latter, in turn, is consistent with the bottom portion of the dip faired through the experimental flutter points. These calculations for the rigid design shape show clearly that the unconventional backward-turning transonic flutter boundary is caused by variation in mass ratio and not by static aeroelastic deformation. Accuracy in predicting this kind of dip, however, does appear to require consideration of static deformation.

Calculations for Flexible Wing

When the wing is treated as flexible in the static-aeroelastic portion of the calculation procedure shown schematically in fig. 8, the "initial shape" input to the

"aeroelastic FL022" iterative calculation of pressures and deformations may be the undeformed shape or, if available, a better approximation to the aeroelastically converged shape. If the latter is used, however, it is still necessary to input the undeformed shape ("jig" shape) of the wing into "aeroelastic FL022" so that the calculated deformations may be added to it in order to obtain the output deformed shape and associated pressure distribution. Since jig-shape measurements for the TF-8A flutter-model wing were not available, a jig shape was calculated by subtracting from the design shape the deformations caused by the load distribution on the design shape at the design condition ($M = 0.99$, $C_L = 0.37$).

For the flexible wing the experimental flutter dynamic pressure was input to the static aeroelastic calculation (fig. 8), and a single pass was made through the computational sequence. Although the outer q-loop has not been closed at this time, the accuracy of the calculated results (triangle symbols in figs. 9(a) and (b)) is well indicated by comparison of the calculated and experimental flutter points. Since the experimental flutter dynamic pressure was input, perfect agreement between calculation and experiment would be indicated by the same flutter dynamic pressure being calculated in a single pass through the outer loop. It is evident in figs. 9(a) and (b), however, that the inclusion of structural flexibility in combination with FL022 leads to excessively high flutter speeds. This result was not unanticipated.

For the higher Mach numbers and higher loading conditions potential-flow methods, including FL022, characteristically produce shockwaves that are too strong and too far aft. Moreover, once the shock has moved aft, it exhibits very little further movement with changes in angle of attack or deformation and hence generates little further change in section lift-curve slopes and aerodynamic centers. Thus, for example, in the present calculations of loading (and hence deformation) at the design condition ($M = 0.99$, $C_L = 0.37$), calculated C_{L_0} was considerably higher and C_{L_α} was considerably lower than corresponding experimental values (from ref. 16). These aerodynamic deficiencies raise doubts concerning the accuracy of the calculated jig shape. In addition, the low values of calculated lift-curve slopes also contribute to the excesively high calculated flutter speeds shown in figs. 9(a) and (b).

In contrast, the wing in a physical (viscous) flow will experience shocks that are weaker and farther forward. Consequently, as flutter dynamic pressure decreases into the transonic dip, the flexible wing deforms less and less, the outer wing sections assume higher local angles of attack, as previously described, shocks strengthen and migrate aft, and the effective section lift-curve slopes increase. This effect of diminishing deformation thus contributes to a still lower flutter dynamic pressure. Since this behavior is not accurately obtained from FL022, it is evident that, as expected, accurate flutter prediction will require the inclusion of viscous effects on shock strength and location. Static aeroelastic and flutter calculations are in progress with the FL022 code replaced by the FL030 code (full-potential, conservation-form, finite-volume code) (ref. 21), including a coupled boundary-layer code (ref. 22) in order to address the current deficiencies.

CONCLUDING REMARKS

Modified-strip-analysis flutter calculations have been made for a supercritical wing with high design Mach number using aerodynamic parameters obtained from the FL022 full-potential-flow code for the design shape (rigid) and for the aeroelastically deformed wing at approximately the flutter dynamic pressure. The unconventional backward turn of the transonic flutter boundary found experimentally at nonzero angles of attack was also calculated with aerodynamic parameters for the rigid design shape and was shown to be caused by variations in mass ratio. Quantitative accuracy in predicting this kind of transonic dip, however, appears to require consideration of static aeroelastic deformation. Inadequacies of the full-potential code at the high subsonic Mach numbers involved led to excessively high calculated flutter speeds for the flexible wing resulting from (1) poor definition of jig shape from the design shape, and (2) low values of section lift-curve slopes and aftward locations of section aerodynamic centers (relative to experiments) caused by excessively aftward shock locations that changed little with changes in angle of attack. The present methodology is valid, but accurate flutter predictions will require the inclusion of viscous effects on shock strength and location, at least for the wing used in this study. Such calculations are in progress.

REFERENCES

1. Farmer, Moses G.; Hanson, Perry W.; and Wynne, Eleanor C.: Comparison of Supercritical and Conventional Wing Flutter Characteristics. NASA TM-72837, 1976.

2. McGrew, J. A.; Giesing, J. P.; Pearson, R. M.; Zuhuruddin, K.; Schmidt, M. E.; and Kalman, T. P.: Supercritical Wing Flutter, AFFDL-TR-78-37, 1978.

3. Yates, E. Carson, Jr.; Wynne, Eleanor C.; Farmer, Moses G.; and Desmarais, Robert N.: Prediction of Transonic Flutter for a Supercritical Wing by Modified Strip Analysis. J. Aircraft, Vol. 19, No. 11, November 1982, pp 999-1004.

4. Houwink, R.; Kraan, A. N.; and Zwaan, R. J.: Wind-Tunnel Study of the Flutter Characteristics of a Supercritical Wing. J. Aircraft, Vol. 19, No. 5, May 1982, pp. 400-405.

5. Yates, E. Carson, Jr.; Wynne, Eleanor C.; and Farmer, Moses G.: Effects of Angle of Attack on Transonic Flutter of a Supercrictical Wing. J. Aircraft, Vol. 20, No. 10, October 1983, pp. 841-847.

6. Yates, E. Carson, Jr.: Calculation of Flutter Characteristics for Finite-Span Swept or Unswept Wings at Subsonic and Supersonic Speeds by a Modified Strip Analysis, NACA RM L57L10, 1958.

7. Yates, E. Carson, Jr.: Modified-Strip-Analysis Method for Predicting Wing Flutter at Subsonic to Hypersonic Speeds. J. Aircraft, Vol. 3, No. 1, January-February 1966, pp. 25-29.

8. Yates, E. Carson, Jr.: Use of Experimental Steady-Flow Aerodynamic Parameters in the Calculation of Flutter Characteristics for Finite-Span Swept or Unswept Wings at Subsonic, Transonic, and Supersonic Speeds, NASA TM X-183, 1959.

9. Yates, E. Carson, Jr.; and Bennett, Robert M.: Use of Aerodynamic Parameters from Nonlinear Theory in Modified-Strip-Analysis Flutter Calculations for Finite-Span Wings at Supersonic Speeds, NASA TN D-1824, 1963.

10. Yates, E. Carson, Jr.: Subsonic and Supersonic Flutter Analysis of a Highly Tapered Swept-Wing Planform, Including Effects of Density Variation and Finite Wing Thickness, and Comparison with Experiments. NASA TN D-4230, 1967.

11. Yates, E. Carson, Jr.; and Bennett, Robert M.: Analysis of Supersonic-Hypersonic Flutter of Lifting Surfaces at Angle of Attack. J. Aircraft, Vol. 9, No. 7, July 1972, pp. 481-489.

12. Yates, E. Carson, Jr.: Flutter and Unsteady-Lift Theory. In "Performance and Dynamics of Aerospace Vehicles." NASA SP-258, 1971.

13. Jameson, A.; and Caughey, D. A.: Numerical Calculation of the Transonic Flow Past a Swept Wing, NASA CR-153297, 1977.

14. Theodorsen, Theodore: General Theory of Aerodynamic Instability and the Mechanism of Flutter. NACA Rep. 496, 1935.

15. Jordan, P. F.: Aerodynamic Flutter Coefficients for Subsonic, Sonic and Supersonic Flow (Linear Two-Dimensional Theory). R. & M. No. 2932, British A.R.C., 1957.

16. Harris, Charles D.: Wind-Tunnel Investigation of the Aerodynamic Load Distribution of a Supercritical Wing Research Airplane Configuration. NASA TM X-2469, 1972.

17. Persoon, A. J.; Horsten, J. J.; and Meijer, J. J.: Measurement of Transonic Dips in the Flutter Boundaries of a Supercritical Wing in a Wind Tunnel. J. Aircraft, Vol 2', No. 11, November 1984, pp. 906-912.

18. Sandford, Maynard C.; Ruhlin, Charles L.; and Abel, Irving: Flutter Studies of Simplified Component Models of a Variable-Sweep-Wing Airplane at Mach Numbers Up to 3.0. NASA TN D-3501, 1966.

19. Desmarais, Robert N.; and Bennett, Robert M.: User's Guide for a Modular Flutter Analysis Software System (FAST Version 1.0). NASA TM 78720, 1978.

20. Whitlow, Woodrow, Jr.; and Bennett, Robert M.: Application of a Transonic Potential Flow Code to the Static Aeroelastic Analysis of Three-Dimensional Wings. AIAA Paper No. 82-0689, 1982.

21. Caughey, D. A.; and Jameson, Antony: Progress in Finite-Volume Calculations for Wing-Fuselage Combinations. AIAA Journal, Vol. 18, November 1980, pp. 1281-1288.

22. Streett, C. L.: Viscous-Inviscid Interaction for Transonic Wing-Body Configurations Including Wake Effects. AIAA Journal, Vol. 20, No. 7, July 1982, pp. 915-923.

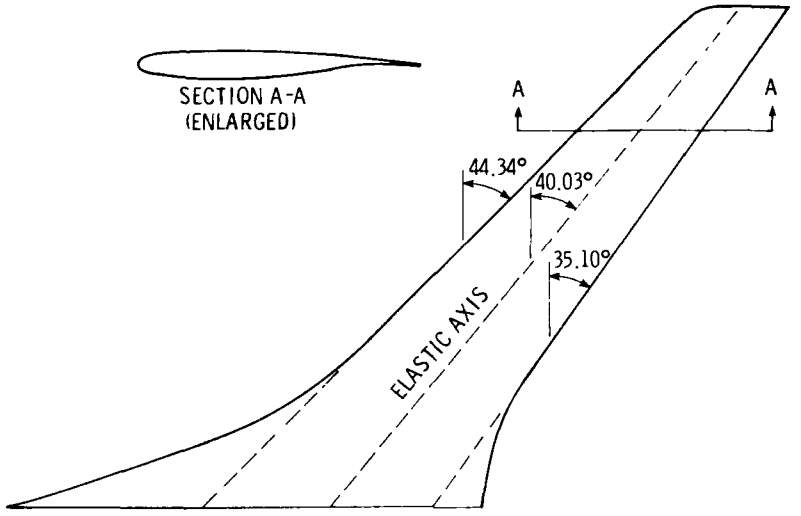

Fig. 1 - Supercritical wing flutter model

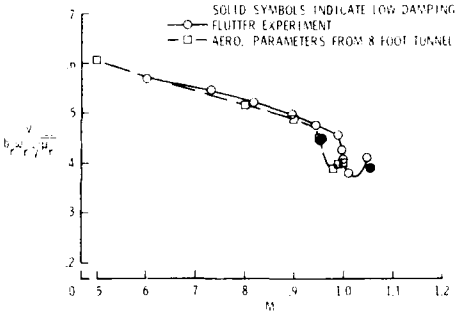

Fig. 2 - Experimental and calculated flutter in Freon-12 at α = 0

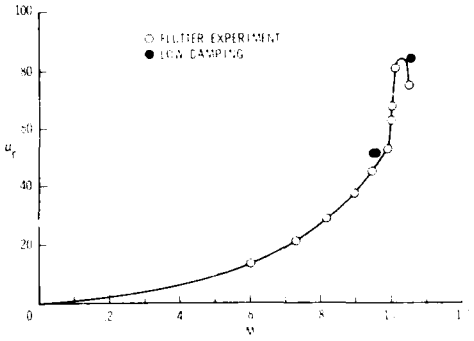

Fig. 3 - Mass ratios for flutter experiments in Freon-12

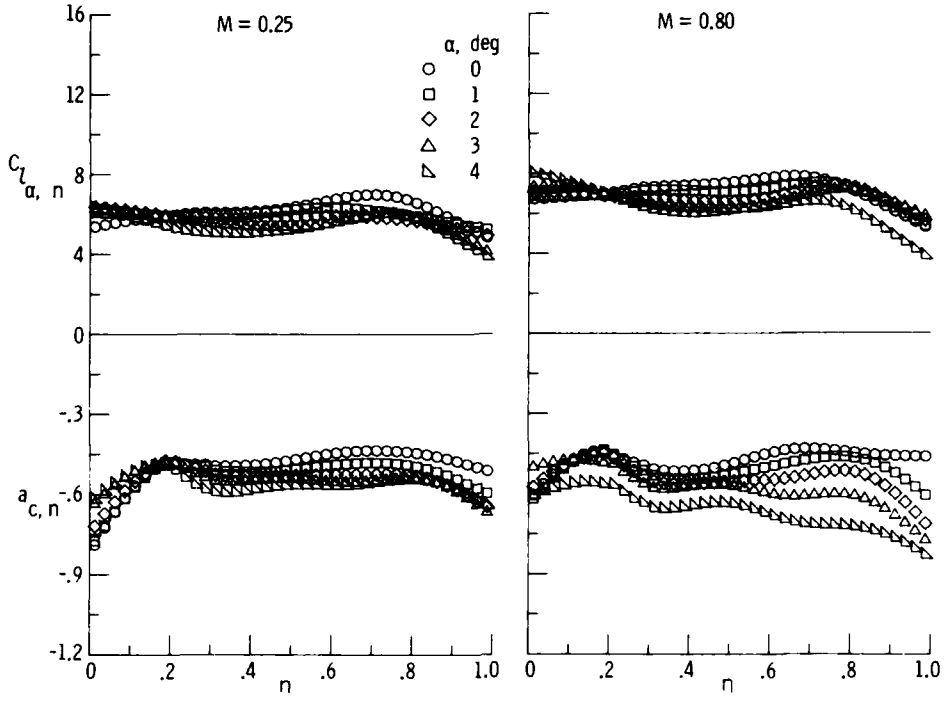

Fig. 4 - Typical aerodynamic parameters for flutter analysis at subsonic Mach numbers

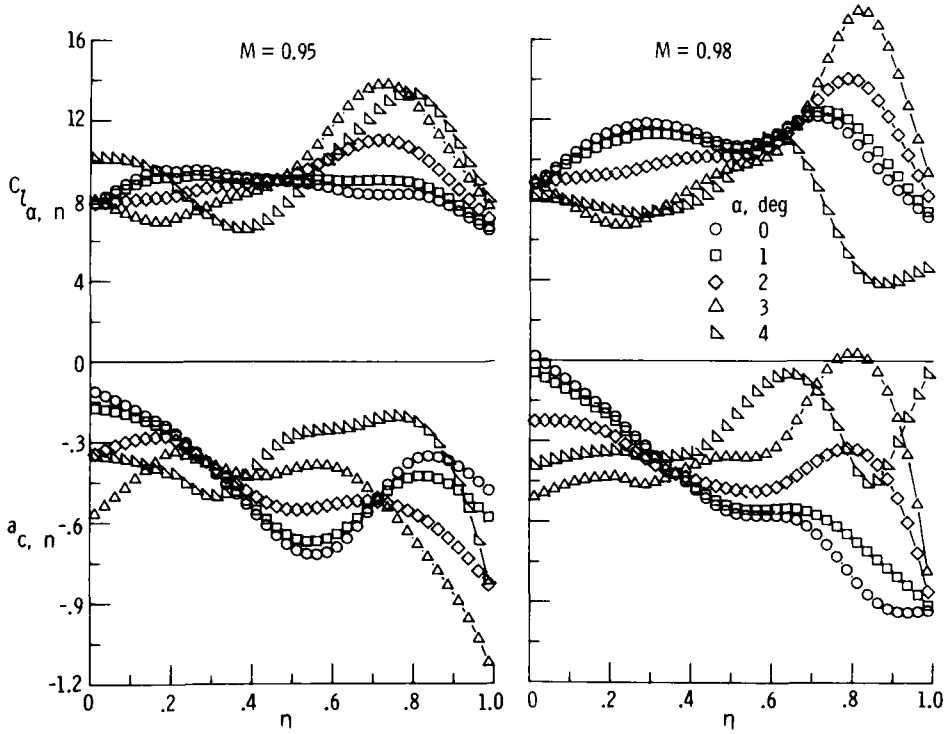

Fig. 5 - Typical aerodynamic parameters for flutter analysis at transonic Mach numbers

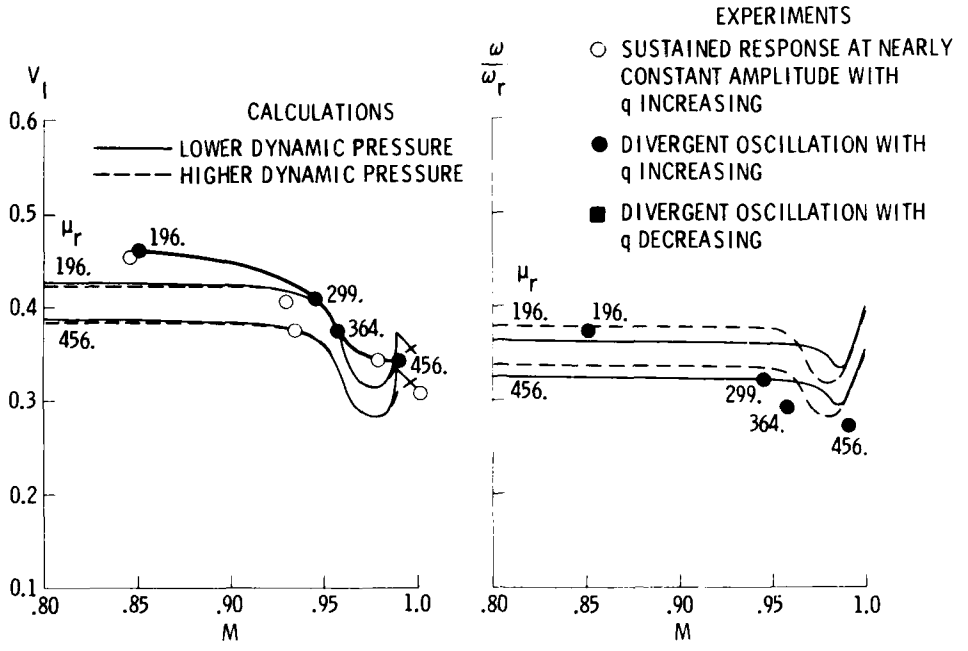

(a) α = 0

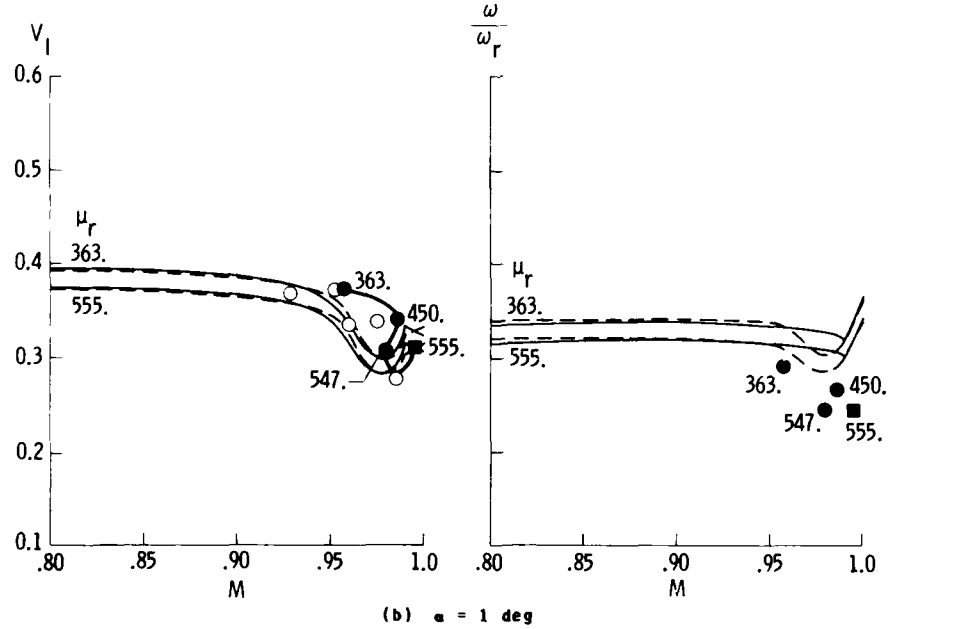

(b) α = 1 deg

Fig. 6 - Flutter in air obtained from experiments and from calculations with experimental aerodynamic parameters

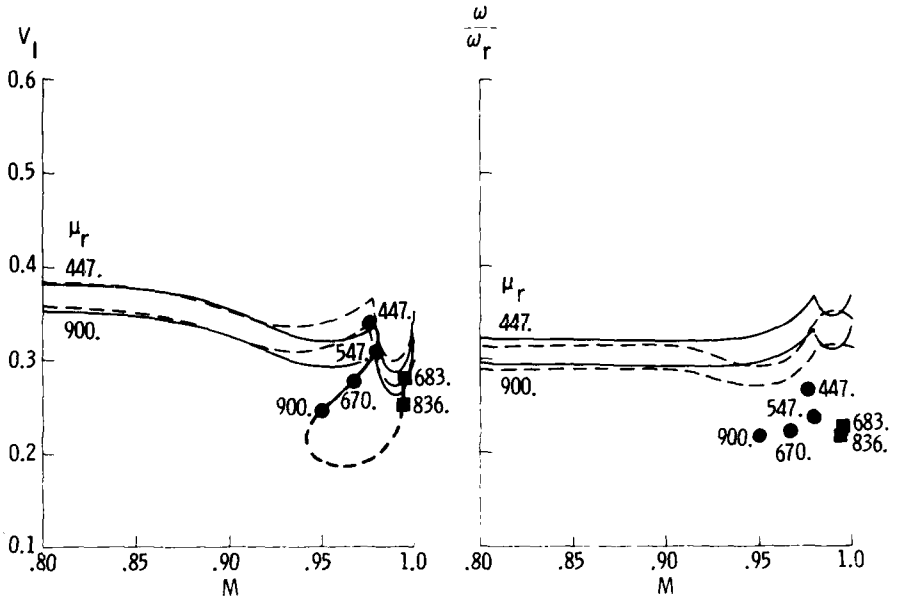

(c) α = 2 deg

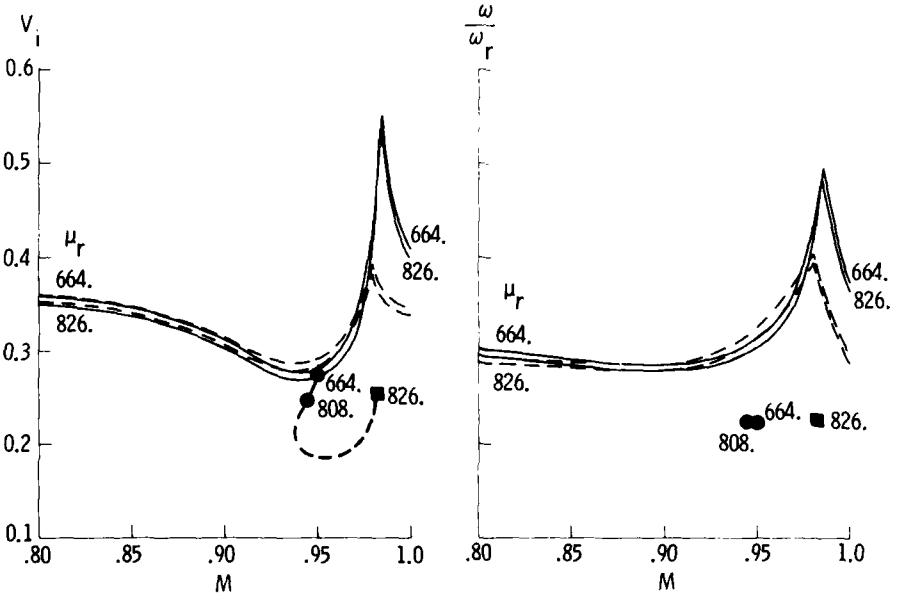

(d) α = 3 deg

Fig. 6 - Concluded

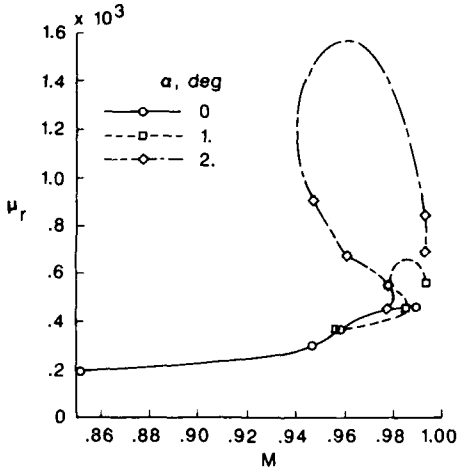

Fig. 7 - Mass ratios for flutter experiments in air

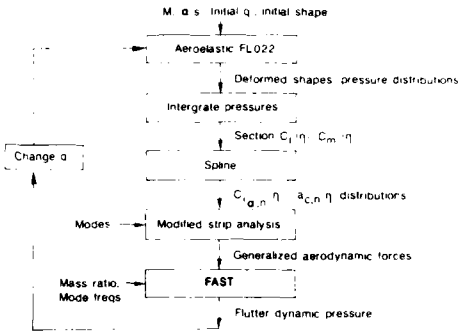

Fig. 8 - Matched static-aeroelastic and flutter calculations

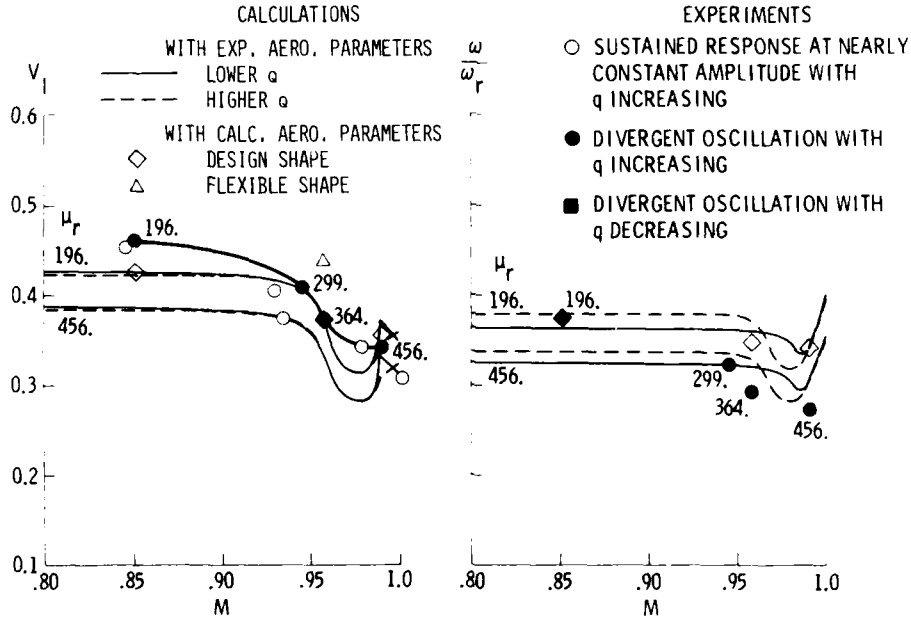

(a) α = 0

Fig. 9 - Flutter in air obtained from calculations with calculated aerodynamic parameters and comparison with previous results

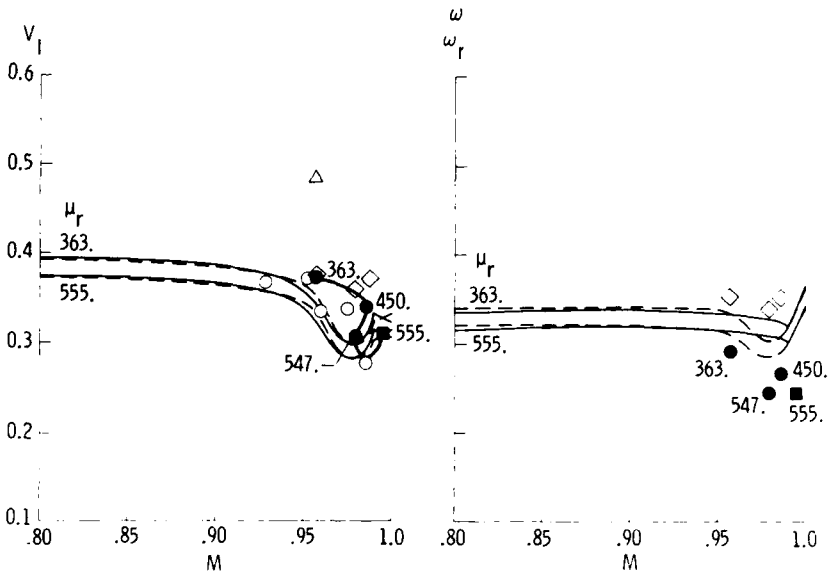

(b) α = 1 deg

Fig. 9 - Continued

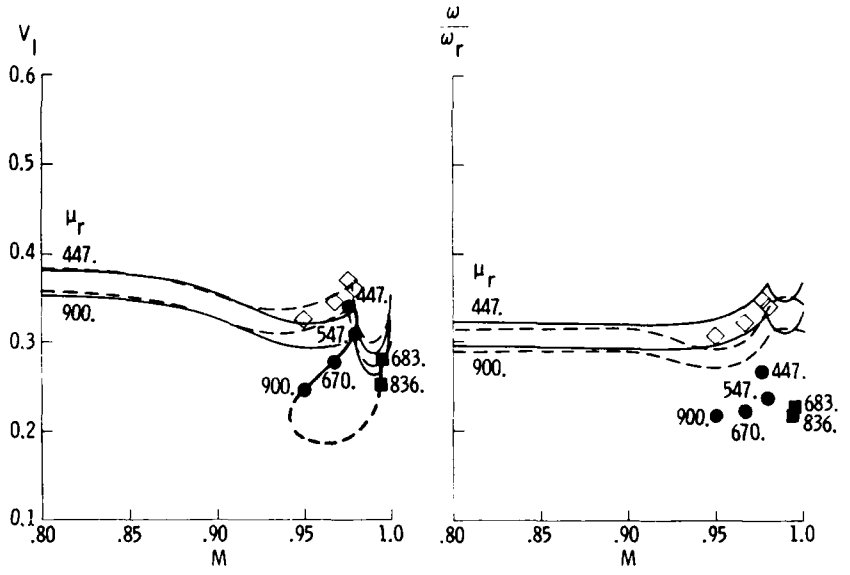

(c) α = 2 deg

Fig. 9 - Concluded

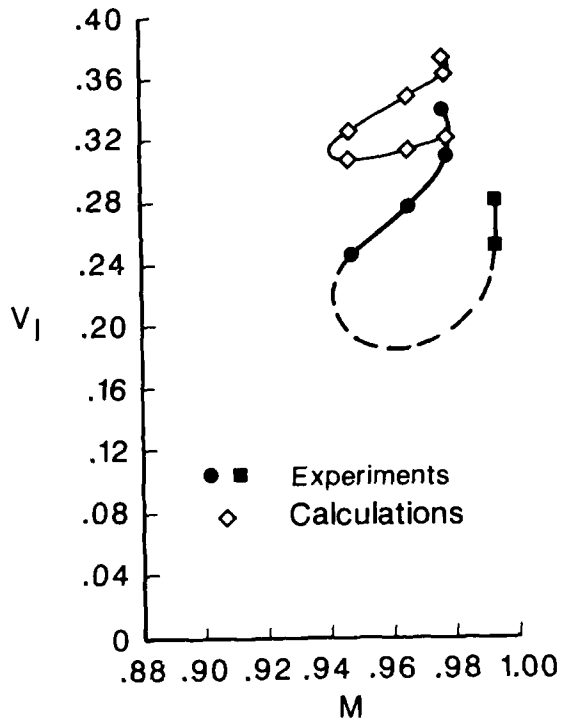

Fig. 10 - Transonic dip from flutter experiments and from calculations with calculated aerodynamic parameters for design shape and mass ratios from fig. 7; α = 2 deg

WING DIVERGENCE OF TRIMMED AIRCRAFT

Ll. T. Niblett
Royal Aircraft Establishment,
Farnborough, Hants, GU14 6TD, England

SUMMARY

By means of a simple theoretical model it is shown that wing divergence of a free aircraft can be defined using the static case of trimmed level flight. The same model also shows that the control angle per 'g' goes to zero at a speed near the fixed-root divergence speed and that there is a large change in the spanwise distribution of airload in going from a low speed to speeds above that of fixed-root divergence.

LIST OF SYMBOLS

A,B,C	square matrices defined in section 3.1
a_1	$dC_L/d\alpha$ for both wing and tailplane
b	defined after Eq.(2-10)
c	wing chord
f	column matrix of generalised forces defined in section 3.1
GJ	torsional rigidity of wing
ℓ	semispan of wing
n	centrifugal acceleration + g
q_e	generalised coordinate of rotation of tailplane about its aerodynamic axis
q_h	generalised coordinate of heave of aircraft
q_p	generalised coordinate of pitch of aircraft
q_{t_1}	generalised coordinate of wing torsion in mode of fixed-root divergence
q_{t_2}	generalised coordinate of wing torsion in mode of free-free divergence
S	wing area
S_t	tailplane area
s	ratio of tailplane area to wing area
V	airspeed
V_D	fixed-root divergence speed
W	weight of aircraft
w	weight of wing as fraction of weight of aircraft
$\bar{\alpha}$	nominal incidence of rigid aircraft for level flight, $W/\frac{1}{2}\rho V^2 S a_1$
η	scaled spanwise coordinate of wing
η_T	scaled spanwise coordinate of tailplane
$\xi_A c$	distance aerodynamic centre of wing is aft of aircraft cg
$\xi_T c$	distance aerodynamic centre of tailplane is aft of aircraft cg
$\xi_a c$	distance aerodynamic centre of wing is aft of wing flexural axis
$\xi_i c$	distance inertia axis of wing is aft of wing flexural
$\bar{\xi}$	ratio of ξ_A to ξ_T
ρ	air density
υ	airspeed as a fraction of fixed-root divergence speed

1 INTRODUCTION

Until serious consideration was given to sweptforward wings, little work had been done on wing divergence recently for, with the coming of transonic flight, straight wings were replaced by sweptback wings and these do not suffer from divergence because their flexural distortion reduces the local incidence, especially towards the tip, and usually this reduction dominates the destabilising effect of torsion. So most sweptback wings have no (real) divergence speed and divergence was something read about in textbooks.

The local incidence of a sweptforward wing built of isotropic materials is increased by the distortions in both flexure and torsion and consequently the divergence speeds of

such wings when their roots are encastered (FRDS) tend to be low. Divergence speeds can be increased by the use of anisotropic materials, which give structures that twist under flexural loads and vice versa, but present indications are that the divergence speed of a sweptforward wing is likely to be nearer flight speeds than is the case for other wings and, although not prohibitively low, might still be critical.

The practical significance of the FRDS can be called into question; for in trimmed flight a wing will pitch as well as twist and bend, and will not suffer divergence until it reaches a speed much higher than the FRDS. In the past it has been the practice to keep aircraft speeds well below their FRDS, even though the root constraint seemed unrealistic, on the grounds that the distortions of an aircraft at speeds near its FRDS would be large. However because divergence speeds were very high this restriction did not really matter. Now that there is a possibility that divergence speeds might be significantly nearer flight speeds, the simple calculations described here have been made to obtain some measure of the aeroelastic effects which are likely to accompany free flight near the FRDS and to confirm or deny the need to retain this restriction.

The reason for the study is the current interest in aircraft with sweptforward wings but the essentials of the phenomena are also exhibited by unswept wings and for simplicity the rectangular unswept wing has been studied. In the absence of sweep the flexural flexibility of the wing can be ignored and the inclusion of a second torsion mode, appropriate to free-free divergence, does not make the number of equations excessive. Rigid-body degrees of freedom have to be added. It is quite common to add only the rigid body mode of pitch about the aircraft cg in free-free divergence calculations but this seems unduly restrictive and here heave and pitch, the rigid-body freedoms necessary to give the equations describing an idealised pull-out were added. Some means of trimming the aircraft had also to be included and for this a rectangular rigid tailplane mounted on the rigid fuselage through a spanwise hinge at its quarter chord was chosen.

In section 2 of the paper the equations describing an idealised trimmed pull-out, of which level flight is a special case, are obtained by the principle of virtual work. Some of the aerodynamic effects usually included in stability and control calculations have been omitted but it is believed that they are of minor importance in the present context.

In section 3 these equations are solved for the symmetric free-free divergence speed, which has been taken to be the speed at which the amplitudes of the coordinates in the trim equation become indeterminate, and for the rigid- and flexible-aircraft trim cases in terms of tailplane angle per 'g'. At speeds near the FRDS the angle of pitch of the aircraft is small and most of the lift is the result of torsional distortion and, prompted by this, the changes in the flexural and torsional moment distributions with speed have been calculated. Because the torsional moments could be calculated in two different ways these calculations also provided a check on the adequacy of the semi-rigid representation.

Finally the results of all the calculations are discussed in section 4. It is concluded from the solutions of these equations that an 'unaugmented' aircraft flying at speeds near the fixed-root divergence speed of its wing will suffer low values of control angle per 'g' and further that the distribution of incidence across the wing will vary considerably with speed.

2 FORMATION OF PULL-OUT EQUATION

2.1 Generalised coordinates

The equations are those for an aircraft, consisting of a rectangular wing, a fuselage and a rectangular tailplane (see Fig 1), at the bottom of a shallow pull-put. Both the fuselage and the tailplane are rigid and they are included as a simple source of trimming moment for the aircraft. Because the efficiency of the tailplane is not of interest, its aerodynamics can lack detail; the lift slopes, $dC_L/d\alpha$, are taken as identical for wing and tailplane and the tailplane is unaffected by wing downwash. Also the axes of rotation and inertia and the aerodynamic axis of the tailplane are taken as coincident to avoid complications of the equations that would have little effect on the final result. Further

assumptions are that there are neither thrust nor drag forces on the aircraft and that the moment coefficient of the wing is zero. Let the speed of the aircraft be V and the radius of the pull-out be r. If the upward centrifugal acceleration of the aircraft is ng, its nose-up pitching velocity is given by

$$\omega = \frac{ng}{V} \quad . \tag{2-1}$$

Take the generalised coordinates of the displacement of the aircraft to be

- q_h - heave of the aircraft in wing chords
- q_p - pitch of the aircraft about its cg
- q_e - rotation of the tailplane about its aerodynamic axis
- q_{t_1} - torsion of the wing about its flexural axis in the mode appropriate to fixed-root divergence
- q_{t_2} - torsion of the wing about its flexural axis in the mode appropriate to free-free divergence.

Take linear displacements as positive downwards and angular displacements as positive nose up.

q_{t_1} and q_{t_2}, the wing torsion coordinates, are the only coordinates which involve the flexibility of the aircraft. The axes used are earth directed being fixed in orientation relative to the earth but moving relative to the earth with the speed of the aircraft.

2.2 Virtual work and strain energy

The upward lift on a small chordwise strip of the wing is

$$L_w = \tfrac{1}{2}\rho V^2 S a_1 \left(q_p + \sin \tfrac{1}{2}\pi\eta \cdot q_{t_1} + (1 - \cos \pi\eta) q_{t_2}\right) \delta\eta \quad , \tag{2-2}$$

where ρ is the density of the air, S is the area of the wing, a_1 is the $dC_L/d\alpha$ of the wing and η is the scaled spanwise coordinate which is zero at the root and unity at the tip of the wing. The lift due to the wing's velocity in pitch has been ignored. $\sin \tfrac{1}{2}\pi\eta$ and $1 - \cos \pi\eta$ are respectively the shape functions of the distortions at fixed-root and free-free divergence of a uniform wing.

A virtual displacement of the aerodynamic centre of the wing can be written

$$\delta z_w = c\left\{\delta q_h + \xi_A \delta q_p + \xi_a \left(\sin \tfrac{1}{2}\pi\eta \cdot \delta q_{t_1} + (1 - \cos \pi\eta)\delta q_{t_2}\right)\right\} \quad , \tag{2-3}$$

where c is the chord of the wing, $c\xi_A$ is the distance the aerodynamic centre of the wing is aft of the aircraft cg, and $c\xi_a$ is the distance the aerodynamic centre of the wing is aft of its flexural axis.

The upward lift on a small chordwise strip of the tailplane is

$$L_T = \tfrac{1}{2}\rho V^2 S_T a_1 \left(q_p + q_e + \xi_T \frac{cnq}{V^2}\right) \delta\eta_T \quad , \tag{2-4}$$

where S_T is the area of the tailplane, a_1 is $dC_L/d\alpha$, $c\xi_T$ is the distance the aerodynamic centre of the tailplane is aft of the aircraft cg, η_T is the scaled spanwise coordinate which is zero at the root and unity at the tip of the tailplane. The lift due to the taiplane's velocity in pitch has been ignored but that due to its velocity in heave is included.

A virtual displacement of the aerodynamic centre of the tailplane can be written

$$\delta z_T = c(\delta q_h + \xi_T \delta q_p) \quad . \tag{2-5}$$

The work done by gravity and centrifugal force in a virtual displacement can be written

$$F\delta q = (n + 1)cW\left\{\delta q_n + w\xi_i \left(\int_0^1 \sin \tfrac{1}{2}\pi\eta \cdot d\eta \cdot \delta q_{t_1} + \int_0^1 \left(1 - \cos \pi\eta\right)d\eta \cdot \delta q_{t_2}\right)\right\} \quad , \tag{2-6}$$

where W is the weight of the aircraft, w is the weight of the wing as a fraction of the weight of the aircraft and $c\xi_i$ is the distance aft from flexural axis to inertia axis of the wing.

The increase in the strain energy of the wing due to virtual displacements in the torsion modes is given by

$$E\delta q = \left(\frac{\pi}{2}\right)^2 GJS^{-1}c \int_0^1 \left(\cos \tfrac{1}{2}\pi\eta \,.\, q_{t_1} + 2 \sin \pi\eta \,.\, q_{t_2}\right)\left(\cos \tfrac{1}{2}\pi\eta \,.\, \delta q_{t_1} + 2 \sin \pi\eta \,.\, \delta q_{t_2}\right) d\eta \quad . \qquad \ldots\ldots (2\text{-}7)$$

For later convenience the substitution

$$-\tfrac{1}{2}\rho V_D^2 Sa_1\xi_a = \left(\frac{\pi}{2}\right)^2 GJS^{-1} \quad , \qquad (2\text{-}8)$$

is made. It will be shown later (see Eq.(2-10)) that, when ξ_a is negative, V_D is the FRDS.

2.3 Assembled equation

At equilibrium the total work done in a virtual displacement is equal to the increase in the strain energy, *ie*

$$L_w\delta z_w + L_T\delta z_T + E\delta q = F\delta q \quad . \qquad (2\text{-}9)$$

(Note that in Eqs.(2-2) and (2-3) etc the lift and linear displacement are positive in opposite directions.)

The separate equations for the work done in the virtual displacements δq_h, δq_p, δq_{t_1} and δq_{t_2}, after evaluation of the integrals, give the matrix equation

$$\tfrac{1}{2}\rho V^2 Sca_1 \left[\begin{array}{cc|cc} 1 + s & s & 1 & [2/\pi \quad 1] \\ \xi_A + s\xi_T & s\xi_T & \xi_A & \\ \hline \xi_a\begin{bmatrix}2/\pi\\1\end{bmatrix} & [1 \quad 0] & -\tfrac{1}{2}\xi_a\begin{bmatrix} \upsilon^{-2} - 1 & -\frac{16}{3\pi}(\upsilon^{-2} - 1) \\ -\frac{16}{3\pi}(\upsilon^{-2} - 1) & 4\upsilon^{-2} - 3 \end{bmatrix} & \end{array}\right] \left[\begin{array}{c} q_p \\ q_e \\ \hline q_{t_1} \\ q_{t_2} \end{array}\right] = cW \left[\begin{array}{c} n + 1 - nb \\ -nb\xi_T \\ \hline (n+1)(2/\pi)w\xi_i \\ (n+1)w\xi_i \end{array}\right] , \qquad \ldots\ldots (2\text{-}10)$$

where $s = S_T/S$,

$b = \tfrac{1}{2}\rho S_T ca_1\xi_T(g/W)$,

$\upsilon = V/V_D$.

The elements of the first row of the square matrix are the lifts on the aircraft due to pitch, tailplane rotation and the two torsion modes. Those of the second row are the moments of these lifts about the aircraft cg. The third and fourth rows give the generalised aerodynamic forces on the wing due to pitch and the torsion modes - the force due to tailplane rotation is zero in the last two rows.

The FRDS ($q_h = q_p = 0$) is the lower of the speeds at which the determinant of the bottom right 2 x 2 matrix is zero. This is $\upsilon = 1$ ($V = V_D$) and the fundamental divergence mode is that associated with q_{t_1}, *ie* $\sin \tfrac{1}{2}\pi\eta$. The higher value of υ is 3.1 which is quite a good approximation to the exact value of 3 corresponding to a mode of $\sin \tfrac{3}{2}\pi\eta$.

3 SOLUTIONS OF PULL-OUT EQUATIONS

The first particular solution of Eq.(2-10) is for the free-free divergence speed.

3.1 Free-free divergence speed

Eq.(2-10) can be written

$$Aq = \bar{\alpha} f \quad , \tag{3-1}$$

where $\bar{\alpha} = W/\frac{1}{2}\rho V^2 S a_1$.

If $q = B\bar{q}$ we can write

$$AB\bar{q} = C\bar{q} \quad \text{(say)} \quad = \bar{\alpha} f \quad , \tag{3-2}$$

and if

$$B = \left[\begin{array}{c|c} \begin{bmatrix} 1 & 0 \\ -1 & s^{-1} \end{bmatrix} & \begin{bmatrix} -1 \\ 1 \end{bmatrix}\begin{bmatrix} 2/\pi & 1 \end{bmatrix} \\ \hline [0] & I \end{array}\right] , \tag{3-3}$$

from Eqs (2-10) and (3-3)

$$C = \left[\begin{array}{c|c} \begin{bmatrix} 1 & 1 \\ \xi_A & \xi_T \end{bmatrix} & [0] \\ \hline \xi_a \begin{bmatrix} 2/\pi \\ 1 \end{bmatrix}\begin{bmatrix} 1 & 0 \end{bmatrix} & -\frac{1}{2}\xi_a \begin{bmatrix} \upsilon^{-2} - 1 + 8/\pi^2 & \frac{4}{3\pi}(4\upsilon^{-2} - 1) \\ \frac{4}{3\pi}(4\upsilon^{-2} - 1) & 4\upsilon^{-2} - 1 \end{bmatrix} \end{array}\right] . \tag{3-4}$$

It can be seen from Eq.(3-4) that the matrix C is singular when $\upsilon = 2$ because then its last column is null. Thus the free-free divergence speed is twice the FRDS. $\bar{q}_4$ is the generalised coordinate of the mode of divergence and, from Eq.(3-3), $(q_p, q_e, q_{t_1}, q_{t_2}) = (-1, 1, 0, 1)\bar{q}_4$. Thus at divergence the absolute incidence of the wing is $\cos \pi\eta$, that of the tailplane is zero and overall there is no lift on the aircraft.

There is another value of υ for which C is singular (and for which the bottom right submatrix of C is singular) which is 5.5. Not unexpectedly, this is not a good approximation to an overtone divergence speed; the mode of overtone divergence is $\cos 2\pi\eta$ and the correct speed is four times the FRDS.

3.2 Rigid aircraft

We show that Eq.(2-10) gives the usual results for a rigid aircraft by putting q_{t_1} and q_{t_2} equal to zero. This reduces the equation to

$$\begin{bmatrix} 1 + s & s \\ \xi_A + s\xi_T & s\xi_T \end{bmatrix}\begin{bmatrix} q_p \\ q_e \end{bmatrix} = \bar{\alpha}\begin{bmatrix} n + 1 - nb \\ -nb\xi_T \end{bmatrix} . \tag{3-5}$$

If we premultiply Eq.(3-5) by $\begin{bmatrix} \xi_T & -1 \\ 0 & 1 \end{bmatrix}$ and put $\xi_A/\xi_T = \bar{\xi}$ we get

$$\begin{bmatrix} 1 - \bar{\xi} & 0 \\ \bar{\xi} + s & s \end{bmatrix}\begin{bmatrix} q_p \\ q_e \end{bmatrix} = \bar{\alpha}\begin{bmatrix} n + 1 \\ -nb \end{bmatrix} , \tag{3-6}$$

from which

$$q_p = \frac{(n + 1)\bar{\alpha}}{1 - \bar{\xi}} , \tag{3-7}$$

$$sq_e = -\left[\frac{(n + 1)(\bar{\xi} + s)}{(1 - \bar{\xi}) + nb}\right]\bar{\alpha} .$$

Now $\bar{\xi} + s \left(= (\xi_A + s\xi_T)/\xi_T\right)$ is the (scaled) cg margin of the aircraft and will be positive if the aircraft is stable. $1 - \bar{\xi}$ will also surely be positive and so the

tailplane angle, relative to the fuselage, will be negative in level flight and the necessary negative angle will increase with increase of normal acceleration.

3.3 Distortions at fixed-root divergence speed

When the aircraft is flying at the FRDS Eq.(2-10) becomes

$$\left[\begin{array}{cc|c} \begin{bmatrix} 1 + s & s \\ \xi_A + s\xi_T & s\xi_T \end{bmatrix} & & \begin{bmatrix} 1 \\ \xi_A \end{bmatrix} \begin{bmatrix} 2/\pi & 1 \end{bmatrix} \\ \hline \begin{bmatrix} 2/\pi \\ 1 \end{bmatrix} \begin{bmatrix} 1 & 0 \end{bmatrix} & & \begin{bmatrix} 0 & 0 \\ 0 & -\frac{1}{2} \end{bmatrix} \end{array}\right] \begin{bmatrix} q_p \\ q_e \\ - \\ q_{t_1} \\ q_{t_2} \end{bmatrix} = \bar{\alpha} \begin{bmatrix} n + 1 - nb \\ - nb\xi_T \\ - - - - - - - - - - \\ (n + 1)(2/\pi)w(\xi_i/\xi_a) \\ (n + 1)w(\xi_i/\xi_a) \end{bmatrix} . \quad (3\text{-}8)$$

From the third row of this matrix equation we have immediately that

$$q_p = (n + 1)\bar{\alpha} w \frac{\xi_i}{\xi_a} . \quad (3\text{-}9)$$

Typical chordwise positions of the aerodynamic centre and inertia axis of the wing, aft of its leading edge, are 25% and 45% respectively. The flexural axis is likely to lie somewhere between 35% and 40% and so $-\xi_i/\xi_a$ is likely to have a value in the range 0.3 to 1.0. The wing weight, w, will be of the order 0.1 and $\bar{\xi}$, which is the ratio of the cg margin of the wing alone to that of the tail alone, will be small. Thus $w(\xi_i/\xi_a)$ will be negative and probably greater than -0.1. Hence the pitch angle will be small and negative at the FRDS and this will be so whatever the value of n. The lift on the wing will be due almost solely to the incidence in the torsional distortion mode.

From the third and fourth rows of Eq.(3-8)

$$q_{t_2} = 0 . \quad (3\text{-}10)$$

Notice that q_{t_2} would not be zero were not the spanwise distributions of lift due to pitch and weight identical, $(a_{t_1p}/a_{t_2p}) = (f_{t_1}/f_{t_2})$.

Making use of Eqs.(3-9) and (3-10) we can replace Eq.(3-8) by

$$\begin{bmatrix} 1 & 1 \\ 1 & \bar{\xi} \end{bmatrix} \begin{bmatrix} s & \\ & 2/\pi \end{bmatrix} \begin{bmatrix} q_p \\ q_e \end{bmatrix} = \bar{\alpha} \begin{bmatrix} n + 1 - nb \\ - nb \end{bmatrix} - \begin{bmatrix} 1 + s \\ \bar{\xi} + s \end{bmatrix} q_p \quad (3\text{-}11)$$

$$= (n + 1)\bar{\alpha} \left[\begin{bmatrix} 1 - \frac{nb}{n + 1} \\ - \frac{nb}{n + 1} \end{bmatrix} - \begin{bmatrix} 1 + s \\ \bar{\xi} + s \end{bmatrix} w(\xi_i/\xi_a) \right] .$$

On premultiplication by $\begin{bmatrix} -\bar{\xi} & 1 \\ 1 & -1 \end{bmatrix}$ *Eq.(3-11) becomes*

$$(1 - \bar{\xi}) \begin{bmatrix} s & \\ & 2/\pi \end{bmatrix} \begin{bmatrix} q_p \\ q_e \end{bmatrix} = (n + 1)\bar{\alpha} \begin{bmatrix} - \bar{\xi} - (1 - \bar{\xi}) \left(\frac{nb}{n + 1} + sw \frac{\xi_i}{\xi_a} \right) \\ 1 - (1 - \bar{\xi}) w \frac{\xi_i}{\xi_a} \end{bmatrix} . \quad (3\text{-}12)$$

The $w(\xi_i/\xi_a)$ term, present in the above equations, brings the effect of the weight of the wing and the position of the inertia axis into account. In the determination of the FRDS the only loading on the wing is the aerodynamic moment about the flexural axis. But in the present case the wing is also loaded by its inertia under normal acceleration and if the inertia axis is downwind of the flexural axis ($\xi_i > 0$), as is usually the case, this loading will augment the distortion due to the aerodynamic force, increasing the lift

still further. To counteract this extra lift the aircraft will fly in a pitched-down attitude at the FRDS (see Eq.(3-9), remembering $\xi_a < 0$).

If the wing is light and near to being mass-balanced about its flexural axis the effect will be small and hereinafter, in the interest of simplicity, it will be taken to be negligible so that Eq.(3-9) is replaced by

$$q_p = 0 \tag{3-13}$$

and Eq.(3-8) by

$$(1 - \bar{\xi})\begin{bmatrix} s & \\ & 2/\pi \end{bmatrix}\begin{bmatrix} q_e \\ q_{t_1} \end{bmatrix} = (n + 1)\bar{\alpha}\begin{bmatrix} -\bar{\xi} - (1 - \bar{\xi})\dfrac{nb}{n + 1} \\ 1 \end{bmatrix} . \tag{3-14}$$

3.4 Tailplane angle per 'g'

The tailplane angle per 'g' at the FRDS can be derived by the differentiation of Eq.(3-14) with respect to n and is given by

$$s(1 - \bar{\xi})\left(\frac{dq_e}{dn}\right)_D = -\bar{\alpha}\{\bar{\xi} + (1 - \bar{\xi})b\} , \tag{3-15}$$

which can be compared with the tailplane angle per 'α' for an identical but rigid aircraft derived from Eq.(3-7) as

$$s(1 - \bar{\xi})\left(\frac{dq_e}{dn}\right)_0 = -\bar{\alpha}\{s + \bar{\xi} + (1 - \bar{\xi})b\} . \tag{3-16}$$

Thus the fractional reduction in tailplane angle per 'g' in going from low speeds to the FRDS is $\left\{1 + \left(\bar{\xi} + (1 - \bar{\xi})b\right)/s\right\}$. b (Eq.(2-10)) will be small when the mass density ratio ($\rho gSc/W$) , the tail volume ($s\xi_T$) and a_1 are small. $\bar{\xi}$ will be small when the tail-off cg margin is small. Thus it is likely that the tailplane angle per 'α' is small at the FRDS. Evaluations have been made of the speed at which this derivative becomes zero for a number of recent aircraft without wing-mounted engines and it has been found that it varies between 95% and 115% of the FRDS. It therefore appears that an aircraft flying near its FRDS will be very sensitive to tailplane angle.

3.5 Torsional and flexural moments

The spanwise torsional moment distribution can be obtained both from the external loads and from the internal forces. Because the solution is not generally exact, these two distributions will not generally be identical; but if they are identical then the solution is exact for that particular case. Generally the distribution given by the external loads will be the more accurate because it depends on the integral of the shape of the total-incidence mode rather than the first derivative of the shape of the torsion mode.

The incidence of the wing at the FRDS is $(\pi/2) \sin \frac{1}{2}\pi\eta$ times what it would be were the wing rigid and the incidence constant. The local torsional moment on a rigid wing varies as $1 - \eta$ whilst that at the FRDS varies as $\cos \frac{1}{2}\pi\eta$. Thus the torsional moment on a flexible wing will be greater than that on a rigid wing over the whole span. The spanwise variations of torsional moment have been calculated for a number of airspeeds and are compared for a number of values of v^2 up to 2 in Fig 2. The exact torsional moment at the wing root is determined solely by the total wing lift and the distance between the flexural and aerodynamic axes and the factor used in normalising the moments is such that this root value is unity. The proportional increase in torsional moment over that experienced by a rigid wing is greater over the outboard part of the wing. It is 50% greater over most of the outer half at the FRDS and 100% greater over most of the outer third when the speed is 22½% higher. The differences between the moments evaluated by the two methods were never greater than a few per cent and, in particular, the moments for the FRDS are exact.

The spanwise flexural-moment distribution can only be obtained from the external loads because the wing has been taken to be rigid in bending. It is given by integrating the shearing force distributions which are identical to the torsional moment distributions. Hence the bending moment on a rigid wing varies as $\frac{1}{2}(1 - \eta)^2$ whilst that on a wing at its FRDS varies as $(2/\pi)(1 - \sin \frac{1}{2}\pi\eta)$. As was the case for the torsional moment the bending moment on a flexible wing is greater than that on a rigid wing over the whole span. The percentage increases in the local bending moment due to flexibility have been calculated for a range of speeds, with w zero, and are given for values of v^2 up to 2 in Fig 3.

Again the greater increases are over the outboard part of the wing. They are much the same as those for the torsion moment - about 50% at the FRDS and 100% at a speed 22½% above. In this case however the root moment is alsc increased by 27% and 49% respectively.

4 CONCLUDING REMARKS

The effects of wing torsional flexibility on a number of aircraft characteristics have been studied with the aim of examining the significance of the FRDS. Although a simplified model has been used, the nature of the results is such that are relevant to the practical case.

A study of the conditions in trimmed and level flight, which is a special case of the pull-out, shows that the aircraft will become unstable near the FRDS. It appears that, in practice, the instability often takes the form of an unstable short-period oscillation at a speed some way below the FRDS[2-4]. The probability that the oscillation can be stabilised by the fitting of a stability augmentation system working through the controls is thought not to be of crucial significance because flight at speeds near the FRDS will be discouraged for other reasons.

It can be shown that the tailplane angle per 'g' will be zero at a speed close to the FRDS where extra wing lift can be obtained simply by increasing the amplitude of the wing torsion mode without altering the trim of the aircraft. Also there is a speed, which is just below the FRDS, at which all the wing incidence is due to distortion of the wing, the aircraft does not pitch as a whole and so there is no common component in the wing and tailplane incidences. Above this speed the rigid-body pitch component of the incidence will be nose down. At speeds above the zero-pitch speed the direction of the lift over the inboard part of the wing is downwards and the lift over the outboard part has to be large enough to counteract this as well as to sustain the weight of the aircraft. The increases in torsional and flexural moments caused by these changes in spanwise loading distribution due to torsional distortion are probably of some practical importance. The increases in the moments over the outer portions of the wing are the greater and are of the order of 50% at the FRDS, 100% at 22½% above the FRDS and almost 200% at 40% above whilst being less than 25% at 70% of the FRDS.

From the above it appears that the problems of flight of a loaded aircraft at speeds near its FRDS are not limited to the destabilisation of the 'rigid-body' short-period oscillation which can be counteracted by feedback to control surfaces. The spanwise variation of incidence over the wing will be very different at low and high speeds. At its simplest, for a wing with no inbuilt twist, the incidence will nearly all be due to pitch alone at low speeds but near the FRDS it will nearly all be due to the mode of fixed-root divergence. This means an increase in the bending moment at the root by about a quarter of the rigid-wing value rising to a half outboard. Twist can be built into the wing but the change in twist between low and high speeds will always be present.

REFERENCES

1 G. Hancock, "Static aeroelasticity - a reappraisal", AIAA Symposium on Structural Dynamics and Aeroelasticity, Boston, Mass., 1965

2 M.H. Shirk, T.J. Hertz, T.A. Weisshaar, "Aeroelastic tailoring - Theory, practice, promise", J. Aircraft, 23, 6-18, 1985

3 G.D. Miller, J.H. Wykes, M.J. Bresnan, "Rigid body structural mode coupling on a forward swept wing aircraft", J. Aircraft, 20, 8, 696-702, 1983

4 M.G. Gilbert, D.K. Schmidt, T.A. Weisshaar, "Quadratic synthesis of integrated aeroelastic controls for aeroelastic forward swept wing aircraft", AIAA Paper 82-1544, 1982

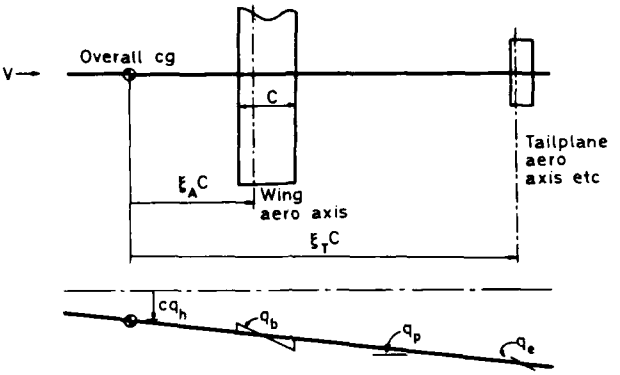

Fig 1 Geometry and generalised coordinates

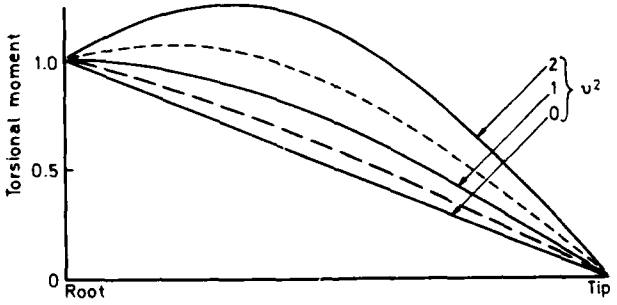

Fig 2 Spanwise variation of torsional moment

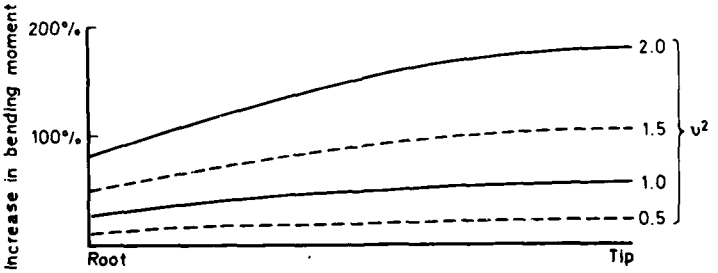

Fig 3 Spanwise variation of increase in bending moment

THE USE OF AEROELASTIC WIND TUNNEL MODELS TO PROVE STRUCTURAL DESIGN

by

H. HOENLINGER
J. SCHWEIGER

MESSERSCHMITT-BOELKOW-BLOHM GmbH.
Helicopter and Airplane Division
P.O. Box 80 11 60, 8000 Munich 80
W.-Germany

and

G. SCHEWE

Deutsche Forschungs- und Versuchsanstalt
fuer Luft- und Raumfahrt
- Institut fuer Aeroelastik -
Bunsenstr. 10, 3400 Goettingen, W.-Germany

SUMMARY

In a wind tunnel study on an aeroelastic carbon fiber fin/rudder model it is demonstrated how structural design methods can be checked by experiment, beginning already in an early stage of the design Emphasis was put on the static aeroelastic investigations, which become more important in high performance A/C design.

Transonic measurements with a rigid balance based on piezo force transducers and an opto-electronic deformation measurement method were successfully performed. It was tried to evaluate rudder efficiencies from these aeroelastic measurements. A non-linear behaviour of the rudder based on geometrical coupling with the fin box played an important roll in the test evaluation.

1. INTRODUCTION

Composite materials associated with structural optimization programs enable the designer to tailor aircraft structures according to static aeroelastic and flutter requirements in addition to the classical weight and stress constraints. An optimization with many constraints, however, makes the design process very complex. In order to avoid mistakes in this difficult design process the structural methods have to be proved successively beginning from early development stage by experiments. The classical means for this investigations are models and wind tunnel testing. But the more sophisticated design methods are applied now, the more refined models and experiments are required.

2. DESIGN PHILOSOPHY FOR AEROELASTIC MODELS

2.1 Similarity Laws

Opposite to aerodynamic wind tunnel models, which simulate only the geometry of the airplane aeroelastic models have also to represent the airplane dynamics in flight. For this the stiffness distribution of the model structure and its masses distribution must be similar to the airplane. The aerodynamic loads on the model were simulated by the flow in the wind tunnel.The only difference between the model in the wind tunnel and the flying aircraft are scale factors (Fig. 2), which have to fulfill the following similarity laws:

- Newton's similarity law for the mass forces
- Cauchy's similarity law for the stiffness forces
- Froude's similarity law for the gravity forces
- Mach's similarity law for the compressibility of the test fluid
- Reynolds' similarity law for the viscosity of the test fluid

The fact that aeroelastic models normally are tested in a wind tunnel limits the validity of the model test results. The physics of the flow in the wind tunnel are different from those of the free atmosphere were the A/C is flying. Due to limitations (power, cooling system ect.) the wind tunnel can only partially simulate the atmospheric conditions of the flight envelope of the A/C.

As far as the fulfilling of the Reynolds similarity is concerned, aeroelastic models have the same problems as aerodynamic models.

2.2 Model Layout and Scaling

The more similarity laws that have to be met by a model, the less free selectable scale factors exist. This in turn complicates the design and the manufacturing of the model. Therefore it is wise to design specialized aeroelastic models, which represent just those parameters of the A/C similar, which are of interest for the investigation. Concerning test velocity one can distinguish between low- and high speed models. For low speed models the Mach similarity can be neglected because compressibility effects are not of interest. Concerning time dimension one can distinguish between static aeroelastic models and flutter models. Static aeroelastic models are stiffness scaled models. The mass scaling can be neglected because only steady and quasisteady effects will be investigated with this type of models. This simplification, however, offers new aeroelastic testing capabilities. Because the mass scale can be neglected to same extent the model can be equipped with more transducers.This makes it possible to measure directly the elastified steady and unsteady pressure distributions. Conventional aerodynamic pressure ploting models are assumed to be rigid and the measured aerodynamics must be elastified by theory. Also efficiency tests are possible with stiffness scaled models.

The classical aeroelastic model, which is the flutter model, cannot be used for this test because too many sensor installations would cause mass problems. A model structure cannot be built as efficient as a real A/C structure and normally it is difficult to fulfill the mass similarity. Therefore the "payload" of a dynamically scaled model is often very small.

For the selection of the length scale there are no general rules, but many restrictions are given by the wind tunnel (blockage, dynamic pressure), the manufacturing,the material, and the model suspension. The scaling of aeroelastic models is an iterativ process, that needs some skill and experience.

2.3 Aeroelastic Models of Optimized Composite Structures

Concerning similarity laws there are no differences between models of conventional metallic structures and composite material structures. If a model simulates the stiffness distribution of a composite material structure, the representation of the anisotropic character of the material is already included. But this is not definite enough for the check of optimization parameters like main fiber direction and composition of the laminate. Therefore it is best in our opinion to build the models with replica laminates of the A/C structure. This, however, will not be possible for all details of the A/C structure,but having selected a reasonable length scale, there should be always a possibility to build a replica of the main carrying structure at least.

In addition this design philosophy also offers the possibility to detect fabrication problems in advance, because these models have to be built already in the predevelopment phase.

2.4 An Example for a Carbon Fiber Model Design

For a transonic aeroelastic wind tunnel study, carbon fiber models of an aeroelastically tailored fin and rudder were designed and manufactured. According to the used optimization procedure, two different skins of the fin box were fabricated. An example for the composition of the laminate and the fiber orientations, which are the output of the optimization program is given in Fig. 4. To be able to build a replica of these skins, the length scale and the design point of the model has to be selected carefully. As can be seen in Fig. 3 a, scale for the skin thickness, which is the most important scale for the replica design can be found from the similarity laws. This scale depends on length scale and pressure ratio of test fluid and atmosphere, and it gives a small possibility to adjust the model design. The skin thicknesses of the A/C and the replica model structure are mainly determined by the number of plies of the laminate if the contribution of the epoxy resin is neglected. To meet skin scale requirements for the model, the number of plies has to be reduced in a way that the percentages for the different fiber orientations of the plies within the laminate composition are similar. Due to this constraint, the exact required model skin thickness cannot always be achieved. This deviations can be adjusted by a proper selection of the pressure ratio. According to the reflections outlined above, it was possible to design and manufacture the fin/rudder model depicted in Fig. 4. Fig. 5 shows some design details.
The skins of the model were fabricated in a negative mold. The core of the model consists of expoxy-foam and represents the honeycomb of the A/C structure. To avoid expensive machining the core was thermoplasically formed by pressing the warmed foam together with the prefabricated skins in the mould. After manufacturing of the ribs and spars, also made from carbon fiber material, the model was glued together in the mould.
The metal parts of the models are the rudder and fin attachments. They are also replicas of the A/C design.

3. TEST PROCEDURES TO SUBSTANTIATE AEROELASTIC DESIGN METHODS WITH MODELS

3.1 General Aspects of Aeroelastic Model Tests

In our opinion the main purpose of aeroelastic models is to check

- mathematical models for the structural dynamics
- design tools and aeroelastic tailoring strategies
- aerodynamic theories

The use of the model test results for certification is limited because the results are strictly valid only for the design point of the model. However, having enough convidence in the calculations, checked by model results the certification procedures for the whole flight envelope can be done by calculations. This combined theoretical-experimental method was found very effective and helps to avoid mistakes.

3.2 Laboratory Testing

Before wind tunnel entry the model properties have to be checked by tests. In general, these are stiffness and ground resonance tests. Assuming that the model has a replica structure and regarding the similarity rules, the stiffness test results (influence coefficients) must be comparable to the stiffness matrix of the mathematical A/C dynamics model.This is demonstrated in Fig. 6 for an example of the fin/rudder model.
In this figure, the influence coefficients of two models, both optimized with different type of laminates for the same requirement, are compared to calculated values. It can be seen that two different optimization procedures came to the same results.

The ground resonance test has a global check function. The measured eigenfrequencies and modes as well as the generalized masses can be used to check the complete dynamics model of the A/C at v = 0 m/sec.

3.3 Wind Tunnel Testing

In the wind tunnel test the flying elastic A/C is simulated by an aeroelastic model. Consequently the test results are apt to check and to update the mathematical dynamics A/C model including aerodynamics. With stiffness scaled models static aeroelastic effects and efficiencies were tested and the results can be used to check and match the calculation. A new and very interesting application of stiffness scaled models is their use as pressure plotting models. A stiffness scaled pressure ploting model is spezialized to measure the air loads and steady and unsteady pressure distribution on the elastic A/C. This is the only possibility to check the "elastification" of the aerodynamic data set already in the predevelopment phase.

The classical dynamically scaled model is mainly used for flutter and active control investigations. Flutter tests are comparable with ground resonance tests. Both tests simulate the complete equation of the mathematical A/C model whereas the stiffness scaled model tests represent just a part of the equation. Therefore the combination of both model types gives the best information for the substantiation of aeroelastic tailoring strategies.

4 WIND TUNNEL MEASUREMENT METHODS

4.1 Aeroelastic Measurement Methods

The classical measurement methods for aeroelastic investigations are quasi- and unsteady pressure measurements vibration-, frequency- and damping measurements. But to substantiate modern structural design methods these tests are not sufficient anymore. Especially for static aeroelastic investigations the air loads and the associated deformations of the structure are of major interest.

The air loads of a stiffness scaled model, however, cannot be measured with a conventional wind tunnel balance. Those balances use strain gauges as sensors and are elastic by definition and they would change the model deformations completely.
Also photogrammetric methods to measure deformations are complicate for wind tunnel applications. This demonstrates that there is a need for new measurement methods for static aeroelastic investigations. Therefore this report will concentrate on air load measurements with a rigid balance and on a simple opto-electronic method to measure deformations.

4.2 General Remarks Concerning a "Rigid" Balance Based on Piezoelectric Force Transducers

In general, high rigidity of the balance is important in all cases when measuring steady and unsteady forces for the following reason: high rigidity leads firstly to a high natural frequency of the entire system (balance, model) and secondly to low interference between the individual force components to be measured. Because of these demands we used a balance which is based on piezoelectric multicomponent force transducers (Kistler 9067). The high stiffness of the piezoelectric force transducers is caused by the fact that the necessary measuring deflections are only a few micrometers, which is one or two orders of magnitude smaller than in the case of strain gauge systems. In addition, the rigidity of the balance is further enhanced by using multicomponent load washers. Thus the mechanical decoupling of the individual force component is superfluous. In addition, a piezoelectric balance features a broad dynamic range of about 6 orders of magnitude for dynamic measurements and nearly 4 orders of magnitude for quasisstatic measurements.

Concerning static measurements the suitability of a piezoelectric system is reduced because the exponential decay of the charge with time constants of 10^3 to 10^6s, and fault currents in the charge amplifier that cause the zero point drift. But these restrictions are only significant when measuring small forces (i.e. small charges) or when the measuring time is very long.

On the other hand it is possible to reduce the error caused by the zero shift by applying a simple correction procedure. Our experience from measurements in a high-pressure wind tunnel (Ref. 3/4), the 3 x 3 m low-speed wind tunnel, and the present measurements show that the accuracy is sufficient for a wide range of aerodynamic force measurements.

4.3 Description of the System Used for the Fin/Rudder Tests

The balance used in this test was manufactured by Kistler Instruments,it is a modified version of the "3-component dynamometer Type 9265". This force plate was orginally designed for measuring cutting forces on machine tools (turning,grinding).

Fig. 9 illustrates the main components of such a force plate. Four 3-component force transducers (B), which, have the form of washers, are prestressed by elastic bolts between two rigid steel plates. One plate, which acts as a base plate (A) is fixed to the wind tunnel wall, while the test model is attached to the second force-conducting top plate (C). Thus the shear forces on the load washers can be transmitted by friction. The assembly of the multicomponent force transducer is illustrated in Fig. 10. The four load washers deliver twelve signals, the proper combination of which allows in principle all six components of the resultant force and the moment to be determined with respect to the geometric midpoint of the four elements. For 3-component measurements of the drag, lift and pitch moments, only shear forces on the load washers are required. Since the sensitivity of all elements to the shear forces is nearly equal, related components can be wired electrically parallel and routed to a charge amplifier (Kistler 5007).

The following signals were added by parallel $X_1 + X_4 = X_{1/4}$; $X_3 + X_2 = X_{3/2}$; $Y_1 + Y_2 = Y_{1/2}$ and $Y_4 + Y_3 = Y_{4/3}$. Thus four signals are produced for a 3-component measurement. The sum of all x -components yields the total X (drag force) and the sum of all y -components the total Y (lift). The pitch moment M can be obtained by the appropriate differences $M \sim (X_{1/4} - X_{3/2}) + (Y_{1/2} - Y_{4/3})$. The four signals fed into integrating digital voltmeters were coupled via an IEC-Bus to a computer which calculates the forces and the drift correction. We used the following drift correction procedure. The readings of the voltmeter and the corresponding time were stored at every measuring point. Knowing the location of the zero point before (flow speed $u_\infty = 0$) and after the measurement, where the flow speed is zero again, we computed the correction for every point in time by linear interpolation. The assumption of a liner drift is justified because the shift of the zero point is dominated by the fault currents in the charge amplifier and not by the exponential decay of the charge.

In case that the application of force is inside and at a maximum distance of 0.1 m above the top plate the maximum load may be 15 kN while the threshold for dynamic measurements is as low as 0.01 N. The interference between both components X and Y is lower than 1% Because of the high rigidity of the quartz elements themselves, the natural frequency is mainly determined by the stiffness of the top plates of the balance.

The balance was calibrated with weights in quasistatic mode. Since balances based on the same type of piezoelectric load washers have similar properties, Refs. 3, 4 may be consult for more details. In these references, the basic aspects of the piezo measuring technique, the force transducers, calibration tests ,and further applications are described.

4.4 Deformation Measurements in the Wind Tunnel

4.4.1 Principle of the Opto-electronic Method

For deformation measurements in the laboratory the transducers are connected with or, in case of touchless sensors, very close to the test specimen. In the wind tunnel this technique cannot be used. In order not to desturb the flow, the measurement must be done either internally in the model or from outside of the wind tunnel test section. At MBB an opto-electronic method was used, which measures the model deformation from outside of the wind tunnel. This method has the advantage to be applicable also for very small and solid aerodynamic models. The principle of the measurement is depicted in Fig. 11. For the measurement an illuminated target point on the test specimen is focussed by a lens on a CCD Sensor (Charge Coupled Device). This sensor is an array of photosensitive elements (pixel) is used for digital image sensing. A computer connected to the sensor electronics dedects the pixel, on which the light, of the target is focussed. When deforming the structure of the test specimen the light of the target point is focussed on another pixel. The travel of the focussed ray is in first approximation proportional to the deflection of the test specimen. The precision of such a measurement is at the present state of our developement below 0.1 mm. This system can only measure deflections in the plane perpenticular to the specimen as can be seen in Fig. 11. The accuracy of the measurement method can be deteriorated by vibrations of the tunnel wall mounted CCD sensor and refraction effects due to density variations in the air flow. The refraction effects cannot be excluded by calibration because calibration can only be done at zero airspeed in the tunnel. But this refraction and vibration effects were found to be small. Some problems may be caused by light reflections on model and tunnel wall, which cause noise in the sensor signal.

4.4.2 Description of the Deformation Measurement System for Wind Tunnel Application

For an effective wind tunnel application of the described opto-electronic method some modifications and improvements were necessary. To be able to check structural design methods it is favourable to measure the deflections of a set of points comparable with the grid of the mathematical model. To reduce the number of CCD sensors and associated cameras and electronics special lenses were used, which were able to focus the light of 3 target points on one sensor. Thus, the deflection of 9 points could be measured with just 3 CCD sensors as depicted in Fig.12. The main problem, however, was to install tiny light points with high emitting intensity on the model without changing the stiffness characteristics of the model. High light intensity was necessary to achieve a reasonable signal to noise ratio for the CCD sensor signal. This problem was solved by installing optical fibers of 200μm diameter inside of the model. The shining end of the optical fiber penetrates the model skin at the centre of the target point to be measured. The other end of the fiber is connected to a powerful light surce as can be seen in Fig. 12. For this prototype test installation of the measurement system also computer software for data reduction was developped and applied successfully.

During wind tunnel test of this system it was found that the measurements were performed fast and the system was simple to handle, which is necessary for industrial wind tunnel testing.

5 STATIC AEROELASTIC TESTS IN THE TRANSONIC RANGE

5.1 Test Objectives

The main objectives of the wind tunnel test were to measure derivatives of an aeroelastic fin and rudder model associated with the deformations of the model structure. From this measurements the rudder efficiencies should be extracted. Flutter investigations were only done to a small extend, because flutter of this optimized fin was predicted outside of the wind tunnel performance.

5.2 Description of the Test Set Up

The sensor installations of the carbon fiber fin/rudder model is given in Fig. 13. At the tip of the fin two accelerometers were mounted for flutter monitoring. At 3 sections 3 light points for the deformation measurements were installed. Strain gauges were glued at the middle and rear fin attachment to measure the root moments.

The rudder is attached to the fin with 3 hinges. It is driven by a hydraulic actuator, which is connected to the rudder with a spring element, soft in bending and a scaled torsional stiffness. The spring element is also equipped with strain gauges to measure rudder hinge moments. To sense the "rigid" rudder angle, a position sensor was installed at the root rip close to hinge line. With the help of this sensor the actuator flexibility could be excluded.

The model was screwed on the piezo balance, which in turn was rigged as stiff as possible on the wind tunnel floor. To improve the boundary layer conditions for the model a ground board was also installed as depicted in Fig. 13.

5.3 Static Aeroelastic Test Program for the Fin/Rudder Model

Two model configurations were tested in the wind tunnel:

Configuration I:
Fin incidence $\beta = 0°$ rudder angle η variable from $\eta = +5°$ to $\eta = -5°$

Configuration II:
Fin incidence β variable from $\beta = +3°$ to $\beta = -3°$ and rudder angle $\eta = 0.°$

The tests were performed at Ma = 0.7, 0.9, 1.2 at variable dynamic pressures.

For both configurations the lift, the drag and rudder hinge moment were measured as functions of the dynamic pressure. The model deformations under steady air loads were measured for various load cases too.

5.4 Test Results and Comparison with Theory

5.4.1 Measurement of Air loads and Efficiencies

Some results of the balance measurements are depicted in Fig. 14/15. The measured lifts and hingemoments as functions of the rudder angle (fin incidence) and the dynamic pressure look reasonable. In a follow on effort the efficiencies of the fin and rudder were evaluated from the load measurements. The efficiency here is defined as the ratio of flexible to rigid derivatives. Because the rigid derivatives cannot be measured with a flexible model by definition, it was tried to find the rigid derivatives by extrapolation of the flexible values. For this the evaluated elastic derivatives were plotted vs the dynamic pressure. This curve was extrapolated to zerodynamic pressure assuming that this would be the rigid value because at very low dynamic pressure the deformation of the structure will be also very small. This extrapolation is shown in Fig. 16.

Normalizing this curves with the "rigid" values will give the efficiencies.These curves, however, are completely different from the classical efficiency curves. To clear this, the extrapolated "rigid" derivatives were compared with the calculated derivatives and it was found that the experimental values are too low. The explantion for this gave the results of the deformation measurements.

5.4.2 Deformation Measurement Results

Fig. 17 gives an example for deformation measurements for high and low airloads as well. Analyzing the rudder deformation due to the air loads it can be seen that for high airloads the rudder angle at the tip is considerably higher than at the root. That means that the mean rudder angle is higher than the commanded angle at the root. But the reference for all measurements is the commanded rudder angle. This is also the explanation for efficiencies 1.0 at high dynamic pressures. The twist of the rudder, which leads to this high efficiencies is caused by the bending of the fin box in conjunction with the actuator and hinge positions. It is a kind of geometrical coupling.

The too small values of the extrapolated "rigid" derivatives can be explained by another elastic effect. In Fig. 17 the deformation of fin and rudder at low dynamic pressure is also given. In this case the rudder behaves as generally expected and the angle at the tip is smaller than the commanded angle shown at the root. In Fig. 18 these two effects are depicted in another diagram, which compares the commanded rudder angle with the angle at the rudder tip. This picture shows a very non-linear behaviour of the rudder, which can only be found using stiffness scaled models instead of classical aerodynamic models. This example also demonstrates clearly the necessity of deformation measurements in aerodynamic and aeroelastic investigations to be able to interpret correctly balance measurements.

6. CONCLUSIONS

In a wind tunnel study on an aeroelastic carbon fiber model it was demonstrated how the structural design methods can be checked by experiment, beginning in an early stage of the design. Emphasis was put on the static aeroelastic investigations, which become more and more important in high performance A/C design.

For this measurements a rigid balance based on piezo force transducers and an opto-electronic deformation measurement method were used successfully. It was tried to evaluate rudder efficiencies and a non-linear behaviour of the rudder was found based on geometrical coupling with the fin. This should be further investigated in detail.

Acknowledgement

The authors wish to express their thanks to Prof. Grueninger, Director of the DFVLR - Institut fuer Bauweisenforschung, Dipl.-Ing. Preuss and Dipl.-Ing. Krapf for their advise and manufacturing the carbon fiber structure of the tested model.Thanks also to H.V. Heerich of Kappa Messtechnik for his support to measure deformations.

REFERENCES

/1/ HOENLINGER, H.
Studien ueber rtionelle Erstellung eines Flattermodells
MBB-Report - EWR 224-68

/2/ HOENLINGER, H. and SENSBURG, O.
Dynamic Testing in Wind Tunnels, Part I
AGARD FMP Symposium at Valloire/Modane - June 1975

/3/ SCHEWE, G.
A Multicomponent Balance Consisting of Piezoelectric Force Transducers for a High-Pressure Windtunnel.
Conf. Proc. Sensor & Systems '82, Vol. 2, Pasadena (USA), 18-20.5.82; and Tech. Messen 49, p. 447
(German Version)

/4/ SCHEWE, G.
Force Measurements in Aerodynamics Using Piezo-Electric Multicomponent Force Transducers. In: Proc. 11th ICIASF 1985 Record (Int. Cong. on Instrumentation in Aerospace Simulation Fac.) Stanford Univ., Aug. 26-28, 1985, p. 263

/5/ TICHY, J. and GAUTSCHI, G.
Piezo-Elektrische Messtechnik - Springer Publishing Co.

	AERODYNAMIC MODEL	AEROELASTIC MODEL
MODEL SIMILARITY	GEOMETRY	GEOMETRY STIFFNESS MASS MACH SIMILARITY
TEST FLUID SIMILARITY	REYNOLDS	REYNOLDS

FIG. 1 COMPARISON OF AERODYNAMIC AND AEROELASTIC MODELS

MASSSTAB SCALE	
LÄNGE LENGTH	$\frac{L_M}{L_F}$
GESCHWINDIGKEIT VELOCITY	$\frac{V_M}{V_F} = \frac{a_M}{a_F} = (\frac{T_M}{T_F})^{1/2}$
STRUKTURDICHTE STRUCTURAL DENSITY	$\frac{\rho_M}{\rho_F}$
MASSE MASS	$\frac{M_M}{M_F} = (\frac{\rho_M}{\rho_F})(\frac{L_M}{L_F})^3$
MASSENTRÄGHEITSMOMENT MASS MOMENT OF INERTIA	$\frac{\theta_M}{\theta_F} = (\frac{\rho_M}{\rho_F})(\frac{L_M}{L_F})^5$
STEIFIGKEIT STIFFNESS	$\frac{EI_M}{EI_F} = (\frac{\omega_M}{\omega_F})^2 (\frac{\rho_M}{\rho_F})(\frac{L_M}{L_F})^6$
FREQUENZ FREQUENCY	$\frac{\omega_M}{\omega_F} = (\frac{T_M}{T_F})^{1/2} (\frac{L_F}{L_M})$
LASTFAKTOR LOADFACTOR	$\frac{N_M}{N_F} = (\frac{V_M}{V_F})^2 (\frac{L_F}{L_M})$
WANDSTÄRKE SKIN THICKNESS	$\frac{tm}{t_F} = \frac{Pm\,Lm}{P_F\,L_F}$

FIG. 2 MODEL SCALES

	STIFFNESS SCALED	DYNAMICALLY SCALED
SIMILARITY	GEOMETRY STIFFNESS	GEOMETRY STIFFNESS MASSES
TASKS	PRESSURE DISTRIBUTIONS (STEADY, UNSTEADY) LOADS AND DEFORMATIONS DIVERGENCE	FLUTTER VIBRATIONS

FIG. 3 COMPARISON OF STIFFNESS AND DYNAMICALLY SCALED MODELS

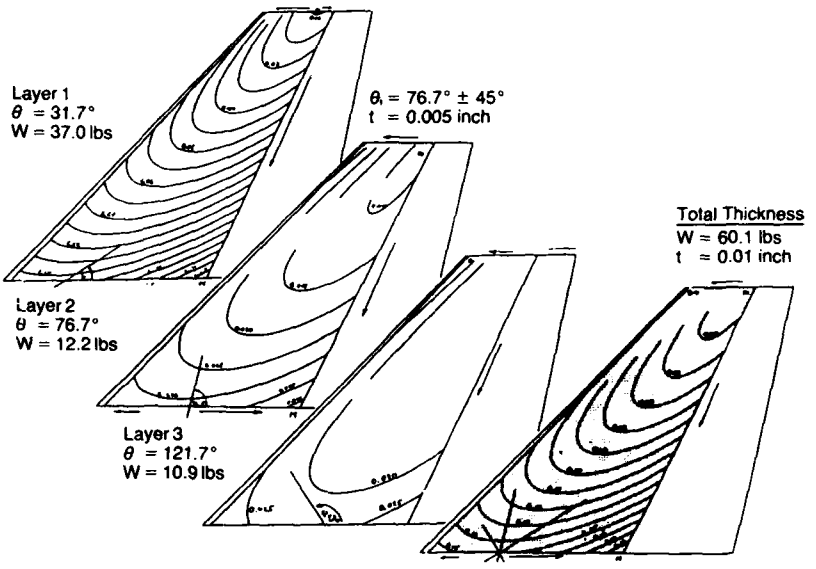

FIG. 4 EXAMPLE OF STRUCTURAL OPTIMIZATION PROGRAM OUTPUT

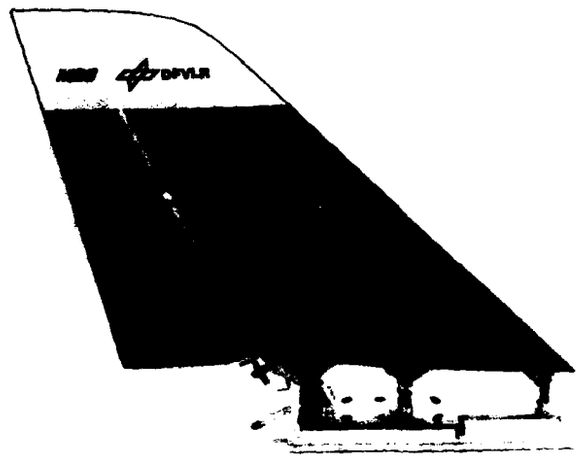

FIG. 5 CFC FIN AND RUDDER MODEL

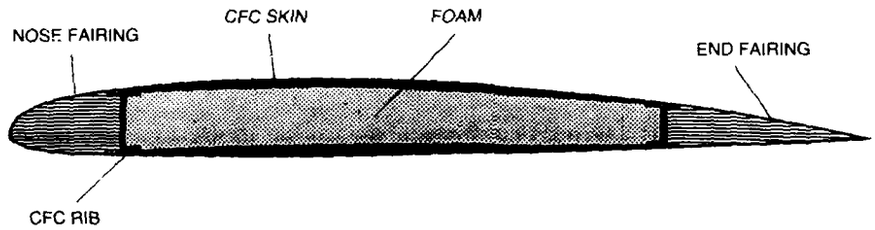

EXAMPLE FOR THE COMPOSITION OF A BALANCED LAMINATE

w = SKIN THICKNESS
t = MIN. PLY THICKNESS (0.05 mm)

FIG. 6 SCHEME OF THE COMPOSITE MODEL DESIGN

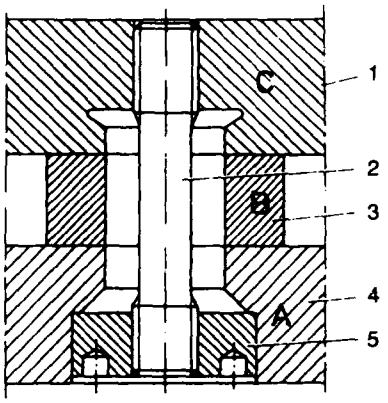

1 PLATE
2 ELASTIC BOLT FOR PRELOADING
3 PIEZO-FORCE TRANSDUCER
4 GROUND PLATE
5 RING NUT FOR PRELOADING

FIG. 9 INSTALLATION OF A 3 COMPONENT FORCE TRANSDUCER

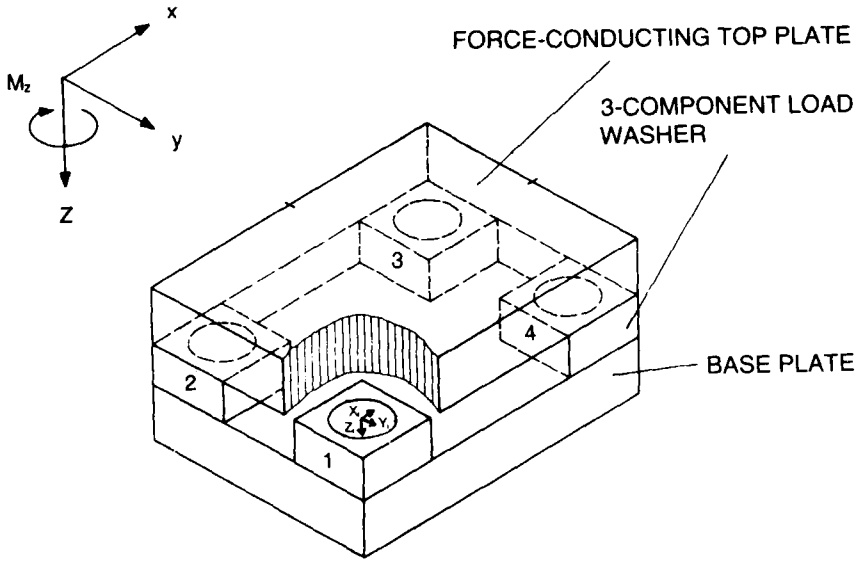

FIG. 10 SCHEME OF THE MULTICOMPONENT PIEZO-BALANCE

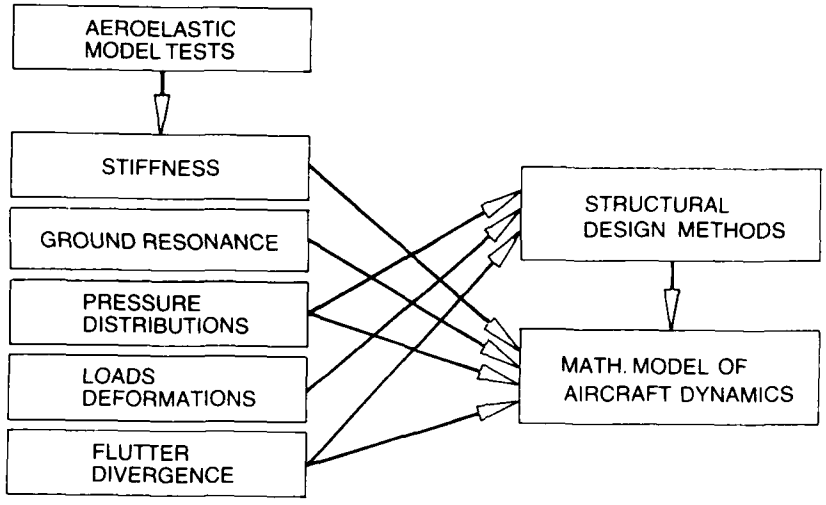

FIG. 7 CHECK FUNCTIONS OF AEROELASTIC TEST PROCEDURES

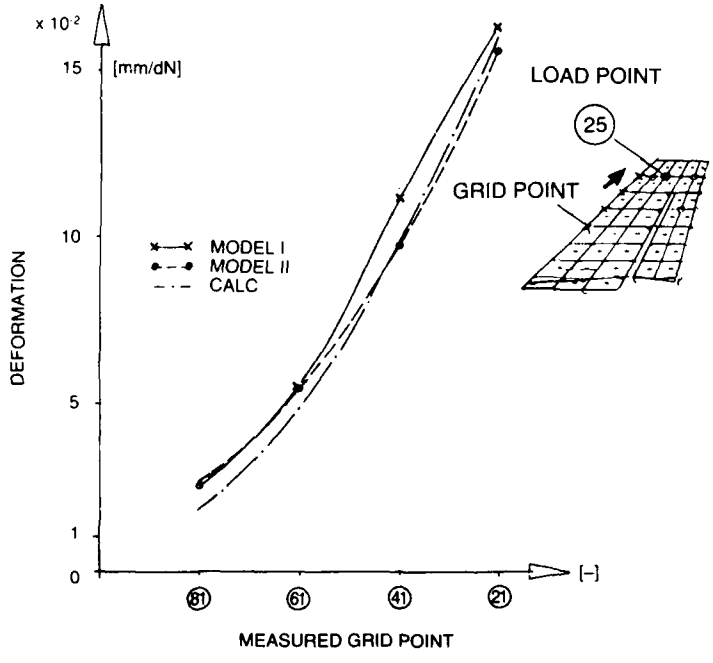

FIG. 8 STIFFNESS TEST RESULTS

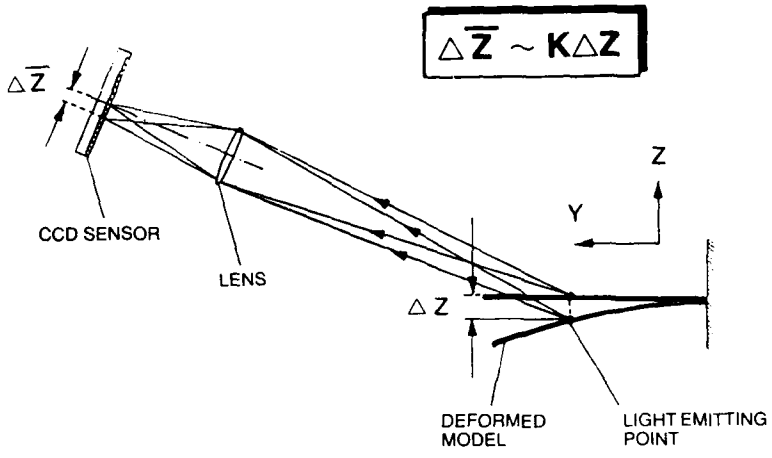

FIG. 11 PRINCIPLE OF THE OPTO-ELECTRONIC MEASUREMENT

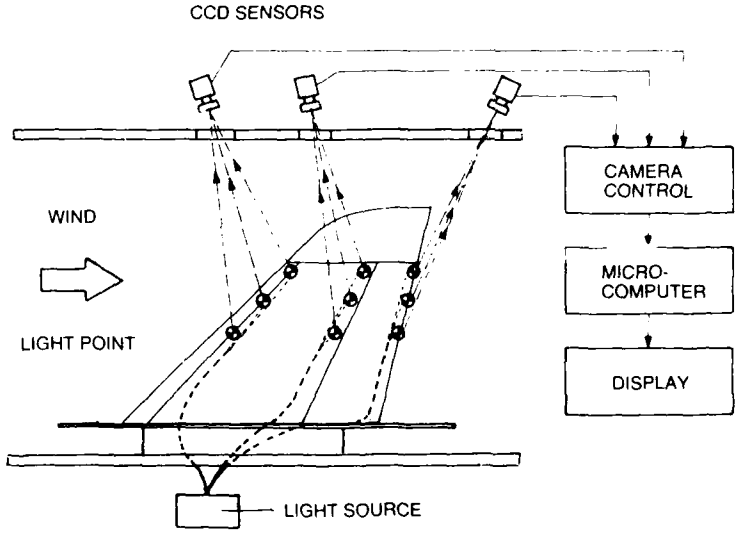

FIG. 12 WIND TUNNEL INSTALLATION OF THE DEFORMATION MEASUREMENT SYSTEM

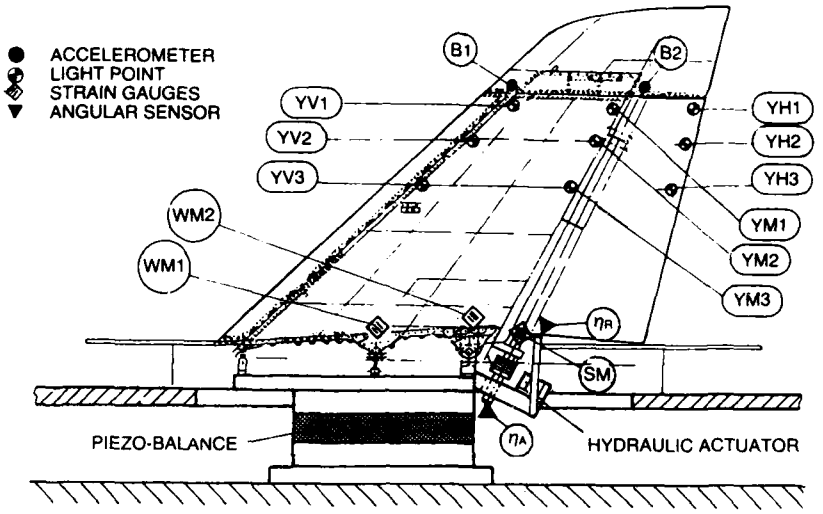

FIG. 13 WIND TUNNEL INSTALLATION OF THE MODEL AND SENSOR POSITIONS

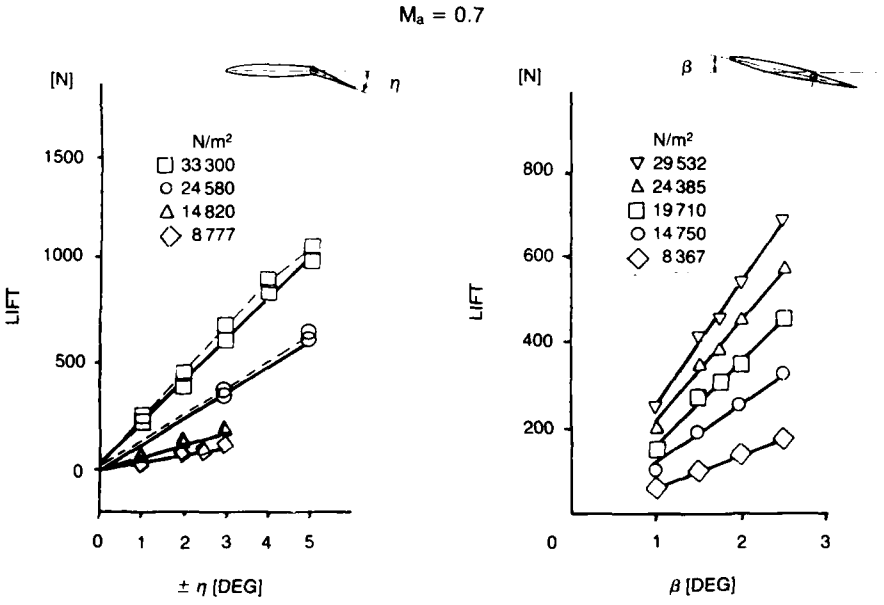

FIG. 14/15 BALANCE MEASUREMENTS WITH THE FIN RUDDER MODEL

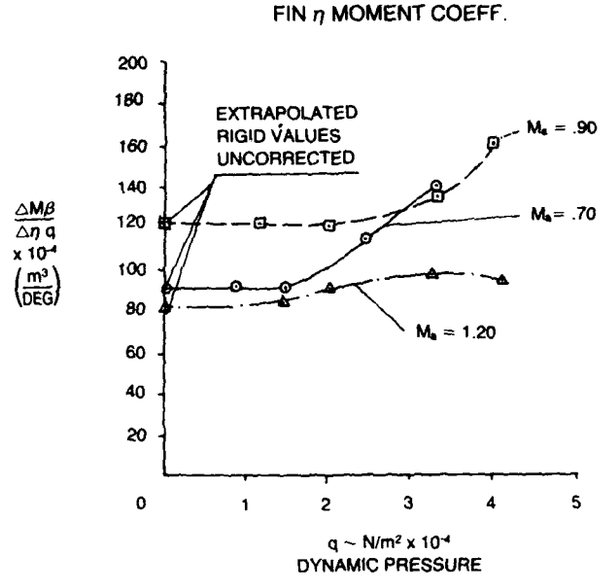

FIG. 16 EFFICIENCY MEASUREMENTS

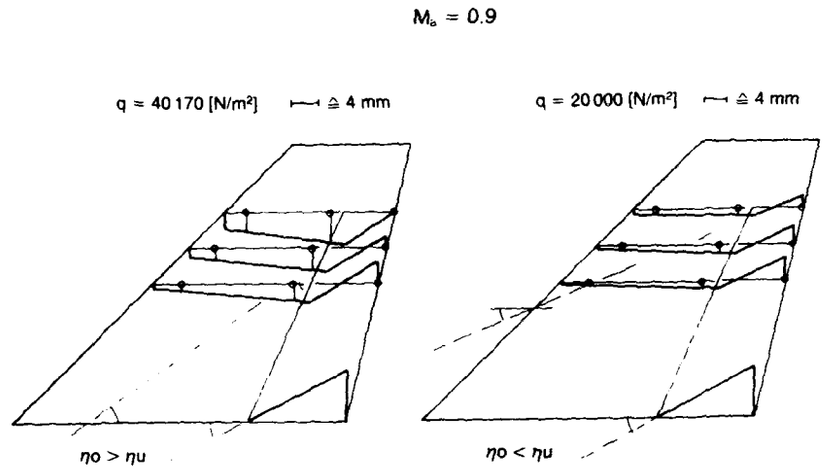

FIG. 17 MEASURED MODEL DEFORMATIONS

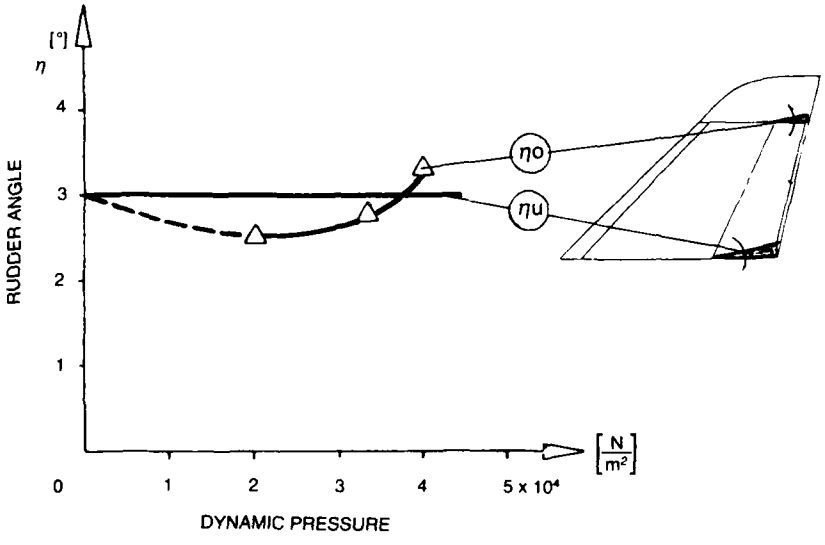

FIG. 18 RUDDER TWIST VS DYNAMIC PRESSURE

PREDICTION OF WING AEROELASTIC EFFECTS ON AIRCRAFT LIFT AND PITCHING MOMENT CHARACTERISTICS

By Clinton V. Eckstrom
Aerospace Engineer
NASA Langley Research Center
Hampton, Virginia 23665-5225

SUMMARY

The distribution of flight loads on an aircraft structure determines the lift and pitching moment characteristics of the aircraft. When the load distribution changes due to the aeroelastic response of the structure, the lift and pitching moment characteristics also change. An estimate of the effect of aeroelasticity on stability and control chacteristics is often required for the development of aircraft simulation models for evaluation of flight characterstics. This presentation outlines a procedure for incorporating calculated linear aeroelastic effects into measured nonlinear lift and pitching moment data from wind tunnel tests. Results are presented which were obtained from applying this procedure to data for an aircraft with a very flexible transport type research wing. The procedure described is generally applicable to all types of aircraft.

LIST OF SYMBOLS

Symbol:	Definition:
C_L	lift coefficient
C_{L_α}	lift coefficient curve slope, per degree
C_{L_H}	horizontal tail lift coefficient
$C_{L_{\delta_H}}$	horizontal tail lift coefficient curve slope, per degree
C_m	pitching-moment coefficient
C_{m_o}	pitching-moment coefficient at zero angle of attack
C_{m_α}	pitching-moment coefficient curve slope, per degree
$C_{m_{\delta_H}}$	horizontal tail pitching-moment coefficient curve slope, per degree
i_H	horizontal tail incidence angle, degrees
m.a.c.	mean aerodynamic chord length, m (in)
q	free stream dynamic pressure, N/m^2 (psf)
S	wing reference area, m^2 (ft^2)
X_A	distance from center of gravity to wing/fuselage aerodynamic center, units of m.a.c., positive forward
$X_H - X_{c.g.}$	distance from center of gravity to horizontal tail aerodynamic center, units of m.a.c., positive aft
α	angle of attack, degrees
α_H	angle of attack at horizontal tail, degrees
$\alpha_{L=o}$	angle of attack at zero lift, degrees
$\alpha_{\epsilon=o}$	angle of attack for zero downwash at tail, degrees
$\Delta\alpha_{L=o}$	incremental change in angle of attack at zero lift, degrees
$\Delta\alpha_{\epsilon=o}$	incremental change in angle of attack for zero downwash at tall, degrees
$\Delta C_{m_{L=o}}$	incremental change in pitching-moment at zero lift, rigid airplane
ΔX_A	incremental change in wing/fuselage aerodynamic center location, units of m.a.c., positive forward
ϵ	downwash angle at horizontal tail, degrees

Symbol:	Definition:
$\epsilon_{\alpha=0}$	downwash angle at zero angle of attack, degrees
δ_H	deflection angle of horizontal tail (elevon), degrees
θ_H	deflection angle of flexible fuselage at horizontal tail station, degress
θ_{HH}	deflection angle of flexible fuselage at horizontal tail station per unit horizontal tail load, radians/lb
$\frac{\partial \epsilon}{\partial \alpha}$	partial of downwash angle with angle of attack, deg/deg

Abbreviations/Superscripts/Subscripts:

CS	cruise shape (wing)
FS	fabrication shape (wing)
TO	tail off

INTRODUCTION

It is well known that aircraft static aeroelastic characteristics can have a significant effect on structural loadings, stability and control characterstics, control surface effectiveness and flight performance characteristics and therefore should be considered during all phases of the vehicle design process. One of the areas where static aeroelastic effects must be considered is in the development of a stability and control data base for use in aircraft simulation models. Such simulation models may be used early in the design process for structural loading evaluations, control law development and evaluation of control capability. The simulation models may also be used for hardware verification, flight plan preparation, and pilot training. Usually the wind tunnel test data on stability and control as well as performance characteristics are obtained from rigid models built to a specific design shape. For a transport type wing the design shape (planform, airfoil shapes, twist distribution, etc.) is usually selected to maximize efficiency at cruise flight conditions whereas for a fighter type aircraft the wing design may be selected for a specific maneuver condition or capability. In either case a structural deflection calculation must be made to define a fabrication shape such that the full scale wing will deform to the desired shape when subjected to the loading expected at the design condition.

For the example described herein the aircraft had a transport type wing for which the given information included (1) the wind tunnel measurements of stability and control characteristics for a rigid model with a cruise shape wing (ref. 1) and (2) the fabrication shape for the full scale wing (ref. 2). What was needed was a prediction of the performance and stability and control characteristics of the full scale aircraft with a flexible wing. The approach was to use a static aeroelastic analysis procedure (ref. 3), which has linear aerodynamic and structural equations, to calculate the aerodynamic characteristics of the aircraft with both a rigid cruise shape wing and a rigid fabrication shape wing and also to do the same calculations for the aircraft with a flexible wing starting in the fabrication shape. The next step was to determine (1) the differences in stability and control characteristics between the rigid cruise shape and the rigid fabrication shape and (2) the changes due to flexibility (aeroelastic effects, defined as a function of flight dynamic pressure). These differences were then applied to the wind tunnel measured data as increments or as ratios to give a nonlinear prediction of the stability and control characteristics for the flexible flight vehicle. The procedure for doing this was developed from and is similar to that of reference 4. The information for the example case presented herein includes the lift and pitching moment characteristics at a Mach number of 0.80, although the calculations were performed for a range of Mach numbers.

AIRCRAFT CHARACTERISTICS

The procedure described was applied to a research wing mounted on a drone vehicle (ref. 5). The size and general arrangement of the research wing and drone vehicle are shown in figure 1. The fuselage is a modified Firebee II target drone vehicle. The research wing was designed for a 2.5-g maneuver load at a gross vehicle weight of 1134 kg (2500-pounds). The wing structural strength and stiffness were determined using an integrated design procedure which included the use of active controls. Wing loading was reduced using maneuver and gust load alleviation. Wing stiffness was reduced using active flutter suppression (ref. 2). Therefore the wing is quite flexible in comparison to most transport type wings in use today. Also inertial effects are small because the wing has no engines, internal fuel, stores, or other large added masses.

A comparison of wing leading edge elevation (droop) and spanwise twist distributions for the wing in both the cruise and fabrication shape is presented in figure 2. The leading edge of the cruise shape wing is a straight line with a very slight downward slope toward the wing tip. The leading edge of the fabrication shape wing droops downward considerably from the cruise shape wing to compensate for the

upward bending that will occur due to the lifting aerodynamic loads experienced at the cruise flight conditions (M = 0.80, C_L = .53, q = 6080 Newtons per square meter (127 psf)). The wing twist distribution for the cruise shape wing (fig. 2) was selected for aerodynamic efficiency reasons relative to spanwise lift distribution and wing tip stall. The fabrication shape wing has a reduced negative twist distribution to compensate for the negative twisting which will occur as a result of bending when the wing is subjected to the aerodynamic loads associated with the cruise flight conditions.

WIND TUNNEL TEST DATA

The wind tunnel tests (ref. 1) were performed on a rigid 0.237-scale model with a cruise shape wing. Data are presented for tests performed at a Mach number of 0.80 with the model in both the tail-on and tail-off configurations. Lift and pitching moment coefficient data are shown in figure 3. The slight difference between the two sets of lift coefficient data results from the lift on the tail. Note that the lift on the tail is downward until an angle of attack of about 6-degrees has been reached. The circles and squares represent actual test data points whereas the solid and dashed lines represent equations which were fit to the test data points. The equations were used to define a set of pseudo "wind tunnel" results such that data at smaller angle of attack increments could be used in subsequent analyses.

For the pitching moment coefficient data (fig. 3) the difference between data for the tail-on and tail-off configurations is considerably greater. The difference is the lift on the tail multiplied by the moment arm length between the tail center of pressure and the vehicle center of gravity (the c.g. is defined as being at 0.25 m.a.c.). Note that the two curves cross at about 6-degrees angle of attack indicating that the lift on the tail changes from negative to positive which is in agreement with the lift coefficient data.

Two additional scale model wind tunnel test measurements are needed to determine downwash at the tail location. They are the horizontal tail lift and pitching moment coefficient curve slopes, per degree deflection. For the example case given these parameters had values of 0.0124 per degree and -0.048 per degree respectively and were assumed to be linear over the angle of attack or horizontal tail deflection angles of interest.

ANALYSIS METHOD

The tasks and procedures for obtaining the predicted lift and pitching moment characteristics for a flexible aircraft are outlined in the flow chart presented in figure 4. The wind tunnel test data for the tail-on and tail-off aircraft configurations referred to on the left side of the chart (fig. 4) have already been presented. The static aeroelastic analyses referred to on the right side of the chart were performed using the Flexible Airplane Analysis Computer Program called FLEXSTAB (ref. 3). As noted on the chart, static aeroelastic analyses are required for: (1) rigid analytical models at both the design cruise shape and the fabrication shape, and (2) a flexible analytical model (initially at the fabrication shape) subjected to various levels of flight dynamic pressure. In each case analysis results are needed for both horizontal-tail-on and horizontal-tail-off aircraft configurations. These linear analysis results are then used to define incremental changes in lift and pitching moment between the two rigid shapes and for the variations of flight dynamic pressure for the flexible model. The incremental changes defined by the linear analysis method are then used either directly, or as ratios, to modify the measured non-linear wind tunnel data using a procedure developed from and similar to that of reference 4.

A basic assumption associated with the prediction procedure is that lift curve intercept changes determined by FLEXSTAB analysis should be applied to the measured wind tunnel data as a shift in angle of attack for zero lift rather than as a change in lift at zero angle of attack. As a result the modified wind tunnel curves are translated along the angle of attack axis with no change in the prediction of maximum lift capability. A second assumption is that the change in lift curve slope for the flexible wing should be proportional to the incremental change in lift. Therefore the correction to be applied to lift curve slope is a function of both dynamic pressure and lift curve slope from the original non-linear lift curve rather than just as a function of dynamic pressure. These assumptions basically define how the prediction procedure is applied as explained in the following sections.

Analysis Results for Lift Coefficient

A comparison of the lift coefficients calculated using the FLEXSTAB analysis procedure is presented in figure 5(a) for the rigid cruise shape wing and the rigid fabrication-shape wing (tail-off aircraft configuration). FLEXSTAB results for lift are in the form of a lift coefficient for zero angle of attack and a lift curve slope from which the angle of attack for lift coefficient equals zero is determined. It is the difference in angle of attack at zero lift (C_L = 0) between calculated results for the cruise shape wing and the fabrication shape wing that is the incremental value to be used in modifying the measured wind tunnel lift coefficients to those expected for the rigid fabrication shape wing. Note that for those two rigid wing shapes there is a shift in angle of attack for zero lift but no change in lift curve slope.

The next step is to calculate the lift coefficient slope and intercept values for the flexible wing (tail-off configuration) using the FLEXSTAB analysis procedure. Lift coefficient slope and intercept values for the flexible wing are shown in figure 5(b).

The effects of flexibility were determined at the various non-zero dynamic pressure values shown. Results for the rigid fabrication shape (fig 5(a)) are presented at zero dynamic pressure for reference purposes as this is the basline condition from which flexibility effects are evaluated. The results for the flexible wing are different from those for the rigid wing shapes in that there is a change in both the slope and intercept values as flight dynamic pressure is changed. The changes in lift curve slope occur because the wing twist distribution for the flexible wing is a function of wing loading which in turn is a function of aircraft angle of attack for any given flight dynamic pressure.

A summary of the calculated incremental changes in angle of attack at zero lift is shown in figure 6. These values are needed as one set of inputs for modifying the measured wind tunnel data to account for the wing rigid shape change, cruise shape to fabrication shape, (shown in figure 6 at zero flight dynamic pressure) and for the aeroelastic effects which are a function of flight dynamic pressure. (These data were obtained from figure 5 at $C_L = 0$). Note that the incremental angle of attack changes for the wing rigid shape change and for the wing flexibility effects are opposite in sign. The fabrication shape wing has zero lift at a larger negative angle of attack than the cruise shape wing because, as shown earlier, the fabrication shape wing has less negative twist along the span than does the cruise shape wing. However as the flight dynamic pressure is increased, the aft swept flexible wing will bend upwards at the tip resulting in an effectively decreasing local angle of attack along the span.

The values of lift curve slopes from figure 5 (b) ratioed to the value of lift curve slope for the rigid case (q = o) are presented in figure 7 as a function of dynamic pressure multiplied by the lift curve slope for the analysis rigid case. The curve defined in figure 7 will be used to determine the ratio by which wind tunnel measured lift curve slopes should be modified or corrected. The abscissa for the data in figure 7 was chosen so that during the modification process, when either the flight dynamic pressure of interest is small, or the slope of the wind tunnel lift curve is small the correction factor, or flexible to rigid ratio, determined from the curve (fig. 7) will be nearer to 1.0 and the modification to the wind tunnel measured lift curve slope will be smaller. In this way the shallow slope of the lift curve (fig. 3) near maximum lift will receive only a very small correction whereas those portions of the lift curve with highest slopes will get the largest corrections.

Analysis Results for Pitching Moment Coefficient

Changing the wind tunnel measured pitching moment coefficient curve to account for wing shape changes is a two step process. The first step is to establish the incremental changes in pitching moment at zero lift as shown in figure 8 for the tail-off aircraft configuration. Pitching moment coefficients as a function of angle of attack calculated for the rigid cruise shape and rigid fabrication shape wings are shown in figure 8(a). Similar results for the flexible wing starting in the fabrication shape are shown in figure 8(b) for several values of flight dynamic pressure. Note that the value of pitching moment for zero lift determined at q = 0 (fig. 8(b)) is the same as for the rigid fabrication shape wing (fig. 8(a)).

A summary of the incremental changes in pitching moment at zero lift are presented in figure 9 as a function of flight dynamic pressure to show the relationship between the increment for changing from the rigid cruise shape wing to the rigid fabrication shape wing (at zero dynamic pressure) and the increments for the flexible wing. Note that the increment between rigid shapes is opposite in sign to the increments due to flexibility.

As previously mentioned, changing the wind tunnel measured pitching moment coefficient curve to account for wing shape changes is a two step process. The first step is to establish the incremental changes in pitching moment at zero lift as shown on figures 8 and 9. The second step is to change the slopes of the pitching moment coefficient curves because of changes in aerodynamic center positions resulting from different wing shapes. Figure 10 presents the incremental changes in aerodynamic center location as a function of flight dynamic pressure resulting from going first from the rigid cruise shape to the fabrication shape, shown at a dynamic pressure of zero, and then for increasing dynamic pressure for the flexible wing. These data were obtained directly from the static aeroelastic analysis results without additional computations. As can be seen the incremental change in aerodynamic center location, due to the wing changing from the rigid cruise shape to the rigid fabrication shape, is negligible in comparison to the changes due to flexibility as dynamic pressure is increased.

Procedure for Modifying Wing Tunnel Data

Lift coefficient is shown plotted in figure 11 versus both angle of attack and pitching moment coefficient to illustrate the first few of several steps in obtaining modified non-linear wind tunnel data. The illustration shown is for changing data from a rigid cruise shape wing to data for a rigid fabrication shape wing. The dashed lines represent wind tunnel measured data for the tail off model configuration. Data points have been selected along the dashed line in increments of 1.0 degree in angle of attack with the exception that the data point at $C_L = 0$ is an interpolated value. Each of these data points also represents a step in the modification process as defined by the i = 0 to i = 8 notation in the center of the figure. The solid lines are the resulting non-linear estimated data for the rigid fabrication shape wing. For lift coefficient versus angle of attack the new data for the rigid fabrication shape wing is simply the measured wind tunnel data (cruise shape wing) shifted over on the angle of attack axis at each data point by the incremental change of angle of attack at zero lift determined

by analysis. This means that each segment between data points on the new curve has exactly the same slope as the original wind tunnel data.

Determining the pitching moment coefficient for the rigid fabrication shape wing is a two step process. The first step is to shift the initial value for pitching moment at zero lift (at i = 0) by the incremental change in pitching moment at zero lift as determined by analysis (fig. 9). The second step is to determine the new incremental values of pitching moment as shown by the equation at the top of figure 11. The new increment in pitching moment for each step, i, along the curve is equal to the increment of the original wind tunnel data plus the product of the incremental change in aerodynamic center, ΔX_A, times the incremental change in lift coefficient for each step. As presented earlier, (fig. 10), there was only a very small change in aerodynamic center in going from the rigid cruise shape wing to the rigid fabrication shape wing, therefore each of the steps along the two pitching moment curves are nearly parallel. The data shown are for values of lift starting at zero and going positive. The same procedure, starting at zero lift and going negative, is used to determine data for the fabrication shape for negative values of lift coefficient.

Introducing flexibility affects (as a function of flight dynamic pressure) into the modification procedure makes changing the lift coefficient curve into a two step process. The first step is to introduce the appropriate incremental change in angle of attack for lift equals zero (fig. 6) similar to what was done for the illustration in figure 11. The second step is to work up the incremental steps (starting from i = 0) in figure 11 by multiplying the wind tunnel measured lift curve slope by the appropriate flexible to rigid ratio for lift curve slope (fig. 7) for each increment and building a new lift coefficient curve in this manner. The procedure for the pitching moment curve remains the same as previously described with the appropriate incremental changes in pitching moment at zero lift and aerodynamic center location coming from figures 9 and 10 respectively.

Lift and pitching moment coefficient results for the flexible airplane in the tail-off configuration are presented in figure 12. Pitching moment is again presented as a function of lift coefficient to show, for the flexible airplane, how the large changes in aerodynamic center affect the slopes of the pitching moment curves. Data for both lift coefficients and pitching moment coefficients are presented for lift coefficient values both greater and less than zero. The plots also show the wind tunnel data for reference purposes. The left side of figure 12 shows how the incremental changes in angle of attack at zero lift coefficient and the changes in lift curve slope with dynamic pressure affect lift coefficient data. The right side of the figure shows how the pitching moment coefficient changes with the rigid shape change and with increasing dynamic pressure for the flexible wing.

Tail Effects

Predictions of wing aeroelastic effects on lift and pitching moment characteristics were also made for the tail-on aircraft configuration. A description of the procedure (ref. 4) used to determine these effects is presented in the Appendix. Figure 13 presents the flow downwash angle at the horizontal tail as derived from measured wind tunnel data by a procedure also described in the Appendix. The flow downwash angle at the horizontal tail is also effected by the rigid and flexible wing shape changes. These effects, which are estimated using the linear static aeroelastic analysis, primarily result in shifting the curve of figure 13 along the horizontal axis but there are also some moderate slope changes that result from wing flexibility. The changes which occur to both the angle of attack at which the downwash angle is zero (intercept) and the rate of change of downwash angle with change in angle of attack (slope) are presented in figure 14. As can be seen from the curve for the intercept, the incremental change resulting from going from the rigid cruise shape wing to the rigid fabrication shape wing (shown at dynamic pressure of zero) is larger in the positive direction than the negative increments for the range of dynamic pressure shown. The changes in slope as a function of flight dynamic pressure are very small. Note that the symbols used on the right half of figure 14 correspond to the dynamic pressure values used on the left half of the figure.

Analysis results are presented in figure 15 for the airplane with a flexible wing but a rigid fuselage in the tail-on configuration, i.e., where the tail effects have been added as a part of the computation process. Note also that the pitching moment coefficient data are now presented as a function of angle of attack. The wind tunnel measured data for the rigid cruise shape wing are again included for reference purposes. The data for lift coefficient looks very similar to that for the tail-off configuration as the lift on the tail does not significantly change the total lift. However, the effect of the tail loading on pitching moment is very significant as was shown earlier in figure 3. Note that the reversal in the pitching moment curve between two and six degrees angle of attack smoothes out considerably at the higher dynamic pressure flight conditions.

Fuselage Flexibility Effects

Comparisons of pitching moment coefficients predicted for the airplane with a flexible wing in the tail-on configuration are presented in figure 16 for calculations which both neglected and included fuselage flexibility. Fuselage flexibility effects the angle of attack at the tail and therefore effects the contribution of the tail to the pitching moment coefficient. Although the fuselage flexibility effect is small in this case, it is still noticeable particularly for the higher angles of attack and dynamic pressures.

Inertia Effects

Because the example wing has no engines, internal fuel, stores or other large added masses the inertial relief effects were found to be negligible. Therefore the analysis for the flexible analytical model were performed at zero angle of attack for all dynamic pressures. If wing masses are large and inertial effects significant it may be necessary to perform the analysis in a piece-wise linear fashion to account for variations in g-loadings with angle of attack and dynamic pressure conditions.

CONCLUDING REMARKS

- o Wind tunnel measurements of aircraft stability and control characteristics are usually made on a rigid model with the wing shaped for the design condition.
- o If flexibility is significant the wing for a full scale aircraft will be built to a fabrication shape which accounts for the deformation expected at design flight conditions.
- o Stability and control characteristics for the full scale aircraft should match wind tunnel measured data at the design flight condition but may be significantly different at off-design flight conditions.
- o A procedure has been presented for using static aeroelastic analysis results to modify measured wind tunnel data to account for aeroelastic effects at different flight conditions.
- o Example results for lift and pitching moment characteristics for a highly flexible transport type wing were presented which show significant changes with dynamic pressure because of flexibility effects.

APPENDIX - ANALYSIS OF TAIL EFFECTS

Analysis of wing shape change and wing flexibility effects for the tail-off aircraft configuration was rather straightforward. Unfortunately, the tail-on aircraft configuration complicates matters considerably, particularily when fuselage flexibility effects on horizontal tail angle are included. The analysis of tail effects is presented in two parts. The first part is an analysis of tail effects for a rigid wing shape change, i.e., in going from the rigid cruise shape wing to the rigid fabrication shape wing (the fuselage is also considered to be rigid). The second part is an analysis of tail effects for the addition of both wing and fuselage flexibility although, as was done in the text, the flexibility effects can be treated separately.

Tail Effects for a Rigid Wing Shape Change

Downwash at Tail: In order to determine the contribution of the horizontal tail to lift and pitching moment characteristics it is necessary to calculate the flow downwash angle at the horizontal tail location. This can be done by comparing moment equations for tail-off and tail-on configurations.

$$C_{m_{TO}} = C_{m_{O_{TO}}} + C_{m_{\alpha_{TO}}} \cdot \alpha \qquad \text{TAIL-OFF} \qquad (1)$$

$$C_m = C_{m_O} + C_{m_\alpha} + C_{m_{\delta_H}} \cdot \delta_H \qquad \text{TAIL-ON} \qquad (2)$$

When the effective angle of attack at the tail (α_H) is zero then the tail load $C_{m_{\delta_H}} \cdot \delta H$ is zero and $C_{m_{T_O}} = C_m$. Setting equations (1) and (2) equal and solving for α, as a function of δ_H, at which α_H is zero,

$$\alpha = \frac{C_{m_O} - C_{m_{O_{TO}}} + C_{m_{\delta_H}} \cdot \delta_H}{C_{m_{\alpha_{TO}}} - C_{m_\alpha}} \qquad (3)$$

The horizontal tail angle of attack, α_H is

$$\alpha_H = \alpha - \varepsilon + i_H + \theta_H + \delta_H \qquad (4)$$

The tail incidence angle, i_H, for the example aircraft is zero and the body bending term, θ_H, is not applicable for the rigid case (flexibility will be added later). Equation (4) for the rigid vehicle is

$$\alpha_H = \alpha - \varepsilon + \delta_H \qquad (4a)$$

Rearranging for downwash angle, ε, when $\alpha_H = o$,

$$\varepsilon = \alpha + \delta_H \qquad (5)$$

Equation (5) is valid for all α but δ_H must correspond with zero tail load, i.e., $\alpha_H = o$.

$$\frac{\partial \varepsilon}{\partial \alpha} = 1 + \frac{\partial \delta_H}{\partial \alpha} \qquad (6)$$

Going back to equation (3) and differentiating with respect to α and solve for $\frac{\partial \delta_H}{\partial \alpha}$

results in

$$\frac{\partial \delta_H}{\partial \alpha} = \frac{C_{m_{\alpha_{TO}}} - C_{m_\alpha}}{C_{m_{\delta_H}}} \tag{7}$$

Substituting (7) into (6) to get $\frac{\partial \varepsilon}{\partial \alpha}$,

$$\frac{\partial \varepsilon}{\partial \alpha} = 1 + \frac{C_{m_{\alpha_{TO}}} - C_{m_\alpha}}{C_{m_{\delta_H}}} \tag{8}$$

Finding δ_H for $\alpha = o$ and no tail load from equation (3)

$$\delta_{H_{\alpha=o}} = \frac{C_{m_{o_{TO}}} - C_{m_o}}{C_{m_{\delta_H}}} \tag{9}$$

and substituting into (5) to get ε for $\alpha = o$.

$$\varepsilon_{\alpha=o} = \frac{C_{m_{o_{TO}}} - C_{m_o}}{C_{m_{\delta_H}}} \tag{10}$$

$$\varepsilon = \varepsilon_{\alpha=o} + \frac{\partial \varepsilon}{\partial \alpha}\,\alpha \tag{11}$$

This procedure for determining downwash angle, ε, as a function of angle of attack, α, is used for both the wind tunnel data and the FLEXSTAB analysis results. In each case it requires data for both the tail-off and tail-on aircraft configurations. A comparison should be made of the downwash determined using FLEXSTAB data with downwash determined using wind tunnel data to assure that there is a good correlation. For the fabrication shape wing the incremental change in angle of attack for zero downwash is:

$$\alpha_{\varepsilon=o} = -\frac{\varepsilon_{\alpha=o}}{\partial \varepsilon / \partial \alpha} \tag{12}$$

$$\Delta\alpha_{\varepsilon=o} = (\alpha_{\varepsilon=o})_{FS} - (\alpha_{\varepsilon=o})_{CS} \tag{13}$$

The inputs for equations (12) and (13) come from FLEXSTAB runs tail-off and tail-on for both the cruise shape and fabrication shape wings. The curve for ε versus α determined from evaluation of wind tunnel data (figure 13) is now translated along the angle of attack axis by the increment $\Delta\alpha_\varepsilon$ (figure 14) to obtain a new curve of modified wind tunnel data for the fabrication shape wing.

Horizontal Tail Loads: Wind tunnel data must be evaluated to determine the lift coefficient for the horizontal tail, C_{L_H}, as a function of angle of attack at the tail, α_H. The angle of attack at the tail is determined for the fabrication shape wing using equation (4a) and the new values of ε for the fabrication shape wing.

Lift Coefficient (Tail On): The lift coefficient for the rigid fabrication shape wing is

$$C_L = C_{L_{TO}} + C_{L_H} \tag{14}$$

Pitching Moment Coefficient (Tail On): The pitching moment coefficient for the rigid fabrication shape wing is

$$C_m = C_{m_{TO}} - C_{L_H} \cdot (X_H - X_{CG}) \tag{15}$$

Tail Effects for a Flexible Wing and Fuselage

The fabrication shape flight wing and the flight vehicle fuselage are both flexible structures and therefore subject to deformation from aerodynamic and inertial loading. The analysis procedure presented here accounts for only the deformation due to aerodynamic loading (no inertial loading).

Downwash at the Tail: The procedure for determining the effects of the flexible wing shape changes on downwash at the tail are essentially the same as for the rigid wing shape changes discussed earlier. However when the flexibility of the fuselage is included in the analysis there are additional terms to consider. Start again by comparing moment equations for tail-on and tail-off configurations.

$$C_{m_{TO}} = C_{m_{o_{TO}}} + C_{m_{\alpha_{TO}}} \cdot \alpha \tag{16}$$

$$C_m = C_{m_o} + C_{m_\alpha} \cdot \alpha + C_{m_{\delta_H}} \cdot \delta_H \tag{17}$$

When the effective angle of attack at the tail, α_H, is zero, then the tail load $C_{M_{\delta_H}} \cdot \delta_H$ is zero, $C_{m_{TO}} = C_m$ and we can equate (16) and (17) and solve for α, as a function of δ_H, at which α_H is zero.

$$\alpha = \frac{C_{m_O} - C_{m_{O_{TO}}} + C_{m_{\delta_H}} \cdot \delta_H}{C_{m_{\alpha_{TO}}} - C_{m_\alpha}} \tag{18}$$

The angle of attack at horizontal tail, α_H, is

$$\alpha_H = \alpha - \varepsilon + i_H + \theta_H + \delta_H \tag{19}$$

From equation (18) α_H is zero and for the example aircraft the all moveable horizontal tail has no incidence angle i_H. Solving for downwash angle ε,

$$\varepsilon = \alpha + \delta_H + \theta_H \tag{20}$$

where θ_H is body bending angle at horizontal tail. Body bending θ_H is a function of:

$$\theta_H = \theta_{H_{\alpha=o}} + \frac{\delta\theta_H}{\partial\alpha}\,\alpha + \frac{\partial\theta_H}{\partial\delta_H}\,\delta_H \tag{21}$$

We now need FLEXSTAB runs with the tail on at α=o and α=o to get $\theta_{H_{\alpha=o}}$ and $\frac{\partial\theta_H}{\partial\alpha}$

Body deflection, at the horizontal tail, due to incremental load due to tail deflection, δ_H, is:

$$\Delta\theta_H = C_{L_{\delta_H}} \cdot S \cdot q \cdot (\delta_H + \theta_H)\theta_{HH} \tag{22}$$

where θ_{HH} is the diagonal element of the free-free structural influence coefficient matrix for the fuselage at the horizontal tail attachment point.

Solving equation (22) for θ_H and differentiating with respect to δ_H results in

$$\frac{\partial\theta_H}{\partial\delta_H} = \frac{C_{L_{\delta_H}} \cdot S \cdot q \cdot \theta_{HH}}{1 - C_{L_{\delta_H}} \cdot S \cdot q \cdot \theta_{HH}} \tag{23}$$

Now subsituting equation (23) into equation (21) and equation (21) into equation (20) results in an equation for downwash at the tail, ε, where the values for the parameters are obtained from FLEXSTAB runs.

$$\varepsilon = \theta_{H_{\alpha=o}} + \left(1 + \frac{\partial\theta_H}{\partial\alpha}\right)\alpha + \left[\frac{1}{1 - C_{L_{\delta_H}} \cdot S \cdot q \cdot \theta_{HH}}\right]\delta_H \tag{24}$$

Equation (24) is valid for all α but δ_H must correspond with zero tail load.

$$\frac{\partial\varepsilon}{\partial\alpha} = 1 + \frac{\partial\theta_H}{\partial\alpha} + \left[\frac{1}{1 - C_{L_{\delta_H}} \cdot S \cdot q \cdot \theta_{HH}}\right]\frac{\partial\delta_H}{\partial\alpha} \tag{25}$$

Going back to equation (18) and differentiating with respect to α and solving for $\frac{\partial\delta_H}{\partial\alpha}$ results in

$$\frac{\partial\delta_H}{\partial\alpha} = \frac{C_{m_{\alpha_{TO}}} - C_{m_\alpha}}{C_{m_{\delta_H}}} \tag{26}$$

Substitiuting (26) into (25) results in

$$\frac{\partial\varepsilon}{\partial\alpha} = 1 + \frac{\partial\theta_H}{\partial\alpha} + \frac{C_{m_{\alpha_{TO}}} - C_{m_\alpha}}{C_{m_{\delta_H}}\left(1 - C_{L_{\delta_H}} \cdot S \cdot q \cdot \theta_{HH}\right)} \tag{27}$$

Now finding δ_H for α = o and no tail load from equation (18)

$$\delta_{H_{\alpha=o}} = \frac{C_{m_{O_{TO}}} - C_{m_O}}{C_{m_{\delta_H}}} \tag{28}$$

and substituting into (24) to get ε for α = o

$$\varepsilon_{a=o} = \theta_{H_{\alpha=o}} + \frac{C_{m_{O_{TO}}} - C_{m_O}}{C_{m_{\delta_H}}\left(1 - C_{L_{\delta_H}} \cdot S \cdot q \cdot \theta_{HH}\right)} \tag{29}$$

Equations (27) and (29) describe the downwash ε as a function of α

$$\varepsilon = \varepsilon_{\alpha=o} + \frac{\partial\varepsilon}{\partial\alpha} \cdot \alpha$$

Horizontal Tail Loads: For the flexible vehicle configuration the angle of attack at the horizontal tail includes the effect of fuselage bending.

$$\alpha_H = \alpha - \varepsilon + i_H + \theta_H + \delta_H \tag{30}$$

where $\theta_H = \theta_{H_O} + \frac{\partial \theta_H}{\partial \alpha} \cdot \alpha + \theta_{HH} \cdot C_{L_{\alpha_H}} \cdot \alpha_H \cdot q \cdot S$ (31)

The assumption is made that θ_{H_O} and $\frac{\partial \theta_H}{\partial \alpha}$ are for the tail-off configuration and that all body bending due to tail loads is contained in the last term. Rearranging equations (30) and (31) and solving for α_H yields

$$\alpha_H = \frac{\alpha \left(1 + \frac{\partial \theta_H}{\partial \alpha}\right) - \varepsilon + i_{H_O} + \theta + \delta_H}{\left(1 - \theta_{HH} \cdot C_{L_{\alpha_H}} \cdot q \cdot S\right)} \tag{32}$$

For the example aircraft $i_H = o$ and for these cases the elevon deflection δ_H is also set to zero. Therefore

$$\alpha_H = \frac{\alpha \left(1 + \frac{\partial \theta_H}{\partial \alpha}\right) - \varepsilon + \theta_{H_O}}{\left(1 - \theta_{HH} \cdot C_{L_{\alpha_H}} \cdot q \cdot S\right)} \tag{33}$$

Lift Coefficient (Tail On): The lift coefficient for the flexible wing and vehicle is

$$C_L = C_{L_{TO}} + C_{L_{\alpha_H}} \cdot \alpha_H \tag{34}$$

Pitching Moment Coefficient (Tail On): The pitching moment coefficient for the flexible wing and vehicle is

$$C_m = C_{m_{TO}} - C_{L_{\alpha_H}} \cdot \alpha_H \cdot (X_H - X_{c.g.}) \tag{35}$$

REFERENCES

1. Byrdsong, Thomas A.; and Brooks, Cuyler W., Jr.: Wind-Tunnel Investigation of Longitudinal and Lateral-Directional Stability and Control Characteristics of a 0.237-Scale Model of a Remotely Piloted Research Vehicle With a Thick High-Aspect-Ratio Supercritical Wing, NASA TM-81790, July 1980.

2. Staff of Boeing Wichita Company: Integrated Design of a High Aspect Ratio Research Wing With an Active Control System for Flight Tests on a BQM-34F Drone Vehicle, NASA CR-166108, June 1979.

3. Hink, G. R.: Snow, R. N.; Bhatia, K. G.; Maier, R. E.; Bills, G. R.; Henderson, D. M.; Bailey, D. C.; Dornfield, G. M.; and Dauria, P. V.: A Method For Predicting the Stability and Control Characteristics of an Elastic Airplane. Volume II FLEXSTAB 1.02.00 Users Manual, NASA Contract NAS2-5006, NASA CR-114713, Oct. 1974.

4. Letsinger, G. R.; and Lewis, G. E.: AFTI-F-111 Stability and Control Report, Revision D, The Boeing Company, Document No. D365-10041-1, August 1983.

5. Murrow, H. N.; and Eckstrom, C. V.: Drones for Aerodynamic and Structural Testing (DAST) - A Status Report, Journal of Aircraft, Volume 16, Number 8, August 1979.

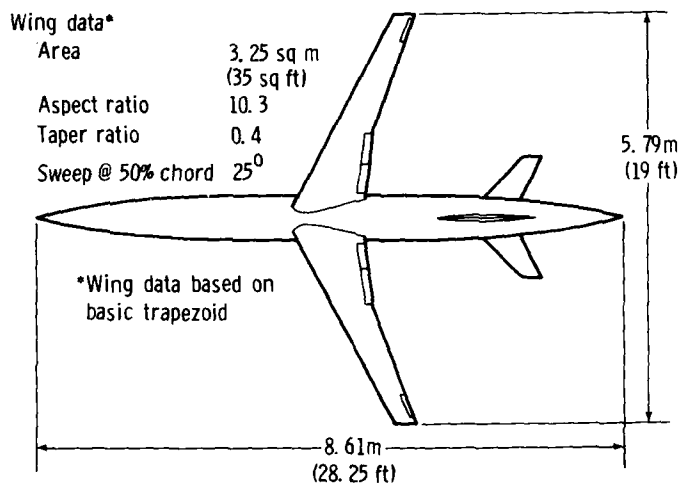

Figure 1.-Aircraft used as example problem.

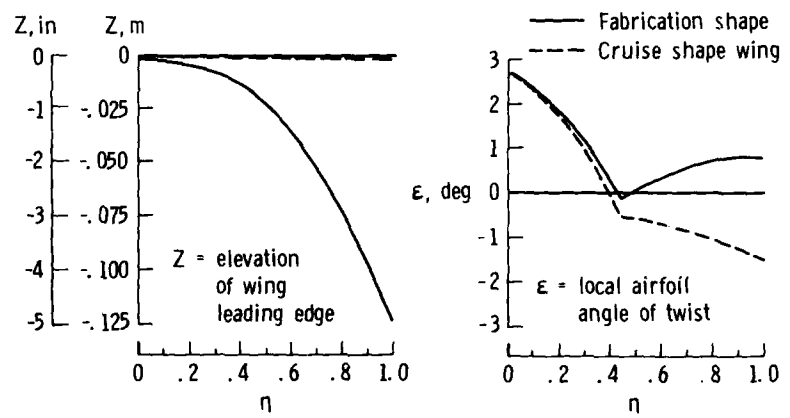

Figure 2.-Comparisons of wing droop and twist distributions for cruise and fabrication shape wings.

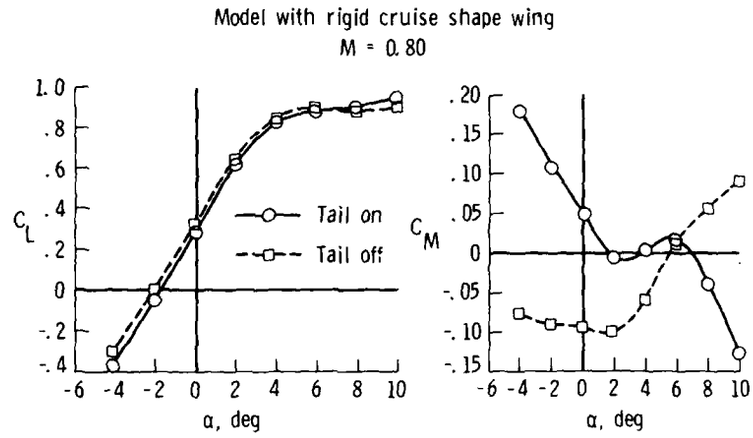

Figure 3.-Lift and pitching moment coefficient data from wind tunnel test.

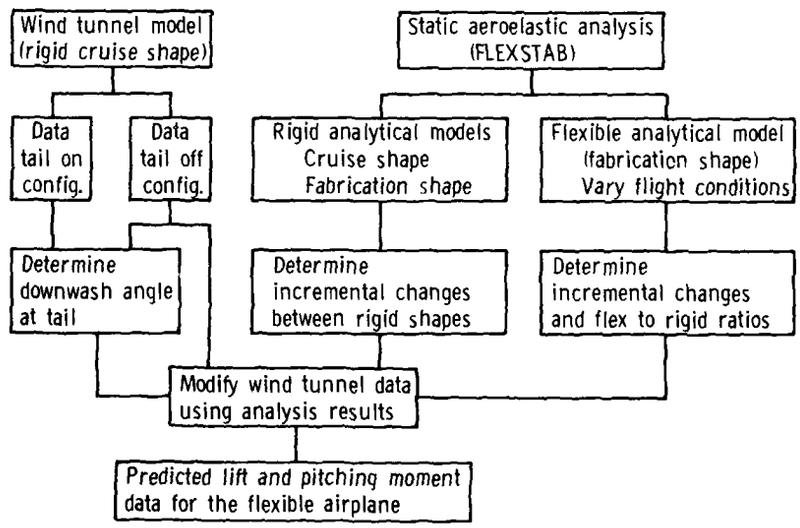

Figure 4.-Flow chart showing analysis procedure.

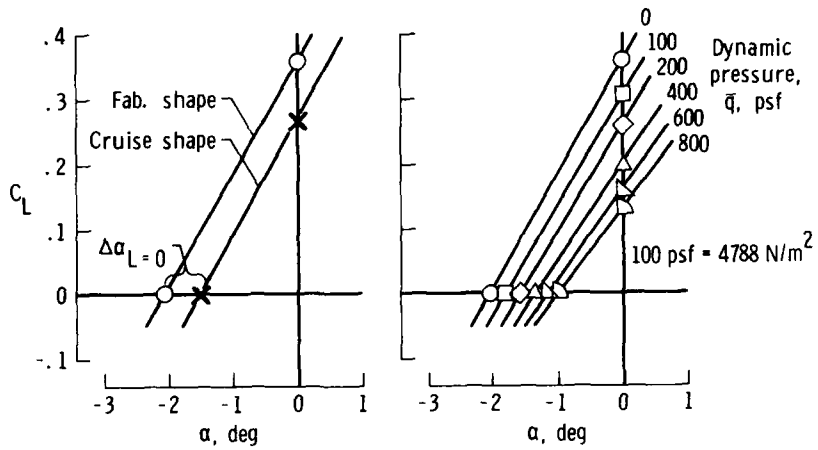

a) Rigid shape change effect. b) Flexibility effects.

Figure 5.-Static aeroelastic analysis of lift characteristics.

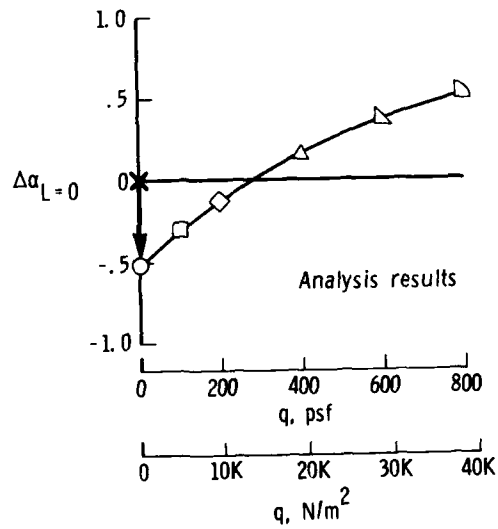

Figure 6.-Incremental changes in angle of attack at zero lift.

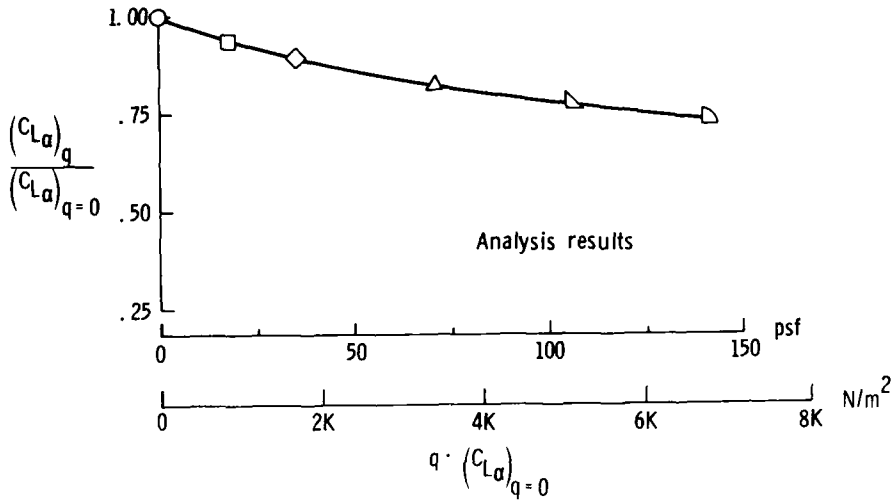

Figure 7.-Ratio of flexible to rigid lift curve slopes.

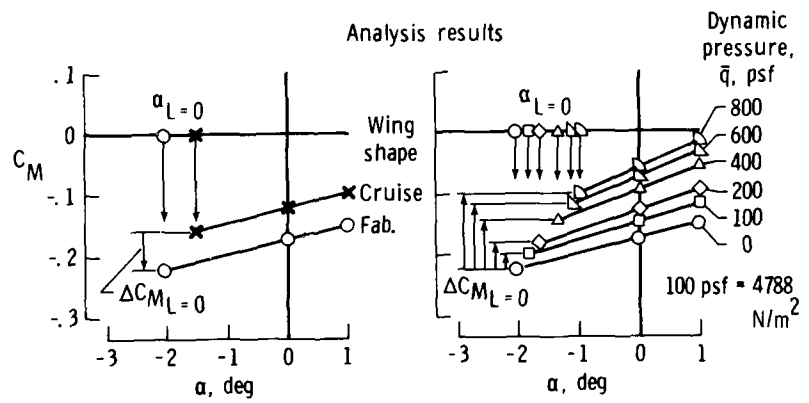

a) Rigid shape change effect. b) Flexibility effects.

Figure 8.-Change in pitching moment cofficient at zero lift.

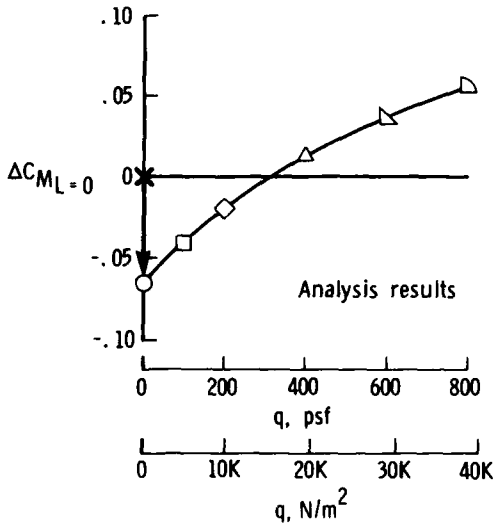

Figure 9.-Incremental changes in pitching moment coefficient at zero lift.

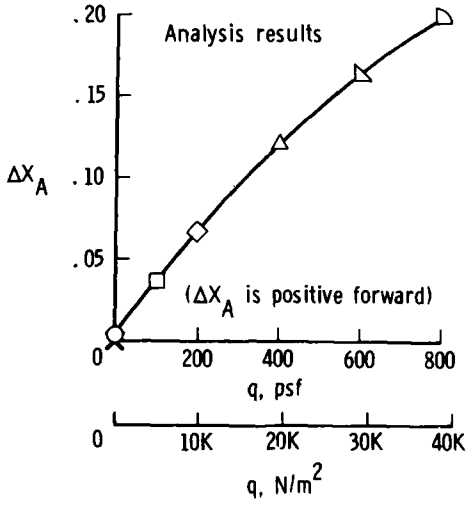

Figure 10.-Incremental changes in aerodynamic center location.

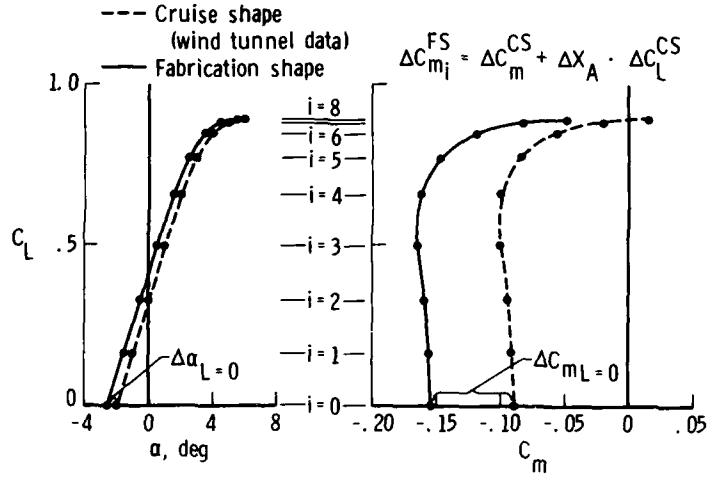

Figure 11.-Procedure for using analysis results to modify wind tunnel data.

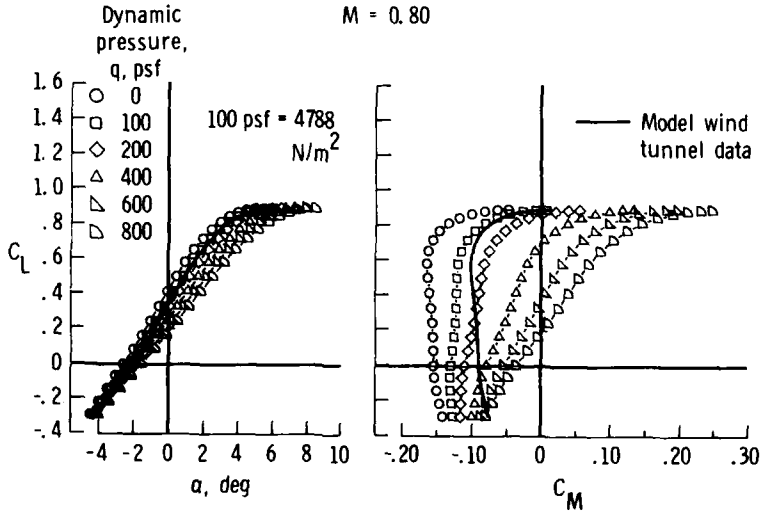

Figure 12.-Analysis results for the flexible airplane - tail off.

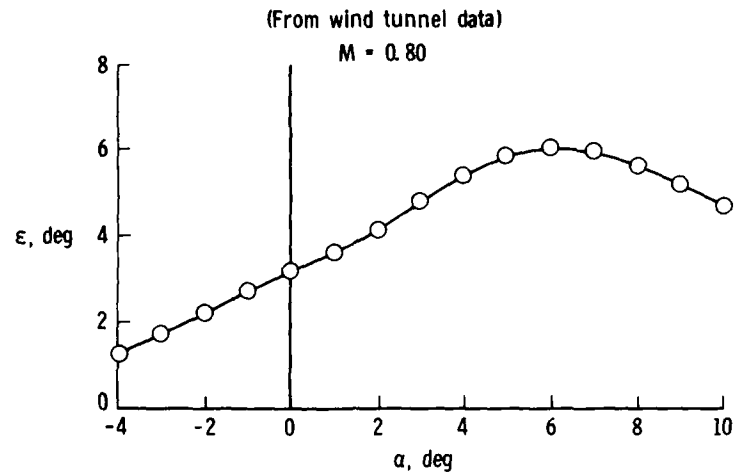

Figure 13.-Downwash at the horizontal tail.

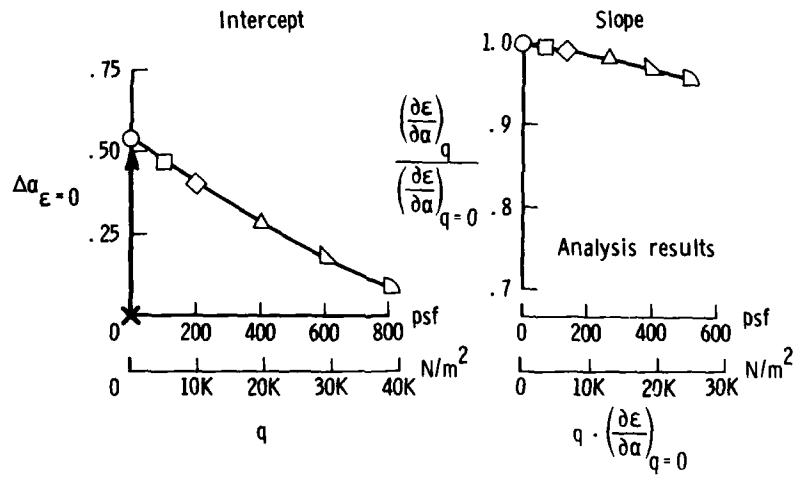

Figure 14.-Changes in downwash at the tail.

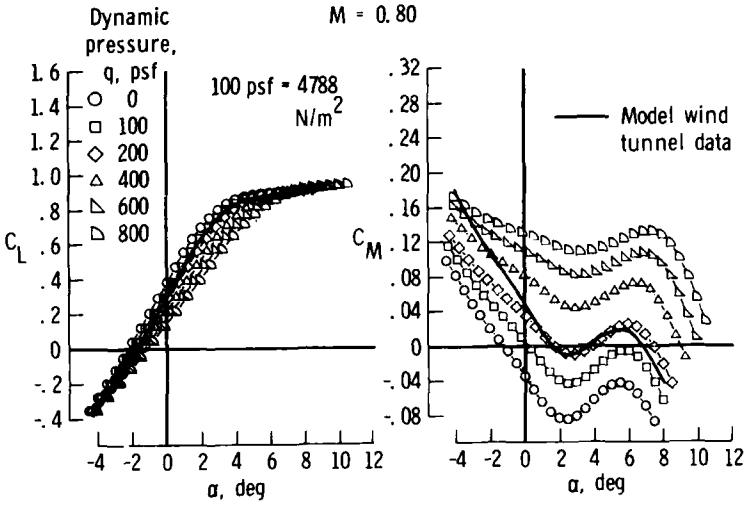

Figure 15.-Flexibility effects for example aircraft.

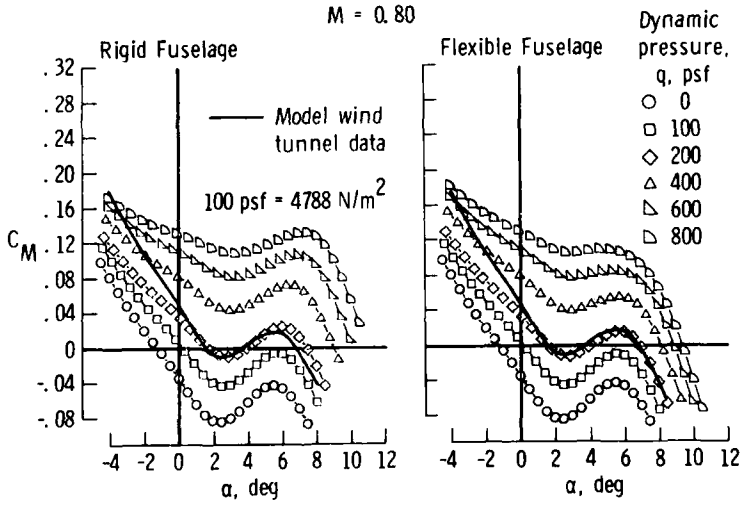

Figure 16.-Effect of fuselage flexibility on pitching moment coefficient.

INFLUENCE DES DEFORMATIONS STATIQUES D'UNE VOILURE SUR L'AERODYNAMIQUE INSTATIONNAIRE

par Roger Destuynder
Office National d'Etudes et de Recherches Aérospatiales (ONERA)
92322 CHATILLON CEDEX - FRANCE

RESUME -

Les avions de transport modernes de grand allongement, type B767 ou AIRBUS, présentent, même pour un facteur de charge n = 1, des déformations statiques importantes caractérisées essentiellement par une torsion induite due à l'angle de flèche de la voilure.

Ces déformations importantes en bout d'aile modifient de façon notable l'écoulement autour de profils du type supercritique, sensible à l'incidence locale en particulier en ce qui concerne l'apparition de chocs à l'extrados.

L'influence de ces déformations sur le phénomène du flottement a été mise en évidence par des essais.

Une série de calculs utilisant des corrections semi-empiriques, extraites d'essais en soufflerie, a été entreprise pour réduire les écarts existant dans le domaine du flottement entre théorie et expérience.

INFLUENCE OF STATIC DEFORMATION ON A WING IN THE UNSTEADY AERODYNAMIC

ABSTRACT -

The modern civil transport airplanes, with large aspect ratio, like B767 or AIRBUS, show even in cruise condition, important static deformations characterized essentially by an induced torsion due to the wing sweep angle.

This deformation principaly important at the wing tip modify the flow around a supercritical profil, very sensitiv to the local incidence.

The déformation influence on the flutter phenomenon was proved by wind tunnel tests on a elastic model.

A series of flutter calculations using semi empirical corrections, extract from wind tunnel tests, was undertaken to reduce the existing difference between theory and expérience.

I - INTRODUCTION

Les avions de transport modernes de grand allongement (type Airbus ou B767) présentent sous facteur de charge n = 1, en croisière, des déformations statiques importantes en flexion et surtout en torsion induite par suite de la flèche de la voilure. Ces déformations, principalement en bout d'aile modifient de façon non négligeable l'écoulement autour d'un profil de type supercritique, très sensible à l'incidence locale, particulièrement en ce qui concerne l'apparition des chocs.

D'autre part si on considère les phénomènes de flottement, le calcul des forces aérodynamiques instationnaires généralisées, portant sur les modes propres de la structure, montre une grande sensibilité de ces forces aux déformations statiques du bout d'aile qui représentent une contribution importante dans les forces globales.

Ce rapport s'attachera principalement à considérer l'influence des déformations statiques dues aux charges aérodynamiques, sur les problèmes de flottement. Le problème des non linéarités des forces instationnaires sur un réacteur en fonction de l'incidence sera évoqué.

II - POSE DU PROBLEME

On a tout d'abord mis en évidence par le calcul et pour des essais en soufflerie l'importance des déformation aéroélastiques d'une voilure de grand allongement correspondant à l'aile supercritique d'un avion de transport moderne.

Par une méthode classique de Rayleigh-Ritz on a calculé, connaissant l'élasticité de la structure dans sa base modale, les déformées statiques correspondantes à différentes charges réparties. Les calculs ont été faits à Mach et incidence de référence constants (Mach = 0,78) (α = + 1,5° et α = - 1,5°).

On a déterminé le vrillage de l'aile correspondant à différentes altitudes de vol c'est-à-dire à $q = \frac{1}{2}\rho v^2$ variable. On a obtenu les courbes des figures 1 et 2.

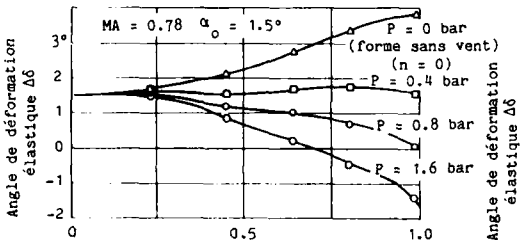

Fig. 1. Angle de déformation élastique dans le sens du courant d'air en fonction de l'envergure.

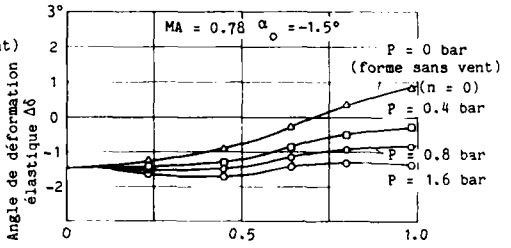

Fig. 2. Angle de déformation élastique dans le sens du courant d'air en fonction de l'envergure.

Les déformées sont calculées à partir de la forme batie (Jig Shape) sans charge. La courbe $\rho = 0$ bar de la figure 1 donne le vrillage de l'aile résultant de l'application des forces de gravité. Les forces sont positives. De l'extrados vers l'intrados, le bord de fuite descend tandis que le bord d'attaque se relève. L'angle de vrillage est positif. La variation de vrillage $\Delta\delta$ fonction de l'envergure η, due aux forces de gravité, est évidemment indépendante du calage initial α_o de l'aile (ici + 1,5 et - 1,5°).

Les forces de portance correspondant à un C_z et Mach donnés ont ensuite été ajoutées sur l'aile en fonction du paramètre $q = \frac{1}{2}\rho v^2$. Ces forces exercent des composantes allant de l'intrados vers l'extrados. Le bord de fuite de l'aile monte tandis que le bord d'attaque descend.

Les courbes de déformations ont été calculées à partir de deux calages initiaux correspondant à deux valeurs de C_z. A partir de ces incidences locales calculées par une méthode itérative très rapidement convergente, on a vérifié sur une maquette de similitude dynamique utilisée en soufflerie que les déformations prévues étaient correctes (figures 3 et 4). La figure 3 donne le déplacement du bord de fuite calculé et mesuré dans les mêmes conditions de chargement. La figure 4 donne l'angle d'incidence locale dû aux charges. La comparaison est correcte.

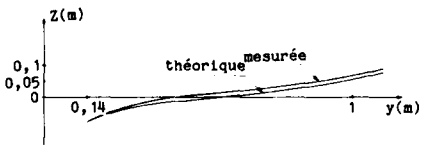

Fig. 3. Evolution de la cote du bord de fuite en fonction de l'envergure, théorique et mesurée. (en croisière)

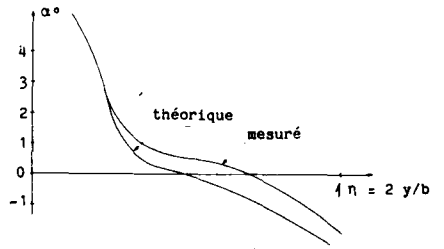

Fig. 4. Evolution de l'angle de vrillage en fonction de l'envergure, théorique et mesurée. (en croisière)

III - CALCUL DES COEFFICIENTS C_z et C_m

La seconde partie du problème a consisté à mesurer les coefficients de portance et de moment instationnaires pour les différentes incidences locales à partir de résultats d'essais quasi-stationnaires et instationnaires effectués en soufflerie sur une maquette dite rigide et ayant une déformée analogue à celle d'une aile d'un avion volant en conditions de croisière à M = 0,78 et Z = 30000 pieds.

Les hypothèses étaient les suivantes :

- Il y a proportionnalité entre les efforts locaux et la déformation résultante.

- L'hypothèse des tranches sans interaction entre elles est prise comme première approximation.

L'intérêt de cette méthode (analogue quant à son principe à celle proposée par Carsen Yates [1 - 2] est de tenir compte des effets de couche limite très importants dans ce type de profil très chargé à l'arrière où la couche limite à une épaisseur maximum.

Les courbes stationnaires de coefficient de portance et de moment, C_z et C_m, en fonction de l'envergure peuvent alors être tracées figures 5 et 6. On constate que le coefficient de portance dépend fortement de la déformée locale due à la charge statique répartie. La faible évolution du coefficient local C_m avec la charge est surprenante.

Le coefficient de portance local et le centre de poussée par tranche ont fait l'objet de comparaison entre calcul et essai sur un modèle rigide pour deux incidences nominales $\alpha = 0$ et $\alpha = +1°$, Fig. 5bis et 6bis. Enfin la courbe 7 donne le coefficient $\partial C_z/\partial\alpha$ de portance instationnaire pour 2 sections à 50 et 75 % de l'envergure en fonction de l'incidence de référence. La variation est très sensible pour des incidences positives de l'aile c'est-à-dire lorsque le vrillage initial décroît en fonction des charges croissantes.

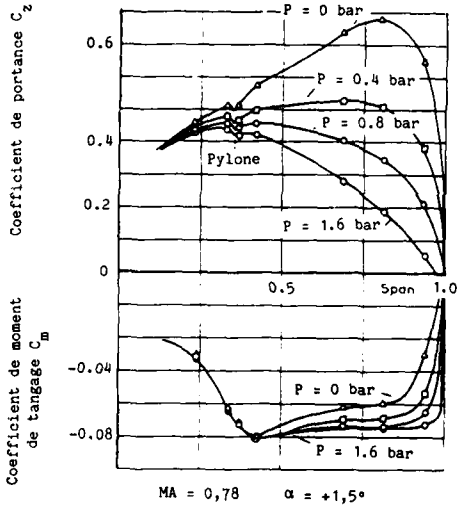

Fig. 5. Coefficient de portance et de moment de tangage en fonction de l'envergure.

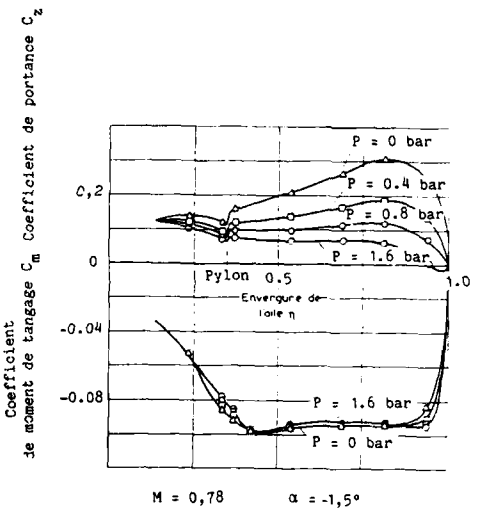

Fig. 6. Coefficient de portance et de moment de tangage en fonction de l'envergure.

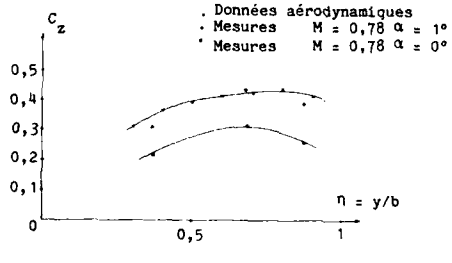

Fig. 5 bis. Distribution de portance en envergure. Calcul - essais.

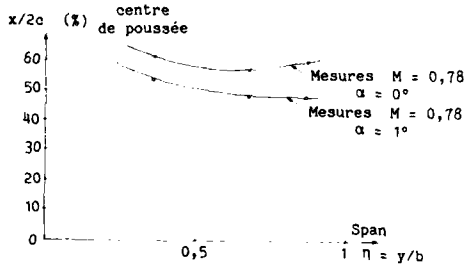

Fig. 6 bis. Position du centre de poussée fonction de η.

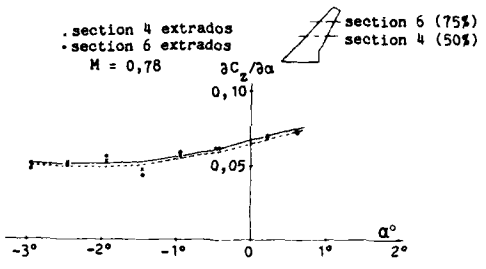

Fig. 7. Evolution de $\partial c_z/\partial \alpha$ locale à incidence nominale variable.

IV - ESSAIS DE FLOTTEMENT

Pour illustrer cette influence une demi maquette de flottement montée à la paroi a été réalisée. La voilure est du type supercritique, l'allongement est de l'ordre de $\lambda = 9{,}2$. Cette maquette est équipée d'un réacteur perméable (figures 8 et 9). Les modes propres de la maquette ont été modifiés par rapport à l'avion de façon à obtenir, par variation d'inertie, un flottement dans le domaine utilisable de la soufflerie. Les essais ont porté en soufflerie essentiellement sur les Mach M=0,60 en bas subsonique sans choc et sur le Mach de croisière M=0,78 à différentes incidences normales. A chaque nombre de Mach et incidence α, le flottement était recherché par variation de la pression génératrice de la soufflerie.

Le modèle était construit comme une maquette de similitude, ayant une déformée statique équivalente à celle de l'avion en croisière pour des charges analogues, c'est à dire que les flèches de la maquette et de l'avion étaient dans le rapport des échelles λ ce qui s'écrit :

$$\frac{\delta_m}{\delta_a} = \lambda = \frac{(M_m g + q_m S_m V_m^2 C_{z_m}) L_m^3 \times EI_a}{(M_a g + q_a S_a V_a^2 C_{z_a}) L_a^3 \times EI_m}$$

Ce qui implique la relation : $$\frac{EI_m}{EI_a} = \lambda^4 \frac{q_m}{q_a} \quad (1)$$

avec $\lambda = \frac{L_m}{L_a}$ (2) indice m = maquette
indice a = avion

avec l'hypothèse que les forces de pesanteur restent faibles devant les forces de portance, ce qui a été vérifié sur cette aile.
L'avion était supposé voler à M = 0,78 et Z = 36000 pieds avec un C_x donné et une incidence α_o correspondante à celle du vol. La maquette tenant compte de (1) avait les mêmes C_z et C_m que l'avion ainsi que les mêmes déformées statiques quelque soit α.

Fig. 8. Maquette montée à la paroi de la soufflerie ONERA S2Ma.

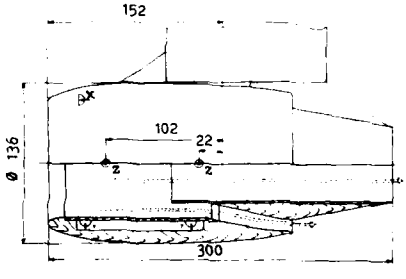

Fig. 9. Géométrie du réacteur.

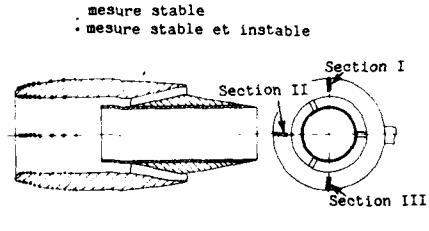

Fig. 9 bis. Moteur monté sur l'aile équipé de capteurs de pression.

Un dispositif particulier (figure 10) permettait d'une part d'exciter la maquette à travers ces conditions limites imposées en flexion et torsion et d'autre part donnait la possibilité d'introduire automatiquement un amortissement positif sur un mode critique par l'intermédiaire d'une boucle de contrôle si un risque de flottement apparaissait.

Dans le cas présent le couplage étudié se faisait par l'intermédiaire du mode de flexion de la voilure à 35 Hz et d'un mode de tangage du réacteur à 45 Hz qui induisait une torsion sur l'aile.

Des calculs préliminaires faits avec une méthode linéaire de doublets (sans correction) avaient permis d'obtenir une vitesse critique de flottement dans le domaine de la soufflerie avec une marge suffisante pour tenir compte des variations possibles dues aux non linéarités.

Enfin il est à noter que le flottement obtenu est sensible, par le calcul tout au moins, à l'introduction ou non des forces aérodynamiques instationnaires sur le réacteur. Les essais ont montré qu'à iso-pression génératrice et à Mach donné M = 0,78, l'entrée en flottement est très sensible à l'incidence globale de la maquette. Un choc apparaît ou non sur l'extrados de la maquette, dû en particulier aux déformations statiques.

La figure 11 donne la représentation, dans le plan des fréquences, de la densité de puissance d'un accéléromètre situé en bout d'aile, en fonction de l'incidence.

On constate que le couplage entre les modes de flexion de l'aile et le tangage du réacteur est de plus en plus violent lorsque l'incidence de l'aile diminue ce qui correspond à un dévrillage de plus en plus faible de l'aile.

Pour $\alpha = -0,7°$ le mode de flexion est très voisin de l'instabilité en flottement et pour $\alpha = -1,5°$ le système, sans boucle de contrôle, est instable. L'introduction automatique d'une loi de contrôle du flottement a permis à partir des résultats en boucle fermée d'obtenir la valeur de l'amortissement négatif de la boucle ouverte ($\xi = -12°/oo$).

La figure 12 montre une représentation des paramètres de fréquence et d'amortissement des deux principaux modes couplés en fonction de la pression génératrice pour un nombre de Mach constant M = 0,78. Afin de pouvoir poursuivre les essais dans le domaine instable dû au flottement, un système de contrôle automatique de l'amortissement a été introduit (figure 13).

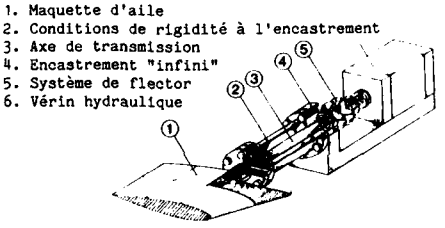

Fig. 10. Principe d'excitation et de sécurité à travers les conditions limites d'encastrement.

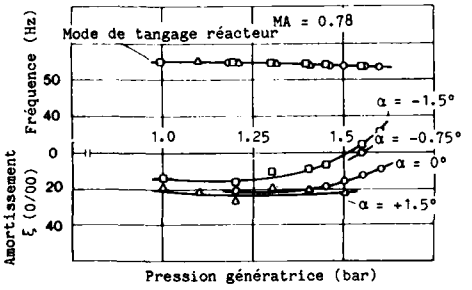

Fig. 12. Variation de la vitesse de flottement fonction de l'incidence.

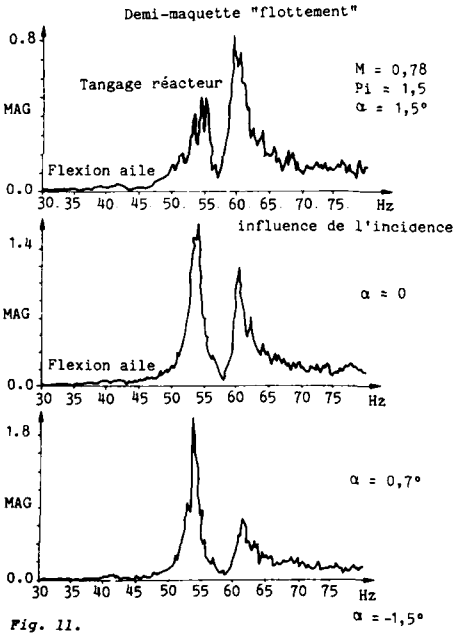

Fig. 11.

Mesure impossible = flottement

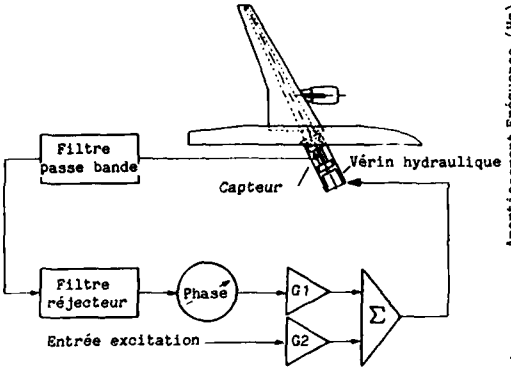

Fig. 13. Bloc-diagramme du système de contrôle.

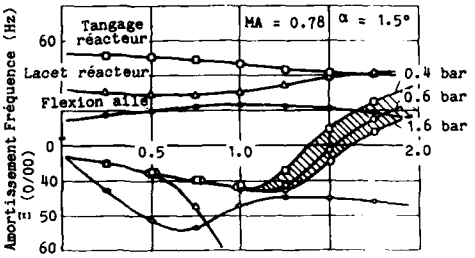

Fig. 14. Influence de la déformée élastique de l'aile sur le flottement.

V - CALCULS TENANT COMPTE DES DEVRILLAGES LOCAUX

Les calculs corrigés par tranche par des coefficients quasi-stationnaires ont été faits avec les hypothèses suivantes :

a) Les corrections appliquées ne dépendent pas de la fréquence réduite $\omega_R = \frac{\omega l}{V}$

b) Les corrections établies à partir d'un mouvement de tangage sont appliquées à des mouvements de roulis.

c) Les corrections tiennent compte de l'angle d'attaque local et de la couche limite mais pas des effets d'interaction entre tranches.

On a tout d'abord effectué trois calculs correspondants à trois déformations en envergure données par trois cas de charges théoriques. L'incidence de référence était de - 1,5° = α à Mach M = 0,78.

On constate figure 14 que pour les faibles pressions dynamiques le comportement de l'aile dépend peu du vrillage. Au contraire pour les pressions dynamiques plus importantes, la vitesse de flottement évolue. Elle est d'autant plus élevée que le dévrillage est important. La tendance fournie par l'essai est bien retrouvée. Le dévrillage de l'aile agit comme un terme stabilisateur au sens du flottement. Toutefois les conséquences d'un dévrillage de l'aile variable avec la charge, ne saurait être pris uniquement en compte comme paramètre agissant sur le flottement.

VI - INFLUENCE DU REACTEUR

Tout d'abord si on compare un calcul de flottement effectué en tenant compte ou en négligeant les forces instationnaires du réacteur, on constate une influence non négligeable de celles-ci principalement due au moment de tangage destabilisateur induit par les forces agissant sur les lèvres du réacteur (figure 15). Le calcul est fait sur le réacteur avec une méthode de doublets linéaires.

Des essais récents ont montré que les coefficients de pressions instationnaires sur un réacteur oscillant étaient fortement non linéaires avec l'incidence. Jusqu'à un nombre de Mach M = 0,70, les calculs et les essais donnent un accord raisonnable pour des incidences de 0 à $\pm$ 2,5°. La figure 16 illustre ce résultat. On peut constater que seuls les 20 premiers pour cent du réacteur portent, d'autre part la partie imaginaire pour cette fréquence réduite ω_R = 0,17 (corde de référence = longueur du réacteur) reste faible.

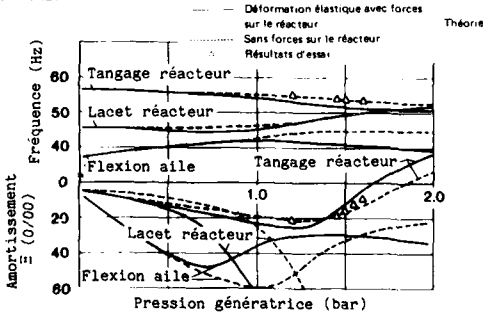

Fig. 15. Comparaison calcul - essais, Mach = 0,78, α = 0°.

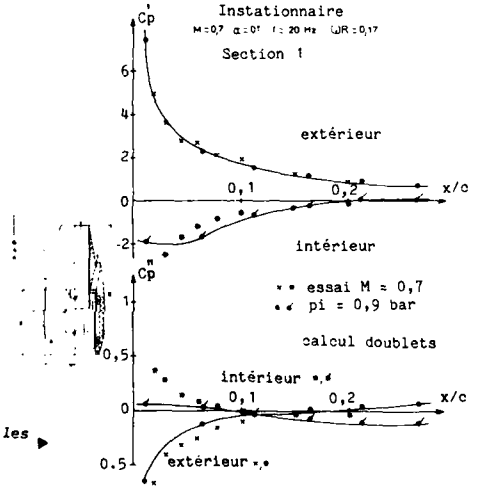

Fig. 16. Influence de l'incidence sur les pressions instationnaires.

Par contre à Mach 0,78 et M = 0,82, une partie du profil externe du réacteur devient supersonique (figure 17). Il en résulte des variations importantes avec l'incidence aussi bien dans le champ des pressions instationnaires que dans le coefficient de moment global instationnaire mesuré par une balance (fig. 18). Par exemple entre $\alpha = 0°$ et $\alpha = + 2,5°$ le coefficient quasi-stationnaire varie de 0,25 à 0,32

($C_m = \left| \frac{1}{q V_{référence}} \times \frac{\partial M^t}{\partial \alpha} \right|$). L'augmentation des coefficients instationnaires, due au mouvement du réacteur, avec l'incidence joue un rôle destabilisateur. Il faut noter que dans cette étude l'influence du fan et de la poussée du réacteur ont été négligées en première approximation.

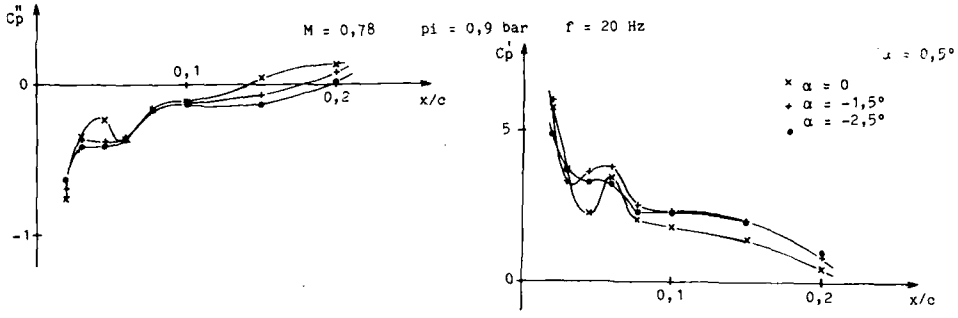

Fig. 17. Influence de l'incidence sur les pressions instationnaires.

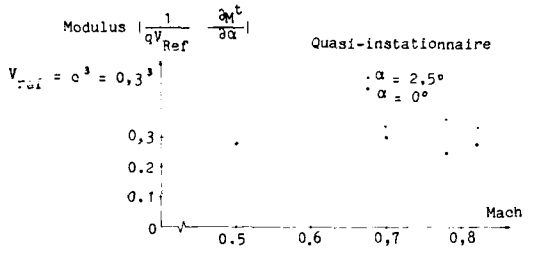

Fig. 18. Variation du coefficient de moment instationnaires (mi-corde) avec le nombre de Mach et l'incidence statique.

VII - CONCLUSION

Une étude de l'influence, sur le flottement, de l'angle d'incidence d'un avion de transport civil moderne en vol, à son Mach de croisière, a été développée.

Plusieurs effets non linéaires résultent de ce paramètre. Tout d'abord le dévrillage en envergure de l'aile avec l'incidence positive croissante entraine un recul de la limite du flottement pour un nombre de Mach et une pression dynamique donnée.

La connaissance exacte de la déformation sans charge est un paramètre important à introduire dans les calculs. D'autre part les théories linéaires (type doublets), corrigées par tranche des valeurs mesurées des coefficients de portance et de moments instationnaires, améliorent de façon sensible la comparaison calcul-essai.

Les méthodes de calculs plus élaborées telles les petites perturbations transsoniques qui prennent en charge les déformées de l'aile, donnent la même tendance.

Enfin on a montré que les forces instationnaires sur les réacteurs doivent être prises en compte par des méthodes non linéaires. L'effet d'incidence positive sur un réacteur joue un rôle défavorable au contraire du dévrillage de l'aile qui tend à restabiliser l'aile, qui aurait une tendance au flottement (ceci étant uniquement valable pour un nombre de Mach et une pression dynamique donnés).

VIII - BIBLIOGRAPHIE

[1] E. Carson Yates Jr., Eleanor C. Wynne, and Moses G. Farmer -
Effects of angle of attack on transonic flutter of a supercritical wing.
J.A. Vol. n° 10, oct. 1983.

[2] E. Carson Yates Jr., Eleanor C. Wynne, Moses G. Farmer and Desmarais R. -
Prediction of transonic flutter for a supercritical wing by modified strip analysis and comparison with experiment.
AIAA Paper 81-0609-1981.

[3] Angélini J.J., Chopin S., Destuynder R. -
Forces aérodynamiques instationnaires induites par les vibrations aéroélastiques d'un réacteur en nacelle.
La Recherche Aérospatiale n° 1974-4.

[4] Mulak P., Couston M., Angélini J.J. -
Extension of the transonic perturbation approach to three dimensional problems.
International Symposium on Aéroelasticity, Nuremberg oct. 1982.

[5] Gravelle A., Hünlinger H., Vogel S. -
Flutter calculation on a supercritical wing in the transonic range. Comparison Theory-Experiment.
14th ICAS Congress Toulouse 9-14/09/1984.

INFLUENCE OF THE STATIC DEFORMATION ON A WING IN THE UNSTEADY AERODYNAMIC

by
R. Destuynder
Office National d'Etudes et de Recherches Aérospatiales
Châtillon
92320
France

ABSTRACT

The modern civil transport airplanes, with large aspect ratio, like B 767 or AIRBUS, show even in cruise condition, important static deformations characterized essentially by an induced torsion due to the wing sweep angle.

This deformation principally important at the wing tip modifies the flow around a supercritical profile, very sensitive to the local incidence.

The deformation influence on the flutter phenomenon was proved by wind tunnel tests on a elastic model.

A series of flutter calculations using semi-empirical corrections, extracted from wind tunnel tests, was undertaken to reduce the existing difference between theory and experience.

I. INTRODUCTION

The modern large aspect ratio civil transport airplanes in cruise conditions (like B 767 or AIRBUS) exhibit important static deformations in bending and torsion along the span (this last deformation resulting mainly from the coupled effect due to wing sweep).

These deformations which are important mainly at the wing tip, modify the flow around a supercritical profile which is sensitive to the local twist angle particularly as far as the shock position is concerned.

Regarding the flutter phenomenon, the generalized unsteady aerodynamic forces, calculated with the structure normal modes, show a great sensitivity to the wing tip static twist which thus gives a major contribution to the generalized forces.

The present paper considers mainly the influence of the static deformation, due to steady loads, on the flutter problem.

The non-linearity of the unsteady forces on an engine as function of the global incidence will also be considered.

II. NATURE OF THE PROBLEM

First we have evaluated, with wind tunnel tests and calculations, the magnitude of the aeroelastic deformation of a large aspect ratio wing with a supercritical profile corresponding to a modern transport airplane.

By the Rayleigh Ritz method, the elastic deformation of a flexible model under steady air loads was estimated, using mode shapes, generalized masses and stiffnesses. Calculations have been made at constant Mach number (Mach = 0.78) and reference angle of attack (α_o = +1.5° and α_o = -1.5°.

The wing twist corresponding to different flight altitudes has been achieved. The figures 1 and 2 show the variation of streamwise elastic twist angle with the span.

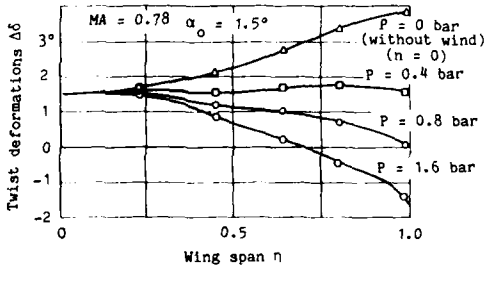

Fig. 1. Elastic twist deformation, streamwise direction, versus span.

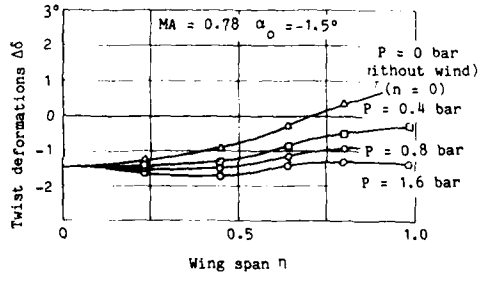

Fig. 2. Elastic twist deformation, streamwise direction, versus span.

The local twists are calculated from the jig shape without loads.

The first curve of the figure 1 corresponding to P = 0 shows the wing twist due to gravity forces only. The resulting twist angle is positive, i.e. its contributions gives a downward deflection to the trailing edge and an upward deflection to the leading edge.

The variation of local twist with the span (η) given by the gravity forces is, of course, independent of the wing reference incidence (here α = +1.5° or α = -1.5°). The lift forces corresponding to given C_L and Mach number are, after that, added as function of the dynamic pressure $q = \frac{1}{2} \rho V^2$.

These forces tend to make the deflection upward at the trailing edge and downward at the leading edge. The twist curves are calculated for two C_L values.

The local twist calculated with a fastly convergent iteration method has been compared to experiment on a dynamic model tested in the wind tunnel (figures 3 and 4).

The figure 3 shows the trailing edge displacement calculated and measured with the same wing load conditions. The figure 4 gives the local wing twist $\Delta\delta$ resulting from the loads. The comparison is satisfactory.

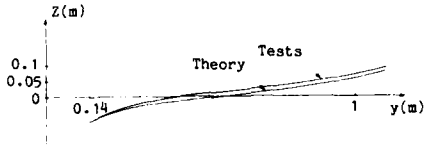

Fig. 3. Déformation of the trailing edge versus span theory - tests. (cruise conditions)

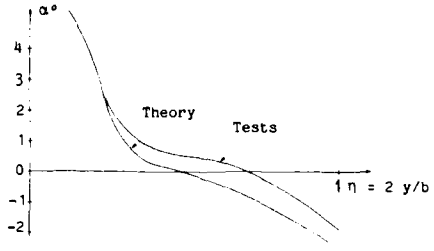

Fig. 4. Evolution of the twist angle versus span theory - tests. (cruise conditions).

III. CALCULATION OF THE C_L and C_M coefficient

The second part of the study consists in deriving the unsteady lift and moment coefficient for different local incidences from wind tunnel tests performed on a model having a deformation similar to the wing of an airplane flying in cruise conditions.

The following assumptions have been made :

- The local loads and local deflections are proportional,

- The strip analysis is taken as first approximation.

The interest of the method (similar to the modified strip analysis of E.C. Yates Jr. [1, 2]) applied to a 3-D theoretical subsonic method is to take account of the boundary layer effects which are very important for this kind of profile, with important loads near the trailing edge where the boundary layer has a maximum thickness.

The curves of steady lift and moment coefficients C_L and C_M versus span can be estimated (figures 5 and 6).

It can be seen that in addition to the Mach number and the global incidence, the lift local coefficient is strongly depending on the local twist resulting from the load.

($q = \frac{1}{2} \rho V^2 = \frac{1}{2} P_S \gamma M^2$).

In the same manner, the small variation of the local C_M coefficient is surprising.

The local lift coefficient and the center of pressure have been an object of comparison between tests and calculation on a rigid model for 2 global incidences α = 0 and α = +1° (figure 6 bis). Finally the curve 7 shows the unsteady lift coefficient $\frac{\partial c_z}{\partial \alpha}$ for 2 sections at 50% and 75% of spanwise location as function of the nominal incidence.

The variaton is very sensitive for positive incidences of the wing that is to say when the twist decreases with the loads.

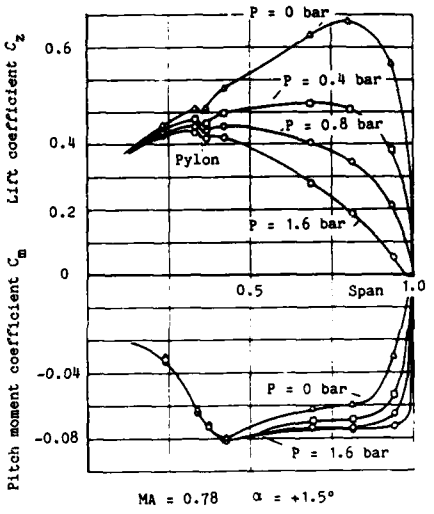

Fig. 5. Lift and moment coefficient in pitch vesus span.

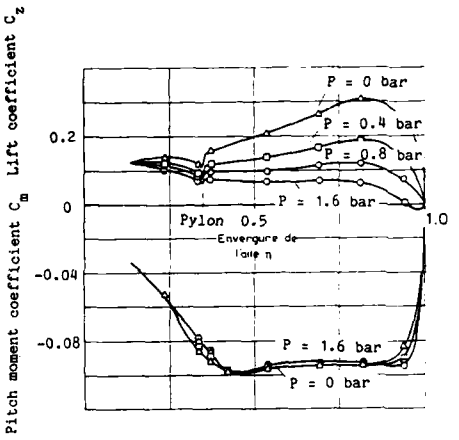

Fig. 6. Lift and moment coefficient in pitch versus span.

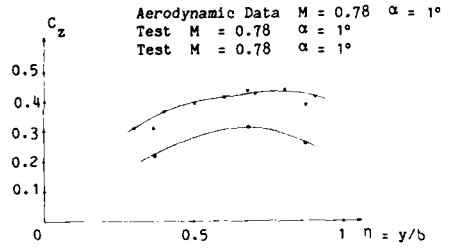

Fig. 5 bis. Lift coefficient distribution versus span.

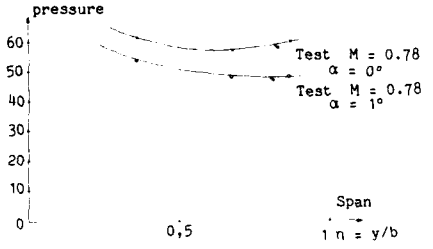

Fig. 6 bis. Center of pressure as function of η.

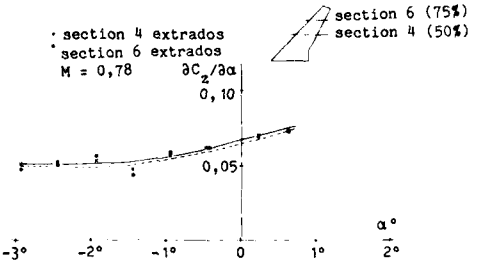

Fig. 7. Variation of the unsteady lift coefficient with the incidence.

IV. FLUTTER TESTS

To illustrate this influence, a half wing flutter model has been built and tested. The wing has a supercritical profile with ar engine (without fan and no thrust) (figures 8 and 9).

The eigen modes have been modified, compared to the airplane to obtain a violent flutter in the useful domain of the wind tunnel. The tests are performed at Mach number M + 0.60 (in subsonic flow without shock) and principally in the cruise conditions (Mach number M = 0.78) for different local incidences.

Fig. 8. Half flutter model mounted at the S2 wind tunnel wall.

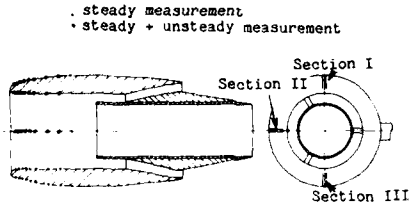

Fig. 9 bis. Engine mounted under the wing equipped with pressure pickups.

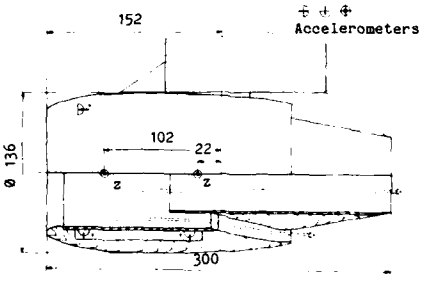

Fig. 9. Engine geometry.

For each Mach number and nominal incidence, the wind tunnel stagnation pressure was varied to reach the critical flutter condition.

The model was built like a Mach scaled model exhibiting static deflection equivalent to the airplane deflection for similar loads.

The model and airplane deflections were related by the scale ratio $\lambda = \frac{l_m}{l_a}$.

$$\frac{\partial_m}{\partial_A} = \frac{(M_{mg} + q_m S_m V_m^2 C_{Lm})\, l_m^3 E_A I_A}{M_{ag} + q_A S_A V_A^2 C_{LA}\, l^3 E_m I_m}$$

∂_m = model deflection.

∂_A = airplane deflection.

This is signifiant if $E_M = E_A$ (elasticity modulus)

$$\frac{EI_m}{EI_A} = \lambda^4 \frac{q_m}{q_A} \qquad (1)$$

with $\lambda = \frac{l_m}{l_A}$; E_m, l_M, S_M, V_m, M_m : model data.

E_A, l_A, S_A, V_A, M_A : airplane data.

with the assumption that the wing gravity forces remain small compared to the lift forces (that is particularly true for the model).

The model, taking into account (1) had the same C_L and C_m on the airplane and the same static deformations for all the values of α but mode shapes were different.

A special device (figure 10) was used to excite the model through the root (fixed in bending and torsion) and also to introduce automatically a positive aerodynamic damping by means of an active control loop, if a flutter risk appears.

In the present case, the main coupling involves the first wing bending mode at 37 Hz and the pitch engine mode at 45 Hz which induces a wing torsion.

Preliminary calculations, performed with the doublet lattice method (without correction) gave a critical flutter speed within the wind tunnel domain. The margin being sufficient to take into account possible variations coming from the non-linearity of the phenomenon.

Finally, it is to be noticed that the computed flutter characteristics are signifiantly modified by the introduction of the unsteady aerodynamic forces on the engine.

The figure 11 shows the power spectral density for an accelerometer located at the wing tip, for several values of the mean incidence (reference incidence α).

We can notice that the coupling between bending wing mode and engine pitch becomes more and more violent when the wing incidence decreases, i.e, when the local untwist becomes smaller.

For $\alpha_{nom} = -0.7°$, the bending mode is close to flutter unstability and for $\alpha = -1.5°$, the system is unstable without control loop.

The automatic introduction of a flutter control law makes possible to use close loop measurements and to derive the negative value of the damping corresponding to the open loop configuration (damping in open loop equal to -14‰).

The figure 12 shows the frequencies and damping for the two principal modes versus the wind tunnel stagnation pressure at constant Mach number M = 0.78.

In order to make possible to achieve the tests in the unstable domain, an automatic control device was introduced (figure 5).

1. Wing model
2. Root stiffnesses conditions
3. Shafting
4. Clamped conditions
5. Flector system
6. Hydraulic actuator

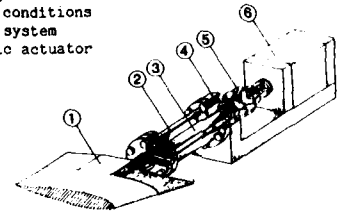

Fig. 10. Excitation principle through the root conditions.

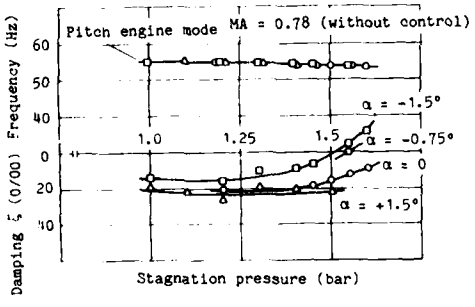

Fig. 11.

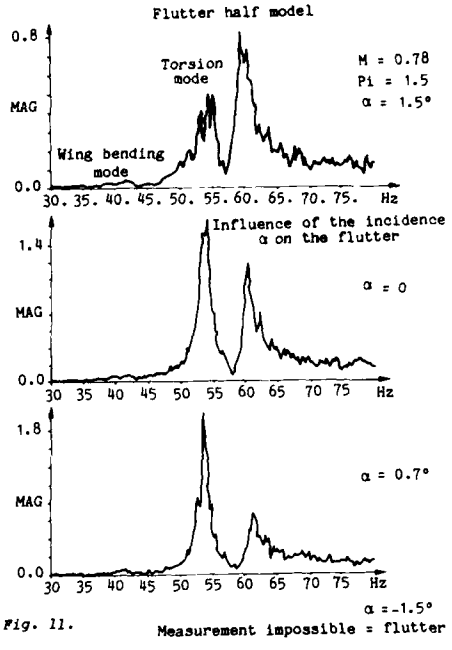

◂ *Fig. 12. Variation of the flutter speed versus incidence α.*

V. CALCULATIONS TAKING INTO ACCOUNT THE LOCAL TWIST

The unsteady aerodynamic forces used in the calculations were modified strip by strip using quasi-steady experimental coefficients.

The following assumptions were made :

a) The applied corrections are independent of the reduced frequency $\omega_R = \frac{\omega l}{V}$.

b) The corrections derived from a pitch oscillation are also valid for a roll motion.

c) The corrections take into account the local twist angle and the boundary layer but ignore the interactions between the strips.

The first three cases which have been computed correspond to spanwise deformations given by three theoretical load cases. The reference incidence angle was $\alpha = -1.5°$ at Mach number M = 0.78.

Figure 14 shows that for small wind tunnel stagnation pressure the influence of the loads (i.e. of the deformation) remains small. On the other hand, for the large stagnation pressures, the critical flutter speed varies.

The speed increases with the pressure that is to say with the untwist. The system is more and more stable when the local twist angle decreases.

VI. Nevertheless the untwist parameter of the wing is not the only parameter acting on the flutter speed.

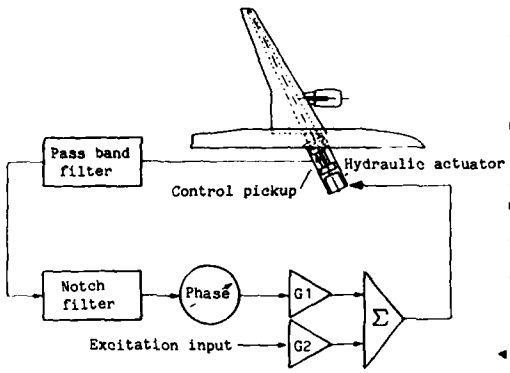

Fig. 13. Bloc-diagram of the control loop.

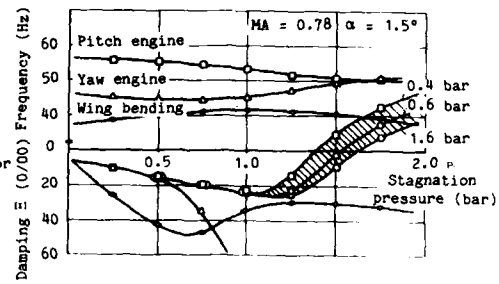

Fig. 14. Influence of the static deflexion of the wing on the flutter.

Engine influence

First, if we compare a flutter calculation with or without the unsteady forces on the engine, we notice a signifiant influence which is related to the aerodynamic destabilizing moment due to pressures acting on the engine lips (figure 15) (calculations are made with a doublet lattice method).

Recent tests show that the unsteady pressure coefficients measured on an oscillating engine are strongly variable with the unsteady incidence.

Till Mach number M = 0.70 tests and linear calculations agree reasonably for the incidences from 0 to 2.5°.

This result is shown by figure 16.

It is possible to see that only the first 20% at the front of the engine give a lift effect ; the imaginary part for the reduced frequency ω_R = 0.17 remains small (the reference chord being the engine length).

On the other hand, at Mach number M = 0.78, the pressures on the external part of the engine become supercritical (figure 17).

From this point, important variations with incidence are noticed in the unsteady pressure field, as well as, in the unsteady global moment measured with a balance (figure 18).

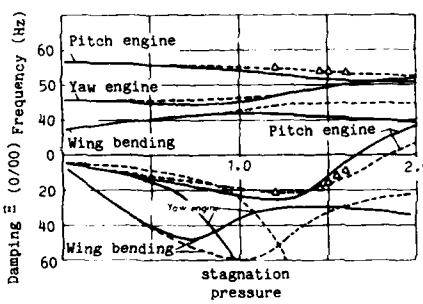

Fig. 15. Comparison theory - tests, Mach = 0.78, α = 0°.

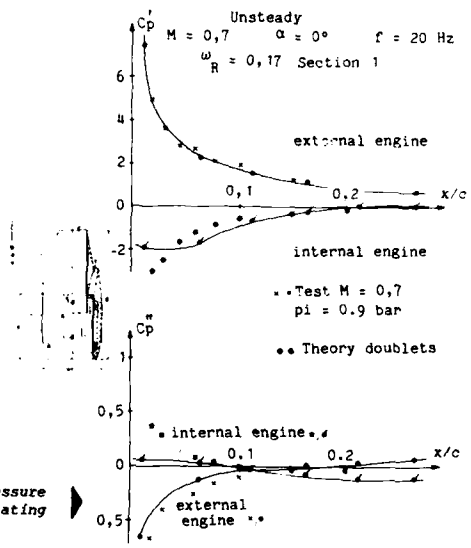

Fig. 16. Comparison theory - tests pressure distribution on the pitch oscillating engine.

For example, between α = 0 and α = +2.5° the quasi-steady moment coefficient varies from 0.25 to 0.32.

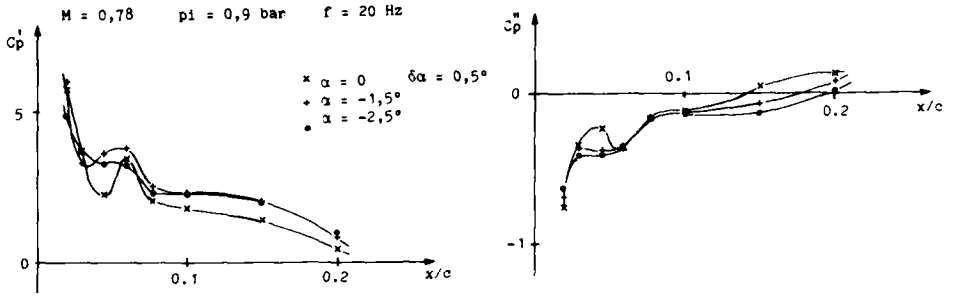

Fig. 17. Influence of the static incidence on the unsteady pressures.

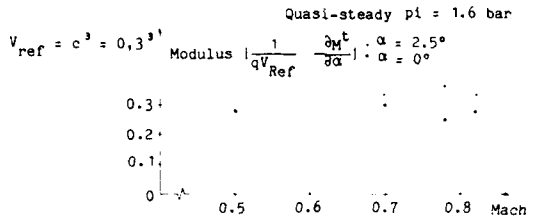

Fig. 18. Evolution of the unsteady moment coefficient (mi-chord) versus incidence α and Mach number.

$$\left(C_m = \frac{1}{q_x V_{reference}} \frac{\Delta M^t}{\Delta \alpha}\right)$$

The increasing value of the unsteady engine C_m pitch coefficient with the incidence has a destabilizing effect.

It is necessary to notice that in this study, the fan and engine thrust effects are not taken into account.

VII. CONCLUSION

An investigation of the variation of the flutter characteristics with incidence of a modern civil airplane in cruise flight conditions has been carried out.

Different non-linear effects have been found.

First, the spanwise untwisting effect associated to positive incidences tends to increase the flutter limits for given values of the Mach number and the dynamic pressure.

An exact knowledge of the wing deflection due to static loads is necessary to make the calculation valid.

The linear theory modified by the strip theory using experimental lift and moment coefficients improves the comparison between tests and theory.

More sophisticated calculations like the small transonic perturbations which take into account the local wing twist give the same tendency.

Finally, it was shown that the unsteady aerodynamic forces on the engine must be taken into account by non-linear methods.

The effect of a positive incidence on an engine has an unfavourable effect opposite to the wing untwist which tends to restabilize the system.

REFERENCES

[1] Carson Yates Jr., Eleanor C. Wynne and Moises G. Farmer, "Effects of angle of attack on transonic flutter of a supercritical wing". J. A. Vol. Nr. 10, Oct. 1983.

[2] Carson Yates Jr., Eleanor C. Wynne, Moises G. Farmer and R. Desmarais, "Prediction of transonic flutter for a supercritical wing by modified strip analysis and comparison with experiments". AIAA paper 81.0609-4981.

[3] J.J. Angelini, S. Chopin, R. Destuynder, "Forces aérodynamiques instationnaires induites par les vibrations aérodynamiques d'un réacteur en nacelle". Recherche Aérospatiale N° 1974-4.
[4] P. Mulak, M. Couston, J.J. Angelini, "Extension of the transonic perturbation approach to the three-dimensional problems". Int. SYmp. on Aeroelasticity, Nuremberg, Oct. 1982.
[5] A. Gravelle, H. Hönlinger, S. Vogel, "Flutter calculation on a supercritical wing in the transonic range. Comparison theory experiments". 14th ICAS Congress, Toulouse, 9-14 Sept. 1984.

MESURE DES DEFORMATIONS DES MAQUETTES EN SOUFFLERIE

par MM.CHARPIN - ARMAND - SELVAGGINI
Office National d'Etudes et de Recherches Aérospatiales (ONERA)
92322 CHATILLON CEDEX - FRANCE

RESUME -

La Direction de la Physique générale et la Direction des Grands Moyens d'Essais de l'O.N.E.R.A. ont défini, mis au point et expérimenté des méthodes et moyens d'essai qui permettent de déterminer avec une précision satisfaisante les déformations sous charges aérodynamiques et massiques de la plupart des maquettes essayées en soufflerie.

Les techniques utilisées font appel :

- à la photographie de mires réfléchissantes,

- à la mesure faite par un torsiomètre à faisceau laser de l'angle entre le faisceau incident et le faisceau réfléchi par une mire rétro-diffusante polarisée,

- à la poursuite par un détecteur optique de position de sources lumineuses créées par des fibres optiques,

- au calcul de déformée, à partir de mesure de contraintes sur une maquette.

Ces différentes méthodes d'essai, utilisées de manière industrielle dans les grandes soufflerie permettent aux constructeurs de s'assurer que leurs maquettes se comportent bien sous charges selon leurs prévisions ; les développements en cours devraient permettre à terme d'accroître les précisions de mesure ainsi que la rapidité d'accès aux résultats définitifs.

MEASUREMENT OF MODEL DEFORMATIONS IN WIND TUNNELS

ABSTRACT -

The Physics and Large Testing Facilities Department at ONERA has defined, developed and tested means and methods for determining with satisfactory precision the deformations most wind tunnel-tested models undergo under aerodynamic and body loads.

The techniques used are :

- photography of reflecting patterns

- torsiometer measurement of the angle between the incident and reflected laser beam on a polarized back scattering target

- tracking the position of optical fiber light sources with an optical detector

- computation of the strain from stress measurements on the model.

With these various test methods, used undustrially in large wind tunnels, manufacturers can insure that the their models behave correctly as predicted under load. The developments under way should make it possible in the end to increase the accuracy of the measurements and reduce the time needed to obtain the final results.

1 - INTRODUCTION

Il y a déjà bien des années que les constructeurs se sont souciés de donner aux maquettes passant en soufflerie les formes que prennent les aéronefs réels en vol sous charge, car les performances de ceux-ci peuvent être notablement altérées par des modifications de géométrie qui semblent a priori mineures ; l'incidence ou la forme d'un profil au voisinage du bord d'attaque sont par exemple des paramètres qui influent considérablement sur les répartitions de pression autour de ce profil. La prévision de ces formes au niveau du projet n'est pas aisée et leur restitution sur la maquette est rendue très difficile

compte tenu des nombreux cas de vol à explorer et de la différence très importante de structure qui existe entre l'aéronef et la maquette. Les cas les plus difficiles à bien représenter sont probablement ceux où les structures font appel aux matériaux composites (fibres, résines) et qui sont soumises à des efforts centrifuges.

Dans la plupart des cas, la forme de la maquette est calculée pour un cas de vol en tenant compte de la différence de déformation qui existe entre le vol et l'essai en soufflerie. Ceci étant, il est important de vérifier que les déformations obtenues en soufflerie sont bien celles qui étaient prévues ou du moins qu'elles s'en écartent très peu. C'est dans ce but que l'O.N.E.R.A. a développé ces dernières années des méthodes de mesure de déformation en cours d'essai avec vent, adaptées aux différents cas d'essais.

Ce document recense et présente les différents types d'essais effectués au centre O.N.E.R.A. de Modane-Avrieux dans lesquels ont été effectivement mises en oeuvre des techniques permettant de mesurer la déformation des maquettes ou parties de maquette ; la plupart de ces techniques font appel à des méthodes optiques qui ont été développées par la Direction de la Physique Générale de l'O.N.E.R.A.

De nouvelles méthodes de mesure des déformations sont actuellement en cours d'étude à l'O.N.E.R.A., notamment au Centre d'Etudes et de Recherches de Toulouse, et ont déjà donné des résultats prometteurs. N'ayant pas encore été appliquées en soufflerie, elles ne sont pas présentées dans ce document.

2 - MESURE DE LA DEFORMATION GLOBALE D'UNE AILE ET D'UN SUPPORT DE MISSILE

Le problème consiste en la mesure de la déformation globale d'une aile et d'un pod support de missile à M = 0,95 dans la veine transsonique de la soufflerie S2MA de section 1,75 x 1,77 m^2. Des mires rétrodiffusantes sont placées sur l'avion pour donner la référence de la mesure et sur le missile. Les mires ont une épaisseur de 0,11 mm. Elles sont constituées d'une pellicule adhésive recouverte de billes de verre de diamètre voisin de 50 microns leur conférant des propriétés catadioptriques : quelle que soit l'incidence du faisceau sur la mire, les billes renvoient la lumière vers sa source. Une conséquence directe de cette particularité est que pour photographier les mires, il faut impérativement que la source lumineuse qui les éclaire soit placée à proximité immédiate de l'axe de prise de vue. La divergence du faisceau rétrodiffusé est de l'ordre du degré, et le flux lumineux qu'il transporte varie de moins de 10% lorsque l'incidence du faisceau sur la cible croît de 0 à 40°. Une photographie est faite sans vent à l'incidence désirée (25 degrés dans notre cas) puis une autre à M = 0,95. La superposition des deux images en prenant comme référence les mires placées sur l'avion donne directement la déformation recherchée. On notera que dans le cas présenté ici (figures 1,2) la déformation n'est pratiquement qu'une translation. Cette technique de mesure aisément mise en oeuvre permet d'obtenir des flèches avec une précision de $\pm$ 0,2 mm (sur les 12 mm mesurés) et une précision sur l'angle de torsion de $\pm$ 0,1 degré.

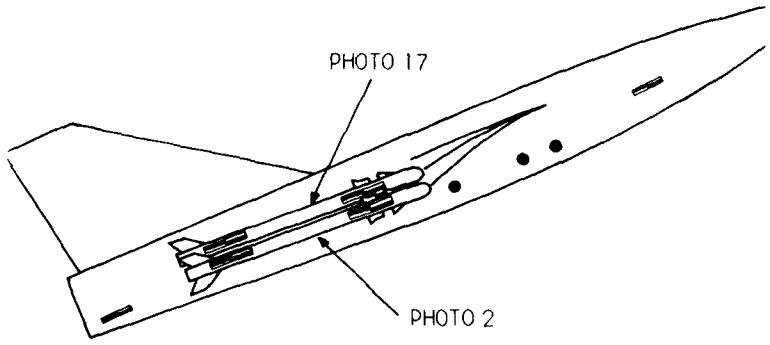

(Fig. 1) DEFORMATION GLOBALE D UNE AILE ET D'UN SUPPORT DE MISSILE (SCHEMA)

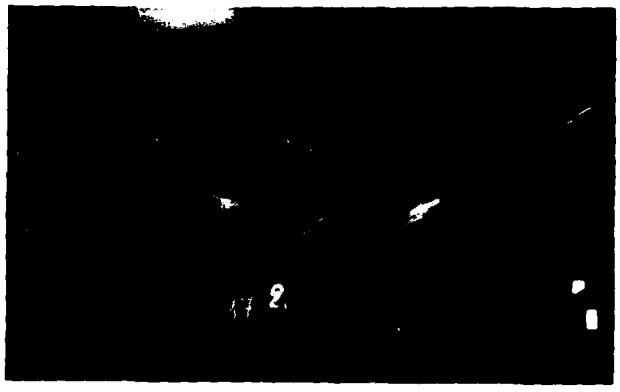

M 8 108

(FIG. 2) DEFORMATION GLOBALE D'UNE AILE ET D'UN SUPPORT DE MISSILE (PHOTO)

3 - MESURE DU DEVRILLAGE D'UNE PALE

Le problème consiste en la mesure du dévrillage d'une pale d'une hélice transsonique de 1 m de diamètre pouvant tourner à 5000 tr/mn, placée à M = 0,75 dans la veine d'essai de 8 m de diamètre de la soufflerie S1MA du centre de Modane-Avrieux (figure 3). Pour ce faire, des mires rétrodiffusantes sont collées sur le saumon d'une des pales et sur le carénage fixe. Il y a deux mires sur le saumon, l'une vers le bord d'attaque, l'autre vers le bord de fuite ; la droite les joignant définit une corde. Le réseau de mires placé sur le carénage fixe permet de définir le trièdre de référence dans lequel sera déterminé le calage global du saumon Σ résultant de la somme du pas de l'hélice et de son dévrillage (figure 4). Un appareil photographique placé sous le plancher photographie les mires lorsqu'elles sont éclairées par l'éclair d'un stroboscope déclenché par un dispositif lié à la partie tournante. Cinq photographies sont prises pour chaque point de mesure. La durée de l'éclair du stroboscope calculée au 1/3 de l'intensité maximale de son pic est de 1,2 μs ce qui donne un flou de 0,3 mm pour une vitesse de rotation de 5000 tr/mn. Un exemple de photographie prise en essai est donné en figure 5. Son exploitation est faite sur un récepteur grossissant équipé de deux réticules mobiles qui permet d'obtenir les distances X1 et Y1 (figure 3) avec une précision de $\pm$ 0,1 mm. La comparaison des calages globaux obtenus avec rotation de l'hélice durant deux essais (avec et sans vitesse d'écoulement amont) et en tenant compte des affichages du pas permet d'accéder aux angles de dévrillage des pales de l'hélice avec une précision de $\pm$ 0,25 degré.

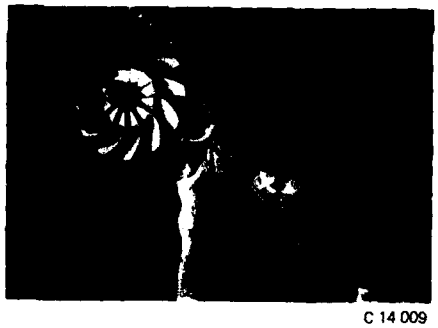

C 14 009

(Fig. 3) MONTAGE D'UNE HELICE TRANSSONIQUE DANS LA VEINE D'ESSAI DE S1MA

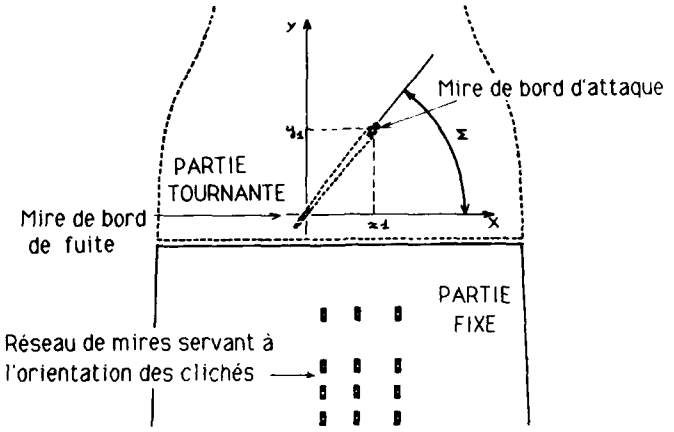

(Fig. 4) MESURE DE DEVRILLAGE D'UNE PALE

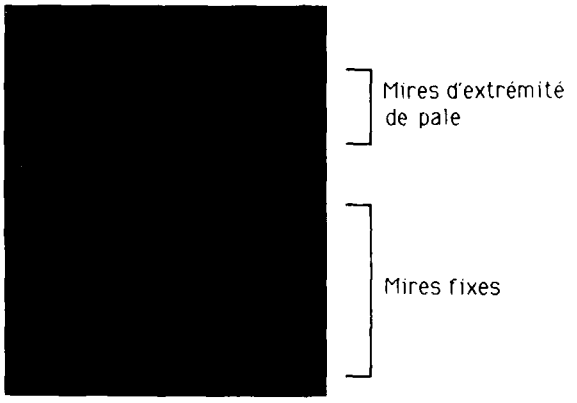

(Fig. 5) EXEMPLE DE PHOTOGRAPHIE PRISE EN ESSAI

4 - DETERMINATION DE LA DEFORMATION DU BORD DE FUITE D'UNE AILE ET DE SA TORSION GLOBALE MESUREE SUR SON SAUMON D'EXTREMITE

Les mesures sont faites sur l'aile d'une demi-maquette d'avion civil montée au plancher de la veine d'essai n° 1 de la soufflerie S1MA (voir figure 6). L'essai est conduit dans une gamme de Mach comprise entre M = 0,5 et M = 0,8, et pour des incidences comprises entre 0 et 3,5 degrés. La demi-envergure de la maquette est de 3,80 m.

C13 772

(Fig. 6) DEMI-MAQUETTE MONTEE AU PLANCHER DE LA SOUFFLERIE S1MA

4.1 - Mesure de la déformation du bord de fuite

Le bord de fuite de la maquette est équipé de 11 mires rétrodiffusantes numérotées de 0 à 10 (voir figure 7). La mire 0 sert d'origine pour l'exploitation des photographies (voir figure 8).

Deux mires réfléchissantes A et B placées au voisinage de la voilure permettent de définir avec précision sur chaque cliché le système d'axe par rapport auquel les mesures sont effectuées (voir figure 8).

L'appareil photographique associé à sa torche flash est placé dans un caisson au début du diffuseur de la soufflerie (voir figure 6).

La restitution se fait sur un appareil de projection équipé de deux réticules orthogonaux liés à un dispositif automatique de numérisation donnant les coordonnées X et Y de chaque mire par rapport à l'origine des axes (mire A, B et mire 0). Un dessin représentant l'image vue sur l'écran de projection est présenté sur la figure 8.

La déformation brute du bord de fuite de la voilure est obtenue en faisant la différence des coordonnées des mires obtenues au cours d'un essai avec vent et au cours d'un essai sans vent. Cette déformation brute est ensuite corrigée de la déformation en roulis de l'ensemble dynamométrique qui mesure les efforts aérodynamiques sur la maquette.

La figure 9 présente l'évolution des déformations du bord de fuite de la voilure en fonction de son envergure relative pour cinq nombres de Mach à une incidence de 2 degrés. A côté du repérage du nombre de Mach est porté le produit Qo x Cz qui représente la charge spécifique moyenne sur la voilure ; si les courbes avaient été tracées en valeurs réduites $\frac{\text{déformation}}{Qo \times Cz}$ elles auraient été pratiquement confondues ; la voilure se comporte comme un système élastique sur lequel la répartition des charges est peu influencée par l'évolution du nombre de Mach.

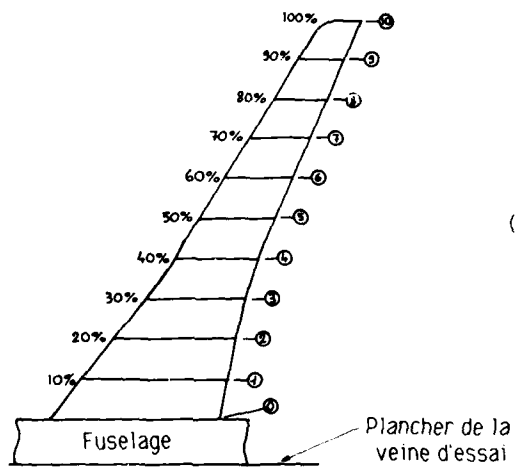

(Fig. 7) POSITION DES MIRES SUR LE BORD DE FUITE DE LA VOILURE

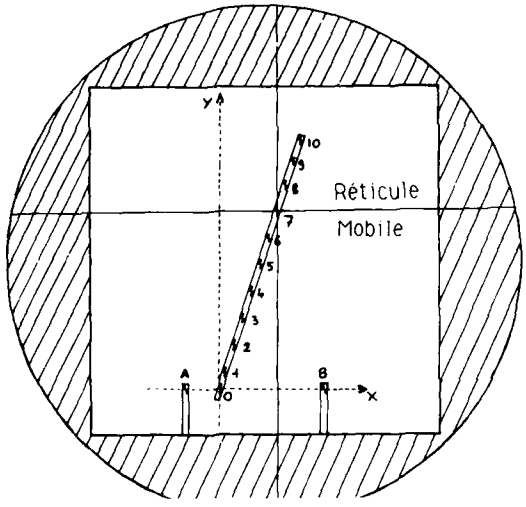

(Fig 8) EXPLOITATION D'UNE PHOTOGRAPHIE DU BORD DE FUITE

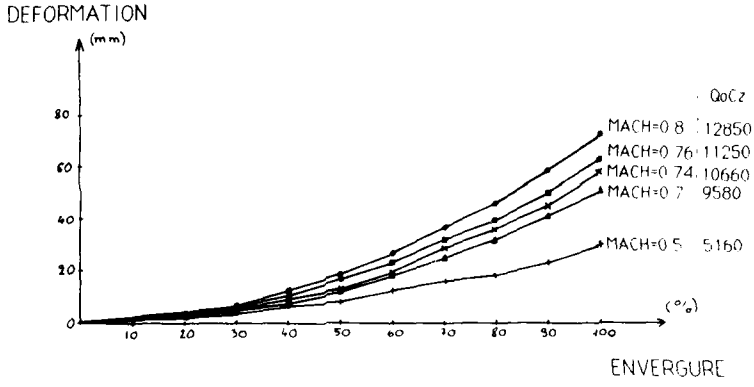

(Fig 9) DEFORMATION DU BORD DE FUITE DE LA VOILURE

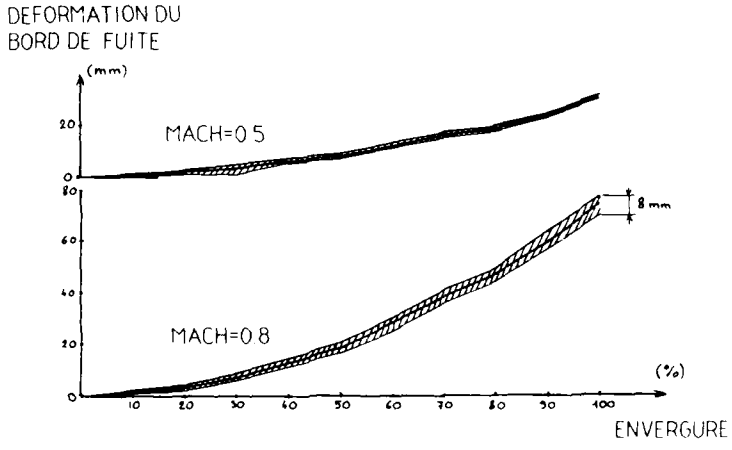

(Fig 10) AMPLITUDE CRETE A CRETE DES VIBRATIONS

Chaque courbe de la figure 9 est en fait définie par la moyenne de 5 clichés consécutifs dont la dispersion donne une idée du niveau de vibration de la voilure ; la figure 10 montre pour M = 0,5 et M = 0,8 les écarts crête à crête relevés le long de l'envergure. Ces écarts crête à crête croissent avec l'incidence (non montré ici) et avec le nombre de Mach pour atteindre 8 mm au niveau du saumon d'extrémité de voilure à M = 0,8.

4.2 - Mesure de la torsion globale d'une aile mesurée sur son saumon d'extrémité

La mesure de la torsion de l'aile est effectuée à l'aide d'un torsiomètre dit OP-BBT associé à une cible rétrodiffusante polarisée collée sur l'extrémité de la voilure. L'adaptation de l'appareillage de base aux essais en soufflerie a fait l'objet de travaux très importants menés à bien par la Direction de la Physique Générale de l'O.N.E.R.A. [1].

4.2.1 - Principe de la mesure

Le détail de la technique de mesure ainsi que les précautions à prendre pour obtenir une bonne précision sont décrits dans le document précité ; nous ne donnerons ici que le principe de fonctionnement du torsiomètre.

Le torsiomètre est constitué d'un émetteur récepteur et d'une cible rétro diffusante polarisée collée sur le saumon d'extrémité de voilure (voir fig. 11).

L'émetteur récepteur comporte un laser dont le faisceau incident polarisé par un prisme polariseur tournant éclaire la cible à travers une bobine de Faraday qui module le plan de polarisation. Le principe de la mesure est le suivant : la cible étant éclairée, on fait tourner le prisme polariseur de manière à obtenir l'extinction du faisceau réfléchi. Cette position du prisme polariseur définit l'origine des mesures angulaires. Si maintenant la cible tourne d'un angle α il faudra faire tourner le prisme polariseur d'un angle α pour obtenir à nouveau l'extinction. La mesure de la position angulaire du prisme polariseur permet donc de définir les angles de rotation de la cible polarisée. Une bobine de Faraday placée sur le faisceau incident et alimentée en courant alternatif module l'orientation du plan de polarisation de ce faisceau.Cette modulation permet de générer le signal d'erreur qui sert à asservir la position du prisme polariseur tournant à la position de la cible. Cette présentation condensée de la technique de mesure ne doit pas faire oublier les difficultés rencontrées au cours de la mise au point ni les recommandations essentielles suivantes :

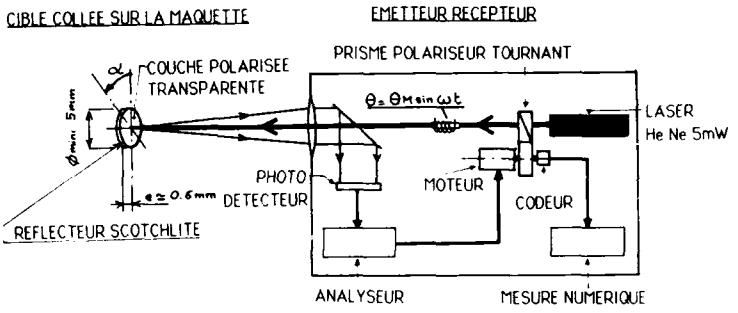

(Fig. 11) TORSIOMETRE

- travailler sans hublot, ni miroir entre l'émetteur et la cible ;

- positionner l'émetteur et la cible de manière à n'avoir que de faibles angles du faisceau incident sur la cible ;

- trier les cibles pour avoir une bonne planéité et une bonne uniformité du plan de polarisation ;

- positionner le rayon incident toujours au même endroit sur les cibles.

4.2.2 - Implantation du torsiomètre dans la soufflerie

La maquette montée au plancher de la soufflerie est équipée de deux cibles rétrodiffusantes collées l'une sur le saumon d'extrémité d'aile, l'autre sur le fuselage. Cette dernière sert de référence ; c'est la différence d'angle de torsion entre ces deux cibles qui donne l'angle de torsion global de la voilure. Le torsiomètre monté sur une platine articulée suivant deux axes orthogonaux est fixé au plafond de la veine d'essai (figure 12). Cette disposition et ce montage permettent de positionner successivement le faisceau laser sur chacune des cibles quelles que soient les variations de positions de celles-ci (fonction de l'incidence de la maquette et des déformations) avec de faibles angles du faisceau incident sur les cibles. Le pointage du faisceau laser sur les cibles en utilisant la platine articulée télécommandée se fait à l'aide d'une caméra vidéo.

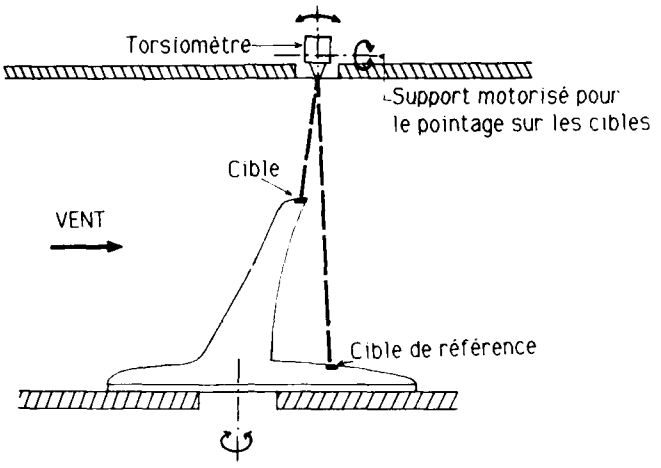

(Fig. 12) IMPLANTATION DU TORSIOMETRE DANS LA SOUFFLERIE S1MA

Des mesures d'angles sont faites sans vent pour les différentes positions géométriques de la maquette (correspondant aux positions prises par la maquette quand on fait varier son incidence) ; la différence entre les mesures avec vent et celles sans vent faites dans les mêmes conditions donne les angles de torsion sous charge.

4.2.3 - Résultats

La figure 13 montre l'évolution de l'angle de torsion en fonction de la charge de portance sur la voilure ; c'est approximativement une droite. Les groupes de points donnent une idée de la dispersion des mesures.

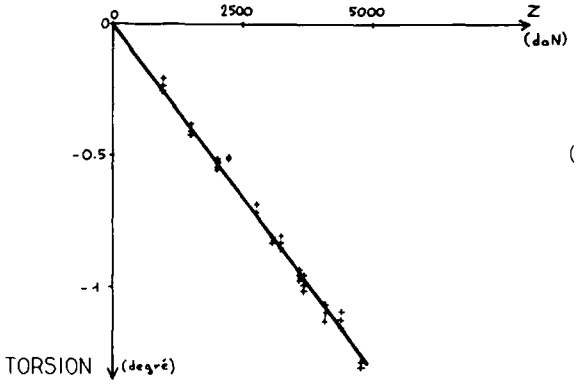

(Fig 13) EVOLUTION DE LA TORSION

4.3 - Validité des résultats obtenus

La platine articulée nécessaire à la poursuite des cibles dans le paragraphe 4.2 est équipée de potentiomètres permettant de restituer la position du saumon d'extrémité de la voilure. La différence de positionnement avec et sans vent donne la déformation globale du bord de fuite de la voilure qui est comparée dans le tableau ci-dessous aux résultats obtenus par la technique photographique du paragraphe 4.1.

Mach	0,5	0,7	0,74	0,76	0,8
Photo bord de fuite (mire n° 10) mm	30	51	58	63	73
Platine de poursuite mm	30	55	60	65	75

Ces valeurs sont assez voisines pour qu'une confiance raisonnable se dégage des résultats obtenus.

La torsion de la voilure a aussi été mesurée, en utilisant la technique photographique du paragraphe 4.1 précédent, pour le point le plus chargé où l'angle de torsion est de - 1,3 degré. Les huit clichés exploités donnent des valeurs de l'angle de torsion compris entre - 1,17 et - 1,34 degré, qui entourent bien les mesures effectuées avec le torsiomètre.

4.4 - Comparaison calculs - essais

L'Aérospatiale avait calculé les déformations qui devaient être observées sur la maquette en essai. La figure 14 montre la comparaison entre les calculs AS et les mesures faites en soufflerie. La concordance est tout à fait satisfaisante.

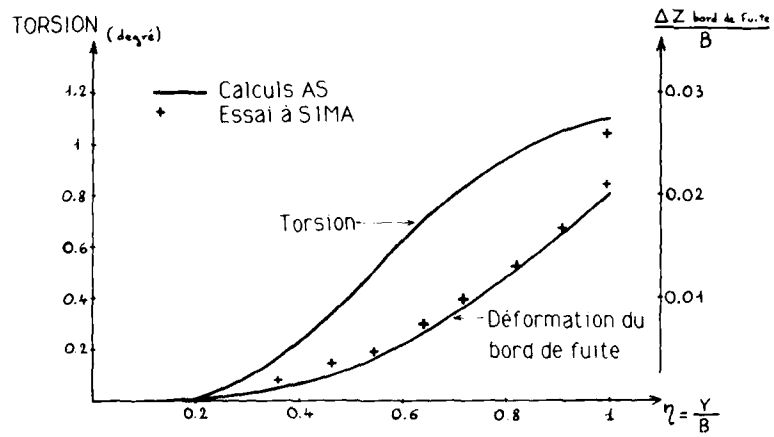

(Fig. 14) COMPARAISON CALCUL - ESSAI

5 - DETERMINATION DE LA DEFORMATION DU BORD DE FUITE D'UNE VOILURE A L'AIDE D'UN DETECTEUR OPTIQUE DE POSITION

La connaissance précise de la position d'un peigne de sillage par rapport à la voilure d'une maquette placée à son amont a nécessité la mise au point par la Direction de la Physique de l'O.N.E.R.A. d'un détecteur optique de position [1] [2] [3]. Cet appareil qui, associé au mécanisme de déplacement du peigne, est capable de poursuivre pas à pas différentes sources lumineuses, a donné en complément de sa fonction d'origine la déformation du bord de fuite de la voilure.

La description détaillée du fonctionnement du détecteur optique ainsi que sa validation en laboratoire sont données dans [1], nous ne présenterons ici que son utilisation dans le cadre d'un essai effectué sur une maquette d'avion civil montée dans la veine d'essai de la soufflerie SIMA.

5.1 - Description de l'équipement et de son fonctionnement

La maquette et son peigne de sillage sont montés sur le même dard support ; le mécanisme de déplacement du peigne supporte aussi le détecteur optique (figures 15 et 16) et peut se déplacer suivant les 3 axes de coordonnées rectangulaires X, Y et Z liés à la maquette. Les positions du détecteur (ou du peigne) par rapport à ce trièdre sont calculées à partir des signaux des potentiomètres du mécanisme de déplacement.

La voilure de la maquette est équipée de 3 fibres optiques A, B, C, dont les extrémités se terminent à 3 positions différentes en envergure (figure 16) dans le bord de fuite de la voilure donnant vers l'aval 3 faisceaux lumineux d'angles d'ouverture 44 degrés. L'éclairage est assuré par un illuminateur composé d'une lampe à iode et d'un condenseur assurant l'introduction de la lumière à l'intérieur des fibres. Cet ensemble est situé à environ 10 m de la maquette.

La partie sensible du détecteur est constituée de 2 plages photo sensibles juxtaposées (figure 17). Quand, par exemple, l'ensemble du dispositif est placé plus bas que le bord de fuite de la voilure, le faisceau lumineux provenant de l'une des fibres optiques éclaire plus la plage photo sensible du bas du détecteur, celui-ci fournit un ordre de montée au mécanisme. Cet ordre s'annule quand l'éclairage est identique sur les deux plages ; le dispositif est alors positionné en face du bord de fuite et l'on relève la valeur des signaux des potentiomètres placés sur le mécanisme afin de calculer la position de celui-ci dans le trièdre X, Y, Z. Les différences de positions relevées avec et sans vent donnent les valeurs des déformations du bord de fuite sous charge.

C 12 771

(Fig 15) MAQUETTE ET SON PEIGNE DE SILLAGE MONTES DANS SIMA

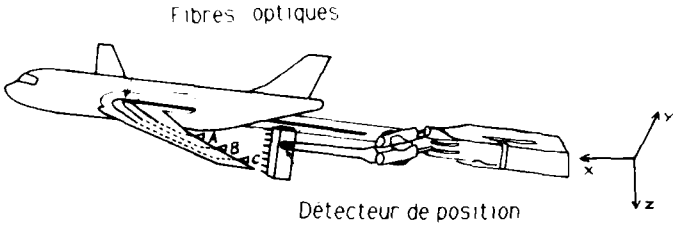

(Fig 16) DEFORMATION D'UNE VOILURE

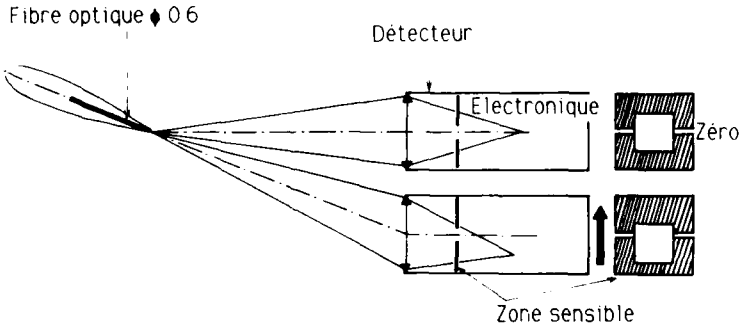

(Fig 17) DETECTEUR DE POSITION

Les coordonnées Xi et Yi de chacune des 3 extrémités des fibres optiques sont déterminées avant l'essai, sans vent. Le détecteur optique n'agit sur le mécanisme de déplacement que pour effectuer des mouvements suivant l'axe des Z et rattraper les déformations de la voilure sous charge.

5.2 - Résultats

Des mesures de déformation ont été faites à M = 0,5 - 0,7 et 0,85 en ajustant à chaque fois l'incidence de la maquette afin d'obtenir un coefficient de portance constant égal à 0,4. Les résultats sont présentés sur la figure 18. L'étagement des courbes ne correspond pas à un effet de Mach mais à une différence de charge sur la voilure correspondant à l'augmentation de la pression cinétique avec le nombre de Mach, la soufflerie S1 travaillant à pression génératrice constante égale à la pression atmosphérique.

Dans les cas d'essais sans vibration la précision des mesures est de l'ordre de 0,1 mm et est limitée par la résolution des potentiomètres placés sur le mécanisme de déplacement ; la sensibilité du détecteur lui-même est voisine de 0,01 mm.

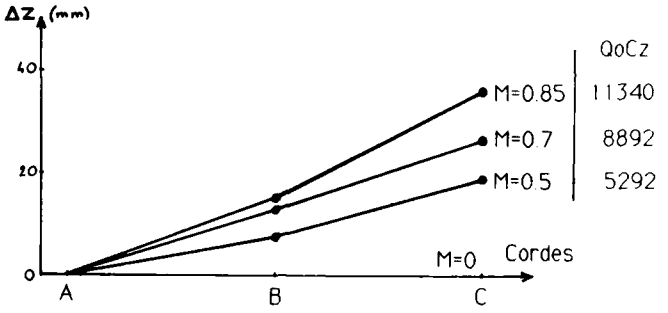

(Fig. 18) FLEXION DU BORD DE FUITE DE L'AILE POUR CZ=0.4

6 - MESURE DES DEFORMEES D'UNE PALE DE ROTOR D'HELICOPTERE PAR INTEGRATION DES CONTRAINTES

6.1 - INTRODUCTION

Les pales d'un rotor d'hélicoptère en fonctionnement subissent des déformations sous l'effet des forces aérodynamiques et massiques qui leur sont appliquées ; la connaissance de ces déformations est nécessaire à plusieurs titres :

- pour entrer dans les méthodes de calcul des rotors comme un élement indispensable dès que le calcul atteint un certain stade de perfectionnement ;
- pour compléter les mesures de pression sur les pales en fournissant les élément nécessaires pour le calcul de l'incidence aérodynamique réelle ;
- enfin, éventuellement, comme une contribution à l'étude des phénomènes vibratoires du rotor.

6.2 - CARACTERISTIQUES DU PROBLEME

Ce paragraphe présente les grandeurs à mesurer et rappelle les conditions des essais de rotor d'hélicoptère effectués dans la soufflerie S1 du centre de Modane-Avrieux.

6.2.1 - Grandeurs à mesurer

Les déformations à connaître en premier lieu sont la torsion et la flexion en battement (figures 19 et 20).

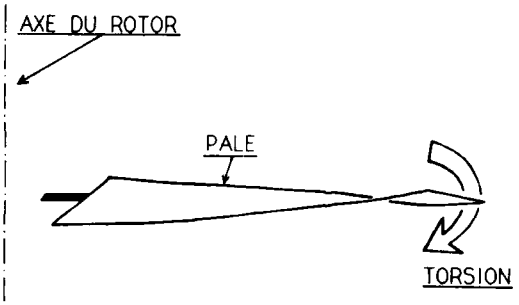

(Fig 19)

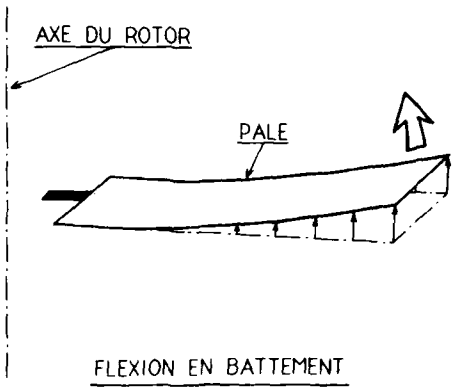

(Fig. 20)

La corde de la pale du rotor essayé est de 210 millimètres. Une torsion de 1/10 de degré induit une différence de niveau entre le bord d'attaque et le bord de fuite d'environ 0,4 millimètre.

Pour un régime établi les déformations sont des fonctions périodiques du temps, de même période que la rotation du rotor.

6.2.2 - Conditions de l'essai (figures 21 et 22)

Rotor tripale)
Diamètre : 4 mètres) plénitude σ = 0,10
Corde : 210 mm)
Profil : NACA 0012 sans vrillage sur toute la longueur de la pale
Excentricité de l'articulation de battement : 78 mm
Régimes de rotation : N_R = 870 à 1 100 tr/mn.
Vitesses en bout de pale : U = 180 à 320 m/s.
Incidence de l'arbre du rotor : α_Q de + 8° à - 32°; possibilité de placer l'axe horizontal.
Pas du rotor γ : de - 2° à + 17°.

Angle de battement β : jusqu'à $\pm$ 5° au cours d'un tour, soit un déplacement du bout de pale de $\pm$ 170 mm autour de la position moyenne.

Pour ces essais la vitesse varie de 0 à 100 m/s, et le paramètre d'avancement $\Lambda = \frac{V}{U}$ de 0 à 0,5.

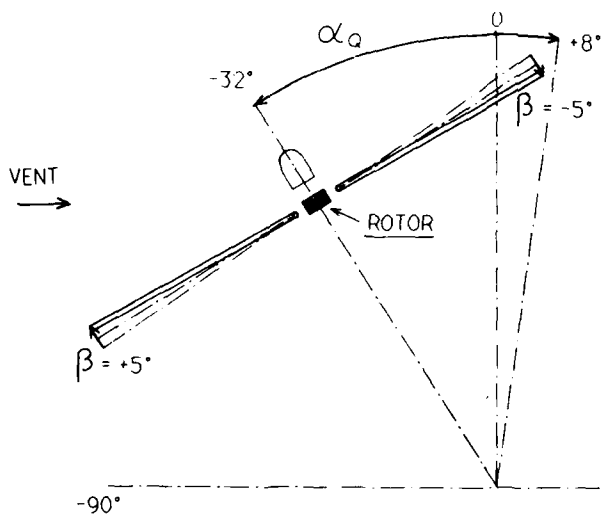

(Fig 21)

C 9 920

(Fig. 22) ROTOR D'HELICOPTERE EN FONCTIONNEMENT DANS LA SOUFFLERIE S1MA

6.2.3 - Caractéristique essentielle du problème

Toute la difficulté de la mesure des déformations apparait dans la comparaison des éléments de ces deux paragraphes : au niveau du bout de pale il faut mesurer des déformations de l'ordre du millimètre sur un objet évoluant à 200 m/s sur une trajectoire qui dépend de nombreux paramètres = α_Q, γ, β.

6.3 - PRINCIPE DU CALCUL

En cours d'essai des ponts de jauges mesurent les moments de flexion en battement et de torsion appliqués à la pale et il est en principe possible de calculer les déformations à partir de ces mesures. Pour les premiers essais, ces calculs ont été effectués avec les hypothèses simplificatrices suivantes :

- les déformations sont élastiques, donc additives. Il est possible de calculer séparément les déformations sous charges moyennes et les déformations sous charges dynamiques, la déformation totale est la somme des deux (figure 23) ;

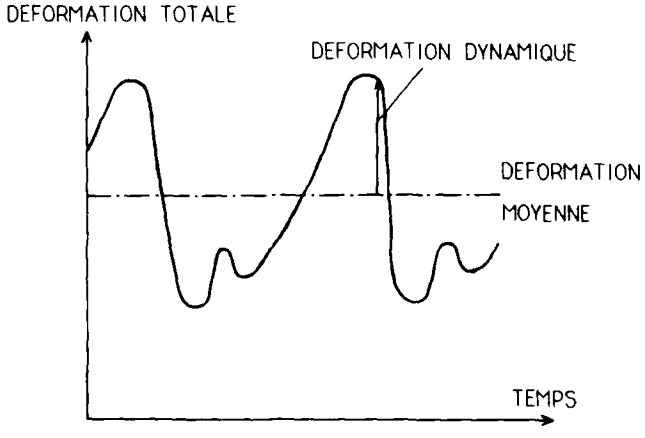

(Fig. 23)

- les coefficients de tarage déterminés sous charge statique sont supposés valables sous charges dynamiques (des précautions sont prises lors de leur mesure pour qu'il en soit ainsi) ;

- les ponts de jauges sont bien réalisés et bien placés, c'est à dire que chacun d'eux n'est sensible qu'à un seul type de déformation. Un pont de flexion en battement, par exemple, ne donne pas de signal lorsqu'on applique un couple de torsion. Il est donc admis qu'on peut calculer indépendamment les deux déformations de la pale (torsion, battement) ;

  - la courbe de répartition des moments en fonction de l'envergure est la courbe la plus tendue passant par les différents points de mesure (figure 24). Une courbe telle que celle tracée en pointillé correspondrait à des systèmes d'efforts compliqués ou bien, dans le cas des vibrations, à des vibrations de fréquences élevées donnant des amplitudes faibles, superposées à une vibration fondamentale (courbe pleine). Dans l'un et l'autre cas, pour une première approximation, seule la courbe tendue est considérée.

La courbe de répartition des moments en fonction de l'envergure étant tracée, l'équation de la déformée de la pale peut être calculée : par une double intégration dans le cas de la flexion, par une simple intégration dans le cas de la torsion.

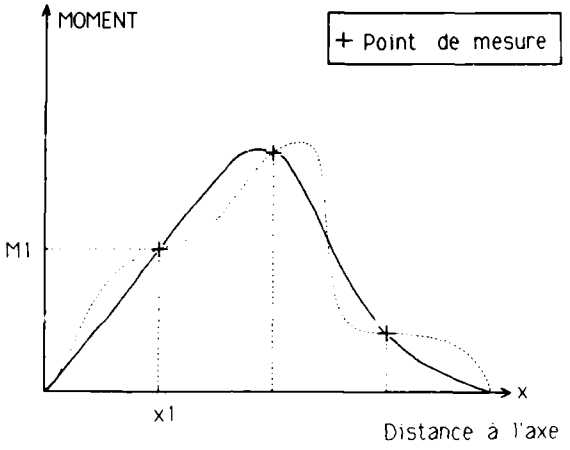

(Fig 24)

Flexion (figure 25)

x : Distance de l'axe d'articulation de la pale en battement (0_1) à une section. Positive vers l'extérieur du rotor (figure 26).
M : Moment de flexion. Fonction de x.
E : Module d'Young du matériau.
I : Moment d'inertie de la pale pour la flexion considérée.
r : Rayon de courbure de la déformée. Fonction de x.
θ : Angle entre deux sections de la pale après déformation.
y : Déplacement perpendiculaire à la pale induit par la déformation.
f : Flèche de la pale, valeur de y à l'extrémité de la pale.
l : Longueur de la pale, de l'origine au bout de pale.

La pale étant considérée comme un corps élancé, il est possible de lui appliquer les équations élémentaires:

$$\frac{1}{r} = \frac{M}{EI} = \frac{d\theta}{dx^2} = \frac{d^2y}{dx^2} \Rightarrow d\theta = \frac{M}{EI}\,dx$$

En intégrant 2 fois :

$$\theta = \int_0^x \frac{M}{EI}\,dx + \theta_0$$

$$y = \int_c^x dx \int_0^x \frac{M}{EI}\,dx + \theta_0 x + y_c$$

En prenant pour la section origine x = 0 $\theta_o = 0$ et $y_o = 0$

$$y = \int_o^x dx \int_c^x \frac{M}{EI}\, dx \qquad \text{et} \qquad f = \int_o^l dx \int_\bullet^l \frac{M}{EI}\, dx$$

Torsion

C : Couple de torsion, fonction de x.
G : Module de torsion.
I_t : Moment d'inertie en torsion.
Z : Angle de torsion
ν : Rotation en bout de pale.
Autres notations inchangées.

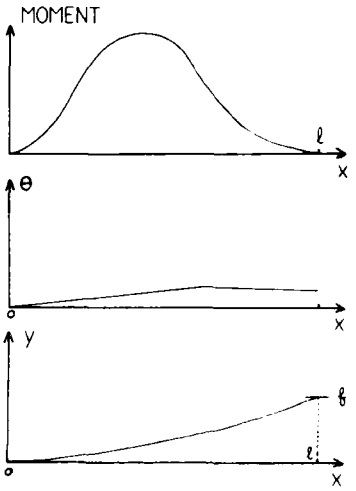

(Fig 25)

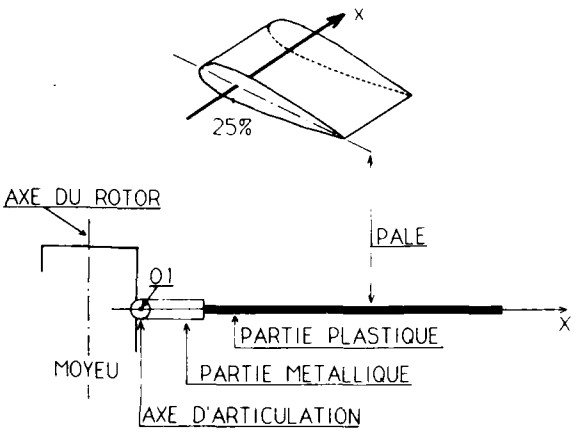

(Fig 26)

6.4 - DIAGRAMME DES MOMENTS

L'axe des x est l'axe de la pale, dans le plan de symétrie de la pale, parallèle au bord d'attaque à 25 % de profondeur, positif vers l'extérieur du rotor. L'origine est choisie en O_1, axe d'articulation en battement (figure 26). Lorsque la pale est libre autour de son articulation, le moment de flexion est nul en O_1.

Les signaux électriques fournis par les ponts de jauges sont transformés en moments et tracés en fonction du temps (donc de l'azimut ψ). Ils présentent les caractères suivants (figure 27) :

- ils sont périodiques, leur période est le tour ;
- les moments détectés par les différents ponts sont en phase ;
- leurs valeurs moyennes sont mal définies ; elles sont connues à 15 % près, parfois moins bien ;
- sous charges dynamiques le matériau des pales se comporte comme un corps élastique et la partie dynamique des signaux est régulièrement périodique en amplitude, fréquence et phase dès que les conditions d'essai sont fixées.

Pour un type de déformation choisi, par exemple la flexion en battement, plusieurs diagrammes de répartition des moments en fonction de l'envergure seront tracés (figure 28) : l'un pour la valeur moyenne des moments, les autres pour les valeurs dynamiques instantanées des moments qui correspondent aux azimuts où tous les moments passent simultanément par un maximum ou un minimum : par exemple sur le dessin de la figure 27 M_{A1}, M_{B1} et M_{C1} pour l'azimut ψ_1 et le temps t_1.

A partir de chacun de ces diagrammes on calculera l'équation d'une déformée élémentaire de la pale ; la déformée totale de la pale à un instant donné sera trouvée par combinaison de ces déformées élémentaires. Ainsi pour l'azimut ψ_1, à l'instant t_1, la déformée totale est la combinaison de la déformée moyenne et de la déformée dynamique à l'instant t_1.

Cette façon de procéder permet de donner une bonne description de l'évolution de la déformée de la pale au cours d'un tour.

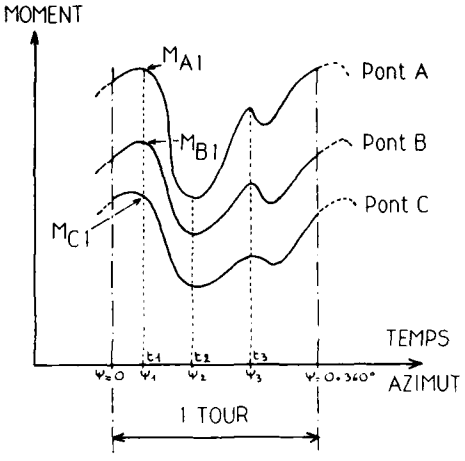

(Fig 27)

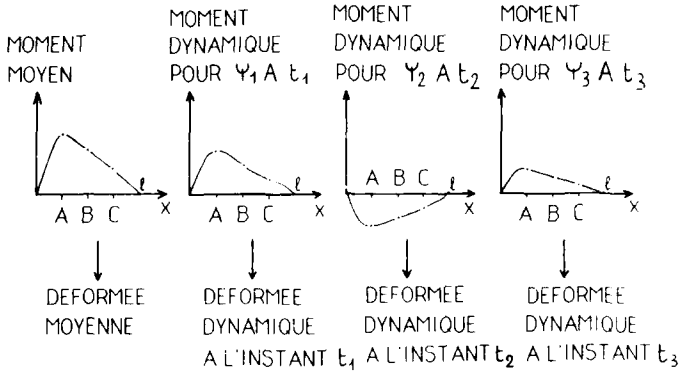

(Fig 28)

6.5 - VALEUR DE E.I (ou GI_t)

Le matériau des pales étant complexe, il est difficile de calculer les termes EI (GI_t). Ces coefficients ont donc été déterminés expérimentalement. Par exemple, dans le cas de la flexion en battement, la pale est encastrée à son attache et chargée à son extrémité libre (figure 29). En mesurant l et f il est possible de calculer EI, en effet :

$$f = \frac{Pl^3}{3EI} \qquad EI = \frac{Pl^3}{3f}$$

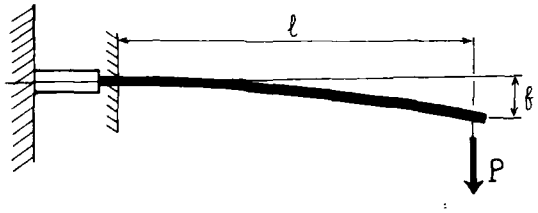

(Fig 29)

Valeurs mesurées pour les pales

flexion en battement : $EI_b = 1\,690\ Nm^2$

torsion : $GI_t = 19\ Nm^2/degré$

6.6 - EXEMPLE DE CALCUL

La suite du document est exclusivement consacrée à l'application de la méthode pour la flexion de battement, sur un cas d'essai moyen, à partir des signaux relevés en cours d'essai.

La figure 30 montre l'évolution du moment de flexion en battement en fonction de l'envergure de la pale (x) pour la valeur moyenne et les valeurs dynamiques aux azimuts ψ = 71°, 172° et 315°. La position des ponts de jauges suivant l'envergure est repérée 2 , 3 ... 8 .

La figure 31 montre l'évolution de l'angle θ entre les sections successives en envergure tracé en fonction de l'envergure de la pale (x). Les trois courbes correspondent aux charges dynamiques pour les azimuts ψ = 71°, 172° et 315° et sont obtenues (au facteur $\frac{1}{EI}$ près) par intégration des courbes correspondantes de la figure 30 précédente.

La figure 32 montre les déformées de la pale sous les charges dynamiques pour les azimuts ψ = 71°, 172° et 315° ; elles sont obtenues par intégration des courbes correspondantes de la figure 31 précédente.

La figure 33 présente directement la déformée moyenne de la pale obtenue par double intégration à partir des valeurs moyennes du moment de flexion présenté sur la figure 30.

Les déformées totales sont obtenues par combinaison des courbes des figures 32 et 33 et sont présentées sur la figure 34. L'axe ox représente la pale non déformée ; c'est cette direction qui est représentée dans l'espace par l'angle battement β . La valeur de la déformée en extrémité de pale correspond à la flèche qui pourrait être mesurée sur le saumon d'extrémité. C'est l'évolution de cette flèche en fonction de l'azimut qui est représenté sur la figure 35 (en s'aidant de calculs non présentés ici).

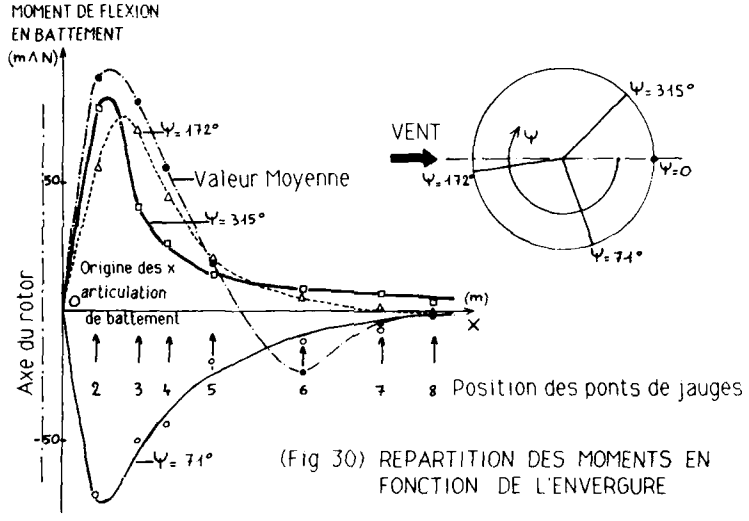

(Fig 30) REPARTITION DES MOMENTS EN FONCTION DE L'ENVERGURE

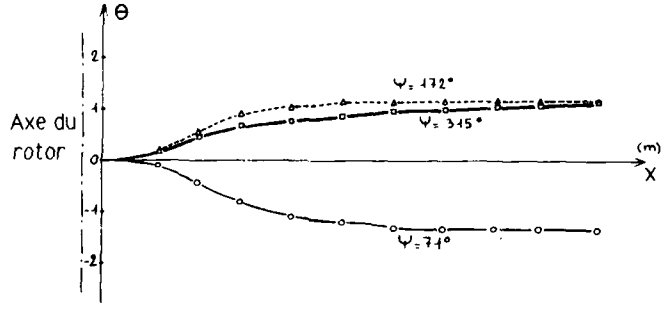

(Fig. 31) EVOLUTION DE L'ANGLE θ SOUS CHARGES DYNAMIQUES

$$\theta(x) = \int_0^x \frac{1}{EI} M(x)\, dx$$

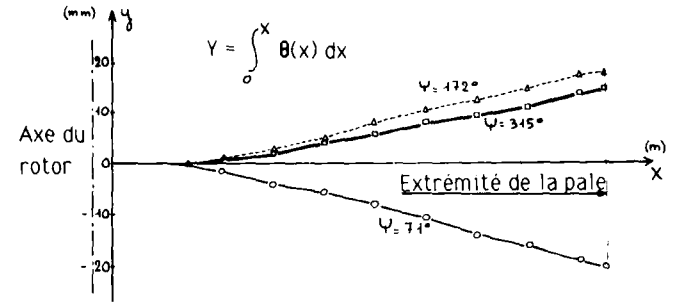

(Fig. 32) DEFORMEES SOUS CHARGES DYNAMIQUES

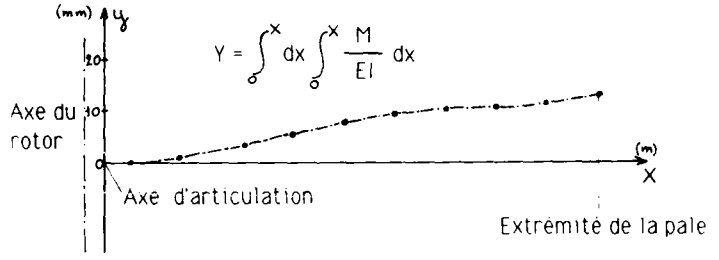

(Fig 33) DEFORMEE MOYENNE

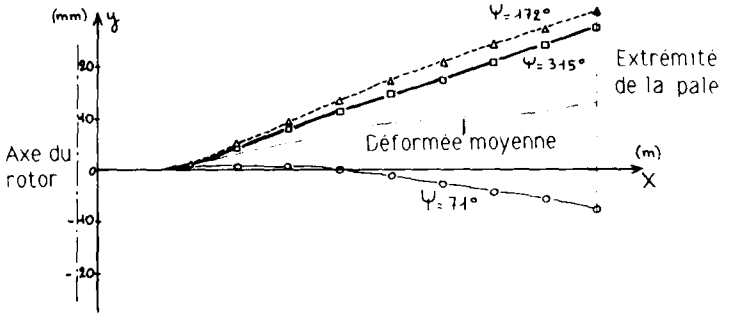

(Fig. 34) DEFORMEES TOTALES EN BATTEMENT

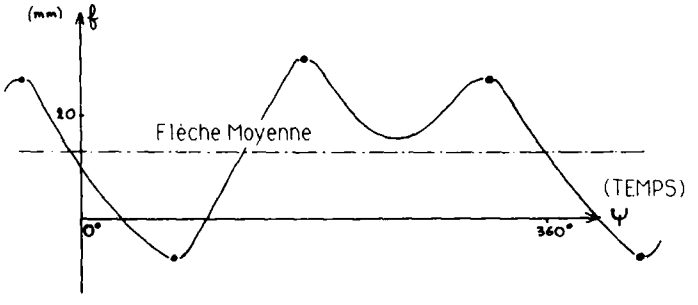

(Fig. 35)

6.7 - CONTROLE EXPERIMENTAL DE LA METHODE

L'inconvénient de la méthode est que, faute de moyens de recoupement, on ne sait quelle confiance accorder à ses résultats. Un contrôle expérimental sans vent a été effectué à l'occasion de travaux exécutés sur le rotor d'hélicoptère.

Les pales sont encastrées sur le moyeu ; le rotor est immobile. Un pot d'excitation entraine l'extrémité de la pale dans un mouvement sinusoïdal imposé. La fréquence et la force d'excitation peuvent être réglées, ce qui permet de détecter les fréquences naturelles des pales, flexions en battement (figure 36).

Pour la fréquence du fondamental de flexion en battement la déformée de la pale est relevée, ainsi que l'amplitude de la force appliquée et le déplacement du point d'excitation. Simultanément les signaux fournis par les ponts de jauges sont traités pour obtenir l'équation de la déformée. Il est alors possible de comparer les résultats du calcul aux mesures expérimentales. Le tableau ci-dessous donne les termes de cette comparaison.

Mode - Fréquence	Force d'excitation	Grandeurs caractéristiques	Expérience	Calcul par intégration
Fondamental de flexion en battement	0,2 N	Flèche en bout d'aile	5,6 mm	6,0 mm
	0,1 N		2,70 mm	3,0 mm

L'accord entre les résultats de l'expérience et du calcul est bon surtout si on considère que le tracé du diagramme des moments est approximatif du fait du petit nombre de ponts de jauges disponibles.

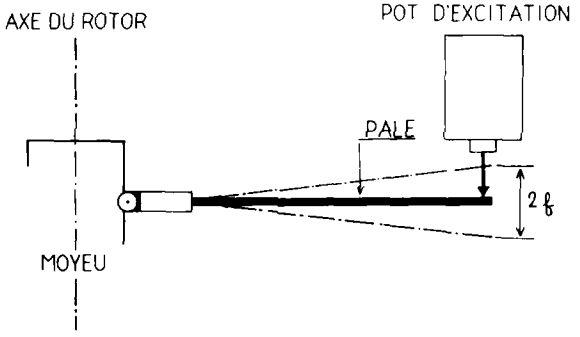

(Fig. 36)

7 - CONCLUSIONS

La direction de la Physique Générale et la Direction des Grands Moyens d'Essais de l'O.N.E.R.A. ont défini, mis au point et expérimenté des méthodes et moyens d'essai qui permettent de déterminer avec une précision satisfaisante les déformations sous charges aérodynamiques et massiques de la plupart des maquettes essayées en soufflerie.

Les techniques utilisées font appel :

- à la photographie de mires réfléchissantes,
- à la mesure faite par un torsiomètre à faisceau laser de l'angle entre le faisceau incident et le faisceau réfléchi par une mire rétro-diffusante polarisée,
- à la poursuite par un détecteur optique de position de sources lumineuses émises par des fibres optiques,
- au calcul de déformée, à partir de mesure de contraintes sur une maquette.

Ces différents moyens d'essai, utilisés de manière industrielle dans les grandes souffleries permettent aux constructeurs de s'assurer que leurs maquettes se comportent bien sous charges selon leurs prévisions ; les développements en cours devraient permettre à terme d'accroître les précisions de mesure ainsi que la rapidité d'accès aux résultats définitifs.

8 - REFERENCES BIBLIOGRAPHIQUES

[1] - J. SURGET
Model attitude and deformation measurement in wind tunnels.
Réunion "Technologie cryogénique" organisée par ETW, Amsterdam, le 15 septembre 1982 -
T.P. n° 1982-91

[2] - M. PHILBERT et G. DUNET
"Télesccpe à écartométrie optique. Application aux mesures"
La recherche aérospatiale n° 1982-3 - mai-juin

[3] - J. SURGET, M. PHILBERT et G. DUNET
"Détecteur optique pour les mesures de position et de déformations des maquettes en soufflerie".
La recherche aérospatiale n° 1982-3 - mai-juin

RECORDER'S SUMMARY

by
E. Carson Yates, Jr., Chief Scientist
Loads and Aeroelasticity Division
NASA Langley Research Center
Hampton, Virginia 23665-5225, U.S.A.

Ten papers were presented at this specialists' meeting, half of which were concerned with aeroelastic-analysis methods for specific types of aircraft. Three of the latter focused on combat aircraft (papers by Sharpe and Newton, by Petiau and Brun, and by Schmidinger and Sensburg), and two involved transport-type aircraft (papers by Roustan and Curbillon and by Eckstrom). Of the remaining papers, two were on static aeroelastic effects on flutter (by Destuynder and by Yates and Chu), two were concerned with designing, building, and testing static aeroelastic models (by Hönlinger, Schweiger, and Schewe and by Charpin, Armand, and Selvaggini), and one addressed the problem of divergence (by Niblett). This distribution of papers seems reasonably representative of the emphasis currently being given to the subject matter.

The paper by Sharpe and Newton showed that even for a relatively close-coupled cranked-delta-wing/canard fighter configuration, fuselage flexibility and freedom can significantly influence roll effectiveness and that even though fighter aircraft are designed for high load factors, inertia loads can significantly affect comparisons of longitudinal stability for the "fixed" and "free" conditions. Thus, aeroelastic modeling of the entire aircraft is needed as early as possible in the design process. Additionally, store loads (both inertial and aerodynamic) are shown to have substantial effects on wing distortion and loads for a variable-sweep fighter. Although important, early design consideration of such loads is difficult because of the multiplexity of store combinations most fighters are intended to carry.

Starting from basic principles and assumptions, Petiau and Brun presented a comprehensive tutorial review of the aeroelastic analysis methodology employed at one aircraft company, including the organization, management, and efficient use of finite-element structural models and both linear and nonlinear aerodynamic methods in application to a range of static and dynamic aeroelastic problems for complete aircraft configurations. Some familiar problems were addressed, such as the structural-aerodynamic interface, use of influence-coefficient methods and modal methods including truncation sensitivity, use of a load-basis method for problem size reduction, and modification of the computational model by use of measured data. For application to control, maneuver, and dynamics problems in general, unsteady aerodynamic forces are represented by the usual methods of rational-fraction approximation or unitary response by means of Fourier decomposition. A few applications of these state-of-the-art procedures were presented.

The paper by Schmidinger and Sensburg begins with a review of some established procedures for making aeroelastic corrections to aerodynamic coefficients and derivatives by use of increments and flex-to-rigid ratios and illustrates their application to the roll maneuver of a fighter configuration with and without wing-mounted stores. The results emphasize again the importance of combined consideration of aerodynamic and inertia forces and their effects on aeroelastic deformations and performance. This paper also presents some results of a design study to configure flaperon controls to meet specified roll requirement while minimizing hinge moment and weight of the composite structure. This seemingly modest and simply stated problem involved conflicting requirements and constraints and became a fairly complex exercise. The need for multidisciplinary computer-aided design opimization processess is again clearly indicated.

The paper by Roustan and Curbillon set forth procedures for making aeroelastic calculations and corrections based largely on linear aerodynamic and structural behavior and illustrated them in application to transport-type aircraft. Variations of coefficients with Mach number in forms like those for the rigid aircraft are represented, however, and, of course, deformations and their effects on loads may not be linear. Effects of aeroelastic deformation on aerodynamic derivatives, loads, handling qualities, control effectiveness and reversal, and divergence were considered. Requirements for aeroelastic analyses and information at various stages of the design process were pointed out, and the need to incorporate flexible-aircraft characteristics in flight simulators was also indicated.

The paper by Yates and Chu presented an attempt to calculate the effects of angle of attack and associated aeroelastic deformation on the flutter of a highly swept supercritical wing for which experiments had shown unconventional transonic flutter boundaries for angles of attack of one degree or more. An iterative procedure was established so that flutter and the statically deformed shape about which the flutter oscillation occurred could be calculated at the same dynamic pressure. The unconventional backward turn of the flutter boundary was calculated and shown to be caused by variations in mass ratio rather than by static aeroelastic deformations as had been suspected. Consideration of the latter, however, may be necessary for quantitative

accuracy. Calculated flutter speeds were unconservative because of the well-known deficiencies of potential-flow theory in predicting steady-state shock strengths and locations at Mach numbers near one. Calculations are continuing with a coupled boundary layer.

The paper by Niblett examines the trim conditions, deformations, loads, and divergence calculated for a highly simplified rectangular-wing/body/tail configuration in free flight and compares the results with conditions at fixed-root divergence speed. It is shown that as speed increases at trimmed condition, the increasing wash-in deformation of the wing must be compensated by an opposing change in angle of attack. Also, at a speed near fixed-root divergence, the horizontal-tail angle change required to produce a given increment of normal acceleration goes to zero.

The paper by Hönlinger, Schweiger, and Schewe discusses scaling requirements, design, wind-tunnel testing, measurements, and interpretation of results for aeroelastic models with emphasis on the modeling of aircraft and components with composite structures. Models with replica laminations are recommended in order to reproduce anisotropic properties faithfully. The design and testing of an aeroelastically tailored fin-rudder model are presented as examples. The development of a piezoelectric force balance is described as an attractive alternative to the conventional strain-gage balance which introduces unwanted flexibility. For the measurement of model deformations under load, an opto-electronic system has been constructed. This system employs charge-coupled devices which are focused on points on the model which are illuminated by the ends of optical fibers imbedded in the model. It would be interesting to compare the features and limitations of this system with the old-fashioned optical lever.

The paper by Eckstrom employed procedures similar to those used by an aircraft company to combine linear aeroelastic analyses with nonlinear wind-tunnel data for rigid models in order to obtain estimates of aerodynamic, stability, and control characteristics for a flexible aircraft. For example, at a given Mach number, calculated increments were applied to angle of attack for zero lift as a function of dynamic pressure, and calculated flex-to-rigid ratios were applied to lift-curve slope as a function of dynamic pressure times rigid-wing lift-curve slope. Thus, maximum lift was not changed, and the nonlinear character of the wind-tunnel data was preserved. Application of the procedure to a pilotless airplane with a very flexible transport-type research wing gave reasonable looking results, but no flexible-wing data were shown for validation.

The paper by Destuynder examined by calculations and experiments the effect of static deformation on the steady and unsteady aerodynamics and flutter characteristics of a supercritical transport-type wing model with pylon-mounted nacelle at angles of attack between plus and minus 1.5 degrees. Calculated deformations were confirmed by experiments. In flutter experiments at Mach number 0.78 and constant stagnation pressure, flutter occurred as angle of attack was decreased to -1.5 degrees - a result that is qualitatively consistent with flutter calculations by Yates, Wynne, and Farmer (fig. 8 of ref. 1 in the paper by Destuynder) for a more highly swept supercritical wing at Mach numbers 0.95 and 0.98. Modification of the unsteady aerodynamic forces by use of experimental steady-state section coefficients to account for wing deformation improved agreement between calculated and measured flutter results and showed trends with increasing stagnation pressure that were similar to those described by Yates and Chu. The results, however, were significantly influenced by nacelle aerodynamics, and the experimental flutter mode involved a considerable amount of nacelle pitching. This is yet another indication of the need to assess and incorporate the aerodynamics of pylon-mounted nacelles in flutter calculations, especially for aircraft with high-bypass-ratio engines.

The paper by Charpin, Armand, and Selvaggini described several methods which have been developed for determining the deformations of models during wind-tunnel testing. Applications are shown; accuracy and limitations are assessed. These methods include (1) photography of reflecting patterns such as the long-used procedure of superimposing or double-exposing wind-on and wind-off images of multiple markings on the model or light reflected from mirrors on the model.- The use of phosphorescent paint and ultraviolet illumination can enhance this capability. Exposure times can also be lengthened to yield a measure of model vibration amplitude. The latter technique was used years ago to measure natural vibration modes of flutter models. Deformations of rotating models, such as propellers, are obtained by stroboscopic illumination; (2) torsionmeter measurement of laser light backscattered from a polarized target.- This is an interesting technique that has produced useful results, but it does not appear to be readily adaptable to the determination of general displacements at multiple points on a model surface; (3) use of fiber-optic light sources and optical detectors.- A similar method was described by Hönlinger, Schweiger, and Schewe. The present method employs detectors supported on a secondary sting behind the model and thus may cause flow disturbances; (4) calculation of displacements by integration of measured strains.- This procedure is most appropriate when model geometry and deformations are of simple form and/or when displacements are sizeable relative to model dimensions. The deformation of helicopter rotor blades or of high-aspect-ratio wings fits these conditions. Acceptable accuracy has been obtained with these methods, but there is still need for a general method for measuring arbitrary deflections at multiple points on models of varying size and shape without flow interference and with minimum sensitivity to vibrations--in a cryogenic environment!

The emphasis on methodology for combat aircraft in this specialists' meeting is entirely appropriate because of the severity of static aeroelastic problems involved in achieving adequate maneuverability and agility of such aircraft in all speed ranges and operating conditions without unacceptable weight penalties associated with added structural mass and/or additional control surfaces and actuators. It is essential not only that we be able to analyze these aeroelastic problems accurately and reliably, but that we be able to design appropriate light-weight structures and appropriate control systems and to do it early in the design process rather than as a late-stage fix. The importance of these requirements was emphasized during recent visits to seven major U.S. aircraft companies by NASA Langley personnel. The companies still rely on linear aerodynamic and structural models to calculate aeroelastic deformations and loads. The aerodynamic/structures/inertia interface still causes difficulty, and the relations between structural stress models and aeroelastic models are still not handled in routine fashion. There is also still a major need for efficient, reliable methods for calculating aerodynamic loads on arbitrary aircraft configurations at transonic speeds and at high angles of attack. Experimental validation of such methods will be especially difficult because of the importance of Reynolds-number scaling and wind-tunnel wall effects.

With regard to design, we have already seen that even the relatively limited design problem addressed by Schmidinger and Sensburg ended up being rather involved. In view of the multitude of design variables associated with controls and control systems, as well as those involved with aeroelastically tailored composite structures, it is obvious that such design problems should be addressed within the framework of computer-aided interdisciplinary design processes, and the SMP should encourage and promote that kind of activity within the constituent countries with all deliberate speed, recognizing, however, that methods disclosure may be limited by proprietary interests.

With regard to aeroelastic analysis, we saw methods involving a wide range of complexity--from the relatively simple adjustment of wind-tunnel data given by Eckstrom to the comprehensive analysis outlined by Petiau. Various levels of analysis are needed for various purposes. Consequently, the SMP should continue to encourage the development of varied capabilities and the reporting of them through its meetings and publications. There appears to be no reason to encourage restrictive standardization of methodology nor to promote any particular favored method at this time.

The papers by Destuynder and by Yates and Chu serve to remind that when aerodynamic behavior is nonlinear, static characteristics (aeroelastic or other) can affect unsteady aerodynamics and, hence, dynamic behavior. Moreover, as was shown in those two papers, the static effects can be quite substantial. The basic message, therefore, is that for conditions involving nonlinear aerodynamic behavior, dynamic response and flutter should be calculated (or measured) about a correct static shape and loading corresponding to the relevant geometrical and flow conditions of interest. The SMP should continue to monitor and report such static/dynamic interactions as appropriate.

Similar comments apply to the subject of aeroelastic modeling and testing. Especially important is the measurement of deflection under load and/or the calculation of deflection from measured loads and structural influence coefficients. Accurate measurements of pressures and forces are of little value unless the configuration shape that generated them is also accurately known.

Finally, those involved in these and subsequent SMP activities should continue to bring to the attention of the Aeroelasticity Subcommittee information on significant problem areas in static as well as dynamic aeroelasticity (e.g., aeroservoelasticity), including those problems that were perhaps not covered in this specialists' meeting.

REPORT DOCUMENTATION PAGE			
1. Recipient's Reference	**2. Originator's Reference**	**3. Further Reference**	**4. Security Classification of Document**
	AGARD-CP-403	ISBN 92-835-0424-0	UNCLASSIFIED

5. Originator	Advisory Group for Aerospace Research and Development North Atlantic Treaty Organization 7 rue Ancelle, 92200 Neuilly sur Seine, France
6. Title	STATIC AEROELASTIC EFFECTS ON HIGH PERFORMANCE AIRCRAFT
7. Presented at	the 63rd Meeting of the Structures and Materials Panel of AGARD, in Athens, Greece, 28 September—3 October 1986.

8. Author(s)/Editor(s)	**9. Date**
Various	July 1987
10. Author's/Editor's Address	**11. Pages**
Various	188

12. Distribution Statement This document is distributed in accordance with AGARD policies and regulations, which are outlined on the Outside Back Covers of all AGARD publications.

13. Keywords/Descriptors

Meetings	Military aircraft
Aeroelasticity	Transport aircraft
Aerostatics	Wind tunnel models
Structural analysis	

14. Abstract

Modern high performance aircraft designs tend to employ very thin airfoils having a degree and a distribution of stiffness far from the ideal; in consequence, there is a loss of control effectiveness and manoeuverability. Moreover, the introduction of the highly forward-swept-wing planform poses a static aeroelastic effect of fundamental importance; these effects are felt at model as well as at full scale. This meeting was organized not only to review instances of these problems but to see how successfully modern tools for structural and aeroelastic analysis can be applied.

The individual papers of the meeting cover many aspects of static aeroelasticity not only for military aircraft but also for modern transport aircraft. The various papers also address problems and recent progress in wind tunnel model testing, in particular measurement of static deformations on wind tunnel models.

AGARD Conference Proceedings No.403
Advisory Group for Aerospace Research and Development, NATO
STATIC AEROELASTIC EFFECTS ON HIGH PERFORMANCE AIRCRAFT
Published July 1987
188 pages

Modern high performance aircraft designs tend to employ very thin airfoils having a degree and a distribution of stiffness far from the ideal; in consequence, there is a loss of control effectiveness and manoeuverability. Moreover, the introduction of the highly forward-swept-wing planform poses a static aeroelastic effect of fundamental importance; these effects are felt at model as well as at full scale. This meeting was organized not only to review

P.T.O

AGARD-CP-403

Meetings
Aeroelasticity
Aerostatics
Structural analysis
Military aircraft
Transport aircraft
Wind tunnel models

AGARD Conference Proceedings No.403
Advisory Group for Aerospace Research and Development, NATO
STATIC AEROELASTIC EFFECTS ON HIGH PERFORMANCE AIRCRAFT
Published July 1987
188 pages

Modern high performance aircraft designs tend to employ very thin airfoils having a degree and a distribution of stiffness far from the ideal; in consequence, there is a loss of control effectiveness and manoeuverability. Moreover, the introduction of the highly forward-swept-wing planform poses a static aeroelastic effect of fundamental importance; these effects are felt at model as well as at full scale. This meeting was organized not only to review

P.T.O

AGARD-CP-403

Meetings
Aeroelasticity
Aerostatics
Structural analysis
Military aircraft
Transport aircraft
Wind tunnel models

AGARD Conference Proceedings No.403
Advisory Group for Aerospace Research and Development, NATO
STATIC AEROELASTIC EFFECTS ON HIGH PERFORMANCE AIRCRAFT
Published July 1987
188 pages

Modern high performance aircraft designs tend to employ very thin airfoils having a degree and a distribution of stiffness far from the ideal; in consequence, there is a loss of control effectiveness and manoeuverability. Moreover, the introduction of the highly forward-swept-wing planform poses a static aeroelastic effect of fundamental importance; these effects are felt at model as well as at full scale. This meeting was organized not only to review

P.T.O

AGARD-CP-403

Meetings
Aeroelasticity
Aerostatics
Structural analysis
Military aircraft
Transport aircraft
Wind tunnel models

AGARD Conference Proceedings No.403
Advisory Group for Aerospace Research and Development, NATO
STATIC AEROELASTIC EFFECTS ON HIGH PERFORMANCE AIRCRAFT
Published July 1987
188 pages

Modern high performance aircraft designs tend to employ very thin airfoils having a degree and a distribution of stiffness far from the ideal; in consequence, there is a loss of control effectiveness and manoeuverability. Moreover, the introduction of the highly forward-swept-wing planform poses a static aeroelastic effect of fundamental importance; these effects are felt at model as well as at full scale. This meeting was organized not only to review

P.T.O

AGARD-CP-403

Meetings
Aeroelasticity
Aerostatics
Structural analysis
Military aircraft
Transport aircraft
Wind tunnel models

instances of these problems but to see how successfully modern tools for structural and aeroelastic analysis can be applied.

The individual papers of the meeting cover many aspects of static aeroelasticity not only for military aircraft but also for modern transport aircraft. The various papers also address problems and recent progress in wind tunnel model testing, in particular measurement of static deformations on wind tunnel models.

Papers presented at the 63rd Meeting of the Structures and Materials Panel of AGARD, in Athens, Greece, 28 September—3 October 1986.

ISBN 92-835-0424-0

instances of these problems but to see how successfully modern tools for structural and aeroelastic analysis can be applied.

The individual papers of the meeting cover many aspects of static aeroelasticity not only for military aircraft but also for modern transport aircraft. The various papers also address problems and recent progress in wind tunnel model testing, in particular measurement of static deformations on wind tunnel models.

Papers presented at the 63rd Meeting of the Structures and Materials Panel of AGARD, in Athens, Greece, 28 September—3 October 1986.

ISBN 92-835-0424-0

instances of these problems but to see how successfully modern tools for structural and aeroelastic analysis can be applied.

The individual papers of the meeting cover many aspects of static aeroelasticity not only for military aircraft but also for modern transport aircraft. The various papers also address problems and recent progress in wind tunnel model testing, in particular measurement of static deformations on wind tunnel models.

Papers presented at the 63rd Meeting of the Structures and Materials Panel of AGARD, in Athens, Greece, 28 September—3 October 1986.

ISBN 92-835-0424-0

instances of these problems but to see how successfully modern tools for structural and aeroelastic analysis can be applied.

The individual papers of the meeting cover many aspects of static aeroelasticity not only for military aircraft but also for modern transport aircraft. The various papers also address problems and recent progress in wind tunnel model testing, in particular measurement of static deformations on wind tunnel models.

Papers presented at the 63rd Meeting of the Structures and Materials Panel of AGARD, in Athens, Greece, 28 September—3 October 1986.

ISBN 92-835-0424-0